2013

Discovery of new biomarkers of mild cognitive impairment and Alzheimer's disease risk in buccal cells using laser scanning cytometry

Maxime Francois
Edith Cowan University

Edith Cowan University

Copyright Warning

USE OF THESIS

The Use of Thesis statement is not included in this version of the thesis.

DISCOVERY OF NEW BIOMARKERS OF MILD COGNITIVE IMPAIRMENT AND ALZHEIMER'S DISEASE RISK IN BUCCAL CELLS USING LASER SCANNING CYTOMETRY

Maxime François

A THESIS SUBMITTED IN FULFILMENT OF THE REQUIREMENTS FOR THE DEGREE OF DOCTOR OF PHILOSOPHY

Edith Cowan University
Faculty of Computing, Health and Science
School of Medical Science
Joondalup, Western Australia

And

CSIRO Animal, Food and Health Sciences
Preventative Health Flagship
Adelaide, South Australia

March 2013

Abstract

Previous studies have shown that mild cognitive impairment (MCI) may reflect the early stages of more pronounced neurodegenerative disorders such as Alzheimer's disease (AD). In clinical practice, patients with AD are not usually identified until the disease has progressed to a stage when primary prevention is no longer possible. Therefore there is a need for a minimally invasive and inexpensive diagnostic to identify those who exhibit cellular pathology indicative of MCI and AD risk so that they can be prioritised for primary prevention. Human buccal cells are accessible in a minimally invasive manner, and exhibit cytological and nuclear morphologies that may be indicative of accelerated ageing or neurodegenerative disorders such as AD.

The hypothesis that a minimally invasive approach using isolated buccal mucosa cells can be used to identify individuals diagnosed with MCI or AD was therefore tested using laser scanning cytometry (LSC). LSC combines the principles of flow cytometry, quantitative imaging and immunohistochemistry with high-content, multi-color fluorescence analysis, and can be used to identify specific cells in a heterogeneous population as well as scoring unique molecular events within them. This study aimed at investigating buccal cell types (buccal cell cytome) by the use of high-content LSC analysis and to detect potential biomarkers of MCI and AD risk i.e. buccal cell types, nuclear DNA content, intracellular neutral lipids, Tau protein and amyloid-β (Aβ) protein. Buccal cells were sampled from the *South Australian Alzheimer's Nutrition & DNA Damage* study (SAND) or the *The Australian Imaging, Biomarker & Lifestyle Flagship Study of Ageing* (AIBL), fixed and stained with labelled fluorescent antibodies (for detection of Aβ and Tau) and/or DAPI, Fast Green and Oil Red O dyes. In an initial study an LSC protocol was developed to identify and measure differences in buccal cell types and nuclear DNA content as well as a significant increase in micronuclei measured in AD (n=10) and Down's syndrome (n=10) compared to their respective controls (n=20). Another LSC protocol measured a significant increase in DNA content and hyperdiploidy (as measured by DAPI fluorescence) as well as a significant decrease in neutral lipid content (measured by Oil Red O staining) in buccal cells of MCI (n=22) and AD (n=15) compared to controls (n=37) from the SAND study. Using another novel LSC protocol a significant increase in Aβ was measured in buccal cells from AD (n=20) compared to controls (n=20) from the AIBL study. Immunocytochemistry and

ELISA experiments showed no significant differences in putative buccal cell Tau protein. The diagnostic value of parameters examined in these studies, individually or in combination was assessed and reported as specificity and sensitivity scores. In these studies, LSC has proven to be an efficient and useful technology for high-content analysis of buccal cells. Moreover, the changes in the buccal cell cytome observed using LSC may reflect alterations in the metabolism, cellular kinetics, gene expression, genome stability or structural profile of the buccal mucosa, and may prove useful as potential biomarkers in identifying individuals with a high risk of developing MCI and eventually AD.

Declaration

I certify that this thesis does not, to the best of my knowledge and belief:

i. incorporate without acknowledgment any material previously submitted for a degree of diploma in any institution of higher education;

ii. contain any material previously published or written by another person except where due reference is made in the text of this thesis; or

iii. contain any defamatory material

Maxime François (May 2013)

Acknowledgements

I express my sincerest thanks to Dr Wayne Leifert who has been a great supervisor and helped me tremendously with scientific and English issues which I experienced during my PhD. But more importantly I thank him for his friendship that helped me go through some of those stressful times.

I would also like to thank Prof Michael Fenech who has always been supportive and provided me with priceless guidance when it was needed the most.

Big thanks go to my family for their financial and moral support and for being there every time I needed them.

My sincere thanks also go to the following:

My academic supervisor Prof Ralph Martins for accepting me, being an off-campus student, as a part of his team.

Dr Verdile Giuseppe for being my contact in Perth and helping me a lot with administration matters.

Dr. Elena Holden and her team for looking after me in USA and teaching me so much about Laser Scanning Cytometry.

Mrs Vanessa Russell and Mr Andrej Nikolic for carrying out lipid analyses on plasma.

Mrs Candita Dang, Miss Tori Nguyen, Miss Sau Lee, Dr Jane Hecker and Dr Jeffrey Faunt for helping me with sampling and processing buccal cell samples onto microscope slides.

Miss Rebecca Rumble and Miss Sabine Matthews for their great communications and for organising sampling and shipping of buccal cells to Adelaide.

To Miss Maryam Hor for performing the visual scoring of buccal cells (chapter 4, section 4.3.7 "*Visual scoring of buccal cytome parameters*"), who is a member of Prof Fenech's laboratory and experienced in the buccal micronucleus cytome assay.
A special thank goes to my close friend Dr. Alex Burgun for all lunches and French style coffees we had over the last four years.

Mrs. Yannick Lerrant who made me appreciate molecular biology at university and without who I would not be where I am now.

I was supported by a scholarship from the government of New Caledonia (*Bourse d'encouragement à la recherche*) and a top-up scholarship from CSIRO P-Health Flagship for which I am extremely grateful to be a recipient.

Publications and Abstracts Arising From This Thesis

Wayne R. Leifert, **Maxime François**, Elena Holden, Ed Luther and Michael Fenech (2011). Automation of the buccal micronucleus cytome assay using laser scanning cytometry. Vol 102, 321-339 *Methods in Cell Biology*.

Zbigniew Darzynkiewicz, Piotr Smolewski, Elena Holden, Ed Luther, Mel Henriksen, **Maxime François**, Wayne Leifert and Michael Fenech (2011). Laser scanning cytometry for automation of the micronucleus assay. Vol 26, No 1 *Mutagenesis*.

Francois M, Leifert W.R, Thomas P, Martins R and Fenech M. (2012) – Automation of the buccal cytome and neutral lipid analyses in human buccal cells by laser scanning cytometry. *Australian Health and Medical Research* (*AHMR) Congress*.

Francois M, Leifert W.R, Thomas P, Martins R and Fenech M. (2012) – Automation of the buccal cytome and neutral lipid analyses in human buccal cells by laser scanning cytometry. *COMBIO 2012*.

Maxime François, Wayne Leifert, and Michael Fenech. (2012) Updated - Biomarkers of Alzheimer's disease in buccal cells. *Lifestyle Approaches for the Prevention of Alzheimer's Disease (LAPAD) Conference*.

Maxime François, Wayne Leifert, and Michael Fenech. (2010) Biomarkers of Alzheimer's disease in buccal cells. *Proceedings of the Australian Society for Medical Research*.

Maxime François, Wayne Leifert, and Michael Fenech. (2010) Biomarkers of Alzheimer's disease in buccal cells. *Proceedings of the 2nd Nutrional Genomics Symposium*.

Wayne R. Leifert, **Maxime François** and Michael Fenech. (2010) Quantification of intracellular protein biomarkers using laser scanning cytometry. *Human Proteome Organisation (HUPO) 9th Annual World Congress 2010*.

Maxime François, Wayne R. Leifert and Michael Fenech (2010) Discovering cytome biomarkers of Alzheimer's disease risk in isolated buccal cells using Laser Scanning Cytometry. *Human Proteome Organisation Congress* (*HUPO), 9th Annual World Congress 2010*.

Elena Holden, Judith Newmark, Connie Wong, **Maxime François**, Michael Fenech, Wayne Leifert, Zbigniew Darzynkiewicz (2011) High-content, high-throughput imaging cytometry for fully automated DNA damage analysis. *American Association for Cancer Research (AACR) 102nd Annual Meeting*.

Presentations

(by the author)

International

2012 Lifestyle Approaches for the Prevention of Alzheimer's Disease (LAPAD) Conference. Poster presentation – Updated *"Biomarkers of Alzheimer's disease in buccal cells"*. Perth. 30, 31 March.

2010 Human Proteome Organisation (HUPO). Poster presentation "*Biomarkers of Alzheimer's disease in buccal cells*". Sydney, Australia, 9th Annual World Congress, 19-23 September.

2010 Quantitative Imaging Cytometry (QIC) Symposium. Invited Workshop instructor "*Cytome diagnostics: Characterisation of DNA damage and cytome biomarkers in human buccal cells using quantitative imaging cytometry*." Boston Children's Hospital, Boston, Massachusetts, USA. 10-12 August.

2010 2nd Nutritional Genomics Symposium. Poster presentation "*Biomarkers of Alzheimer's disease in buccal cells*". Adelaide, Australia. 30 July.

2010 Quantitative Imaging Cytometry (QIC) Symposium. Invited Workshop instructor "*Automated cytome diagnostic*". CSIRO Food and Nutritional Sciences, Adelaide, Australia. 28, 29 January.

National

2012 Australian Health and Medical Research (AHMR) Congress. Poster presentation "*Automation of the buccal cytome and neutral lipid analyses in human buccal cells by laser scanning cytometry*". Adelaide, Australia. 26 November.

2012 COMBIO 2012. Poster presentation "*Automation of the buccal cytome and neutral lipid analyses in human buccal cells by laser scanning cytometry*". Adelaide, Australia. 25 September.

2011 The Centre of Excellence for Alzheimer's Disease Research and Care - One Day Symposium. Oral presentation "*Advances in Biomarkers of Alzheimer's disease in buccal cells*". Perth, Australia. 16 June.

2010 AUSBiotech SA Finalist Competition. Oral presentation *"Biomarkers of Alzheimer's disease in Buccal Cells with Laser Scanning Cytometry*". Adelaide, Australia. 30 September.

2010 The Australian Society for Medical Research (ASMR). Poster presentation "*Biomarkers of Alzheimer's disease in buccal cells*". Adelaide, Australia. 9 June.

2010 CSIRO Preventative Health Flagship Retreat. Poster presentation "*Biomarkers of Alzheimer's disease in buccal cells*". Adelaide, Australia. 26 October.

Abbreviations

8-OHdG	8-hydroxy-2deoxyguanosine
Aβ	Amyloid-β
Ab	Antibody
ABCA1	ATP-binding cassette transporter
AD	Alzheimer's disease
AIBL	The Australian Imaging, Biomarker & Lifestyle Flagship Study of Ageing
ALT	Alanine aminotransferase
ANOVA	Analysis of variance
AP	Alkaline phosphatase
APOE	Apolipoprotein E
APP	Amyloid precursor protein
AST	Aspartate aminotransferase
AUC	Area under the curve
BC	Buccal cells
BM	Buccal mucosa
BMI	Body mass index
C	Control
Cer	Ceruloplasmin
CI	Confidence interval
CK	Cytokeratin
CSF	Cerebrospinal fluid
CSIRO	Commonwealth scientific and industrial research organisation
DAPI	4',6-diamidino-2-phenylindole
DMSO	Dimethyl sulfoxide
DNA	Deoxyribonucleic acid
DS	Down's syndrome
EDTA	Ethylenediaminetetraacetic acid
eGFR	Estimated glomerular filtration rate
ELISA	Enzyme-linked immunosorbent assay
ESR	Erythrocyte sediment rate
Et:Ac	Ethanol:Acetic acid

FA	Formaldehyde
Fe	Iron
FISH	Fluorescence *in situ* hybridization
FT3	Free thyroxine
FT4	Free triodothyronine
GGT	Gamma-glutamyl transferase
HCl	Hydrochloric acid
HDL-C	High-density lipoprotein cholesterol
HDL	High-density lipoprotein
HLL	High light green
HPLC	High-performance liquid chromatography
LDL	Low-density lipoprotein
LDL-C	Low-density lipoprotein cholesterol
LH	Leutenizing hormone
LL	Light loss
LLG	Low light green
LSC	Laser scanning cytometry
NaCl	Sodium chloride
MCH	Mean cell hematocrit
MCHC	Mean corpuscular haemoglobin concentration
MCI	Mild cognitive impairment
MCV	Mean corpuscular volume
Mg	Magnesium
MMSE	Mini mental state examination
MN	Micronuclei
MPV	Mean platelet volume
mRNA	Messenger ribonucleic acid
NFT	Neurofibrillary tangle
ns	Not significantly different
O Con	Old control
ORO	Oil Red O
PBS	Phosphate buffer saline
PCR	Polymerase chain reaction
PCV	Pack cell volume

PD	Photo detector
PE	Phycoerytrhin
PI	Propidium iodide
PiB	Pittsburgh B
Pl	Plasma
Plt	Platelet count
PMT	Photomultiplier tube
PS	Presenilins
qRT-PCR	Quantitative reverse transcription-polymerase chain reaction
RCC	Red blood cell count
RDW	Red cell volume distribution
RNA	Ribonucleic acid
ROC	Receiver-operating characteristic
SAND	South Australian Alzheimer's Nutrition & DNA Damage
SEM	Standard error of the mean
Trf sat	Tranferrin saturation
Tris	Tris(hydroxymethyl)aminomethanehydrochloride
TrP	Triethyl phosphate
TSH	Thyroid stimulation hormone
WCC	White cell count
Y Con	Young control

Table of Contents

CHAPTER 1

CHAPTER 3

List of Figures

List of Tables

CHAPTER 1

1. LITERATURE REVIEW

1.1 ALZHEIMER'S DISEASE

1.1.1 History

Alzheimer's disease (AD) is the sixth leading cause of death in the United States and the most common form of dementia (Alzheimer's Association, et al. 2011). According to the World Health Organisation, the number of people suffering from AD worldwide is around 18 million and at least 4.9 million new cases are reported annually with a predicted prevalence worldwide of 80 million people suffering from the disease over the next 30 years (Ferri, et al. 2005). AD is a progressive neurodegenerative disorder, characterised by the gradual onset of dementia and leading to death usually between 7 and 10 years after diagnosis. AD is the leading cause of dementia in the elderly and affects about 5% of individuals at age 65 (Villemagne, et al. 2005). AD patients have been reported with behavioural and psychological symptoms such as lack of cooperation, tremors, depression and lack of concentration, often correlated with loss of cognitive functions (Marin, et al. 1997; Waldemar, et al. 2007; Fernandez, et al. 2010). The disease was first described by Dr. Alois Alzheimer, a German physician who published a case report detailing the pathological changes in the cerebral cortex of a 51 years old woman, Auguste Deter, with progressive dementia in the year 1907. He identified three neuropathological features in his examination of the brain of Mrs. Deter which were (1) "unusual, striking changes of the neurofibrils", (2) "deposition of a particular substance in the cortex" and (3) "numerous fibres that glia have developed" (Alzheimer, et al. 1995; Graeber, et al. 1997). Since their first description, "senile" plaques and neurofibrillary tangles (NFTs) have been the hallmark histopathological features of AD and are employed in the histological diagnosis of the disease post-mortem (Khachaturian. 1985; Mirra, et al. 1991; Hyman, Trojanowski. 1997).

1.1.2 Diagnosis

The pathogenic processes of AD are likely to begin years before clinical symptoms are observed. Indeed the early clinical signs indicating risk for AD are referred by the term

of mild cognitive impairment (MCI) that corresponds to the following criteria: Normal activities of daily living and general cognitive function but with subjective memory impairment and abnormal memory for age (Petersen, et al. 1995a; Petersen, et al. 1999; Petersen. 2000). Currently, clinical diagnosis of AD is based upon criteria of cognitive decline, memory impairments, visuospatial and language impairment as measured by the mini mental state examination (MMSE) (Petersen, et al. 2009). However this suite of tests can only provide a possible or probable diagnostic of AD in living subjects and the definitive diagnostic can only be made during post-mortem by the observation of the senile plaques and NFTs in the cerebral tissue (Armstrong. 2006; Nelson, et al. 2012).

1.1.3 Pathology

1.1.3.1 Amyloid-β

Amyloid-β (termed Aβ) is a 39-42 amino acid peptide produced by the proteolytic cleavage of the cell membrane-associated amyloid precursor protein (APP) (Martins, et al. 1991; Runz, et al. 2002). Amyloid deposits consist of abnormally misfolded proteins and are composed primarily of Aβ insoluble peptides of approximately 42 kDa generated from the precursor APP encoded on chromosome 21 (Selkoe. 2001). APP is an integral membrane protein with a single membrane-spanning domain, a large extracellular amino terminus and a short cytoplasmic carboxyl terminus (Martins, et al. 1991). APP is processed following two different pathways, called amyloidogenic and non-amyloidogenic. The non-amyloidogenic pathway involves the enzyme α-secretase (metalloproteases such as the tumor necrosis alpha converting enzyme and Adam10) which cuts within the sequence of the Aβ peptide at the 17^{th} amino acid. Following this pathway, no intact Aβ peptide is released and therefore no aggregation occurs. The amyloidogenic pathway on the other hand results in the production of Aβ peptides after cleavage of the APP by first the β- then the γ-secretase. After processing of APP by β-secretase, identified as the beta-site APP-cleaving enzyme 1, two products are generated, an extracellular soluble stub called sβAPP and an intracellular C-terminal stub called C99, respectively. The γ-secretase activity, regulated by presenilins (PS1 and PS2), is then involved to cleave the C99 at residues 40/42/43 of the Aβ sequence, generating intact Aβ peptides which aggregate rapidly into oligomers and ultimately plaques, Aβ42 being toxic to neurons and directly associated with AD pathology (Pastorino, Lu. 2006; Grosgen, et al. 2010). The Aβ42 peptide is neurotoxic and

proinflammatory, impairs memory, and represents a major constituent of cerebral amyloid plaques associated with AD (Braak, Braak. 1991; Selkoe. 1991; Barger, Harmon. 1997; De-Paula, et al. 2012).

1.1.3.2 Neurofibrillary tangles

Aberrant Tau protein is present in neurodegenerative diseases called "tauopathies" and is one of the early established hallmarks of AD in which Tau proteins accumulate in its' hyper-phosphorylated form and can lead to NFTs within neurons (Grundke-Iqbal, et al. 1986; De-Paula, et al. 2012). Encoded on a single gene located on chromosome 17 (Huang, Jiang. 2009) the Tau protein is known to have various molecular weights since there are multiple isoforms produced by alternative splicing. Six isoforms are known to exist in adult brain and the proper function of Tau depends on its state of phosphorylation regulated by several kinases, phosphatases and other Tau related proteins. The activity of protein phosphatase 2A has been shown to be compromised in AD affected brain (Gong, et al. 1993; Gong, et al. 1995; Wang, et al. 2007) and has been strongly implicated as a cause of abnormal hyperphosphorylation of Tau (Iqbal, Grundke-Iqbal. 1998; Iqbal, et al. 2005). The Tau protein in its' hyper-phosphorylated form is the main component of NFTs in AD and appears in senile plaques and dystrophic neurites in an insoluble form. This results in Tau being difficult to remove and may lead to neuronal death (Spires-Jones, et al. 2009).

1.1.3.3 Apolipoprotein E4

Apolipoprotein E (apoE) is a glycoprotein of 34 kDa synthesised in the central nervous system and is implicated in cholesterol and lipid metabolism. The gene coding for this protein is located on chromosome 19 and three common isoforms exist, known as apoE2, apoE3 and apoE4. The APOE ε4 allele was discovered to be a strong genetic risk factor for AD in a familial late-onset AD population (Strittmatter, et al. 1993). Individuals with one APOE ε4 allele are three to four times more likely to develop AD than those without this variant allele; however the ε4 allele is neither essential nor sufficient on its own to cause AD. The three apoE protein isoforms differ from each other by a single amino acid, and that difference induces an interaction between the carboxyl and amino terminal domain of apoE4 which does not occur in the two other isoforms apoE2 and apoE3 (Mahley. 1988; Dong, et al. 1994; Dong, Weisgraber. 1996;

Richard, Amouyel. 2001). The existence of this intramolecular domain interaction is believed to render apoE4 more susceptible to undergo proteolysis (Ye, et al. 2005; Mahley, et al. 2006) and this interaction is one mechanism that contributes to the astrocytic dysfunction associated with apoE4 (Zhong, Weisgraber. 2009; Zhong, et al. 2009). Exactly how APOE ε4 allele and the apoE4 protein influence the pathophysiology of AD is still unknown, but individuals who have this "risk" allele appear to be affected by AD at an earlier age and develop a heavier amyloid burden in their brains. However, studies on apoE4 and its role in AD have suggested several potential mechanisms including modulation of Aβ-caused synaptic and cholinergic deficits (Buttini, et al. 2002) as well as lysosomal leakage and apoptosis in neuronal cells (Ji, et al. 2002). Moreover, APOE ε4 genotype (heterozygous) was shown to correlate (P=0.002) with the accumulation of intraneuronal Aβ by immunohistochemistry experiments performed on brain tissue from 20 AD patients and 10 controls (Christensen, et al. 2010). Studies have also suggested a role of apoE4 in the impairment of the antioxidative defense system and mitochondrial function (Miyata, Smith. 1996; Gibson, et al. 2000; Kamino, et al. 2000; Ohta, et al. 2004), dysregulation of neuronal signaling pathways (Herz, Beffert. 2000), altered phosphorylation of Tau and NFT formation (Strittmatter, et al. 1994; Tesseur, et al. 2000; Huang, et al. 2001; Ljungberg, et al. 2002; Harris, et al. 2003; Brecht, et al. 2004) and acceleration of age-related neurodegeneration (Buttini, et al. 1999). Therefore it appears that carriers of the APOE ε4 allele exhibit a range of altered states of cellular signaling which in combination, may lead to a higher susceptibility to AD.

1.1.3.4 Lipids

There have been several studies that demonstrated a variety of lipid classes (e.g. ceramide, cholesterol, plasmalogen, and sulfatide) are substantially altered at a very early stage during AD pathogenesis (Han, et al. 2001; Han. 2005). Additionally, the phospholipid and neutral lipid composition was found to be modified in different regions of the brain of subjects who had suffered from AD (Soderberg, et al. 1990). It was reported that n-3 long chain polyunsaturated fatty acids (mainly docosahexaenoic acid, which is essential for cerebral functions), as well as monoenes (mainly oleic acid) declined in lipid rafts of brain tissues sampled post-mortem from the frontal cortex of AD subjects, when compared to age-matched controls ($P<0.05$) (Martin, et al. 2010).

Alterations in lipids were also observed in mice with cholesterol, phospholipids, docosahexaenoic acid and arachidonic acid that were significantly reduced in the cortex of 9 month old AD mice compared to age-matched control mice (Yao, et al. 2009). Additionally, docosahexaenoic acid was found to exert potential protective actions towards neurotoxicity (i.e. amyloid burden, synaptic dysfunction, and learning and memory deficits) induced *in vivo* by Aβ in AD mice (Oster, Pillot. 2010). Cholesterol levels have been outlined as a risk factor for AD (Martins, et al. 2006; Martins, et al. 2009) and in brains of aging and AD patients, cholesterol metabolism was found to be affected resulting in an increased level of total cholesterol (Cutler, et al. 2004; Xiong, et al. 2008). Previous studies in both animal (transgenic mice FAD mutants $APP_{K670N,M671L}$ and $PS1_{M146V}$) and cellular (primary neurons) AD models indicated that intracellular cholesterol distribution can regulate Aβ (considered the main biomarker of AD) biogenesis in the brain (Puglielli, et al. 2003). Moreover variations in cholesterol levels of plasma membrane may play a role in the regulation of Aβ production and APP endocytosis (Cossec, et al. 2010). Additional data indicated that levels of cholesterol and its precursors were reduced in cerebrospinal fluid (CSF) sampled from AD (Kolsch, et al. 2010). Furthermore, relative to controls, altered levels of plasma apoE in AD have been observed (Taddei, et al. 1997; Gupta, et al. 2011). Evidences suggest that it is conceivable that lipid metabolism plays an important role in the neuropathological development of AD.

1.1.4 Biomarkers of AD risk

1.1.4.1 Relevance of a test for AD

The pathogenic processes of AD are likely to begin years before clinical symptoms are observed and as the prevalence of AD is doubling every five years between 65 and 85 years of age (WHO Press. 2006), the need of biomarkers has become urgent. Moreover AD does not only alter the quality of life, health and wellbeing of those affected but also leads to a significant financial burden in society (Sloane, et al. 2002). The mechanisms responsible for AD are unclear, and effective therapies are lacking. However, in combination with clinical methods and cognitive tests, it is anticipated that biomarkers will soon contribute to a more accurate assessment of the pathology caused by AD before the onset of cognitive dysfunction. Therefore, biomarkers for an early diagnostic of the disease would tremendously benefit the community as treatment strategies will

likely to be most effective in preserving brain function, if administered early in the disease process before symptoms develop.

1.1.4.2 Rationale for the use of peripheral tissue for biomarkers of AD

The scientific community has been actively investigating potential early biomarkers of AD. Currently, the majority of investigators have used blood, CSF or brain imaging. In terms of direct brain imaging, Pittsburgh B (PiB) compound was used and shown to be able to readily detect Aβ protein aggregation forming senile plaques in specific regions of the brain, however it has been shown in some case reports that the accumulation of large plaques are necessary for PiB imaging to be useful (Leinonen, et al. 2008; Cairns, et al. 2009). Additionally, CSF has been used to identify changes in Tau protein levels (Blennow, Zetterberg. 2009; Prvulovic, Hampel. 2011). However, these methods of investigations are either too invasive and/or expensive (Blennow, Zetterberg. 2009; Thambisetty, Lovestone. 2010; Hampel, Prvulovic. 2012). Therefore, if screening of populations of individuals is to be performed, more suitable, easily accessible tissues would need to be utilised, also using diagnostic tests at much lower costs with high specificity and sensitivity. This need for minimally invasive tests could be achieved by targeting surrogate tissues reflecting systemic susceptibility as recent evidence indicates that AD is not a disorder restricted to pathology and biomarkers within the brain, but also appears in non-neural tissues (Schupf, et al. 2008; Thomas, et al. 2008b; Arnold, et al. 2010; Migliore, et al. 2011; Neumann, et al. 2011).

1.1.4.3 Peripheral tissue as source for AD biomarkers

1.1.4.3.1 Fibroblasts

The plausibility that AD risk is reflected in cellular biomarkers in peripheral tissue has been investigated by studying some well-known markers of genomic instability that have been reported to increase with age, and therefore suggest that the capacity for repair of DNA damage may also be altered in AD (Fraga, et al. 1990; Goukassian, et al. 2000; Wilson, et al. 2008). Micronuclei (MN) are acentric chromosomal fragments occurring during cell division and one of the well characterised biomarkers of genomic instability. In fibroblasts for example, MN frequency has been shown to be increased with advancing age (Antoccia, et al. 1993) as well as in AD (Trippi, et al. 2001; Migliore, et al. 2011). Down's syndrome (DS) is also considered a premature ageing

syndrome leading to dementia and is associated with abnormally high levels of DNA damage (Jovanovic, et al. 1998; Perluigi, Butterfield. 2012). Furthermore, DS (trisomy 21) patients express brain changes that are histopathologically indistinguishable from AD by the 4th decade of life (Geller, Potter. 1999; Thomas, Fenech. 2008). As the APP gene is encoded on chromosome 21 (Selkoe. 2001), it has been suggested that one of the underlying mechanisms of AD could be the altered expression of this gene, leading to accumulation of the aggregating form of Aβ peptide. Peripheral tissue such as skin fibroblasts from familial and sporadic AD has been shown to exhibit a 2-fold increase in trisomy 21 levels when compared to controls (Geller, Potter. 1999). Moreover, an increase in immunostaining of amyloid peptides (Aβ40, Aβ42) as well as an imbalance between free cholesterol and cholesterol ester pools has been observed in fibroblasts of AD (Pani, et al. 2009a). The capacity of fibroblasts to spread in culture was also observed to be altered in AD, as well as their calcium content that was shown to decrease in terms of cytosolic free calcium ($p<0.001$) and increase in terms of total bound calcium when compared to age-matched controls (Peterson, Goldman. 1986; Peterson, et al. 1986).

1.1.4.3.2 White blood cells

Tau protein, one of the main proteins known to be associated with AD interacts with microtubules, actin filaments and intermediate filaments to play a key role in regulating the organisation and integrity of the cytoskeleton (Binder, et al. 1985). An increase in the phosphorylation levels of Tau was reported to occur due to the compromised function of protein phosphatase 2A in AD brains (Gong, et al. 1993; Gong, et al. 1995). Tau protein was shown to be elevated in CSF of AD patients and is an accepted biological marker of AD (Blennow, Zetterberg. 2009; Prvulovic, Hampel. 2011). This important marker of AD has also been investigated in lymphocytes. As a result, both phosphorylated and non phosphorylated forms of Tau were detected by Western blot and shown to be significantly increased in AD compared to controls (approximately 2-fold increase), with a direct correlation between those two forms of Tau (Armentero, et al. 2011). In terms of DNA damage, differences were also observed in AD. Evidence of the nuclear accumulation of γH2AX, a phosphorylated protein that accumulates following induction of DNA double strand breaks, has been observed in astrocytes of AD brains (Myung, et al. 2008). Oxidative stress which results in the accumulation of

oxidised DNA base adduct 8-hydroxy-2deoxyguanosine (8-OHdG), is also believed to be involved in a number of neurodegenerative diseases (Giasson, et al. 2002; Migliore, Coppede. 2002; Perry, et al. 2002) and has been shown to occur prior to the pathology hallmarks of AD (Nunomura, et al. 2001). An approximate 5-fold increase in 8-OHdG was observed in CSF of AD compared with controls ($P<0.001$) and may partly explain the DNA damage that has been observed in AD cases (Abe, et al. 2002). The comet assay, which can be used to assess both single and double strand breaks in DNA, has been utilised to demonstrate that peripheral leukocytes exhibit an increase in DNA damage markers in AD with respect to controls ($P<0.001$) (Migliore, et al. 2005). Individuals with MCI have also been used to study biomarkers of AD since this group shows an approximate 50% of conversion into AD over 4 years (Petersen, et al. 1995b) and it is interesting to note that the level of oxidative damage is lower in AD compared with MCI (Migliore, et al. 2005). This may suggest that this type of DNA damage decreases as the disease progresses further. Genomic instability markers such as MN seem to increase in lymphocytes with age (Fenech, Morley. 1986) and AD when compared to healthy controls (Migliore, et al. 1997; Migliore, et al. 1999; Migliore, et al. 2011).

Another marker of genetic instability, telomere length, is known to change with ageing and in some cell types involves progressive telomere shortening. Telomeres are highly conserved DNA sequence repeats (of TTAGGG) involved in the maintenance of genome stability. Telomere length can be assessed by a variety of methods including southern blot, flow cytometry, quantitative fluorescence *in situ* hybridisation (FISH) or by quantitative reverse transcription-polymerase chain reaction (qRT-PCR) (Bull, et al. 2009; Kimura, et al. 2010; Takubo, et al. 2010; O'Callaghan, Fenech. 2011). Shortened telomeres have been shown to be associated with an increased risk of cardiovascular disease and degenerative disease such as cancers (Artandi, et al. 2000; Samani, et al. 2001; Cawthon, et al. 2003; Wu, et al. 2003). Studies have shown a decrease in telomere length in lymphocytes isolated from AD (Panossian, et al. 2003; Jenkins, et al. 2006). The telomere shortening has also been investigated in white blood cells of confirmed AD cases and found to be significantly shorter in those AD patients compared with young and old controls ($P<0.0001$) (Thomas, et al. 2008b). Lymphocytes from AD cases or first degree relatives also show substantial differences relative to controls with respect to intracellular lipids (Pani, et al. 2009b). Oil Red O

(ORO) staining (indicative of accumulation of neutral lipids) has been used to demonstrate higher levels of neutral lipids in peripheral blood mononuclear cells of probable AD patients (Pani, et al. 2009b). This study from Pani et al. 2009b demonstrated that approximately 85% of isolated lymphocytes from AD had high neutral lipids levels (mainly cholesterol ester) as well as an increased content of the Acetyl-Coenzyme A acetyltransferase-1 protein (the enzyme that catalyses the formation of cholesterol esters in cells) compared with cognitively normal age-matched controls. These data suggest that intracellular cholesterol ester levels are systematically increased in AD patients and support the hypothesis of altered lipid metabolism in AD.

1.1.4.3.3 Platelets

Platelets have also been investigated in AD and found to express changes with the disease state. For instance the ratio of two isoforms products of APP processing that occurs in platelets was studied as a potential biomarker and found to be decreased in platelet membranes in AD and MCI compared with their respective controls (Padovani, et al. 2002; Schneider, et al. 2009; Borroni, et al. 2010). The presence of phosphorylated and non phosphorylated Tau protein was detected by immunofluorescence as well as different variant forms of Tau using Western blot techniques. Those different immunoreactive fractions of Tau separated by Western were combined to obtain a ratio of high (>80 kDa) and low (<80 kDa) molecular weight bands. The ratio of the high/low molecular weight bands (when quantified by imaging) was found to be significantly increased in AD compared to healthy controls (t-test P=0.0001) (Neumann, et al. 2011).

1.1.4.3.4 Olfactory epithelium

Olfactory dysfunction is common in neurodegenerative diseases, appears as one of the first symptoms in AD and is commonly used to assess memory in mice (Yang, Crawley. 2009; Cheng, et al. 2011). In humans, the olfactory epithelium was shown to be a peripheral tissue reflecting changes in AD by expressing Aβ and hyperphosphorylated Tau at various rates. Detection was performed by immunohistochemistry and a significant increase in frequency of both Aβ ($P<0.001$) and hyperphosphorylated Tau ($P<0.05$) was observed when compared to controls (Arnold, et al. 2010). Post-mortem neuropathological examinations of participants' brains were also undertaken and a strong correlation was determined between Aβ frequency in olfactory epithelium and

averaged Aβ frequency in multiple cortical regions (i.e. hippocampus, entorhinal cortex, amygdala, superior/middle temporal gyri, angular gyrus, mid-frontal gyrus, and anterior cingulate cortex); ($P<0.001$) (Arnold, et al. 2010). A slighter but still existent correlation was also found when examining hyperphosphorylated Tau in olfactory epithelium and in brains ($P<0.03$) (Arnold, et al. 2010). Therefore, presence of Aβ and Tau immunostaining should also be investigated in peripheral tissue such as olfactory epithelium.

1.1.4.3.5 Plasma

Biomarkers of risks are a key in the prediction of AD; amyloid plasma levels have been investigated and linked to an increase in the risk for AD. A review of cross-sectional and longitudinal studies that examined plasma levels of Aβ indicates that baseline levels of Aβ40 and Aβ42 might predict higher rates of progression towards AD (Song, et al. 2011). Moreover higher levels of Aβ42 were also associated with a 3-fold increase of AD risk (Schupf, et al. 2008). Levels of plasma amyloid also seem to decrease following conversion to the disease and have been more recently studied as a predictive marker of cognitive decline (Cosentino, et al. 2010). The evidence discussed above suggests that AD is a systemic disorder that can be reflected in peripheral tissue and therefore investigations involving minimally invasive tissue for sampling cellular biomarkers of MCI/AD risk need to be further investigated.

1.2 BUCCAL CELLS

1.2.1 Buccal cells as a material for analysis

Buccal mucosa (BM), like the brain and skin epithelium cells, are derived from differentiated ectodermal tissue during embryogenesis and therefore would be a non-neural tissue that may have the potential to reflect the underlying pathological changes observed in AD. Buccal cells have been used as a source of tissue in a variety of biochemical and molecular biology studies using an assortment of different techniques to collect the cells including; cotton swabs (Richards, et al. 1993), cytobrushes (Richards, et al. 1993; Patten, et al. 1996; Garcia-Closas, et al. 2001; King, et al. 2002), a “swish and spit” method (Hayney, et al. 1996; Lum, Le Marchand. 1998; Feigelson, et al. 2001) a modified Guthrie card (Harty, et al. 2000) and a method of rubbing cheeks

against teeth to exfoliate cells (King, et al. 2002). The results from those studies demonstrated that high quantities of buccal cells, more than a million, could be obtained and then subsequently used in a variety of assays; such as DNA analysis using PCR or other genotype tests (de Vries, et al. 1996; Hayney, et al. 1996; Lum, Le Marchand. 1998; Guangda, et al. 1999; Myerson, et al. 1999; Le Marchand, et al. 2001), for isolation of mRNA for gene expression profiling, Western blots for detection of proteins and immunocytochemistry (Hattori, et al. 2002; Michalczyk, et al. 2004; Spivack, et al. 2004), high-performance liquid chromatography (HPLC) (Borthakur, et al. 2008) and ion transporter assays (Patten, et al. 1996). Ideally invasive procedures should be avoided in AD patients due to age and presenting medical issues, therefore buccal cells could offer an appropriate alternative as a relatively non-invasive and easily accessible source of tissue for analysis. Furthermore, buccal cells have been shown to be osmotically stable in hypotonic solutions including water (Lee, et al. 1994), and are more difficult to disrupt or lyse than typical cultured cells or tissue [unpublished observations], making them more easily processed with less risk of losing intracellular contents during investigation procedures. Additionally, we have found that buccal cells can be readily preserved for Western blotting of cellular protein, cytology and immunocytochemistry studies by isolation directly into Saccomanno's solution (contains 50% ethanol) and stored at 4^{o}C for up to 4 weeks [unpublished observations – see later sections of this thesis]. Therefore it would be possible to isolate buccal cells from patients in remote regions and facilitate storage of samples in laboratories.

1.2.2 Morphological changes in buccal cells

For the BM to be a valuable tissue to study for biomarkers of AD, the BM would need to exhibit changes within the cells that correlate well with the disease state. Structurally, the BM is a stratified squamous epithelium consisting of four distinct layers (Veiro, Cummins. 1994; Masters, et al. 1997; Squier, Kremer. 2001) as shown in Figure 1. First the stratum corneum lines the oral cavity. Below this layer, is located the *stratum granulosum*, and the *stratum spinosum* containing populations of differentiated, apoptotic and necrotic cells. The next layer contains the *rete pegs* or *stratum germinativum* composed of basal cells, which, by cell division and DNA replication regenerate and maintain the profile, structure and integrity of the BM (Squier, et al. 1976). The basal cells are believed to differentiate and migrate to the keratinised surface

layer in 7 to 21 days. With normal ageing the efficiency of cell regeneration decreases (Hill. 1994a; Squier, Kremer. 2001) resulting in a thinner epidermis and underlying cell layers (Hill. 1994b). The protective function of the *stratum corneum* is not altered (Hull, Warfel. 1983) but the *rete pegs* adopts a more flattened appearance (Thomas. 2001; Burns, et al. 2004).

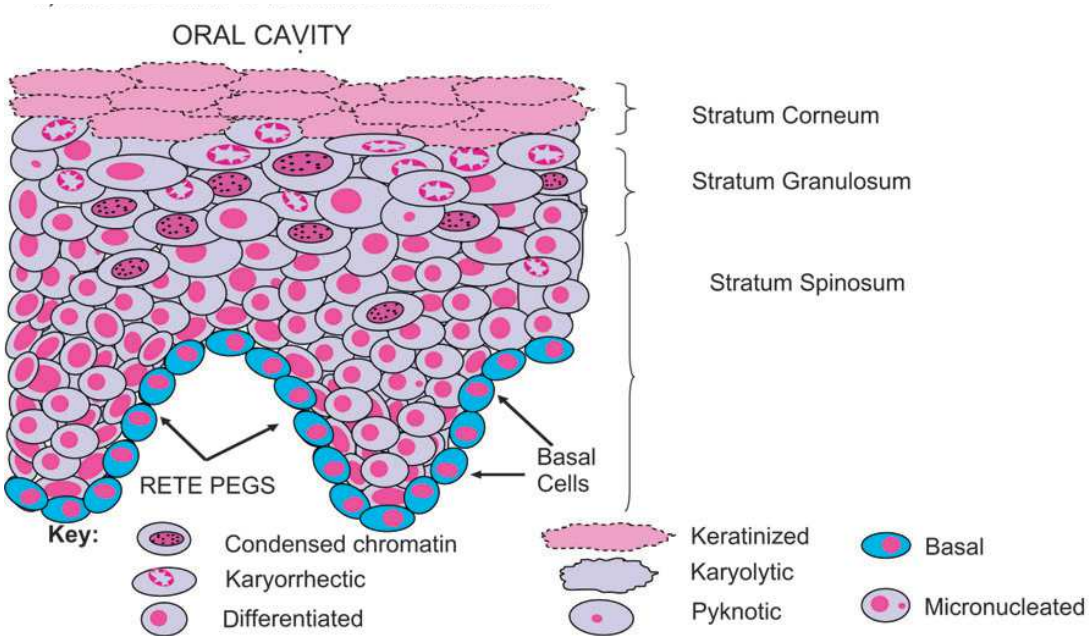

Figure 1: Diagrammatic representation of a cross section of normal BM.
The mucosa of healthy individuals illustrating the different cell layers and possible spatial relationships of the various cell types are shown. Adapted from Thomas et al. 2009.

Since buccal cells and the nervous system are derived from the same germ cell layer, the ectoderm, the regenerative potential of BM might be affected in parallel with the regenerative potential of the brain, which is found to be altered in AD. One study investigated the BM's different cell types and its composition in AD compared with age-matched controls (Thomas, et al. 2007). Frequencies of the various cell types have been measured and an alteration of the BM composition was shown to occur in AD. A significant decrease in the frequency of basal cells, karyorrhectic and condensed chromatin cells ($P<0.0001$) were found in an AD cohort, whilst a significant decrease in the frequency of condensed chromatin cells and increase in MN ($P<0.001$) were observed in a DS cohort when compared to the age-matched control groups (Thomas, et al. 2007; Thomas, et al. 2008a) as shown in Figure 2. Using two parameters, basal cells

and karyorrhectic cells, separation of AD and controls reached a specificity of 96.8% and sensitivity of 82.4% (Thomas, et al. 2007). This segregation of cell types has also been shown possible in an automated manner using imaging analysis by laser scanning cytometry (LSC) (Leifert, et al. 2011), making this cytome assay more feasible for scoring on a larger study scale. Another study aimed at assessing morphologic and cytometric aspects of cells of the oral mucosa of AD patients using the Papanicolaou staining method (Papanicolaou. 1948). A visual assessment of cell types was made by microscopy and cytological parameters were measured using the Image J analysis software. The results of that study demonstrated a significant reduction in the number of intermediate cells ($P<0.05$) as well as in their nuclear:cytoplasmic area ratio ($P<0.0001$) in the AD group compared to the controls (de Oliveira, et al. 2008). Both studies suggest that changes occur in the BM of those diagnosed with AD in terms of cytological features and cell type composition which may indicate a decrease in the regenerative capacity of the BM in AD. Additionally APP is ubiquitously expressed and may be involved in stimulation and proliferation of keratinocytes where they are mostly expressed in the basal layer (Kummer, et al. 2002). Investigation of APP expression in the BM may therefore reveal information regarding the regeneration potential of that tissue.

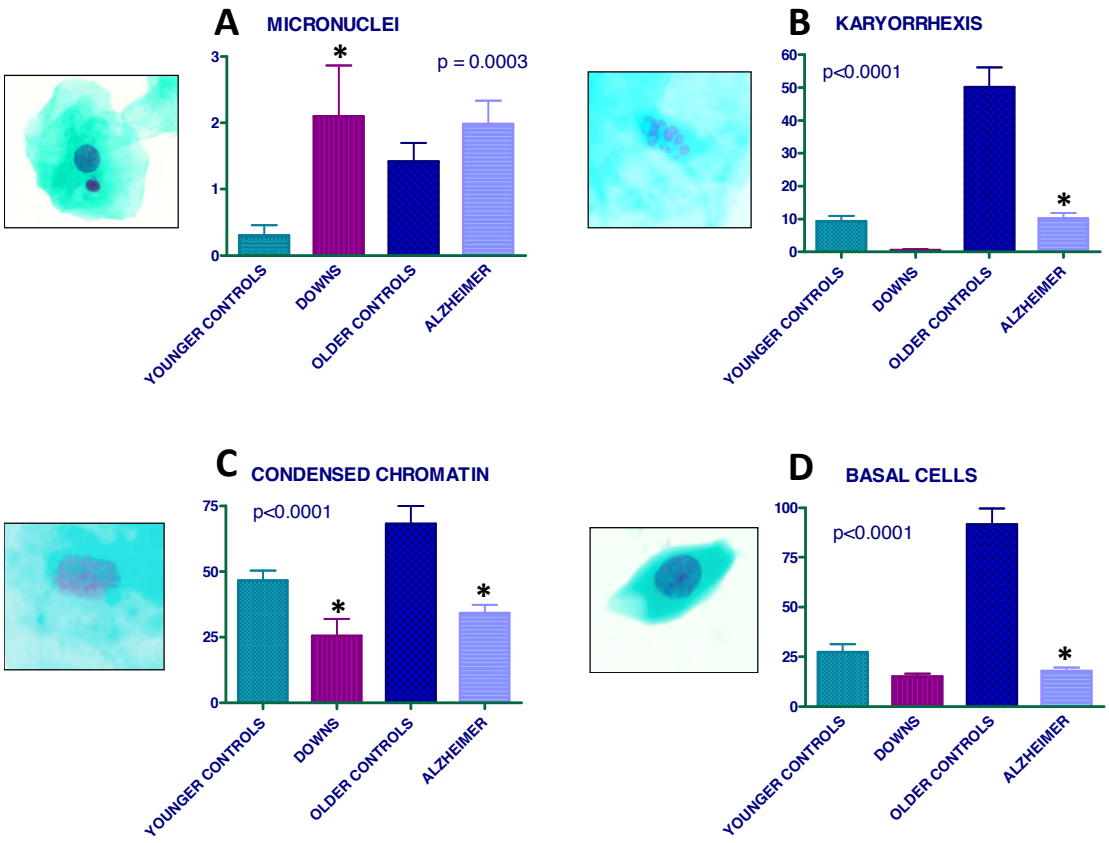

Figure 2: Buccal micronucleus cytome in AD and DS.
Shows the number of (A) MN, (B) karyorrhectic cells, (C) cells with condensed chromatin and (D) basal cells scored per thousand cells between AD (n=31), DS (n=21) and their respective controls (n=56). A picture of a cell associated to each bar graph is shown as an example of these parameters measured. Adapted from Thomas, et al. 2007 and Thomas, et al. 2008a.

1.2.3 Cytokeratins – Biochemical cell type segregation

Buccal cells contain groups of structural proteins called cytokeratins (CK) (Anderton. 1981), that are found to be expressed in a tissue specific manner (Moll, et al. 1982a; Tseng, et al. 1982). Buccal cells normally express CK 4,5,13,14 and possibly 19 depending on their cell types (Moll, et al. 1982a; Vaidya, et al. 1989); CK5 and CK14 are predominantly expressed in the basal layer but after a period of differentiation and migration, buccal cells begin expressing CK4 and CK13 accompanied with a progressively reduced expression of CK5 and CK14 (Clausen, et al. 1986). Additionally our preliminary results (unpublished observations) showed that some buccal cells were positive for CK5 whilst others were positive for CK13, others were both CK5 and CK13 positive, whilst yet another population of buccal cells were negative for CK5 and CK13

(Figure 3). Another study also showed that CK10 and CK8 were detected in low amounts in buccal cells using immunocytochemistry and that β-actin was abundant and could be used as a loading control in Western blotting (Clausen, et al. 1986). Interestingly, differential expression of CK proteins, such as CK5, has been observed in carcinomas of the BM (Vaidya, et al. 1989; Lueck, Robinson. 2008). For instance, in mucoepidermoid carcinoma there was a strong correlation of high levels of CK5 expression (in oral mucosa) with poorer survival times ($P<0.001$). Specifically, at the completion of that study, 12 (of 13) patients with high levels of CK5 expression were deceased, compared with 6 patients out of the 18 patients with the lowest values of CK5 expression (Lueck, Robinson. 2008). Since CK expressions have been widely shown to differ in the BM with cell types (Moll, et al. 1982a; Vaidya, et al. 1989), developmental stage (Banks-Schlegel. 1982; Moll, et al. 1982b), tissue differentiation (Tseng, et al. 1982; Woodcock-Mitchell, et al. 1982; Clausen, et al. 1983; Sun, et al. 1983; Breitkreutz, et al. 1984; Schweizer, et al. 1984) and pathological conditions (Loning, et al. 1980; Steinert, et al. 1980; Staquet, et al. 1981; Bowden, et al. 1983; Matoltsy, et al. 1983; Winter, et al. 1983; Weiss, et al. 1984), they could provide information on the proliferation and differentiation profile depending on the disease state. Furthermore CK staining of BM may offer a convenient immunocytochemical manner of separating cell types which can also be scored in an automated manner in AD patients.

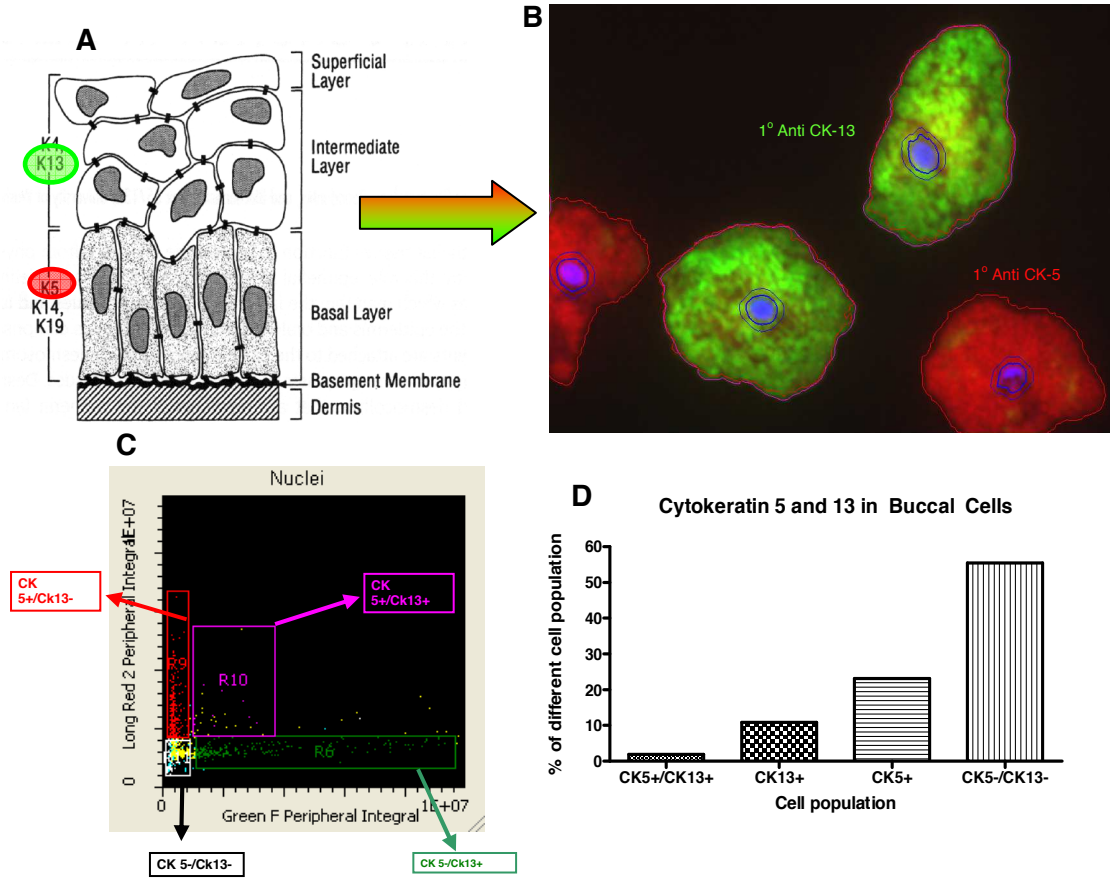

Figure 3: Preliminary results using immunocytochemistry techniques showed a difference in expression of CK5 and 13 within buccal cells.

(A) Schematic showing the differential expression of CK within the buccal cell layers. (B) CK5 and 13 were detected using an immunocytochemistry dual-staining technique, cells expressing CK13 were detected with a secondary antibody 488 Alexa Fluor (Green) and cells expressing CK5 were detected with a secondary antibody 647 Alexa Fluor (Red). (C) Using LSC different populations of cells were separated depending on the type of CK expressed. (D) From the scattergram in (C), the percentage of buccal cell types based on CK5/13 expression is shown.

1.2.4 Buccal cells and Tau

Accumulation of Tau forming NFTs in the brain is one of the main hallmarks of AD and has a major role in neuronal death. Hattori et al. (Hattori, et al. 2002) demonstrated the presence of multiple bands of Tau on Western blots, that were the non-phosphorylated form of Tau protein in buccal cells with the prominent appearance of two bands at approximately 65 kDa and 110 kDa, using the monoclonal BT-2 antibody. Using enzyme-linked immunosorbent assay (ELISA) techniques, total Tau protein was shown to be significantly elevated within buccal cells of AD compared with age-matched controls ($P<0.01$). Furthermore, the increase in Tau of oral epithelium was shown to be significantly correlated with the Tau level in CSF and was also higher in

AD subjects when diagnosed at a younger age of onset than with patients at later age of onset (Hattori, et al. 2002). Therefore it is feasible that oral Tau may be measurable and may be a useful predictive biomarker of AD; however this has not been verified yet in other studies and awaits replication.

1.2.5 Buccal cells and amyloid

Aβ is the main component of senile plaques appearing in the brains of AD. It is generated by the processing of its precursor APP. The expression of APP was shown to be present in the buccal pouch of hamsters and APP is believed to promote the development of oral carcinogenesis (Ko, et al. 2007). The biopsy of oral tissues for instance has been advocated as an alternate method of detecting amyloid deposition in amyloidosis (Stoopler, et al. 2003) confirming that amyloid can accumulate to detectable levels in peripheral tissue such as the liver in systemic amyloidosis (Lovat, et al. 1998). APP has previously been investigated in young adult Wistar rats and localised by immunohistochemistry in several peripheral tissues, i.e. liver, kidney, spleen, pancreas, salivary gland, testis and ovary (Beer, et al. 1995). Moreover as APP is a protein ubiquitously expressed in humans, it makes amyloid protein and all its' variants (e.g. monomers, dimers, oligomers, etc…) a rational and plausible target to be investigated in the BM of AD patients (Kimberly, et al. 2005). It is plausible that a genetic or acquired predisposition for amyloidogenic processing of APP could be evident not only in the brain but also in epithelial tissue.

1.2.6 Buccal cells and DNA damage

Genomic DNA damage has been associated with AD (Thomas, Fenech. 2007), particularly DNA damage in astrocytes of AD hippocampal regions as mentioned earlier (Myung, et al. 2008). Genomic instability has been reported to increase with age and therefore the capacity for DNA damage repair may also be altered (Fraga, et al. 1990; Goukassian, et al. 2000; Wilson, et al. 2008). In buccal cells a buccal micronucleus cytome assay was developed by Thomas et al. to score DNA damage, cell death and regenerative potential (Thomas, et al. 2007; Thomas, et al. 2009). A DS cohort was used as a model for premature ageing and presented a significantly elevated level of MN compared with both the older and younger control groups ($P<0.0001$) (Thomas, et al. 2008a). The same buccal micronucleus cytome scoring assay was performed on an

Alzheimer's cohort and showed a slightly elevated MN score in the AD group when compared to age-matched controls, but this difference did not reach statistical significance (P=0.11) (Thomas, et al. 2007). Genomic changes such as aneuploidy of both chromosomes 17 and 21, containing respectively the genes coding for Tau and APP (Iqbal, et al. 1989; Koo. 2002), has also been investigated in buccal cells. Aneuploidy levels of chromosomes 17 and 21 were shown to increase in buccal cells in AD and DS compared to their respective controls (Thomas, Fenech. 2008). Additionally, DNA double strand breaks have been detected in human buccal cells using an immunofluorescent antibody against γH2AX (Gonzalez, et al. 2010), therefore confirming that MN and γH2AX are two important DNA damage biomarkers that can be detected and may be altered in buccal cells from patients with AD. Oxidative stress has also been studied in leukocytes and exfoliated BM using HPLC after DNA isolation (Borthakur, et al. 2008) and because the association between accumulated oxidative DNA damage and ageing is well documented, it is possible that the BM may show changes in 8-OHdG levels from AD buccal samples; however this is yet to be tested.

1.2.7 Buccal cells and lipids

Studies have previously shown that a variety of lipid species can be detected in buccal cells, including sphingomyelin, cholesterol-3-sulfate, cholesterol, cholesterol esters, free fatty acids and triacylglycerols (Devereux-Graminski, Sampugna. 1993). Previous studies investigated the relationship between fatty acid composition of the BM and dietary intake (McMurchie, et al. 1984; Sampugna, et al. 1988) and have shown that the lipid composition of buccal cells could reflect changes in the dietary intake (e.g. the proportion of linoleic acid increased after exposure to a high polyunsaturated/saturated fat ratio diet). However, Kirby et al. (Kirby, et al. 2010a; Kirby, et al. 2010b) have measured the fatty acid composition of buccal cells from children and found there was no association of their fatty acid levels with fatty acid deficiency symptoms, learning and behaviour. However there is no evidence to date of research investigating changes of lipid levels in buccal cells in neurodegenerative diseases such as Alzheimer's.

1.2.8 Buccal cells and telomere length

Telomere shortening has also been investigated in buccal cells of confirmed AD cases and healthy age- and gender-matched controls. A significantly shorter telomere length was observed in buccal cells of the older AD group compared to the controls (P=0.01) and a similar but stronger trend was observed in white blood cells (P<0.0001) (Thomas, et al. 2008b).

1.2.9 Summary

Evidence that pathologic changes of AD are reflected in peripheral tissues such as plasma, fibroblasts, olfactory epithelium, platelets, white blood cells and buccal cells lead us to conclude that AD is plausibly a systemic disorder and that such tissues are of use to be a source of potential biomarkers (Table 1). However, investigating a tissue like the BM for new sources of biomarkers for AD is desirable for routine diagnostics because cells can be collected in a minimally invasive manner.

Table 1: Summary of results from case-control studies showing an association of specific biomarkers with AD within peripheral tissues.

Peripheral Tissues	Variations observed
Fibroblast	• ↑ MN frequency (Trippi, et al. 2001; Migliore, et al. 2011) • ↑ Trisomy 21 levels (Geller, Potter. 1999) • ↑ Immunostraining of Aβ and ↓ β-Secretase 1 (Pani, et al. 2009a) • ↑ Rate of cholesterol esterification (Pani, et al. 2009a) • Expanded pool of neutral lipids (Pani, et al. 2009a) • Altered pattern of spreading in culture (Peterson, et al. 1986) • ↓ Free calcium content (Peterson, et al. 1986) • ↑ Bound calcium content (Peterson, Goldman. 1986)
White Blood Cell	• ↑ Telomere shortening (Thomas, et al. 2008b)
Lymphocyte	• ↑ Neutral lipids accumulation (Pani, et al. 2009b) • ↑ Total Tau (Armentero, et al. 2011) • ↑ MN frequency in Ch13 and Ch21 (Migliore, et al. 1997; Migliore, et al. 1999; Migliore, et al. 2011) • ↑ Telomere shortening (Panossian, et al. 2003; Jenkins, et al. 2006)

Leukocyte	• ↑ Double strand breaks and oxidative damage (Migliore, et al. 2005)
Platelet	• ↓ APP Isoforms (130kDa/110kDa) ratio in membranes (Padovani, et al. 2002; Schneider, et al. 2009; Borroni, et al. 2010) • ↓ High kDa/Low kDa forms of Tau ratio (Neumann, et al. 2011)
Plasma	• Baseline levels of Aβ may predicts ↑ rate of progression towards AD (Song, et al. 2011) • ↑ Aβ42 associated with ↑ of AD risk (Schupf, et al. 2008) • Plasma amyloid levels linked with cognitive decline (Cosentino, et al. 2010)
Nasal Cell	• ↑ Abundance ratings for Aβ and phosphorylated Tau (Arnold, et al. 2010)
Buccal Cell	• Distribution of various cell types (Thomas, et al. 2007) • Nuclei/Cytoplasmic size ratio in intermediate cells (Papanicolaou. 1948) • ↑ MN frequency in DS (Thomas, et al. 2008a; Leifert, et al. 2011) • ↑ Tau and correlation with ↑ Tau in CSF (Hattori, et al. 2002) • ↑ Aneuploidy levels of Ch17 and Ch21 (Thomas, Fenech. 2008) • ↑ Telomere shortening (Thomas, et al. 2008b)

1.3 LASER SCANNING CYTOMETRY

Since the aim of this study was to develop the LSC method for high-content buccal cell analysis, the following sections discuss the principal and applications of the LSC technology. A biomarker by itself may not be sufficient for a 100% accurate diagnostic test but a combination of several biomarkers successfully correlated to the development of the disease may provide more accurate information on the disease state. To develop such a screening-test for biomarkers an automated high-content analysis technology is required. CompuCyte Corporation (Westwood, Massachusetts) is a pioneer in quantitative imaging cytometry and CompuCyte's iGeneration LSC instruments provide accurate, precise and quantitative measurements of cellular and tissue constituents, which are coupled with quantification of fluorescence, absorbance and light scatter imaging. LSC is therefore a technology of choice to simultaneously detect, localise and

quantify protein biomarkers in buccal cells as well as defining changes in the cell parameters and BM cell type and cytome profile of AD.

1.3.1 iGeneration LSC instrument characteristics

LSC is a recent technology that is capable of quantifying fluorescence and chromatic events simultaneously within cells as well as tissues. The technology has the quantitative ability of flow cytometry but allows evaluation of cell populations *in situ* (i.e. retention of cellular and/or tissue architecture). A laser scanning cytometer is equipped with up to four excitation lasers chosen from a palette of six possible wavelengths: 405 nm, 488 nm, 532 nm, 561 nm, 594 nm and 633 nm. It is also equipped with up to four photomultiplier tubes (PMTs), each detecting a specific wavelength range to collect emitted fluorescence from the samples, and two photo detectors (PD), 488 Light Loss (LL) and 633 LL to measure absorbance (Figure 4). As the laser light intersects the sample, scattered or transmitted light is simultaneously directed to one or more solid-state photosensors. The photosensors and PMT signals are converted into 14-bit pixel values that are then assembled into high-resolution images.

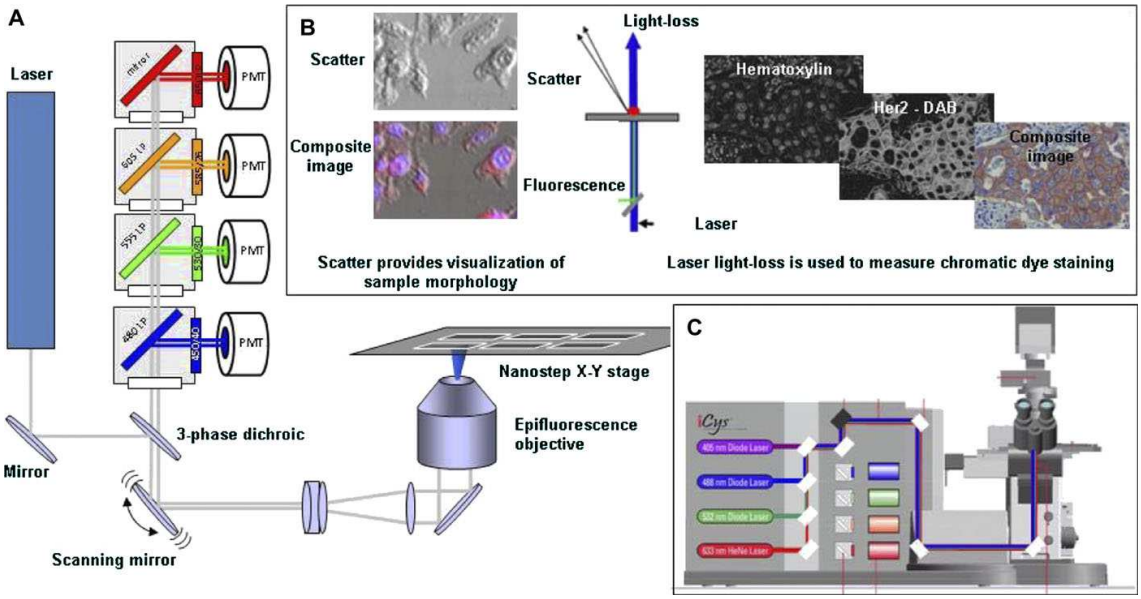

Figure 4: iGeneration LSC technology schematic diagrams (CompuCyte Corporation).
(A) Fluorescent measurement optical path. (B) Absorbance/scatter optical path and examples of corresponding images. (C) iCys Research Imaging Cytometer diagram.

1.3.2 Advantages

The analytical capabilities of LSC are comparable to those of flow cytometry but with fewer limitations, therefore assays originally developed for flow cytometry analysis can be adapted for the LSC, for example immunophenotyping of peripheral blood leukocytes (Tarnok, Gerstner. 2003). With the use of LSC, unlike flow cytometry, subcellular localisation of the fluorochrome can be quantified and once measured the preparation can be reanalysed with another probe(s). Furthermore, the slides can be stored and archived for further analysis. LSC incorporates image-processing techniques into the analysis and the measured sample is not lost and can be rescanned. LSC generates images of high quality as the lasers provide an intense concentration of monochromatic excitation light at the optical plane of the cell to allow better separation of fluorescence emission from excitation. As a result, detection of cell constituents can generally be made with higher measurement sensitivity than in conventional fluorescence imaging analysis. Additionally, LSC can quantify laser light scatter and absorption along with the fluorescence emissions and employ laser light scatter in a unique bright field visualisation mode. Moreover, compared to confocal microscopy which uses sharply focused laser beams to illuminate very small area of the sample at any given time, the beam is as collimated as possible to allow depth of field of typically 20-30 μm. This allows quantification of all of the fluorescent light emitted from the entire cell depth at each spatial location. As an example, LSC was shown to be useful in tissue section analysis such as brain slices from an AD case, where cell cycle dysregulation in subpopulations of neurons was observed in 120 μm of thick section of parahyppocampal gyrus that was scanned by adjusting the focus to capture several sections of 30 μm depth each (Mosch, et al. 2006). This design permits scanning relatively large sample areas making the instrument suited for automated experiments where large numbers of cells are to be examined. LSC also has advantages in protein detection, quantitation and localisation studies, since the use of Western blots comes with a number of limitations, i.e. the requirement for a large amount of sample matter and the inability to quantify the signaling molecules in individual cells and organelles; therefore leading to results that may not be representative of a particular cell type or organelle of interest (Grierson, et al. 2005). In contrast, LSC requires fewer samples and can allow analysis of localised cell-signaling molecules within specific cell types or organelles. Additionally the laser scanning cytometer is fully automated with an autofocus and automated stage. The exact position of each cell scanned is therefore

recorded and the LSC images generated can be visually examined. A disadvantage of LSC is the relatively slower speed at which data is captured relative to flow cytometry or imaging cytometry due to the very intensive scanning.

1.3.3 Events and generation of data

LSC generates data in a way similar to imaging analysis software by generating images produced as pixel maps with values directly linked to the dyes analysed. The signal can therefore be localised and boundaries can be drawn around pixels with contours of different sort, these include primary or threshold contour, background, integration, peripheral and phantom contours. An example of the different contours can be seen in Figure 5.

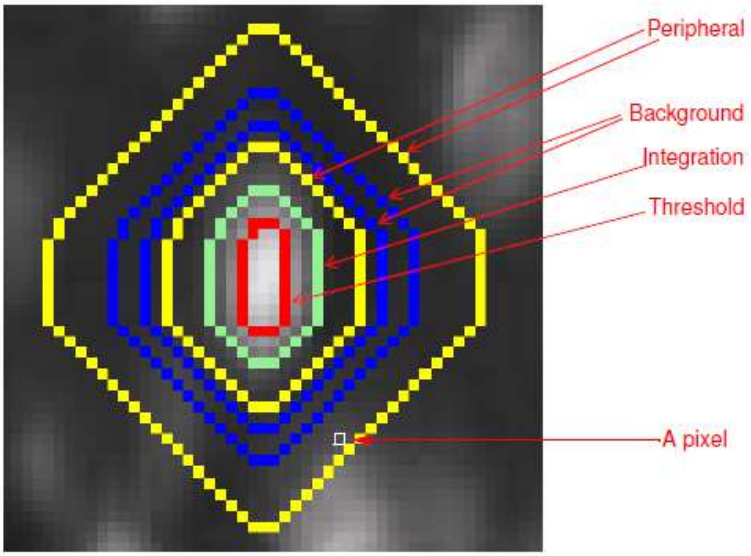

Figure 5: Example of the different contours mapped around an event (shown in white).
From iCyte User Guide.

The threshold contour is set to define fluorescent "events" analysed, it can be accompanied by an integration contour to include further pixels within the total signal collected. The background contour made of two lines can be used to calculate the background fluorescence for an event. Finally the peripheral contour can be used to quantify pixel values within two boundary lines set at the periphery of an event. This possibility of contouring events in images allows increased specificity and flexibility in

generating data. These data are generated in an automated and high-content manner, which can include X and Y event positions, event area, event counts, circularity, integrated fluorescence of an event (Integral), MaxPixel (maximal pixel intensity/event), perimeter, peripheral Integral and peripheral Max Pixel. The LSC data can be subsequently displayed in scatter plots, histograms, distribution plots, and statistic tables.

1.3.4 Applications

LSC has traditionally been used with fluorescently labeled cell culture (live or fixed cells) samples and tissue sections. Some examples of LSC applications include: fine-needle aspirate biopsies analysis (Gerstner, Tarnok. 2002; Juan, et al. 2011); cellular DNA content analysis (Kamiya, et al. 1999; Gerstner, et al. 2005; Tsujioka, et al. 2008); spatial resolution of nuclear vs. cytoplasmic fluorescence (Darzynkiewicz, et al. 1999); cellular morphometry and cell cycle analysis using maximal pixel intensity (Gorczyca, et al. 1996; Luther, Kamentsky. 1996; Kuliffay, et al. 2010); detection of apoptosis (Darzynkiewicz, et al. 2004; Lin, et al. 2004); analysis of enzyme kinetics (Bedner, et al. 1998); drug uptake (Bedner, et al. 1998); ligand binding (Bedner, et al. 1998); evaluation of cytoplasmic/nuclear translocation (Deptala, et al. 1998); FISH analysis (Kamentsky, et al. 1997); cell-to-cell interactions (Darzynkiewicz, et al. 1999); immunophenotyping (Tarnok, Gerstner. 2003) and quantification of fluorescent immunohistochemistry labeling in tissue sections (Gorczyca, et al. 1998; Pruimboom-Brees, et al. 2005). More recent studies have investigated histone phosphorylation of H2AX with correlation to cell cycle phase (Huang, et al. 2004; Tanaka, et al. 2007; Zhao, et al. 2009), as well as cell cycle dysregulation in neurons (Mosch, et al. 2006). LSC also offers the ability to investigate the chromatin texture of nuclei on top of DNA content and cell cycle (Kuliffay, et al. 2010). Applications of LSC to human scoring methods in cell cycle research and medical application were undertaken. In a phagocytosis and cell cycle progression study, the use of LSC was compared with microscopic counting performed by five human operators. No statistical difference between the counts of operators was observed and LSC measures of phagocytic rate were found to be comparable with those from different human operators (Coelho, et al. 2012). These results indicate the adaptability of human scoring methods to an automated laser scanning cytometer. Moreover, in medical application when compared

with routine cytology, LSC was shown to predict malignancy in laryngeal lesions by investigating simultaneous parameters such as DNA content and CK (Gerstner, et al. 2005). LSC was found to have a higher specificity and higher predictive value than routine cytology proving to be a useful tool in cancer research. LSC has also been previously utilised in identification and validation of biomarkers and possible combinations for improving diagnosis of rheumatoid arthritis patients by antibody detection (Fueldner, et al. 2012). The combination of biomarkers was shown to be possible with a novel reliable method such as LSC, and additionally resulted in better segregation between patients than did single-marker analysis. Additionally, a study suggested LSC as a tool for the quantification of cell cycle activity in neurons of an AD case (Mosch, et al. 2006). By designing an automated method to detect abnormalities in the DNA content of neurons, LSC scans on brain tissue of this Alzheimer's patient have been performed with the use of dual immunolabelling (Cyanine 5 and Cyanine 2) conjugated secondary antibodies with propidium iodide (PI). This study demonstrates a great potential of LSC for analysing the two and three dimensional distributions of neuronal cells in a short time, suggesting the application of LSC for routine pathological use in ways manual scoring would not allow (Mosch, et al. 2006). LSC has been proven to be useful for a panel of applications and will likely be ideal for automated high-content cell analysis, as in this study.

1.4 AIM

In order to treat AD early before the neurodegeneration has progressed to a widespread and irreversible stage of the disease process, there is need for a biomarker or combination of biomarkers that enable early presymptomatic and predementia diagnosis, at least at the symptomatic stage of MCI, and differentiation from other forms of dementia. Therefore the aim of this study was to investigate a minimally invasive tissue, the BM, as a source of biomarkers for AD in the South Australian Neurodegenerative Disease (SAND) and The Australian Imaging, Biomarker & Lifestyle Flagship Study of Ageing (AIBL) cohorts. Several proteins and cell parameters that have already been shown as altered in AD, such as Tau protein, Aβ, aneuploidy, lipid accumulation, were investigated in buccal cells. This investigation was carried out by developing new LSC methods for automated high-content analysis for

early use as a diagnostic test of AD risk. It was anticipated that the combination(s) of the parameters measured would increase the likelihood of a positive diagnosis for AD, and that buccal cells may be a promising tissue for this diagnostic. The focus on buccal cells was justified due to the minimally invasive and painless procedure required for collection which is ideal for population monitoring studies.

1.5 HYPOTHESIS

1. Aneuploidy is increased in buccal cells of MCI and AD cases.
2. Neutral lipids are present in buccal cells and elevated in MCI and AD.
3. Tau and Aβ are present in buccal cells and elevated in MCI and AD.

CHAPTER 2

2. BUCCAL CYTOME AND MICRONUCLEUS STUDY IN AD

2.1. INTRODUCTION

The buccal mucosa (BM) is an easily accessible tissue for sampling cells in a minimally invasive manner and does not cause undue stress to study subjects. Buccal cells can be used to study regenerative capacity of the BM which is dependent on the number and division rate of the proliferating basal cells, their genomic stability and their propensity for cell death. This approach is increasingly being used in molecular epidemiological studies to investigate the impact of nutrition, lifestyle factors, genotoxin exposure and genotype on DNA damage and cell death (Thomas, et al. 2009). Since the BM is of ectodermal origin, defects in BM cells may reflect potential physiological changes that occur in other ectodermal derived tissues such as fibroblasts and nervous tissue. A method utilising light and fluorescence microscopy has previously been developed to study DNA damage events such as micronuclei (MN) frequency and cell death in buccal cells adopting a buccal micronucleus cytome approach (Thomas, et al. 2007; Thomas, et al. 2008a; Darzynkiewicz, et al. 2011). Furthermore, the presence of MN in epithelial cells is of particular interest because MN are one of the best established biomarkers of DNA damage, representing chromosome breakage and mal-segregation events (Fenech, Crott. 2002). The various cell types and nuclear anomalies in the BM, which are observed and scored in a buccal micronucleus cytome assay, are shown schematically in Figure 6.

The buccal micronucleus cytome assay is well validated using visual scoring by light microscopy (Thomas, et al. 2009); however applicability on a large scale for appropriate biomonitoring is hampered by lack of automated high-throughput technology. Visual scoring of the buccal cytome and MN is time consuming particularly because large numbers of cells (1000-2000) and/or donors need to be analysed to obtain statistically relevant data. This is particularly important when scoring MN due to the low baseline frequencies observed (Ceppi, et al. 2010). The buccal micronucleus cytome assay has previously been used in our laboratory to measure distinct differences between the cytome profiles associated with normal ageing relative to that for premature ageing

clinical outcomes such as Down's syndrome (DS) and AD (Thomas, et al. 2007; Thomas, et al. 2008a). Therefore, to determine whether laser scanning cytometry (LSC) could be applied to score buccal cells in a similar manner to the visual scoring of the buccal cytome assay, the same microscope slides as used in studies (Thomas, et al. 2007; Thomas, et al. 2008a) were selected for this "first hands on LSC" study. The aim was to investigate if the buccal micronucleus cytome assay was adaptable on the laser scanning cytometer in an automated manner, and to discover the tools supplied by the iCyte software. Since this technology is very complex, it was necessary to first understand the subtleties of the software to also foresee the potential use of such a technology on investigating several protein biomarkers of AD simultaneously within buccal cells in a high-content and automated manner.

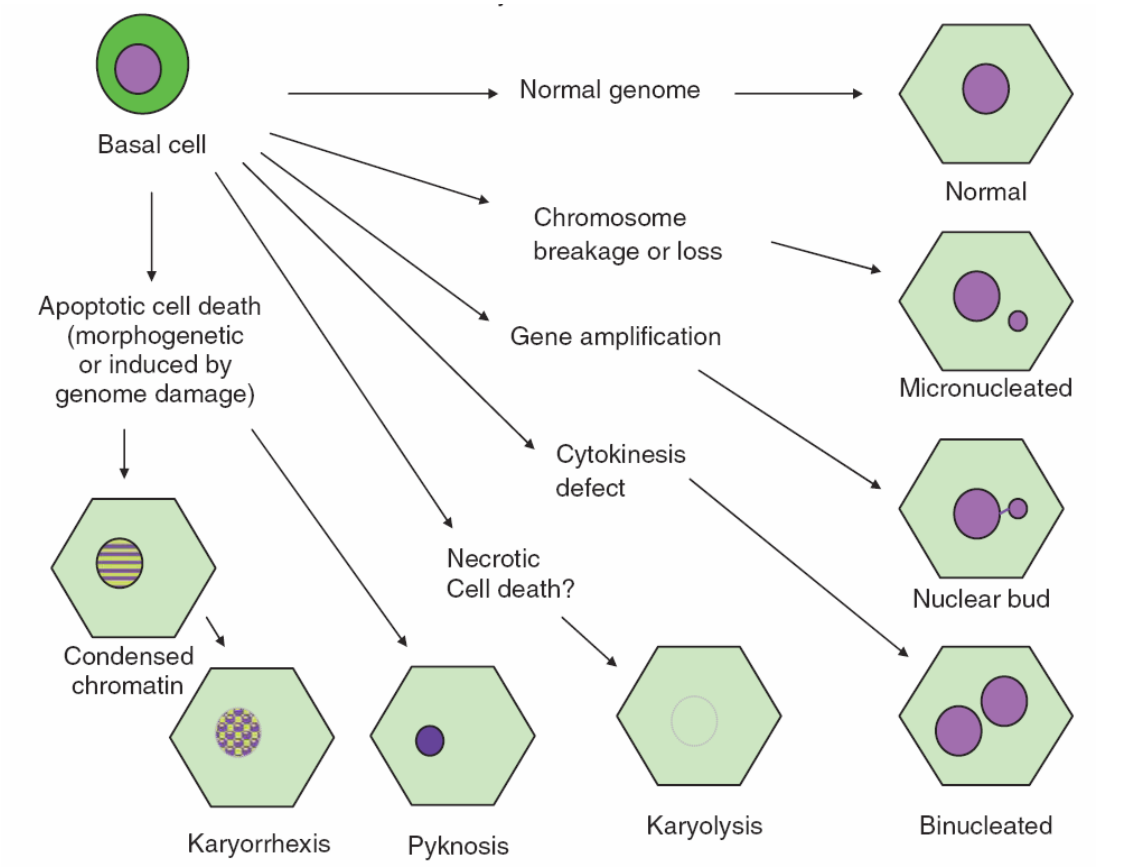

Figure 6: The various cell types scored in the buccal micronucleus cytome assay.
Adapted from Thomas et al. 2008a.

2.2. MATERIAL AND METHODS

2.2.1 Human ethics

Human research ethics approval was obtained from CSIRO Animal, Food and Health Sciences, Adelaide, South Australia, Adelaide University and Southern Cross University human experimentation ethics Committees.

2.2.2 Chemical and reagents

All chemicals were of the highest quality grade: Tris(hydroxymethyl)aminomethanehydrochloride (Tris), ethylenediaminetetraacetic acid (EDTA), Sodium chloride (NaCl), Schiff's reagent, Light Green were from Sigma-Aldrich (Castle Hill, NSW, Australia), ethanol and glacial acetic acid were from Ajax Finechem (South Australia), DePex was from Merck (Kilsyth, VIC, Australia).

2.2.3 Buccal cell sampling and preparation

Buccal cell isolation and preparation was as previously described (Thomas, et al. 2009). Before sampling, the inside of the mouth was rinsed gently with 30 mL distilled water to remove debris. Buccal cells were sampled using a soft bristle, flat headed toothbrush rotated 20 times against one cheek in a circular motion and then the toothbrush containing cells was transferred to 30 mL tubes containing "buccal cell buffer" (0.01 M tris(hydroxymethyl)aminomethane, 0.1 M ethylenediaminetetraacetic acid, 0.02 M NaCl, pH 7.0) and cells were dislodged from the toothbrush by agitation of the toothbrush in the buffer. A new toothbrush was used to sample from the contralateral cheek, as above and placed in the same buccal cell buffer. The suspension was then centrifuged 10 min at 581 xg at room temperature. Supernatant was discarded and 10 mL of fresh buccal cell buffer was added. Cells were centrifuged twice more and finally resuspended into 5 mL of fresh buccal cell buffer. Cells were separated using a syringe with an 18G needle, and then filtered with a 100 μm nylon filter to remove cell clumps. The cell concentration was determined using a Coulter counter and adjusted to 80,000 cells/mL. Buccal cells were cytocentrifuged (using a Shandon cytocentrifuge) for 5 min at 600 rpm onto microscope slides and air-dried for 10 min.

2.2.4 Buccal cell fixation and staining

Cells were fixed in a slide-staining rack containing 50 mL of ethanol:acetic acid mix (3:1) for 10 min at room temperature followed by further air-drying for 10 min at room temperature. Microscope slides containing the fixed cells were immersed for 1 min each in Coplin jars containing 50% (vol/vol) ethanol then 20% (vol/vol) ethanol. Cells were washed for 2 min in a Coplin jar containing purified (Milli-Q) water. Slides were placed in a Coplin jar containing 5 M HCl for 30 min and then rinsed in running tap water for 3 min. Slides were drained and placed in a Coplin jar containing Schiff's reagent for 60 min in the dark at room temperature. Slides were rinsed for 5 min in tap water and then in Milli-Q water. The cells were counterstained by immersing in Coplin jars containing 0.2% (wt/vol) Light Green for 30 sec and rinsed in Milli-Q water. Slides were then air-dried for at least 45 min before coverslips were applied with DePex mounting medium.

2.2.5 Laser scanning cytometry

Microscope slides containing fixed/stained buccal cells were inserted into a standard 4-slide carrier and analysed by iCyte® Automated Imaging Cytometer (CompuCyte Corporation, Westwood, MA, USA) with full autofocus function, inverted microscope, three laser excitation (Argon 488 nm, Helium-Neon 633 nm and Violet 405 nm), 4 photomultiplier tubes (PMTs) for quantitation of blue, green, orange and red fluorescence and dual channel absorption/scatter detector. In this study, excitation was at 488 nm and 633 nm, a Long Red emission filter was used for fluorescence and 488 LL and 633 LL photo detectors (PDs) for absorption were used (Table 2). Typically 1000-3000 cells were analysed using iCyte cytometric analysis software version 3.4.10. The "CompuColor" feature in iCyte was used to provide a green pseudocolour in the cytoplasm (as green is the colour of cytoplasm when visualised under light microscopy), additionally nuclei were coloured orange.

Table 2: Laser and detector selection for buccal cells.

Target	Dyes	Excitation Lasers (nm)	Detectors
Nuclei	Feulgen	488	488 LL (Absorbance) + Long Red (Fluorescence)
Micronuclei	Feulgen	488	488 LL (Absorbance) + Long Red (Fluorescence)
Cytoplasm	Light Green	633	633 LL (Absorbance) + Long Red (Fluorescence)

Abbreviations; LL, light loss (absorption)

2.2.5.1 Low resolution scan

Routinely a rapid overview scan was initially performed at low resolution using a 20× objective to locate and capture the entire area of the sample (cytospot) that was subsequently analysed in greater detail. The resolution of an overview scan is low due to large (10 μm) step increments used to acquire the image of the entire sample; however the low resolution scan is only used to identify regions for high resolution scans.

2.2.5.2 High resolution scan

To obtain high resolution images for analysis, smaller individual (rectangular) scan areas are defined for the high resolution scan using a 20× objective as outlined in Figure 7B. In high resolution scans, small (0.5 μm) laser increment steps are used thus yielding higher resolution detailed "images". It was found that a 20× objective was sufficiently adequate for both the low resolution and high resolution scans to analyse the buccal cell cytome. The user typically defines the size and shape of these regions (shown in blue in Figure 7A and B) and where they will be placed. Rectangular regions were randomly placed over the cytospots within the defined low resolution region (as shown in green) but being careful not to overlap these scan regions. If there was an obvious artifact present e.g. an air bubble, then this area was excluded from analysis. The size of the high resolution scan regions was always set to 1500 × 1110 pixels (or multiples thereof). This size accommodates the most optimal scanned image size for buccal cells contained within the "field images". Furthermore, by doing this, the laser scanning cytometer could automatically re-focus at the start of each scanned 1500 × 1110 pixel

region. This conveniently allows for any re-focusing corrections that might be required if a larger single scan region was used. Additionally, if there was a particular reason that a scan region should be excluded from analysis in the main data set, it could easily be excluded later when analysing data or defining the scattergrams.

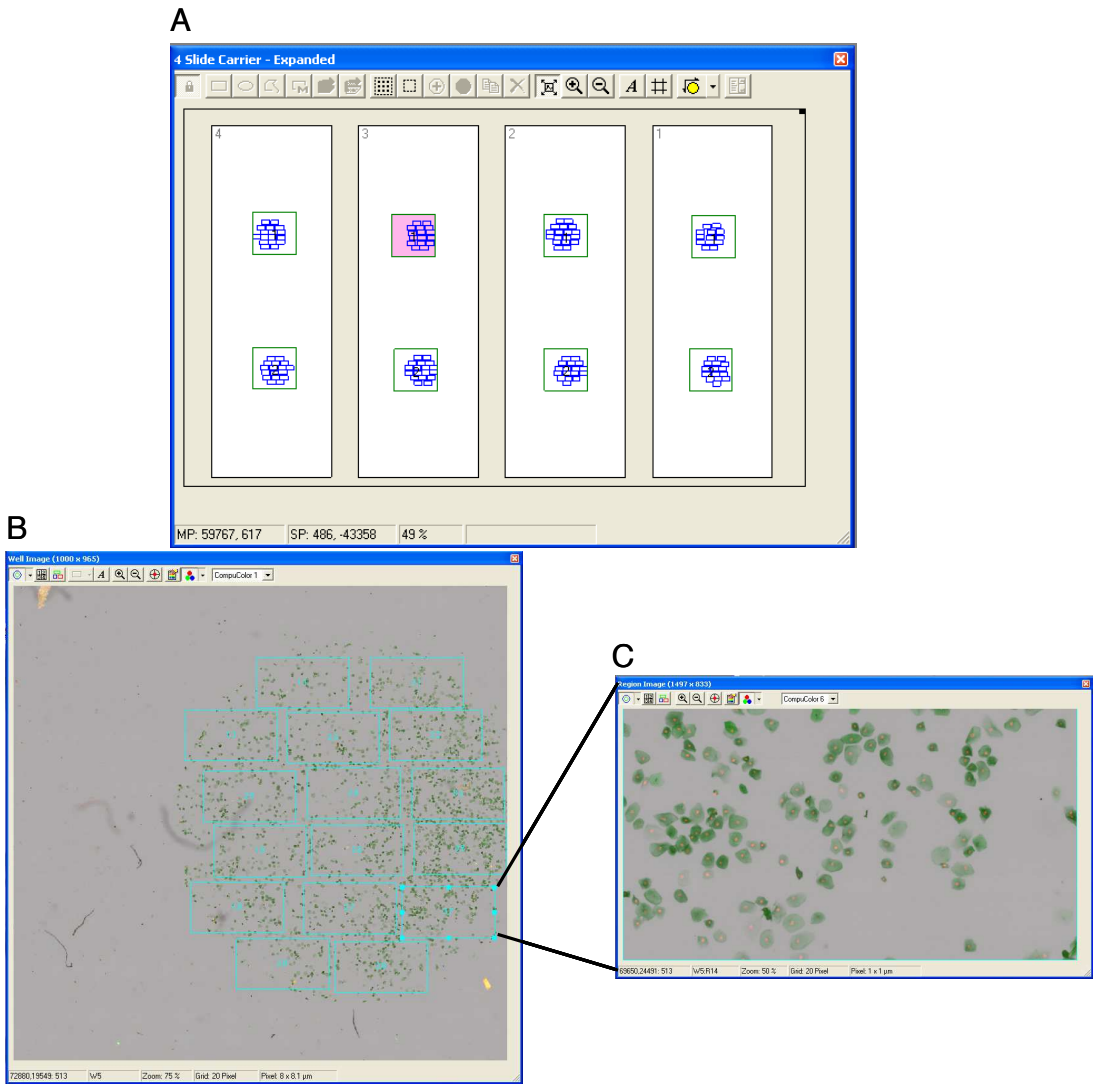

Figure 7: Low and high resolution scans.

(A) Shows a diagram of 4 slides to be analysed by LSC from right to left. Typically, 2 cytospots containing buccal cells are prepared on a microscope slide. The green boxes are the regions in which a "low resolution" scan of the cytospots are initially performed. This allows the user to define the cytospot region containing the cells. The smaller blue rectangles within the green boxes are regions that are scanned at higher resolution for data analysis (see text for full explanation). (B) A typical low resolution scan "well image" of buccal cells on an entire cytospot with cyan coloured scan regions overlayed, (C) an example of region image "3.7" that consists of a mosaic image showing individual buccal cells stained with Light Green (cytoplasm, green colour) and Feulgen (nuclei, orange colour).

In the protocol described here, a multi-pass scan was performed to increase the range of signals that could be detected and therefore to optimise image quality. The blue (488 nm) and red (633 nm) excitation lasers are used separately, to allow separation of fluorescence collected from dyes that have similar emission spectra, but different excitation spectra. The two component dyes in this analysis that fall into that category are as follows: Feulgen targets the DNA of cells and fluoresces in the long red region when excited with a 488 nm light source, while Light Green targets the cytoplasm of cells which also fluoresces in the long red region when excited with the red laser (633 nm), hence the use of a multi-pass scan. Additionally, the absorbance (Light Loss) can also be detected using the 488 and 633 LL PDs. When quantification of the fluorescence signal was required, the PMT voltages should be set so that the brightest pixel value (equivalent to 16,000 units) is just below saturation (e.g. 15,000 units). In the example shown (Figure 8) the PMT voltage was set to 38 for the blue laser with excitation in the Long Red channel. The signal intensity can be viewed using the profile feature in the profile window. The "Offset" values (which are used to set the background fluorescence) were set to decrease the background to a pixel value of between 200 - 400 units; in this case for Long Red (with blue laser excitation) the offset setting was -0.03. By carrying out the above procedure this ensured the maximum dynamic range of fluorescence data that could be obtained, hence this was ideal for the quantification and comparison of data between samples.

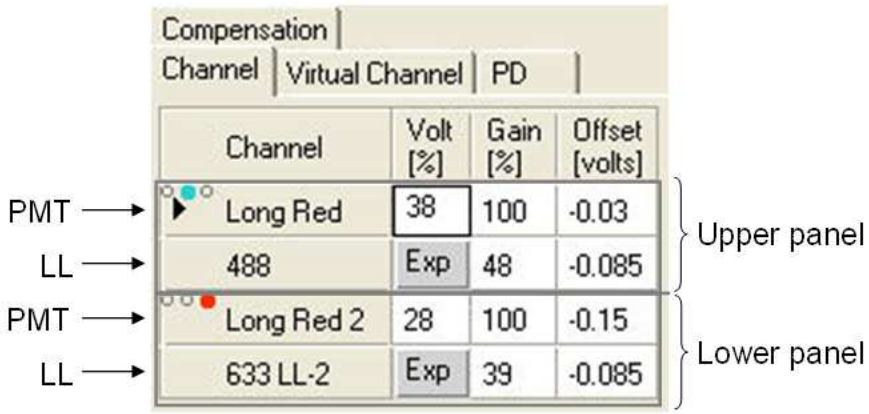

Figure 8: Detector module with selection of lasers and channels.
Setting the channels for excitation and emission: the settings show that in this example the 488 nm excitation laser was used in the 1st pass of the scan (as indicated in the upper panel by a blue filled circle) whilst the text in the upper panel shows the photomultiplier tube (PMT) settings and light loss (LL) detector settings used for detecting emission ie "Long Red" and "488" (which are filters for fluorescence at 633 nm and absorbance at 488 nm, respectively). These settings were used to quantify Feulgen fluorescence and absorbance (light loss) for nuclei and MN. The lower panel shows that the red laser (as indicated by a red filled circle) was used to excite the sample on the 2nd pass of the scan. In this instance, the fluorescence emission was at long red ("Long Red 2"), and light loss (absorbance) at 633 (red) was also being recorded ("633 LL-2"). These settings were used to quantify red fluorescence and absorbance (light loss) of Light Green stain (for cytoplasm). The "volt" and "offset" features are described further in the text.

2.2.5.3 Virtual channels and compensation

Virtual Channels are used to perform mathematical operations on originally acquired channels to create new "virtual" channels. They are used to increase a weak signal, to add signals together or to isolate the individual fluorescence signals when two or more may overlap in one or more channels (typically termed "compensation"). In our experiment several virtual channels were created to allow compensation of both absorbance and fluorescence as shown in Table 3.

Table 3: Virtual channels for compensation of fluorescence and absorbance.

Virtual Channel	Input Channel	Operator	Purpose
Fluorescence compensation			
LR Fluor M	Long Red	Multiply 0.25	Adjustment factor for Light Green compensation
LR2 Fluor M	Long Red 2	Multiply 0.3	Adjustment factor for Feulgen compensation
Feulgen	Long Red	Subtract LR2 Fluor M	Compensated for Feulgen stain
Light Green	Long Red 2	Subtract LR Fluor M	Compensated for Light Green stain
Absorbance compensation			
Blue I	488 LL	Invert	Convert from brightfield to darkfield
Red I	633 LL2	Invert	Convert from brightfield to darkfield
Blue M	Blue I	Multiply 0.005	Adjustment factor for Light Green compensation
Red M	Red I	Multiply 0.05	Adjustment factor for Feulgen compensation
Blue C	Blue I	Subtract Red M	Compensated for Feulgen stain
Red C	Red I	Subtract Blue M	Compensated for Light Green stain

To properly define and evaluate the compensation settings, it was necessary to monitor the distribution of events in scattergrams using the random segmentation "phantom" feature (Figure 9). In the scattergram shown in Figure 9, a cyan region (R35) was drawn around events that fall on areas of the slide where there are no cells and a complementary region (R25) was defined around the events that fall on cells. Events from R35 are excluded and region 25 was used as a gate for further compensation. Both the fluorescence (Figure 9C) and the absorbance (Figure 9E) scattergrams of the uncompensated events show a slant in the Y direction towards the X direction (cyan line). In the compensated scattergrams (Figure 9D and F) that line moves towards a more vertical positioning, indicating proper compensation has been achieved.

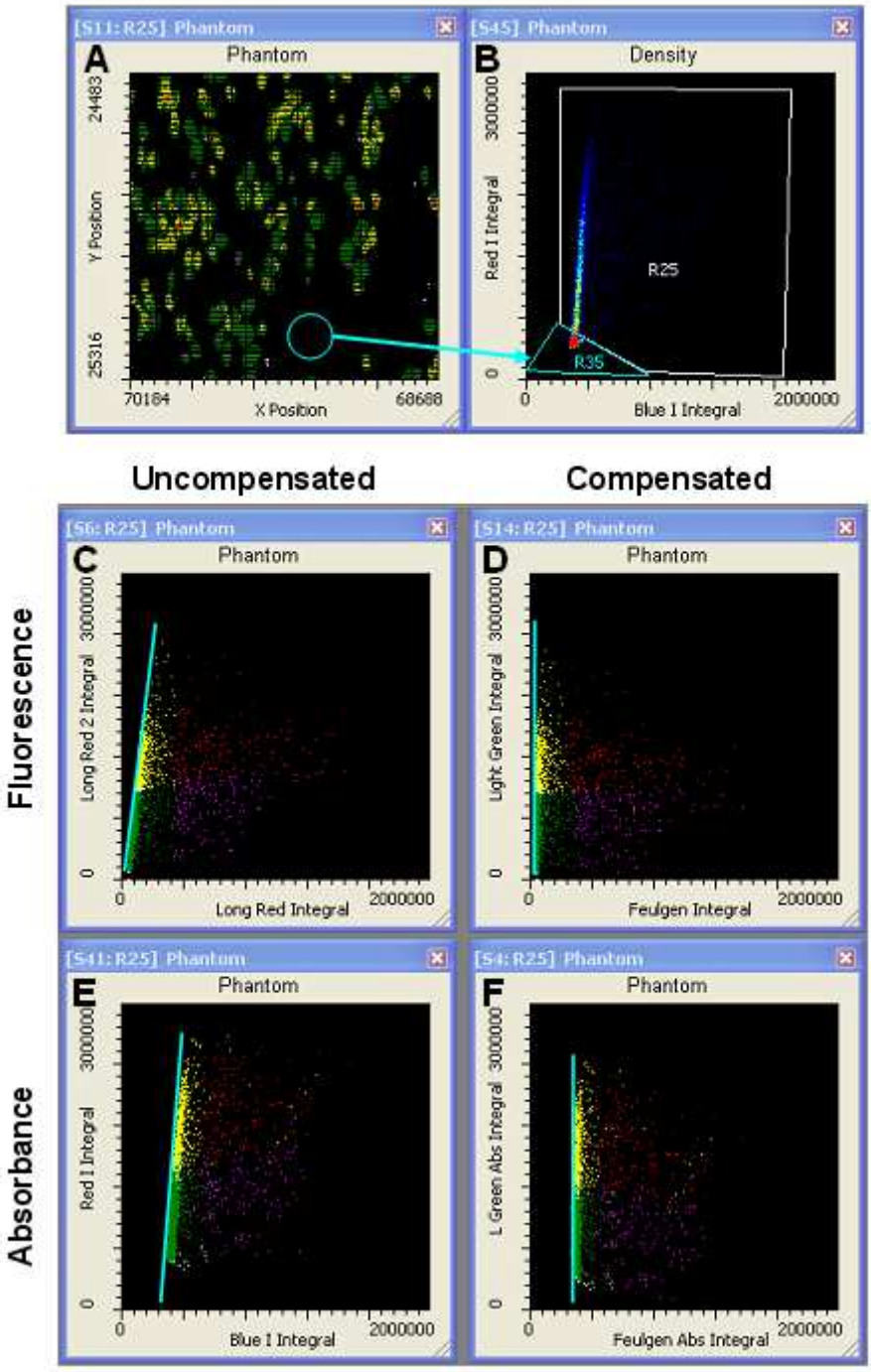

Figure 9: Phantom and compensation.
(A) Phantom was generated using the "phantom" feature in iCyte which shows the location of cells (coloured) and where there are no cells (black). This allows the user to define the compensation parameters described in detail in the text and shown in (B). Uncompensated (C) and compensated (D) fluorescence, whilst uncompensated (E) and compensated (F) absorbance data are shown. The "Integral" data was defined as fluorescence per event for the selected channel.

2.2.5.4 Segmentation of events

In this study one of the aims was to capture three main buccal cell events that could be analysed further for scoring and quantification, namely the cell boundary for identifying and scoring whole cells as well as the nucleus boundary and micronucleus boundary (Figure 10). Following a high resolution scan using a 20× objective and using the "protocol" settings as shown in Figure 11, the clear demarcation lines for cell periphery, nuclei and MN were generated in iCyte as shown in Figure 10. The contour lines are automatically drawn around an event such as the cytoplasmic boundary, nucleus or micronucleus using a user-defined threshold for the pixel values for a particular fluorescent colour. Buccal cells are large in diameter and occasionally the cells overlap over two scan fields. In our version of the iCyte software, cells falling on the scan boundaries were excluded from the analysis.

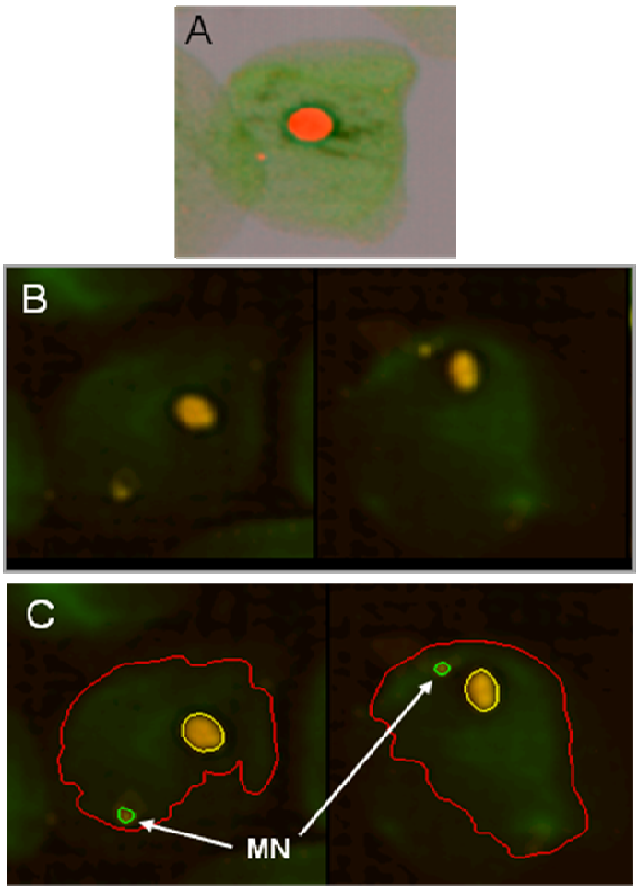

Figure 10: LSC images with contouring representation.
LSC generated images of buccal cells showing MN. (A) High resolution image of buccal cell showing a single micronucleus (orange) within the cytoplasm (green). (B) "CompuColor" generated gallery images of 2 buccal cells showing distinct MN, and (C) the same cells shown in (B) demonstrating the "segmentation" feature of the iCyte-generated contour lines around the cytoplasmic periphery (red), nucleus (yellow) and micronucleus (MN; green).

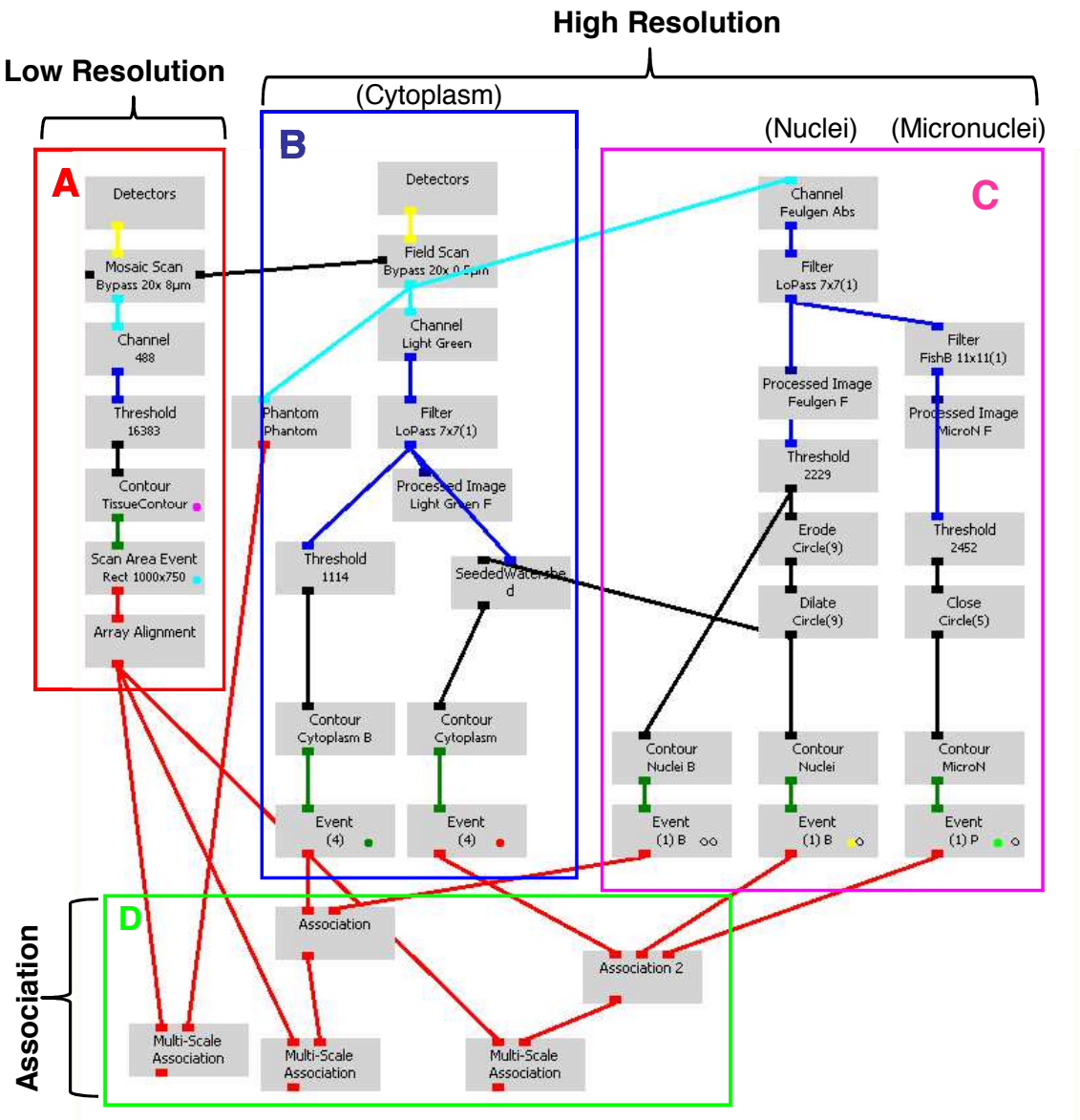

Figure 11: LSC software protocol.
The iCyte "protocol" was separated into 4 parts (A, B, C and D) with all parts being associated together using the "association" module (part D). The first scale (A) provides the settings used for the "low resolution" scan using a 20× objective. The resulting mosaic scan (shown in Figure 7B) was associated with the second scale settings including parts B and C which contain all the settings for the "high resolution" scan (as described in text). Part D was the individual component associations. All events are associated with each other, which provides a very powerful analysis tool that link parent events to sub-events.

2.2.5.5 Identification of buccal cell types

To classify all buccal cells, we generated a scoring system similar to that used previously (Thomas, et al. 2009) which consisted of the following cell types: basal, transitional and differentiated normal viable cells; karyolytic cells (i.e. lacking a nucleus), dead/dying cells (<2N) and hyperdiploid cells (>4N) using the protocol pathways as shown in Figure 11. Ideally, the iCyte-identified events are defined by a single segmentation of the cytoplasmic periphery. Since buccal cells are occasionally grouped together it was necessary to use the iCyte algorithm "seeded watershed". This feature divides the groups of cells into individual cells using nuclei as the basis for segmentation. The assumption was that each cell segmented from a group of cells will contain a single nucleus. As a result, karyolytic cells which do not contain nuclei are eliminated from the segmentation. Furthermore groups of karyolytic cells were not observed. To fully score all cells on the slides the scores obtained from the two segmentation scales i.e. "Contour Cytoplasm B" (which is used only to identify the number of cells without nuclei i.e. karyolytic) and "Contour Cytoplasm" (which identifies cell types with nuclei) are combined, one without and one with the seeded watershed feature, respectively (also see Figure 11B). The score of the karyolytic cells obtained from "Contour Cytoplasm B" are then added to the scores of all other cell types obtained from "Contour Cytoplasm". Cell type segregation was defined by using a scattergram to separate cell aggregates (Figure 12A) (that could not be separated adequately by the seeded watershed algorithm) followed by another scattergram plotting the Light Green Integral value against the Circularity of the cytoplasm (a measure of the roundness of the object), where a lower Circularity value indicates a higher roundness for the event measured allowing identification of debris (Figure 12B). From the gate R1 (Figure 12B) a scattergram was then designed to separate cells based on differences in nuclear staining by plotting their DNA content vs. the Area of the cytoplasm. Figure 12C shows "<2N" (R45) and ">4N" (R13) cells, whilst regions 46 and 47 were defined as Euploid cells. Region 47 was defined as "differentiated cells" due to their large cytoplasmic area. Region 46 was a source for a new scattergram of the Area of Cytoplasm vs. Light Green Intensity (Figure 12D). The following regions are then defined; intensely-stained green "basal" cells (R6) and lighter stained "transitional" cells (R4). A battery of the cell types scored is shown in Figure 13.

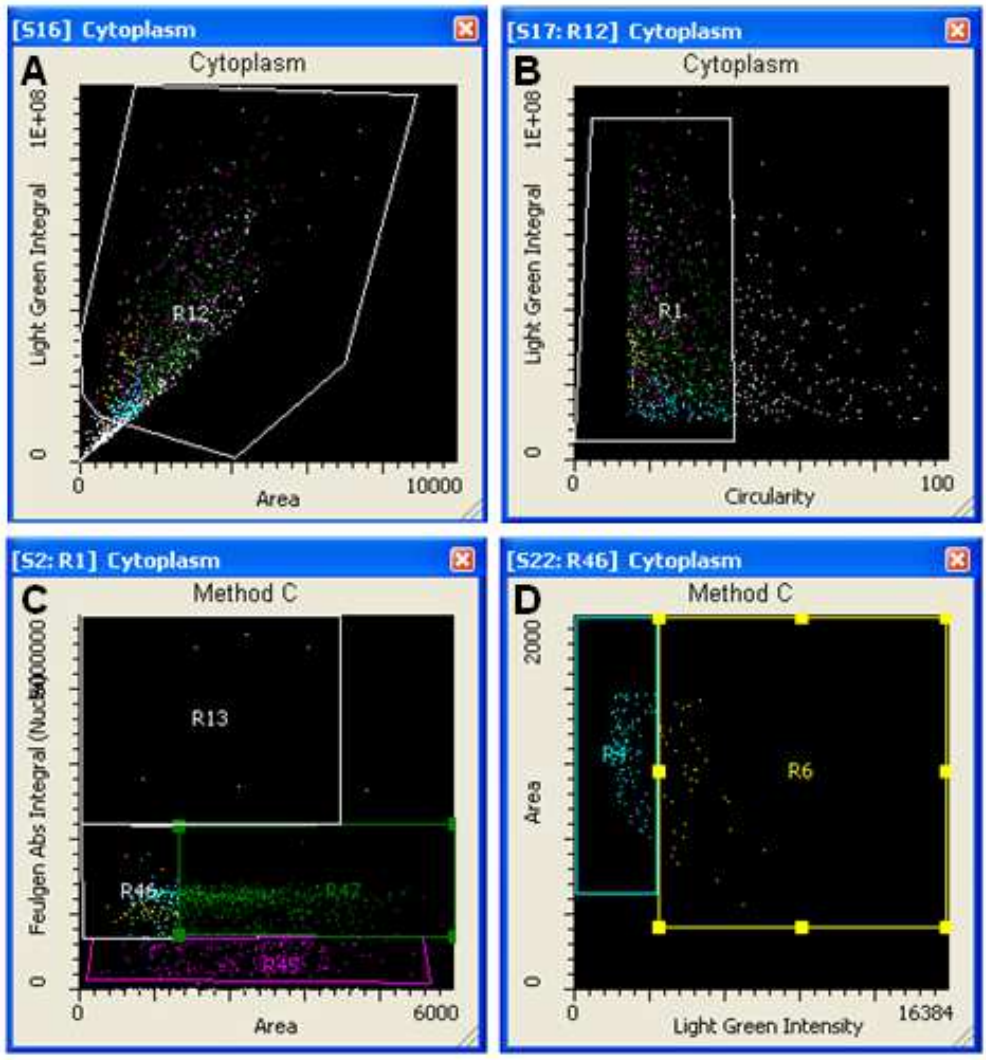

Figure 12: Scattergrams for separation of cell types.
The identification and scoring of basal, transitional and differentiated buccal cell types. The scoring of the buccal cell types was achieved by the following criteria: (A) excluding "events" that are either too small or too large to be a buccal cell, (B) have a high "circularity" feature (i.e. are not round in shape), (C) cells that have abnormally high or low nuclear content (i.e. >4N or <2N as shown in R13 and R45, respectively), and euploid cells shown in R46 and R47, with R47 containing the differentiated cells, and (D) was the final stage of cellular classification of basal (R6) and transitional (R4) cells (obtained from scattergram region R46 in (C)). Karyolytic cells are not scored in this set of gating procedures; however Figure 14A and B demonstrates the scoring procedure for karyolytic cells.

Identification of karyolytic cells (cells without a nucleus) are determined based on the original segmentation (Cytoplasm B) pathway (i.e. no "seeded watershed" algorithm applied) shown in Figure 11B and Figure 14A and Figure 14B. The percentage of karyolytic cells was obtained with gating region "R23" in Figure 14B. An example gallery of the cell types scored is shown in Figure 13.

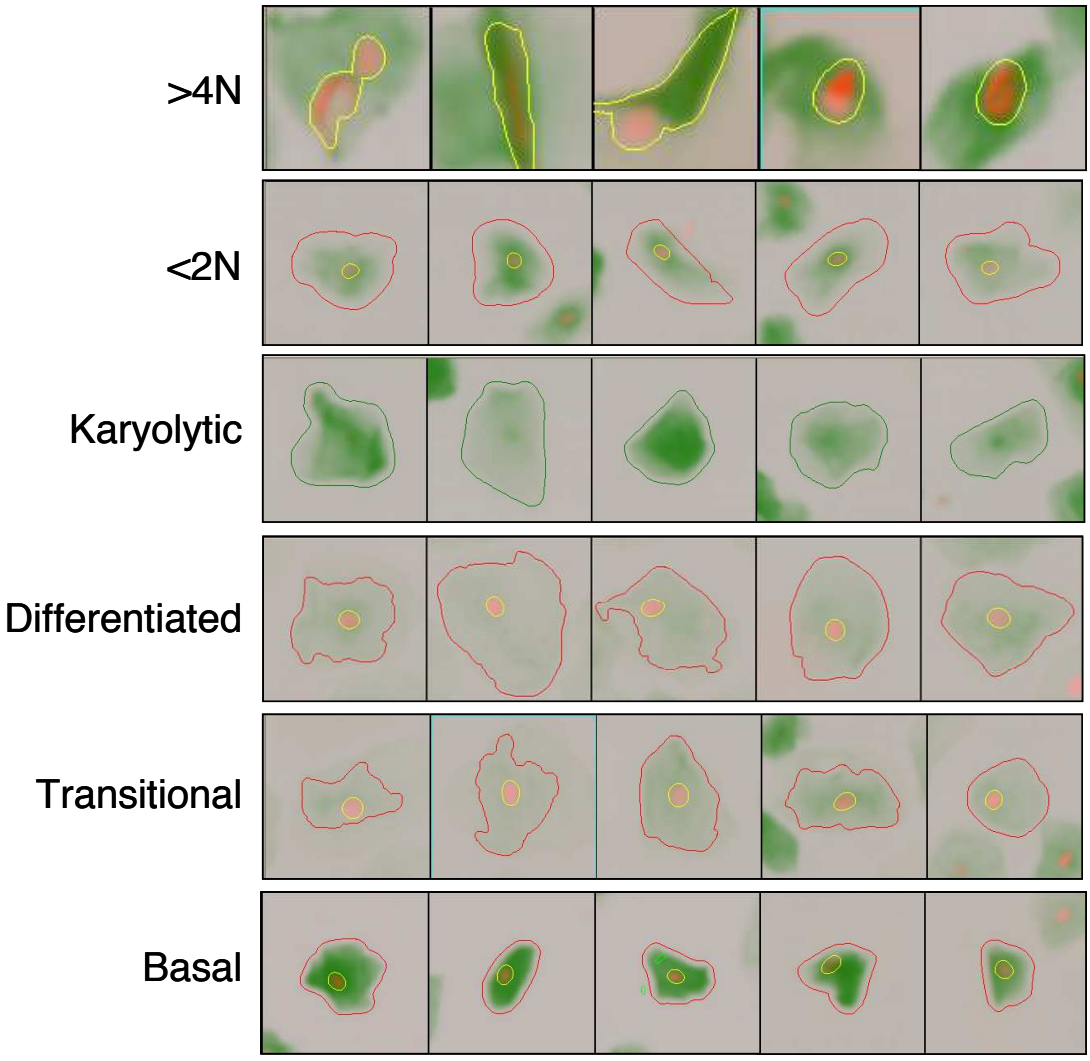

Figure 13: Gallery of images generated by LSC of different cell types.
Gallery images of buccal cells showing the various cell types scored using the automated human buccal cell micronucleus cytome assay by LSC.

2.2.5.6 Nucleus and micronucleus

To identify and score nuclei and MN (Figure 11, part C), various input parameters are used in iCyte such as Feulgen absorption and area of the Feulgen stained event. It is important to notice that both fluorescent and absorption properties of Feulgen stain were examined and compared with LSC, hence fluorescent and absorption compensation were performed in Figure 9. Since the fluorescent signal was found to be more defined, it was decided that fluorescence would be used to measure DNA content and score MN. The identification of nuclei can be used in conjunction with the cellular segmentation. Both features become associated with the "Cell event" and data obtained from identified nuclei can be correlated to the data obtained from identified cells. The total amount of signal detected (usually the "Integral") in nuclei will define the "DNA content" and hence the ploidy status of that cell. The two modules in Figure 11, part C labeled "Contour Nuclei B" and "Contour Nuclei" have identical settings. However, "Contour Nuclei B" was associated with "Contour Cytoplasm B" (in part B); and "Contour Nuclei" events was associated with the "Contour Cytoplasm" segmentation in part B. It was necessary to create these two linked events to allow association of nuclei detection with each cell segmentation pathway. The "micronuclei segmentation" was based on the nuclei segmentation however a smaller size (area) restriction was defined, since buccal cell MN are typically 1/16 to 1/3 of the main nucleus size (Thomas, et al. 2009). A "FISH B" filter was added to the micronucleus segmentation to enhance the spatial resolution of the images, highlight small spots, and therefore increases detection of MN. A peripheral contour around the MN was routinely applied to segregate the MN that are located within a cell from those that are not (by quantifying the Light Green intensity of the peripheral contour) as shown in Figure 14. Using these approaches it was possible to accurately score MN in human buccal cells using LSC.

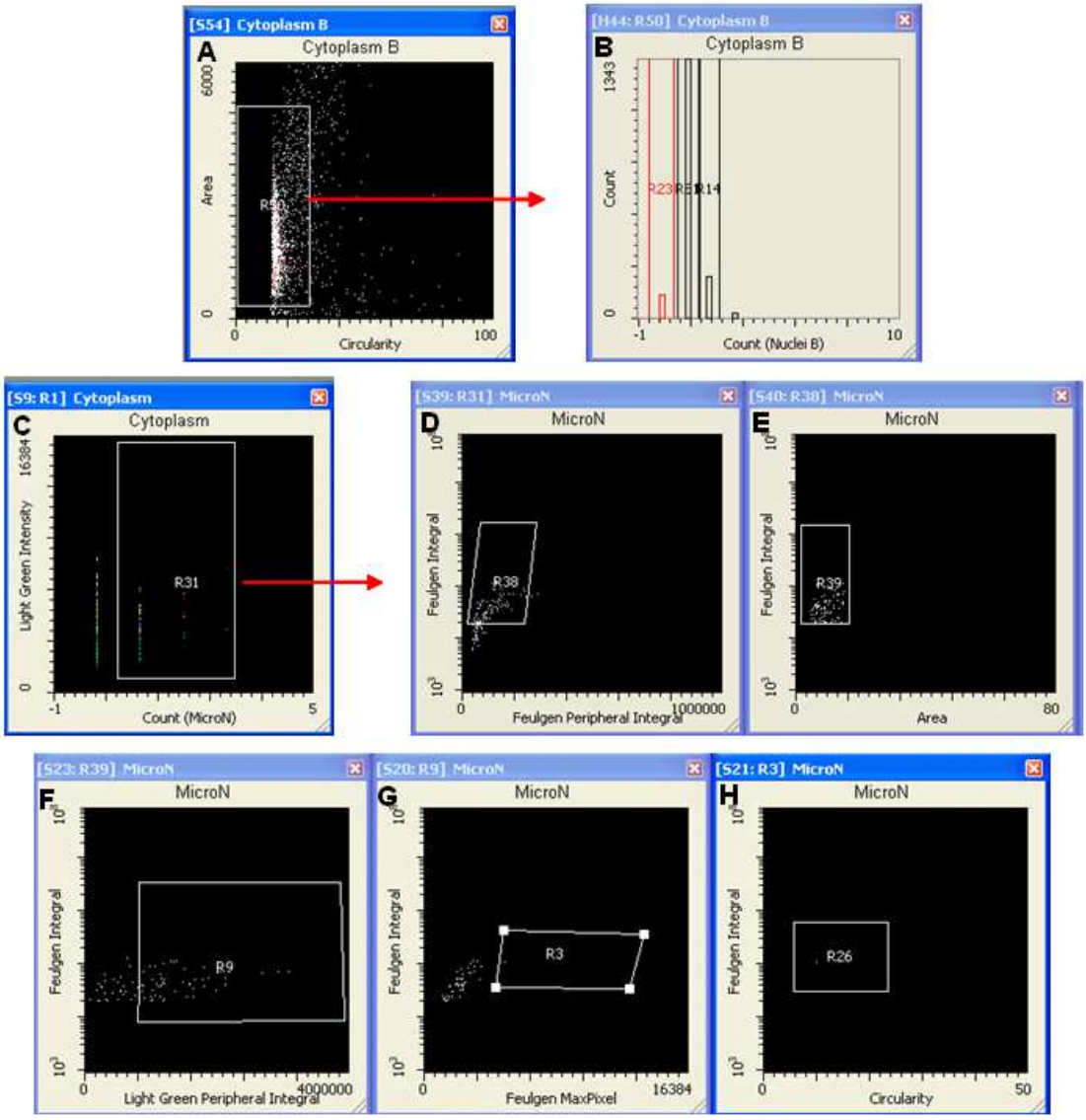

Figure 14: Scattergrams for identification of karyolytic cells and true MN.
(A) and (B) identification of karyolytic cells (cells without a nucleus) are determined based on the segmentation (Cytoplasm B) pathway (i.e. no "seeded watershed" algorithm applied). The percentage of karyolytic cells was obtained with gating region "R23" in Figure 14B. The MN segmentation pathway yields many events that are not MN, and the process of filtering through the events to define true MN entails several steps. The MN identification starts with the same two scattergrams as for cell differentiation status (Figure 12A and B), and a further scattergram is gated on region R1 (of Figure 12B). Following this step, all cells that contain a nucleus associated with potential MN are identified from the Region 31 (C). Several criteria are applied to the MN; (i) an initial gate (R38 in D) was defined to eliminate candidate events that have Feulgen staining surrounding them; this precludes counting bright spots in nuclei. (ii) From Region 38, another gate (R39 in E) restricts candidates to those with a pre-determined area. (iii) Then a scattergram showing the Light Green stain (fluorescence) Peripheral Integral value of the MN vs. the Feulgen Integral (DNA ploidy) of the MN (F) was used to differentiate candidate MN with no Light Green staining around them, and those with (green) cytoplasm surrounding them (R9). Candidates not having the proper intensity of the Feulgen staining are excluded by plotting the Feulgen MaxPixel value of MN and defining a gate (R3 in G). The final step in the MN process was to use a morphology based "circularity feature" to eliminate very irregular candidates from the scoring (H). The circularity feature was plotted against the Feulgen Integral (DNA content) of the cells. Lower circularity values translate to rounder objects. The region was defined around low circularity objects (R26). MN detected in Region 26 can further be associated to their cell type.

2.2.5.7 DNA content

The total DNA content of the cells was based upon the Feulgen Fluorescence Integral (Figure 15). The Feulgen Fluorescence Max Pixel, a feature that is closely related to the condensation state of the chromatin is plotted as a scattergram in Figure 15A. The total DNA content (Feulgen Fluorescence Integral) is plotted as a histogram in Figure 15B. Several regions were gated defining different nuclei states; <2N, 2N, >2N.

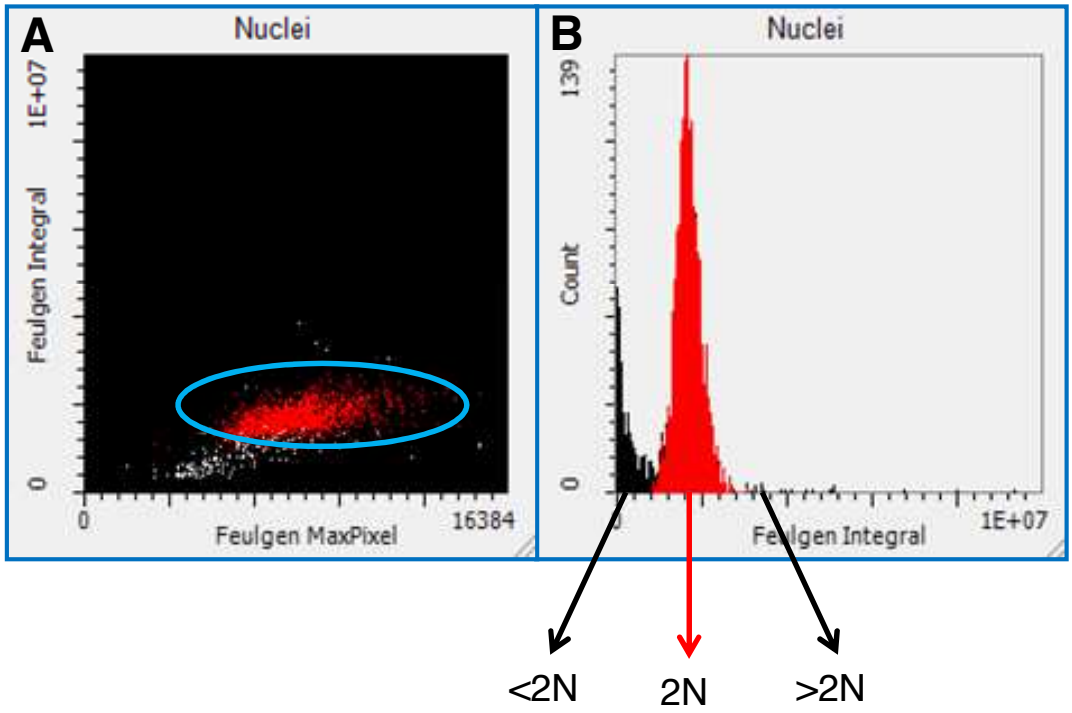

Figure 15: Identification of ploidy peaks.
DNA content of human buccal cells from a healthy subject. Scoring criteria was based on Feulgen Fluorescence Integral (integrated fluorescence per event) and Feulgen Fluorescence MaxPixel (brightest pixel value per event). (A) Nuclear content can be viewed on a scattergram with 2N nuclei located within the blue circle. (B) A histogram plot of the same data in left panel showing the delineation of <2N, 2N and >2N peaks and the frequency of DNA content "events" scored, with the majority of buccal cells being scored as 2N.

2.2.5.8 Statistics

One-way analysis of variance (ANOVA) analyses were carried out to determine the significance of the cellular parameters measured between the controls, Down's and AD groups. Pairwise comparison of significance between Down's, AD and their respective controls, was determined using Tukey's test. ANOVA values were calculated using GraphPad Prism 5 (GraphPad Software Inc., San Diego, CA, USA). Significance was accepted at $P<0.05$.

2.3 RESULTS

2.3.1 Random phantom segmentation

From initial observations, it was noted that the staining intensity of cell cytoplasm differed between participants, therefore this warranted further investigation. As described in section "*2.2.5.3 Virtual channels and compensation*" the "phantom" feature was used to compare the staining intensity of cell cytoplasm between groups. The phantom feature generates random grey circles of the same size all over the images generated during scans (Figure 16).

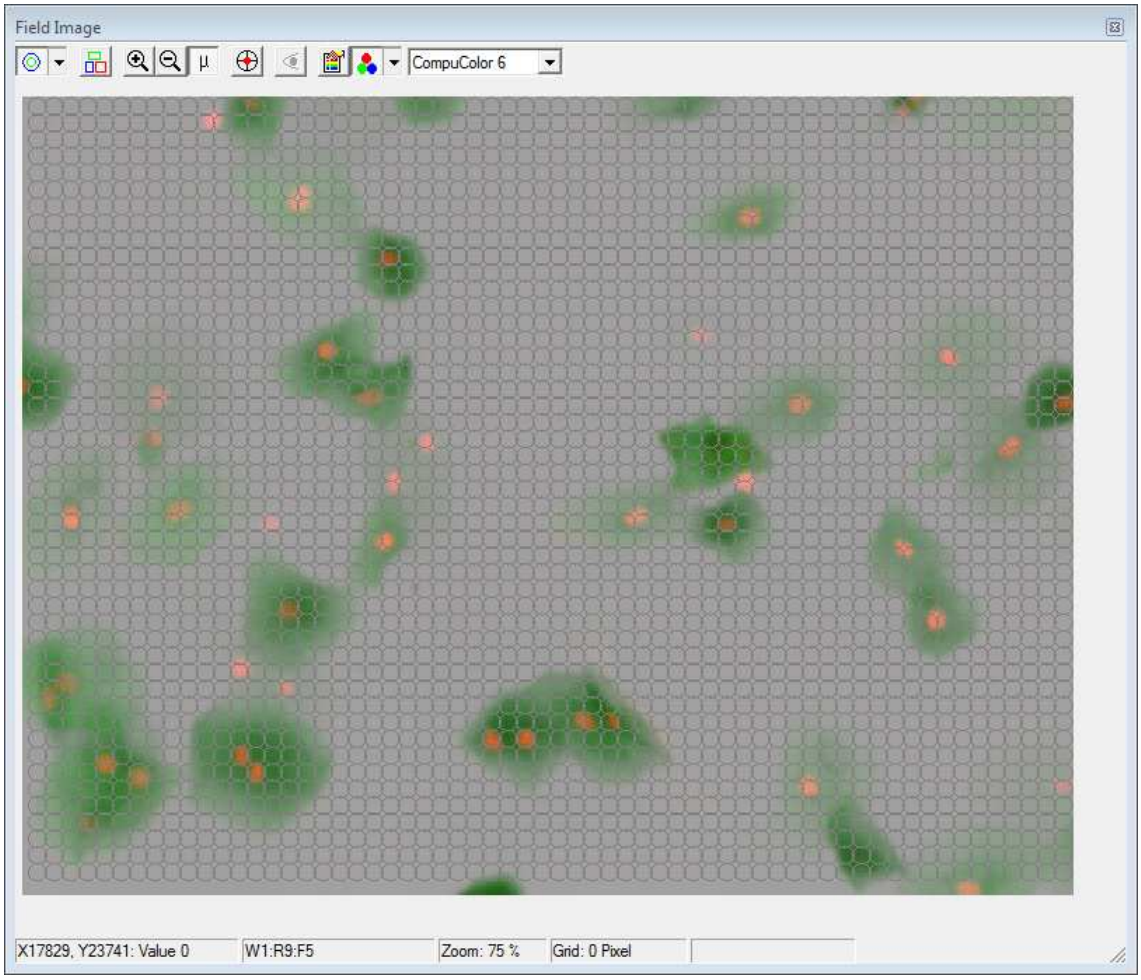

Figure 16: Example of phantom contours generated on a field image.
Cytoplasm and nuclei of buccal cells are represented in green and bright orange, respectively. Phantom contours are represented by grey circles.

Each of these circles can be represented by a dot on a scattergram (see Figure 9) and used for compensation. They can also be used to investigate the distribution of a signal on a tissue section. Hence, these circles were separated with a cut-off value depending on the total Light Green staining signal, i.e. low Light Green staining or high Light Green staining. Figure 17 represents the distribution of these circles falling into these two categories, expressed in percentage, for each of the groups. Interestingly it was observed that buccal cells from Down's and AD groups were significantly more intensely stained when compared to their respective controls (P<0.001 and P<0.01, respectively).

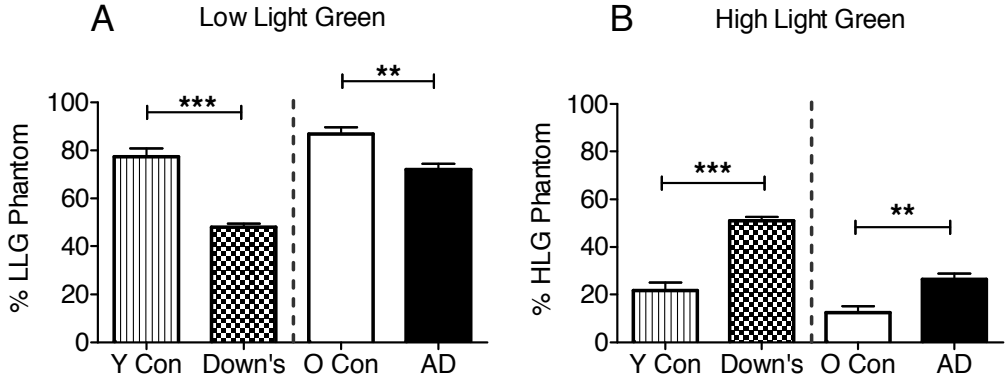

Figure 17: Representation of cytoplasm staining intensity by random phantom segmentation.

Random phantom segmentation measurements were done on young control (n=10), DS (n=10), old control (n=10) and AD (n=10) groups. (A) It can be seen that a lower percentage of phantom circles collected a low intensity of Light Green in the Down's (P<0.001) and AD (P<0.01) groups compared to their respective controls. (B) The percentage of highly Light Green stained circles was found to be higher in Down's (P<0.001) and AD (P<0.01) when compared to their respective controls. Abbreviations; AD, Alzheimer's disease; Down's, Down's syndrome; HLG, High Light Green; LLG, Low Light Green; O Con, Old controls; Y Con, Young controls; **, P<0.01; ***,P<0.001.

2.3.2 Cell cytome

This first attempt to separate buccal cell types, as described in section "*2.2.5.5 Identification of buccal cell types*", showed some differences in their percentages between groups (Figure 18). Basal cells for instance, were found to be significantly higher in DS when compared to young controls (P<0.01) whilst no significant differences were observed between these two groups when looking at transitional, differentiated and karyolytic cells. When comparing the AD and old control groups, no

differences were exhibited in the percentage of basal and differentiated cells. However a significant decrease in the percentage of transitional and karyolytic cells was observed (P<0.05 and P<0.01, respectively; Figure 18).

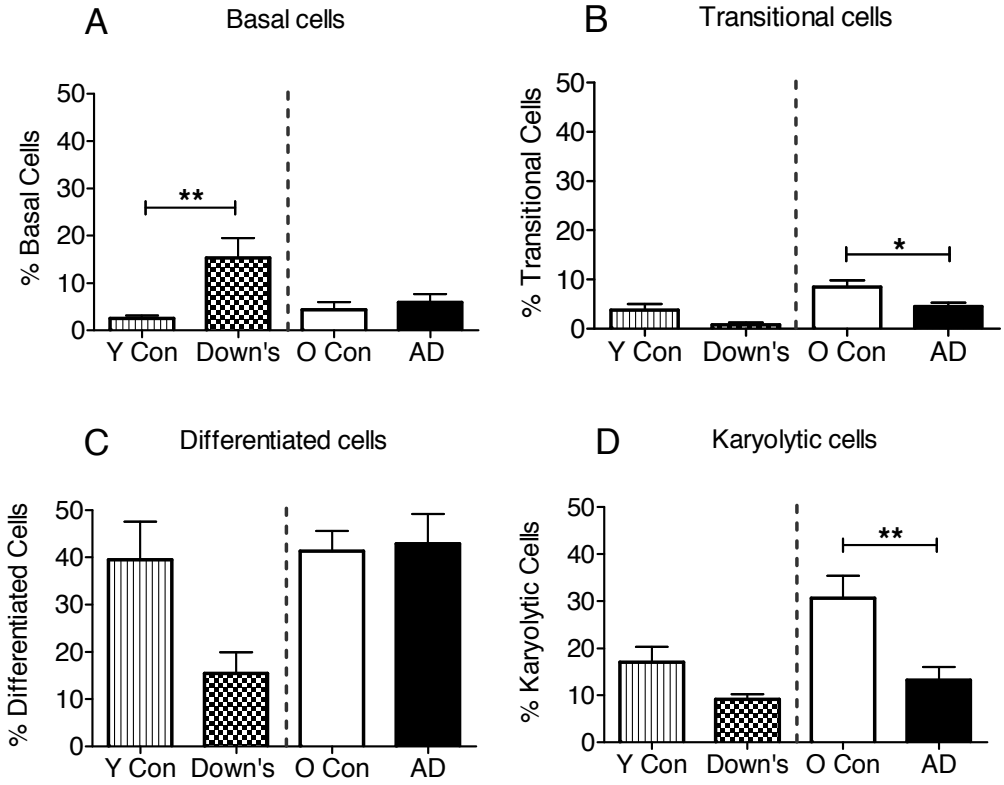

Figure 18: Distribution of the different cell types in DS, AD and controls.

(A) The percentage of basal cells was found to be significantly increased in DS (n=10) in regards to young controls (n=10), (P<0.01). (B) The AD group (n=20) showed a lower percentage of transitional cells when compared to old controls (n=10), (P<0.05). (C) No differences in the percentage of differentiated cells were observed between groups. (D) Karyolytic cells were found to be lower in AD when compared to old controls (P<0.01). Abbreviations; AD, Alzheimer's disease; Down's, Down's syndrome; O Con, Old controls; Y Con, Young controls; *, P<0.05; **, P<0.01.

2.3.3 Ploidy

The DNA content was measured and <2N, 2N and >2N nuclei peaks were separated as described in section "*2.2.5.7 DNA content*". Figure 19 shows the percentage of each of these peaks obtained between Down's, AD and their respective controls. No statistically significant differences were observed between groups. However there was a trend for an increase in >2N nuclei in Down's and AD relative to their respective controls and with ageing.

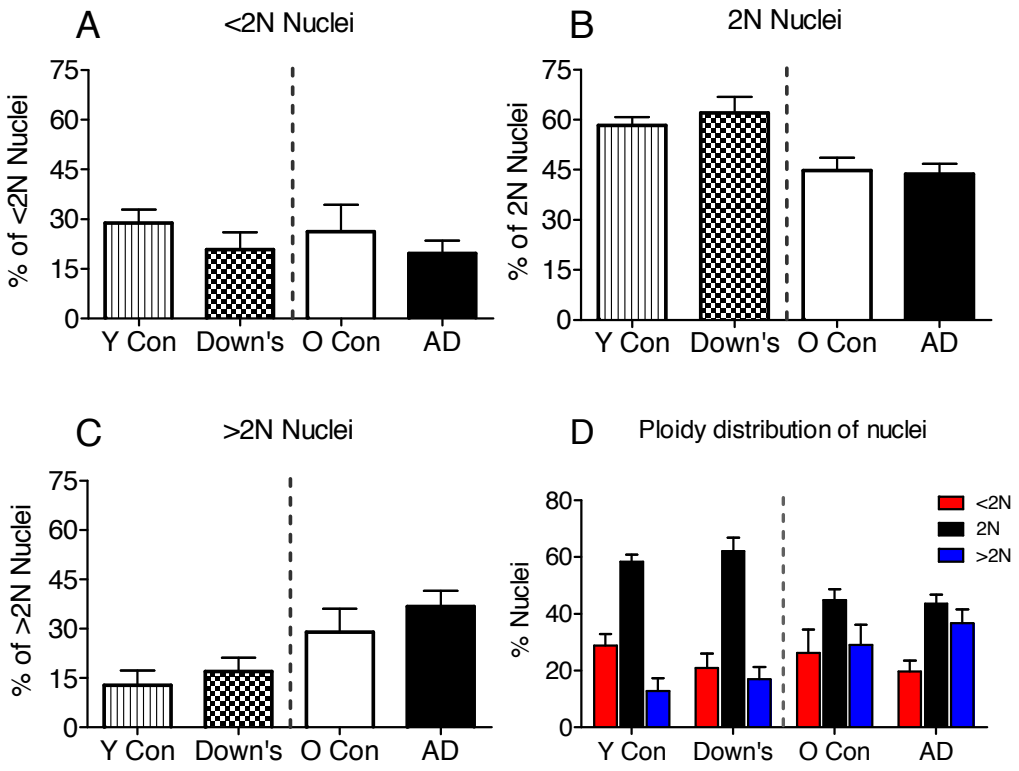

Figure 19: Ploidy distribution of buccal cells in Down's, AD and controls.
Ploidy measurements were done on young control (n=10), DS (n=10), old control (n=10) and AD (n=10) groups. No differences were observed in percentage of (A) <2N Nuclei, (B) 2N Nuclei and (C) >2N Nuclei between Down's, AD and their respective controls. (D) A bar graph reporting together the distribution of <2N Nuclei (red), 2N Nuclei (black) and >2N Nuclei (blue) for each groups. No significant differences were observed but there was a small increase in the percentage of >2N Nuclei accompanied by a small decrease in the percentage of <2N Nuclei occurred in Down's and AD, when compared to their respective controls. Abbreviations; AD, Alzheimer's disease; Down's, Down's syndrome; O Con, Old controls; Y Con, Young controls.

2.3.4 Micronuclei count

MN were detected and scored as described in section "*2.2.5.6 Nucleus and micronucleus"*. MN scores were reported as the number of MN detected per 1000 buccal cells analysed. Figure 20 shows the difference in MN scores between groups. A strong increase was observed between Down's and young controls (P<0.001) as well as AD and old controls (P<0.01).

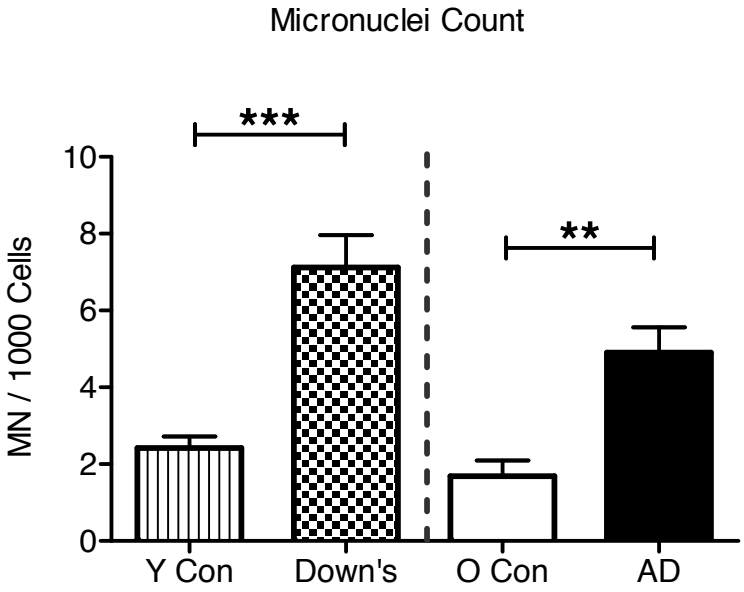

Figure 20: MN scores for Down's, AD and control groups.
MN scores are expressed in number of MN measured in 1000 buccal cells counted. Down's (n=10) and AD (n=10) exhibited an approximate 3-fold increase (P<0.001 and P<0.01, respectively) in their MN score when compared to their respective controls (n=20). Abbreviations; AD, Alzheimer's disease; Down's, Down's syndrome; MN, Micronuclei; O Con, Old controls; Y Con, Young controls; **, P<0.01; ***, P<0.001.

2.4 CONCLUSION

This initial attempt at developing a LSC protocol permitted a more rapid analysis of microscope slides compared to the visual scoring method previously applied. The buccal micronucleus cytome assay was successfully adapted on the laser scanning cytometer, however not all the features of visual scoring could easily be incorporated into the LSC protocol. For example binucleated cells and nuclear bridges were not able to be scored even after several attempts at developing protocols to measure these features. However, new measures were developed in the LSC protocol that could not be done by visual scoring such as DNA content and Light Green cytoplasm staining intensity. Therefore it was possible to use LSC to provide more quantitative data that is obtained without subjectivity.

Light green is an acid dye containing three sulphonic acid groups that bind to the free basic side chains of proteins (Lillie, Conn. 1969) and is a critical component of Papanicolaou stains which have been successfully employed in paraffin section and cytological smears, and can also be successfully combined with immunoreactions (Johnson, Klein. 1956; Elzay. 1983; Dalquen, et al. 1986; Albert, et al. 2012). Light green was also used in staining techniques for evaluation of MN, cytological and cytometric changes in buccal cells (Ayyad, et al. 2006; de Oliveira, et al. 2008). Additionally, Light Green stain was used in combination with the Feulgen stain for visual contrast of DNA and protein in cells (Oud, et al. 1984), and this latest combination of stains has been utilised to develop the buccal cytome assay (Thomas, et al. 2007; Thomas, et al. 2008a; Thomas, et al. 2009). Interestingly the differences in Light Green staining of buccal cells from one participant to another, quantified by the use of random phantom segmentation, showed an increase in the percentage of intensely stained cells in both Down's and AD groups compared with age-matched controls. Although the difference in staining was observed in this study, it is not known why this staining difference exists and therefore it would need to be replicated in future studies to verify if it can be repeated. Although this study did not analyse the Light Green staining in the different cell types, it is possible that there is different Light Green staining intensity among the different cell types, which may partly explain the differences in staining.

In this study there were differences in the scoring of the buccal cell types resulting in a significant decrease in karyolytic cells in AD relative to control ($P<0.01$). This trend is similar to that observed with visual scoring in a previous study (Thomas, et al. 2007). The percentage of transitional cells also decreased in AD ($P<0.05$), however this result could not be compared with visual assessment as transitional cells were not a category of buccal cell types in visual scoring study. Since LSC separation of cell types is based on user-defined cut-off values and drawn regions, these fixed parameters therefore permitted separation of this new category of cells that did not belong either in differentiated or basal cell categories. Although this study clearly demonstrates LSC can be useful for categorisation of buccal cell types, it must be noted here that the cells on the slides were not at an optimal concentration and therefore "spread" for LSC analyses. The cells on slides were originally prepared for visual scoring purposes. The high cell concentration on slides (cytospots) led to overlapping cells as well as numerous sheets of cells present on slides. The watershed algorithm feature of LSC software normally used to separate and contour adjacent events, was unfortunately not possible to adapt for such large cell groups even after extensive consultation with the software developers at CompuCyte Corporation. However, we have been working in collaboration with CompuCyte Corporation and the newer version of the software will likely include a developed algorithm based on a seeded approach to better manage the separation of clumps of large cells.

The measure of DNA content was another example of an important parameter that could easily be quantified by LSC but could not be assessed visually within buccal cells. However Feulgen is a stain that can be quantified with LSC by either using its absorbance or fluorescent properties. Although no significant differences were observed in DNA content, strong variations in signal intensity were noticeable between the absorbance and fluorescence of Feulgen when collected by LSC. In this study Feulgen exhibited a stronger signal when fluorescence was measured and therefore DNA content was quantified by the use of fluorescence. This stain may not be ideal for LSC analysis and a more common fluorescent dye such as PI or DAPI preferably, should also be considered for future studies (presented in later chapters) since it has been successfully used in LSC applications previously (Huang, et al. 2004; Darzynkiewicz, et al. 2010; Darzynkiewicz, et al. 2011).

Visual scoring of buccal cells showed trends for an increase in MN scores in Down's and AD when compared to their respective controls (Thomas, et al. 2007; Thomas, et al. 2008a). MN were efficiently detected by this LSC staining protocol and a similar increase was observed. MN are widely used markers of genomic instability, but the buccal micronucleus cytome assay is time consuming and subject to individual variations between scorers. Therefore it would be of valuable interest to compare visual and LSC MN scoring systems applied on different tissues to lead toward a more robust and validated automated MN detection system in future studies. The LSC protocol developed here corroborated the previous findings that MN were increased in DS and AD. To further improve cell type segregation with LSC, microscope slides prepared exclusively for LSC analysis with stains ideally selected would need to be prepared. Additionally further investigation of ploidy levels with commonly used nuclei stains in fluorescent analysis should be performed. The LSC protocol developed here could also be adapted to make use of molecular probes to investigate more specific aspects of DNA damage, including DNA adducts, aneuploidy and chromosome break measures (Ramirez, et al. 1999; Van Schooten, et al. 2002; Schwartz, et al. 2003), as well as DNA double strand breaks (e.g. γH2AX (Tanaka, et al. 2007; Tanaka, et al. 2009; Zhao, et al. 2009)) and measures of oxidative damage to DNA (e.g. 8-OHdG) within the nuclei of buccal cells (unpublished observations).

Although the LSC is a useful technology for automation of the buccal micronucleus cytome assay, it requires specific changes in the preparation of microscope slides and staining of buccal cells to be properly compared with visual scoring. This protocol should preferably be specifically adapted by combination with detection of other markers of AD risk for high-content analysis using LSC.

CHAPTER 3

3. SOUTH AUSTRALIAN NEURODEGENERATIVE DISEASE (SAND) STUDY

3.1. INTRODUCTION

Since the buccal mucosa (BM) is of ectodermal origin, defects in the BM cells may reflect potential for pathology in other tissues of ectodermal origin such as the nervous system. Biomarkers that may identify individuals who are at an early stage of AD would be useful as this would allow timely preventative intervention. In a recent pilot study by our group the validation of the full spectrum of biomarkers scoreable in the buccal micronucleus cytome assay was determined using a cytological classification of BM cells (Thomas, et al. 2007; Thomas, et al. 2008a; Thomas, et al. 2009). These studies showed that individuals who had just been clinically diagnosed with AD and prior to any medication have a significantly different buccal cytome profile compared to unaffected age- and gender-matched controls. In particular, there was a significant reduction in both basal and karyorrhectic buccal cell frequency which are associated with regenerative potential and cell death, respectively. The odds ratio for diagnosing individuals with AD having a combined basal and karyorrhectic frequency of <41/1000 cells is 140 with a specificity of 97% and a sensitivity of 82% (Thomas, et al. 2007), representing a potential biomarker for clinically diagnosed AD cases. These differences relative to controls were also evident in Down's syndrome (DS), which is a syndrome of accelerated aging and high propensity for development of AD (Thomas, et al. 2008a). Both conditions were also associated with elevated DNA damage as measured by an increase in buccal cell micronucleus frequency which is a biomarker of whole chromosome loss and/or breakage. Furthermore, DNA content (aneuploidy) is a marker of DNA damage resulting from chromosome mis-segregation and has been demonstrated to occur in the brain of human AD patients (Mosch, et al. 2007) and in human buccal cells (Thomas, Fenech. 2008). However, to our knowledge DNA content has not been determined in a quantitative and automated manner in human buccal cells previously.

There have been several studies demonstrating that a variety of lipid classes are substantially altered at a very early stage during AD pathogenesis (Han, et al. 2001; Han. 2005). Furthermore, relative to controls, altered levels of plasma apoE in AD have been observed (Taddei, et al. 1997; Gupta, et al. 2011). It has previously been indicated that Aβ generation in the brain can be regulated by intracellular cholesterol distribution in both animal and cellular AD models (Puglielli, et al. 2003). A recent report shows that skin fibroblasts from patients with diagnosis of probable sporadic AD display an imbalance between free cholesterol and cholesterol ester pools (Pani, et al. 2009a). Furthermore, Oil Red O (ORO) staining (indicative of accumulation of neutral lipids) has been used to demonstrate higher levels of neutral lipids in isolated peripheral blood mononuclear cells of probable AD patients (Pani, et al. 2009b). Since there is a lack of data available on accumulation of neutral lipids within buccal cells, we aimed to measure total neutral lipids in buccal cells using ORO staining as part of our high-content laser scanning cytometry (LSC) protocol (Leifert, et al. 2011).

The aim of this study was to use an automated high-content buccal cytome approach to assess whether buccal cell parameters could be used as a relatively non-invasive automated high-content analysis method for identifying those at risk of developing AD. We have developed and utilised an automated LSC cytome protocol in which various cell types, DNA content and neutral lipid content and their ratios were quantified to identify which parameters, if any, were most strongly associated with those subjects who were diagnosed with mild cognitive impairment (MCI) or classified as AD as compared to healthy age-matched controls.

3.2. MATERIAL AND METHODS

3.2.1 Recruitment and human ethics approval

Approval for this study was obtained from CSIRO Animal, Food and Health Sciences, University of Adelaide and Ramsay Healthcare Ethics Committee's. MCI and Alzheimer's patients were recruited at the College Grove Private Hospital, Walkerville, Adelaide, South Australia, following their initial diagnosis and prior to commencement of therapy. Diagnosis of AD was made by clinicians according to the criteria outlined by the National Institute of Neurological and Communicative Disorders and Stroke-Alzheimer's Disease and related Disorders Association (McKhann, et al. 1984), which are the well recognised standards used in all clinical trials. Inclusion/exclusion criteria were as follows; (1) Control Group (n=37): male or female, aged 55 and above, not clinically diagnosed with MCI or AD, no family history of MCI, AD. (2) MCI group (n=22): male or female, aged 55 and above, clinically diagnosed with MCI, no family history of MCI or AD. (3) AD group (n=15): male or female, aged 55 and above, clinically diagnosed with AD, no family history of MCI or AD. Exclusion criteria for all groups were as follows: patients who are undergoing chemotherapy/radiotherapy treatment for cancer, patients supplementing with micronutrients associated with genome maintenance (e.g. folate, vitamin B12) above recommended dietary intakes. Age, sex and Mini mental state examination (MMSE) scores information for each group are shown in Table 4.

Table 4: Clinical characteristics.

Means and standard errors from the mean (SEM) are reported for each group (95% CI in parentheses). Means with no associated letters are not significantly different from other means. Means with different letters are significantly different from each others. Significance is accepted at $P<0.05$. Abbreviations; F, Female; M, Male; MMSE, Mini mental test examination.

	Control	MCI	AD
Sex (M:F)	11:26	7:15	3:12
Age (year)	76.1 ± 1.5 (72.9-79.3)	75.3 ± 1.8 (71.5-79.2)	77.7 ± 2.8 (71.6-83.7)
MMSE score	28.4 ± 0.3 (27.8-28.9) **(a)**	26.2 ± 0.5 (25.1-27.3) **(b)**	21.2 ± 1.1 (18.8-23.5) **(c)**

3.2.2 Chemicals and reagents

All chemicals were of the highest quality grade: NaCl, Tris(hydroxymethyl)aminomethanehydrochloride (Tris), ethylenediaminetetraacetic acid (EDTA), sodium citrate, 4',6-diamidino-2-phenylindole (DAPI), formaldehyde, glycerol, 1-[2,5-Dimethyl-4-(2,5-dimethylphenylazo)phenylazo]-2-naphthol (Oil Red O), triethyl-phosphate and Fast Green were from Sigma-Aldrich (Castle Hill, NSW, Australia). Phosphate buffered saline (PBS) was from Invitrogen (Mulgrave, Victoria, Australia).

3.2.3 Buccal cell isolation

Consented participants had a one-off buccal cell sample collected after the brief information session outlining the purpose of the study. Buccal cells were collected by placing a small flat-headed toothbrush against the inner part of the cheek and rotated 20 times in a circular motion. Both left and right cheeks were sampled separately and then the toothbrushes containing cells were placed into 10 mL of buccal buffer (10 mM Tris, 0.1 M EDTA, 20 mM NaCl, pH 7.0) and agitated vigorously to dissipate the cells. Buccal cell samples were then placed in a refrigerator at 4^{o}C and were processed later that day as follows. After a brief centrifugation at 1000 xg for 10 min, the supernatant was removed and the cells resuspended in 5 mL of buccal buffer and repeated two more times. The cell suspension was vortexed and then homogenised for 2-3 min in a tissue homogenizer (15 mL Wheaton USA VWR) to increase the number of single cells in suspension. Left and right cheek cell populations were pooled in a 30 mL container then cells were drawn up into a syringe using an 21G needle and resuspended by drawing the suspension up and down 5 times. Cells were then passed through a 100 μm filter in a swinex filter holder to remove large aggregates of cells. Cell concentration was measured using a haemocytometer and cells transferred to a microscope slide using a Shandon Cytospin 4 (600 rpm) at a concentration of 60,000 cells/mL to obtain a final cell density of approximately 3,000 cells per cytospot done in duplicate. Slides were then air-dried for 15 min and subsequently transferred to 0.4% formaldehyde in PBS for 10 min, rinsed for 1 min with ultra pure water and air dried for 1 h, then stored in sealed microscope boxes with desiccant at -20°C until the staining procedure was performed. Details were recorded in an Excel file and backed up (i.e. participant number, initials of sampler, day of sampling, cell concentration, number of slides,

number of eppendorf tubes, box number where tubes and slides were stored, any notes and comments).

3.2.4 3T3-L1 Control cell line

ORO is a commonly used stain to detect neutral lipids and has been mainly used on tissue sections. However there appear to be no publications that have demonstrated ORO staining of human buccal cells, therefore it was necessary to investigate a positive control to ensure that the ORO staining procedure developed for buccal cells would detect neutral lipids in cells known to contain relatively high concentration of neutral lipids. A control cell line 3T3-L1 (CL-173) was therefore used, 3T3-L1 is a cell line derived from 3T3 cells that have a fibroblast-like morphology, but, under appropriate stimulation, the cells differentiate into an adipocyte-like phenotype. After differentiation the cells increase the synthesis and accumulation of triglycerides. After 3T3-L1 cells reached 100% confluence they were incubated with a differentiation medium over 15 days and accumulation of lipid droplets were observed over this period.

3.2.5 Staining of slides for LSC

Microscope slides containing buccal cells were defrosted at room temperature and stained in batches of 8 including a positive-stained control slide. Microscope slides were then washed 3 times for 30 sec each in 1% triethyl phosphate in ultra pure water and then incubated with ORO staining working solution (3 mg/mL ORO in 36% triethyl phosphate) previously filtered with a bottle top filter (0.45 μm porosities), for 45 min in the dark, to stain for neutral lipids. Slides were then washed 3 times with 1% triethyl phosphate and nuclei stained with DAPI (0.2 μg/mL) for 5 min. The excess of DAPI was removed by rinsing the slides in 300 mM NaCl, 34 mM sodium citrate and then slides were further stained in 0.2% (w/v) Fast Green for 30 min in the dark, to stain cytoplasm. The excess Fast Green was removed by rinsing the slides for 1 min with running tap water. Slides were then mounted with coverslips and PBS:Glycerol (1:1) medium. To avoid drying, the coverslips were sealed around the edge and slides were kept in the dark in a microscope box with desiccant at -20°C for up to two days prior to analysis by LSC.

3.2.6 Lipid analysis in plasma

Cholesterol, triglyceride, low- and high-density lipoprotein cholesterol levels (LDL-C and HDL-C) were measured in plasma. Lipid analysis for cholesterol, triglyceride LDL-C and HDL-C was performed on a Hitachi 902 Automated Analyser using Roche kits (Catalogue numbers: Cholesterol #11489232216, Triglycerides #11488872216 and HDL #04713109190). LDL cholesterol was calculated using the Friedewald equation (Friedewald, et al. 1972).

3.2.7 Laser scanning cytometry

3.2.7.1 Lasers and detectors

Microscope slides containing freshly stained buccal cells were inserted into a 4 slide carrier and analysed by iCyte® Automated Imaging Cytometer (CompuCyte Corporation, Westwood, MA). Lasers selected for high-content assays were 405 nm, 488 nm and 633 nm to detect DAPI, ORO and Fast Green, respectively. The blue photomultiplier tube (PMT) was used to collect fluorescence from DAPI and the Long Red PMT was utilised to capture fluorescence from Fast Green. As ORO is a chromatic stain, the 488 photo detector (PD) was set up to quantify its absorbance properties (Table 5).

Table 5: Laser and detector selection for buccal cells.

Target	Dyes	Excitation Lasers (nm)	Detectors
Cytoplasm	Fast Green	633	Long Red (Fluorescence)
Nuclei	DAPI	405	Blue (Fluorescence)
Neutral Lipids	Oil Red O	488	488 LL (Absorbance)

Abbreviations; LL, light loss (absorption)

3.2.7.2 Low and high resolution scans

Large rectangular low resolution scan areas were drawn around cytospots to locate cells with a low resolution scan using a 20x objective and a large (10 μm) laser increment step (Figure 21A). To obtain high resolution images for analysis, multiple small individual rectangular (1000 x 932 pixels) scan areas were defined for the high resolution scan (Figure 21B). It was found empirically that this size accommodates the

most optimal scanned image size for buccal cells. A 40x objective and small (0.5 µm) laser increment steps were used thus yielding high resolution detailed ‘‘images”. Each of the small individual rectangular scan areas generate a mosaic “Region Image” (Figure 21C) that is composed of six “Field Images” of higher resolution (Figure 21D).

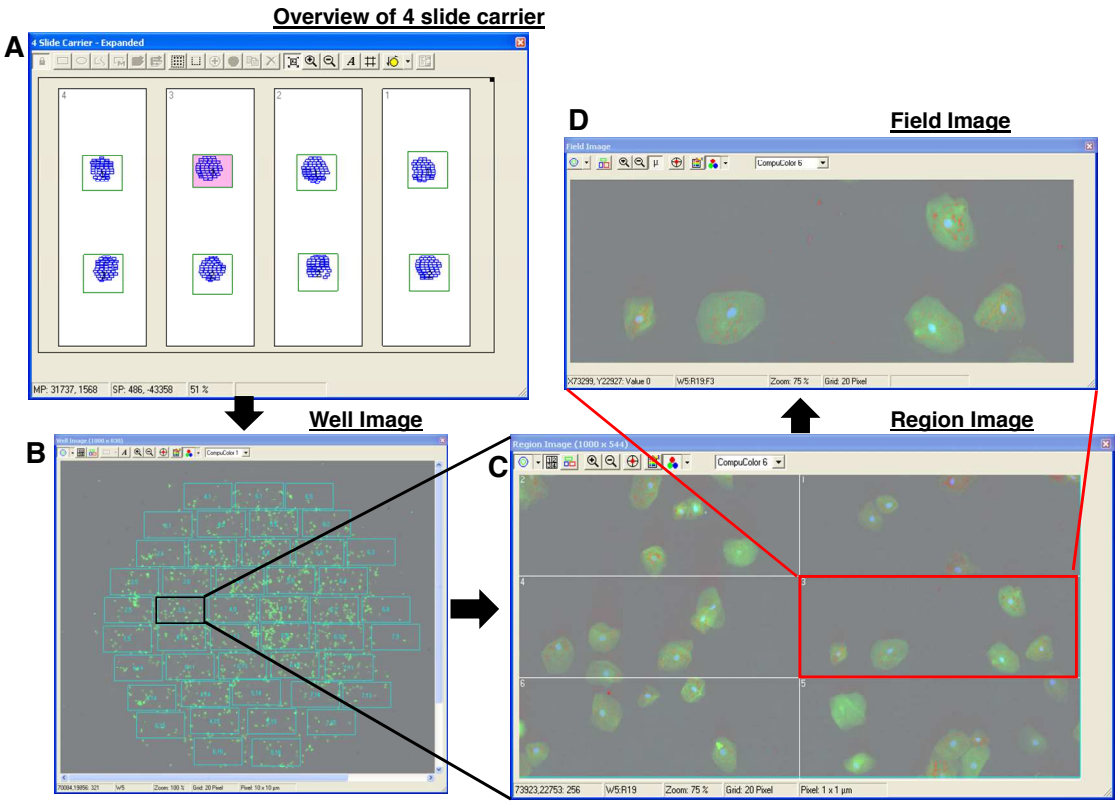

Figure 21: Low and high resolution scan representation.
(A) Slides were inserted into a 4 slide carrier and large rectangular low-resolution scan areas were drawn around cytospots shown in green. (B) This low resolution scan generated a “Well Image” to locate cells and allows the user to select many smaller rectangular high resolution scan areas to capture all cells on the cytospots (cyan). (C) Each one of those rectangles was scanned with a 40x objective and viewed with higher resolution as a “Region Image”. (D) Each “Region Image” is a mosaic image made of six high resolution “Field Images”. Field images are the last resolution stage and were used to quantify fluorescence and absorbance with iCyte Imaging software.

3.2.7.3 Setting up the dynamic range

In this study, detector settings were adjusted to capture clean and intense signal with the lowest background as possible. The dynamic range of a pixel for appropriate viewing of signal spreads from 0 (black) to 16,383 a.u. (white). This dynamic range can be seen in the y axis in Figure 23B. The voltage of PMTs must be adjusted to ensure that each fluorescent signal is collected and represented within that dynamic range. Therefore for

each laser used, the fluorescence or absorbance generated was captured and PMT voltages were adjusted for the most intense signal to be measured within that dynamic range, just below saturation (16,383 a.u.). For example, Figure 22 shows blue and long red PMT voltages were set at 31% and 35% respectively. In order to reduce background, off-set values were set at -0.01 and -0.07 for blue and long red channels respectively. Since the 488 PD collects absorbance, gain and off-set values were set differently in order for the background to be as close as saturation as possible. It was then necessary to create a virtual channel named "Blue I" to invert the absorbance signal for further quantification. This feature is commonly used in tissue analysis by LSC. To check and adjust the signal level of 488 absorption as well as to adjust the focus, a magenta line was manually drawn on a "Field Image" (Figure 23A) where values for both 488 Light Loss (LL) and "Blue I" were presented along that line in a "profile" window with 488 LL shown in gray and "Blue I" shown in red (Figure 23B).

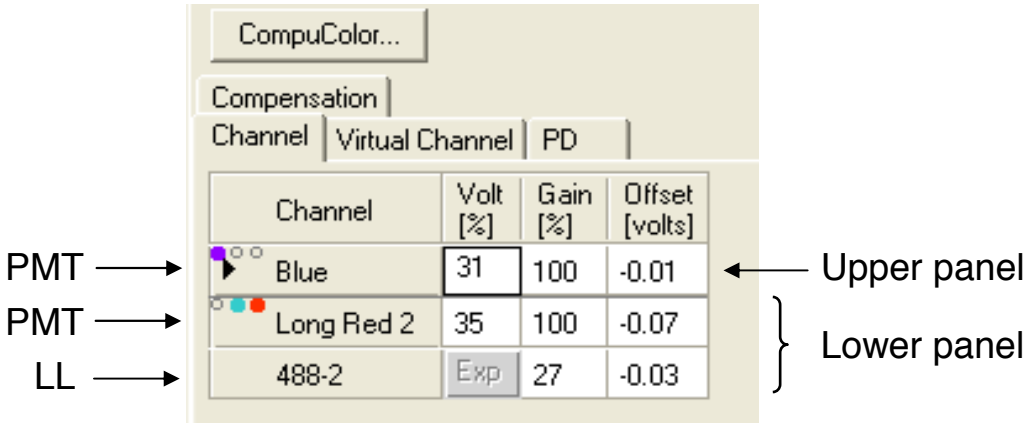

Figure 22: Setting the minimum and maximum fluorescence in the dynamic range.
Detector module of the high resolution scan. As shown in this picture the scan was separated into two paths to avoid further compensation. The first one (upper panel) used the 405 nm laser while the second path (lower panel) used both 488 nm and 633 nm lasers simultaneously. Voltage and Offset values were set to collect an intense and clean signal for both blue and long red 2 (fluorescent) channels while gain and Offset were adjusted for 488-2 LL channel. Abbreviations; LL, Light Loss; PMT, Photomultiplier tube.

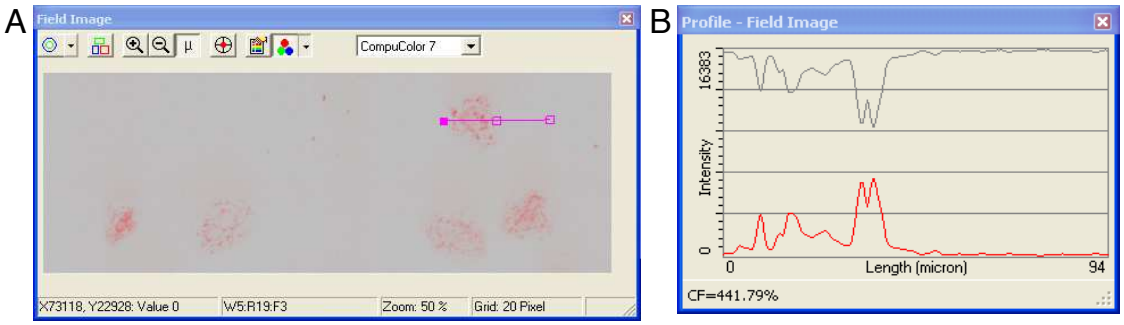

Figure 23: Field image and signal viewing.
As previously described in Figure 21, (A) a "field image" is shown and represents light loss (absorption) from the 488-2 channel. A magenta line was manually drawn overlapping the entire cell and each pixel along that line is then plotted (from left to right) on a graph for both those channels (Profile - Field Image) as shown in (B). The y axis represents the dynamic range for detection of pixel values. It can be seen that the original absorbance signal (grey) was set just below saturation and was then inverted as shown by the red line (which is the newly created virtual channel "Blue I").

3.2.7.4 LSC protocol and segmentation of events

A LSC protocol was created to combine Fast Green, DAPI and ORO detection and analyses (Figure 24). This protocol was separated in two main parts, (A) a low resolution scan scale, to generate an overview of cytospots, and (B) a high resolution scan scale whereby scale B is used for all parameters to be set up and to detect, contour and quantify the three main primary parameters namely, cytoplasm, ORO content and nuclei. From top to bottom in region B1 (the parameters which define the "cytoplasm"), the first module "Channel" is set to detect signal fluorescence collected in the Long Red 2 (fluorescence) channel. A filter was then applied to this signal using the second module using the "HiGauss 7x7" filter. This process slightly amplified the signal permitting a better contouring of cell cytoplasm border. The third "Threshold" module is a scalable feature that was used for defining and contouring the signal collected as an "event" (cytoplasm), i.e. pixel values that were below this threshold value (1162 in this example) were not considered as Fast Green but background signal. Once the threshold was applied and a line was drawn by the software marking the cell periphery of the cytoplasm border (using the threshold feature), the line was given a colour using the "contour" module. In the "Contour" module, the colour of the line manually drawn around cytoplasm was selected (in this scale green) and contouring was set to occur only for a cell with an area value of 200 μm^2 to avoid contouring around cellular debris. This value was determined empirically for the large buccal cells. The last module

named “Event” in B1 contained settings for defining contours. In this scale a background contour was set to subtract the Fast Green background signal to the signal measured within cytoplasm. (B2) The second part of the high resolution scan allowed detection and contouring of ORO staining, the channel used was “Blue I” (inverted absorbance of ORO) as described in section “*3.2.7.3 Setting up the dynamic range*” (Figure 23). The “HighGauss 7x7” was used as for B1 and the threshold in this example for ORO contouring was set to 2789 to allow for the detection of neutral lipid droplets. A “Watershed” module was also used since this algorithm allowed contouring of neutral lipid droplets that were touching or very close to each other. Much like the cytoplasmic “contour” setting, the ORO contour was drawn by the software around the periphery of ORO spots within the cytoplasm and this line was coloured magenta as shown by the “contour” module in B2. Additionally a size “inclusion” parameter was set to 1000 μm^2 to allow exclusion of any potential contaminating large non-specific staining or washed ORO overlaying cells (although these non-specific events were rarely observed, this feature was still used within the protocol). (B3) Represents the third channel “Blue” and was set up to define and quantify the signal collected from nuclei stained with DAPI. The “HiGauss 9x9” filter was used to enhance texture of nuclei and therefore chromatin condensation. The threshold was set at a relatively low value of 1278 a.u. in this example to further ensure the proper exclusion of karyolytic cells (with no nuclei). A “Close” feature was added to B3 to improve contouring of nuclei with low DNA content. The colour of the contour selected was blue. (C) Represents the “Association 2” module that allowed association of the three channels quantified and the selection of primary and sub-events. The “Multi-Scale Association” module allowed association of the low and high resolution scans so that all data or every pixel could be linked together for analyses. Note that both scales B2 and B3 (ORO and Nuclei respectively) were both sub-events of the primary event, which was the cytoplasmic staining. By setting up the sub-events in such a way, it allowed the ORO and nuclei to be directly linked to the cytoplasm. It was necessary to set up the scales B2 and B3 in such a way to eliminate false negative signals.

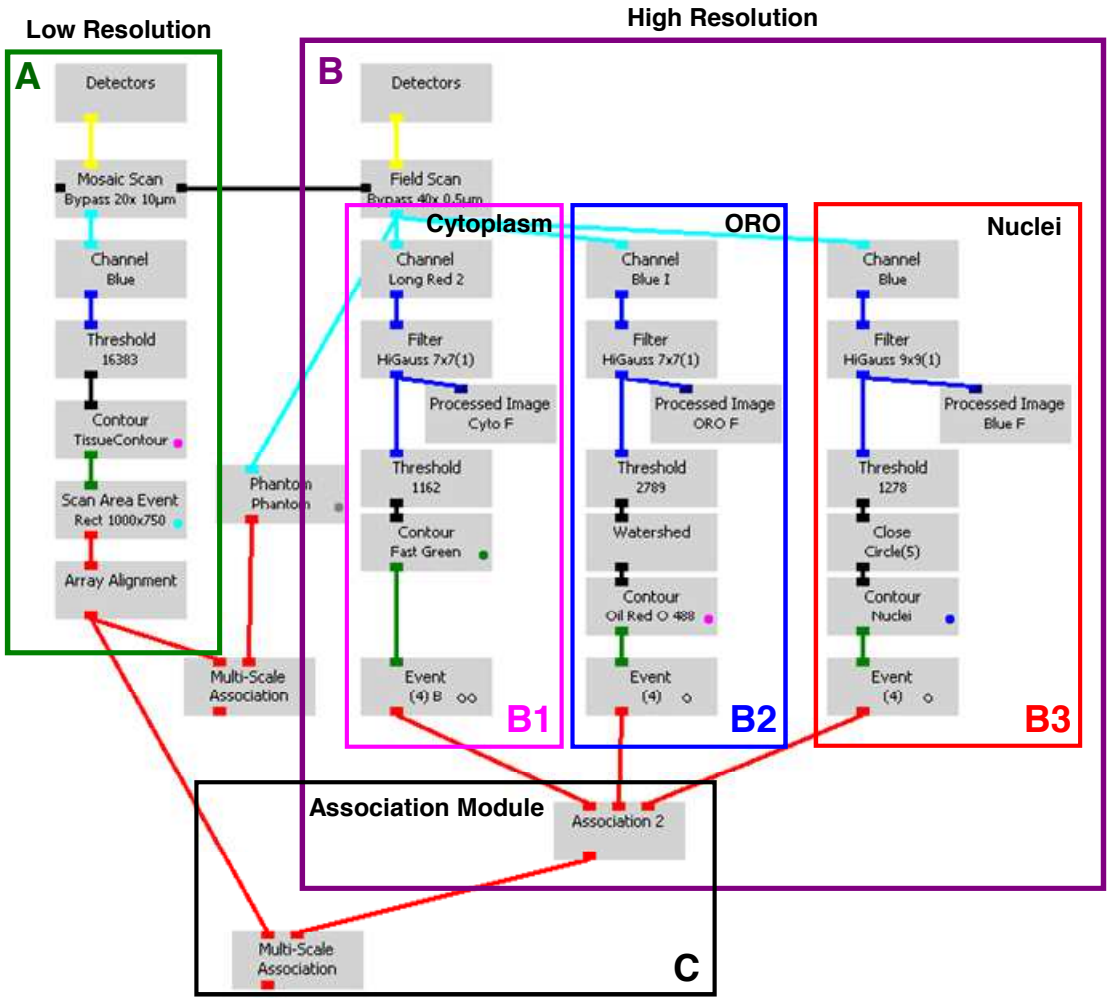

Figure 24: LSC protocol.
A schematic showing the LSC protocol that was developed for the high-content analysis of the buccal cytome, neutral lipids and DNA content simultaneously. (A) The first part of the protocol contains the parameters that were used to provide a low resolution scan to locate cells on slides that would subsequently be analysed in detail using the "High Resolution" scan. (B) The second part of the protocol shows all the modules that were used to define and quantify the parameters; cytoplasm (B1), ORO (B2) and nuclei (B3). (C) Represents the modules used to associate scales between each other. All modules and filtering processes are described in detail in section *"3.2.7.4. LSC protocol and segmentation of events"*.

An example of a field image can be seen without (Figure 25A) or with the three events (cytoplasm, nuclei and neutral lipids) contoured (Figure 25B).

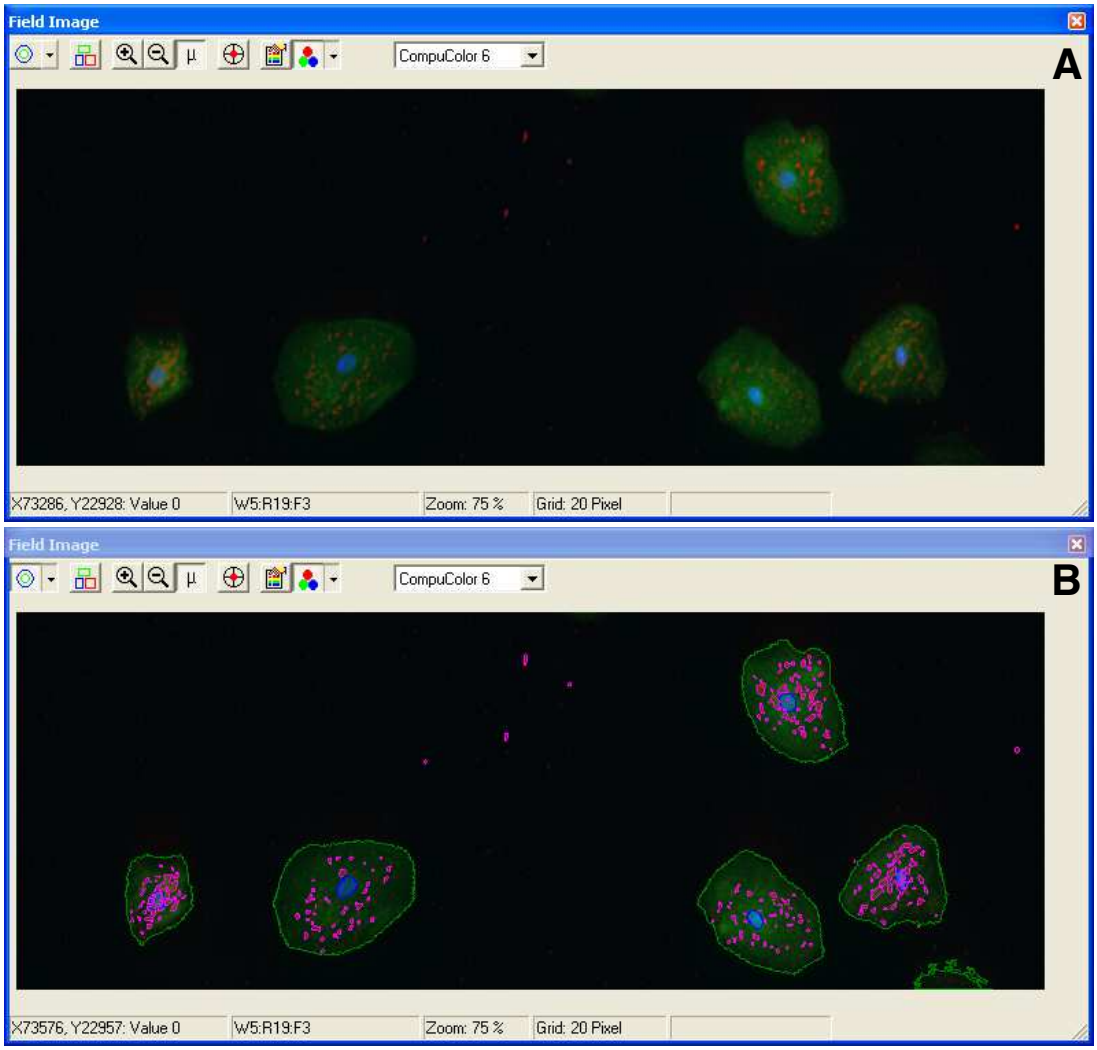

Figure 25: Field image with and without contouring.
A same field image generated by LSC represented, (A) without and (B) with contour feature activated; a green, blue and magenta contour is automatically drawn (by the mean of the settings previously selected in the LSC protocol; see Figure 24) around cytoplasm, nuclei and neutral lipids, respectively.

Prior to each batch scan the same region from a control slide of buccal cells stained with Feulgen was scanned with a 488 laser to ensure that all settings and measurements had not drifted over the course of the study (no variation was observed). With each batch scan the staining control slide containing buccal cells sampled from the same individual (healthy male aged 42) was also analysed with LSC. This procedure was done to ensure that all staining was not different from batch-to-batch (there was no variation in this study). The fluorescence (and absorbance where appropriate) of events were recorded as follows: area, count (number of events scored), circularity (a high circularity value indicates a less circular/oval perimeter of the event), maximum pixel (the highest pixel

value of an event is reported), fluorescence or inverted absorbance Integral (the total amount of fluorescence within an event obtained by the addition of all its pixel values). To eliminate false positive signals (i.e. not associated within the cells) from the analyses, the primary contour events in iCyte were based on cell cytoplasm staining i.e. the Long Red 2 Integral, whilst the secondary events (sub-events of the primary) were allocated to nuclear and neutral lipid staining. By setting up the iCyte software in such a manner, this ensured that any nuclear and neutral red signals that were analysed in this study were always located within cells and false positive signals were excluded. Indeed we noted that there was minimal (to none) false positive on the slides for all parameters examined.

Buccal epithelial cells isolated from the BM were not always completely dissociated into single isolated cells, but rather, we noted they exist as populations of single cells and groups of cells. To identify the individual cell types within the population of buccal cells (the buccal cytome) using LSC it was necessary to apply mechanical dissociation procedures (homogenising, passing the cell suspension through a small orifice e.g. 21G needle and a porous Millipore membrane) to the isolated buccal cell samples. Nevertheless, following this stringent protocol, some cells remained in small clusters of 2-6 cells on the microscope slides. Therefore our initial aim was to analyse all cells on the microscope slides, regardless of whether the cells were isolated single cells or those that were in small groups of 2-6 cells that were not completely dissociated during the mechanical separation procedures. Additionally, using the iCyte software we were able to analyse the isolated single cells in more detail by LSC and classify these cell types (as basal, transitional, differentiated and karyolytic) based on cytoplasm area and several nuclear staining parameters such as circularity, Integral and area. Figure 26 shows the two different ways of analysing buccal cells with LSC. Cells belonging to a group of cells in a clump could not be contoured separately but could be analysed to provide data for all cell types combined (Figure 26A), whilst single cells could be contoured individually and therefore separated between different cell types (i.e. basal, transitional, differentiated and karyolytic, Figure 26B). DNA content, ploidy, circularity and neutral lipid content was assessed by these two ways. Firstly the entire microscope slide was considered as a tissue section, and all nuclei were examined to obtain nuclear content data; the relative DNA content of the cells was determined by the Integral of DAPI fluorescence values. Neutral lipid content was determined from the ratio of ORO

area/Fast Green (cytoplasm) area. Secondly, single cells on the microscope slide were classified in a similar manner to previously, using the buccal cytome approach (Thomas, et al. 2007; Thomas, et al. 2008a; Thomas, et al. 2009). This allowed us to score the cell population consisting of basal, transitional, and differentiated or karyolytic type cells by using an automated scoring system with the iCyte software that will be described in the next section "*3.2.7.5 Automation of the buccal cell cytome*". Thus, it was then possible to investigate DNA content and neutral lipids in more detail within the defined cell populations.

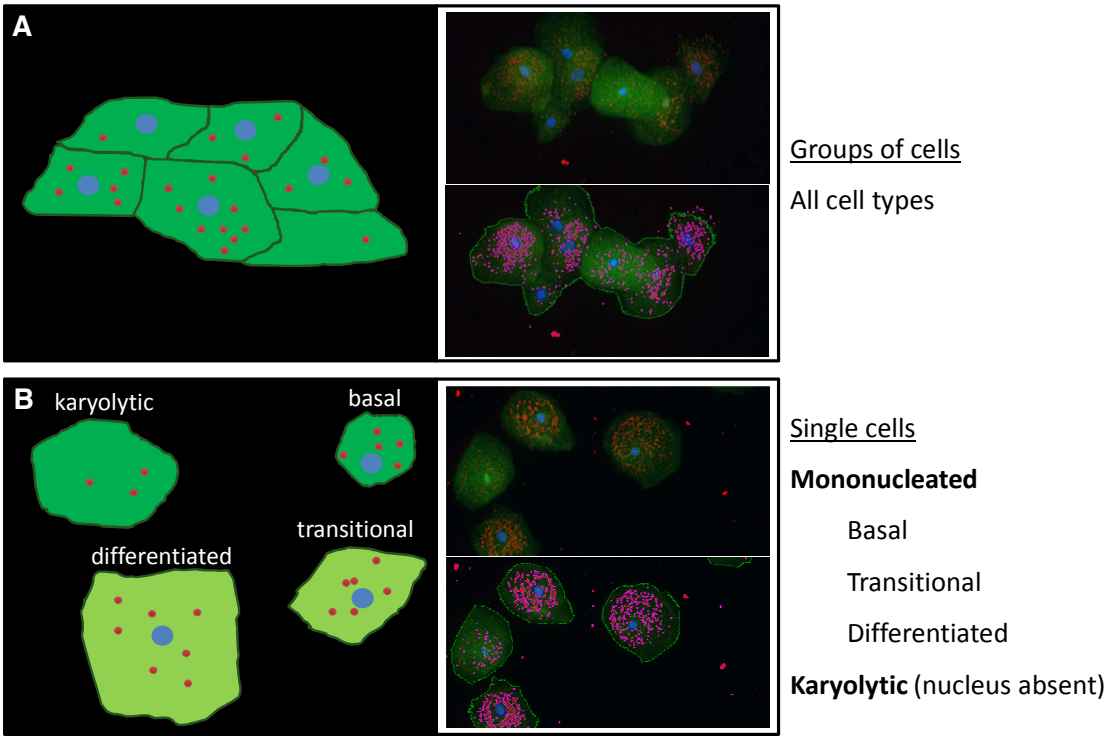

Figure 26: LSC Schematic for buccal cell analysis.
(A) Group of cells are contoured as a single event and utilised for analysis of all cell types. (B) Single cells are contoured individually and allow for analysis of different cell types. The magenta, blue and green contours represent ORO, nuclei and cell cytoplasm, respectively.

3.2.7.5 Automation of the buccal cell cytome

Identification of single cells for scoring in the automated buccal cytome assay consisted of identifying various features of the cells, then generating scattergram plots of those features and finally separating the scattergrams into sub-regions for analysis (Figure

27). Since the stains and the LSC protocol used in this study was very different compared with the previous study (Chapter 2), another method of defining cell types was necessary. Once this protocol was complete (Figure 24) the same "template" protocol was always used for all study participants ensuring there was no variation in the parameters being measured. Essentially, this resulted in a buccal cytome "fingerprint" for each individual sample being analysed and allowed for the quantification of the distribution of the different cell sub-types for each individual to be compared without subjectivity. Following a scan of multiple regions within a cytospot, all data generated were compiled into an initial scatterplot, this initial scatterplot was generated from the features shown in Figure 24. Cells were first plotted onto a scattergram segregating cells depending on their cytoplasmic Area and Long Red 2 Integral within the cytoplasm (Figure 27A). A region R1 was set and this gated data allowed a second scattergram (Figure 27B) to be created. This process allowed the exclusion of large clumps of buccal cells and very small debris from the analyses. The second scattergram then used the number of nuclei detected per cells as well as "Circularity" value to further separate cells. Circularity is a measure of irregular shape of cells indicating an increasing degree of non-circular shape (e.g. a higher circularity value indicates a higher non-circular, more irregular shape). The second scattergram (Figure 27B) generated data showing cells with 0, 1 or more nuclei. In the category where cells containing >1 nuclei were observed (these were visually checked using the "image gallery" function in the software), it was found that these events were in fact sheets of cells that were not fully dissociated during the cell preparation process and thus contoured as one event (thus each cell in the group contained a single nucleus). A region (R2) was then selected on the scatterplot B to identify karyolytic cells and a region (R3) was selected which identified single cells with one nucleus. Region R3 did not include contoured events having a circularity value of more than 175 (this cut-off point was found to optimally exclude very rare events such as large false positive stains from true single cells). For classification and scoring of single cell types using the buccal cytome approach, sheets of cells were not included in further LSC analysis steps. Additionally in this protocol binucleated cells were not scored and indeed our previous results have demonstrated that binucleated buccal cells are relatively rare events occurring less than 1% of all scored cells (Thomas, et al. 2009).

Single mononucleated cells which were subsequently scored in the automated buccal cytome assay were further categorised into 3 new regions based on the cytoplasm area as well as the $Area_{nuclei}/Area_{cytoplasm}$ ratios (Figure 27C). Following this procedure, buccal cells were categorized as basal (R9), transitional (R11) or differentiated cells (R12) based on their cytoplasmic area and $Area_{nuclei}/Area_{cytoplasm}$ ratio. To verify that this categorisation of cells was similar to that used in our previous (non-automated) study using visual scoring techniques (Thomas, et al. 2007; Thomas, et al. 2008a; Thomas, et al. 2009), galleries of cells within each region (R9, R11 and R12) were viewed to allow the proper categorisation based on the cytoplasm area as well as the $Area_{nuclei}/Area_{cytoplasm}$ ratios. An example of those cells types can be seen (Figure 28) with an increasing area and a higher $Area_{nuclei}/Area_{cytoplasm}$ ratio from basal to transitional to differentiated cells. Karyolytic cells were characterised by the lack of nuclei (blue contour), indeed no DAPI signal was detected.

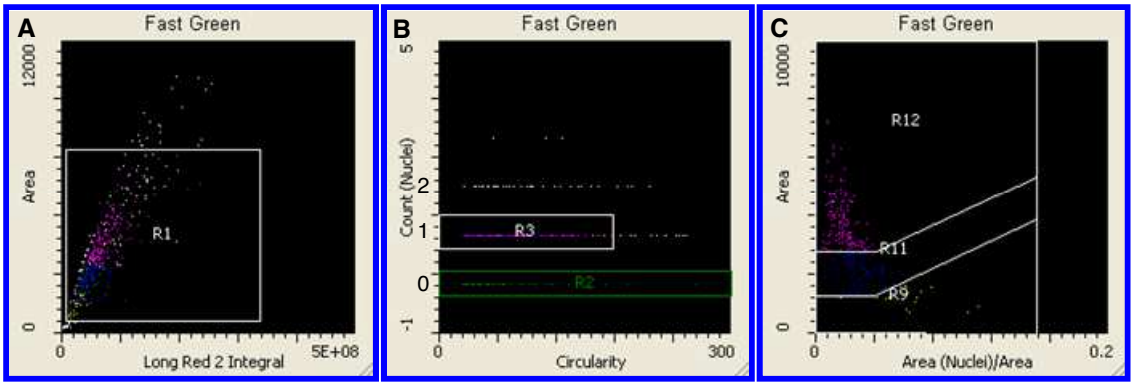

Figure 27: Protocol to classify buccal cell types.
(A) A region (R1) was selected to exclude small debris and large sheets of cells based on Area and Long Red 2 Integral values of "Fast Green" (cell cytoplasm) contoured events. (B) R1 was gated onto a second scattergram to separate Karyolytic cells (R2) and single mononucleated cells (R3) from clumps of cells as well as from false positives events. (C) A scattergram gated from R3 in (B) was used to separate single cells based on their Area and $Area_{Nuclei}/Area_{Cytoplasm}$ ratio. Cells were categorised as follows, basal (R9), transitional (R11), differentiated (R12).

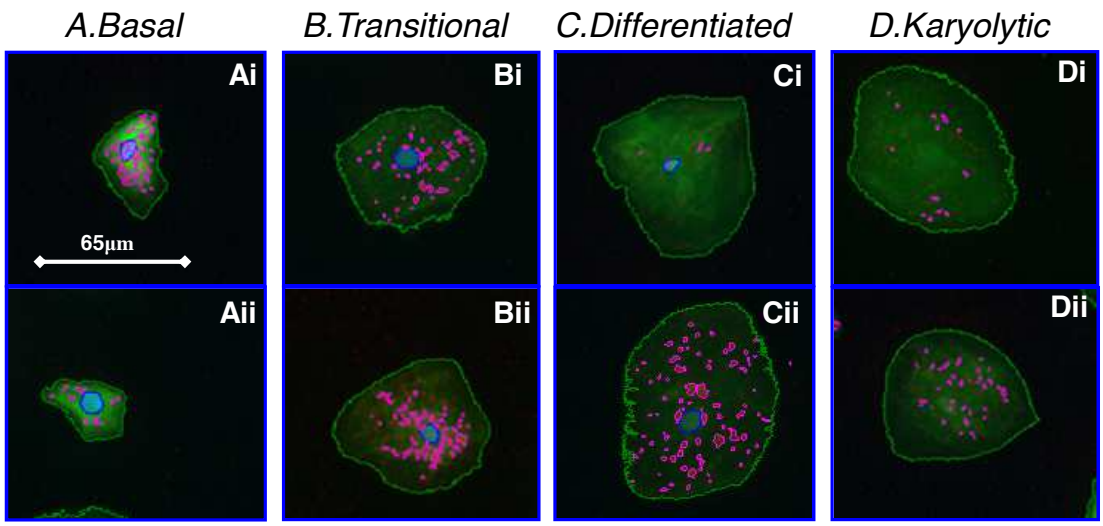

Figure 28: Cell types gallery.
LSC Images of (A) basal, (B) transitional, (C) differentiated and (D) karyolytic cells.
The magenta, blue and green contours represent ORO, nuclei and cell cytoplasm, respectively.

3.2.7.6 Measurement of DNA content

To discriminate cells in particular phases of the cell cycle, DNA content of nuclei was measured (Figure 29). A frequency histogram showing the number of nuclei ("count") versus the "Blue Integral" calculated from DAPI staining or nuclei was first created to separate nuclei depending on their DNA content (A). Three regions were selected from the different peaks obtained; (R15), (red) separated <2N from 2N nuclei (R16), (black) and a third region (R14), (magenta) segregated all >2N nuclei. Nuclei were also plotted on a scattergram (C) to demonstrate the variability in the Blue Integral and Blue MaxPixel (an indication of chromatin condensation) relationships (Figure 29B).

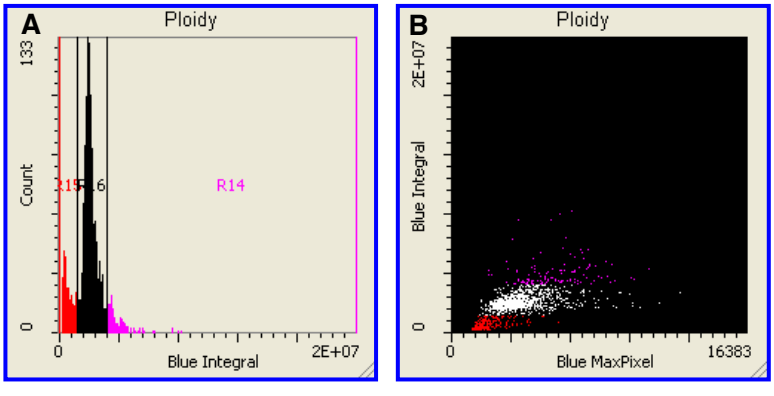

Figure 29: DNA content measurements.
Histogram and scattergram used to separate nuclei depending on their DNA content. (A) DNA content. Three regions were selected to separate peaks of <2N (R15, red), 2N (R16, black) and >2N (R14, magenta) nuclei. (B) A scattergram generated to show the relationship between Blue Integral and blue MaxPixel.

3.2.7.7 Data and statistics

3.2.7.7.1 Generation of data

Statistics were generated for each cytospot examined as shown in Figure 30.

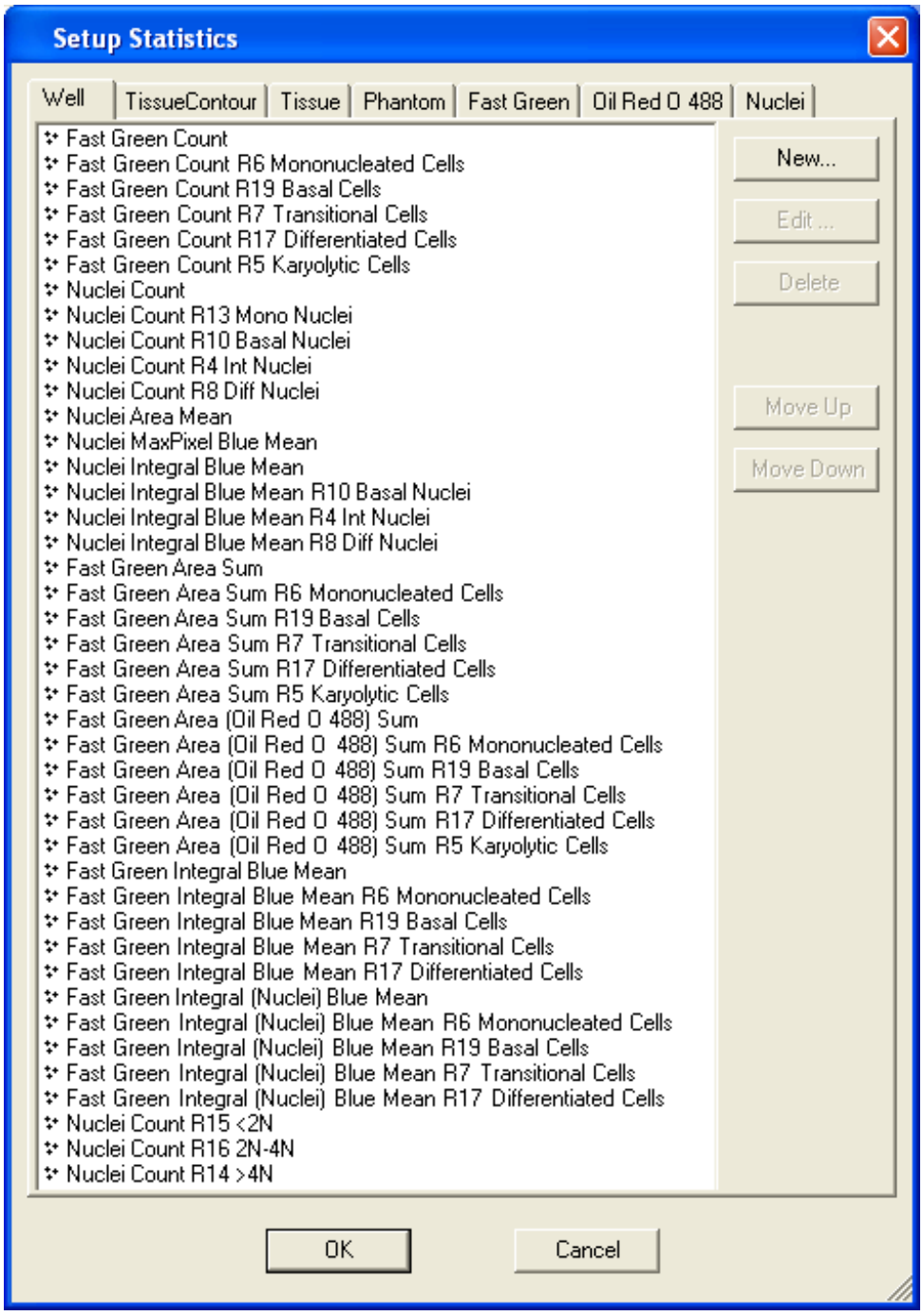

Figure 30: Data output.

An example of the data files that were collected for each cytospot examined by LSC. Each file was exported directly to Excel for data manipulation and analysis.

3.2.7.7.2 Statistical analysis

One-way analysis of variance (ANOVA) and linear correlation analyses were carried out to determine the significance of the cellular parameters measured between the control, MCI and AD groups. Pairwise comparison of significance between these groups was determined using Tukey's test. ANOVA and correlation values were calculated using GraphPad Prism 5 (GraphPad Software Inc., San Diego, CA, USA). Significance was accepted at $P<0.05$. Column statistics were generated and receiver-operating characteristic (ROC) curves were carried out for selected parameters and their combinations between the control and MCI groups as well as AD groups to obtain area under the curve (AUC), confidence interval (CI), P-values, sensitivity and specificity scores.

3.3 RESULTS

3.3.1 ORO Staining and protocol development

3.3.1.1 Triethyl phosphate vs. isopropanol – Dissolution of ORO.

In preliminary assays only weak ORO signal was observed after staining buccal cells by the method of Mutoh et al. 2009, in which ORO is usually dissolved in 60% isopropanol to make up a stock solution. However dissolution of the solid was incomplete even after constant shaking and heating of the solution to 60°C overnight. This resulted in a solution containing a large quantity of insoluble ORO aggregates which after being removed by filtration, left the solution a light red colour. However, Koopman and Schaart have worked on a protocol to improve the ORO staining procedure (Koopman, et al. 2001). They showed that when isopropanol was replaced by another solvent such as triethyl phosphate, dissolution of ORO was significantly enhanced. Therefore, ORO solid was mixed with 60% triethyl phosphate followed by gently mixing overnight at 60°C, resulted in complete dissolution of the solid. Both stock solutions were tested for staining and noticeable differences were observed, with a more intense ORO staining of buccal cells when the stock solution was prepared in triethyl phosphate as a solvent compared with isopropanol as the solvent.

3.3.1.2 Fixative conditions

To determine which fixation method was most suitable for ORO staining, two fixation methods were tested using 3T3-L1 cells before and after differentiation to adipocytes. Cells were either fixed with 0.4% formaldehyde in PBS or with ethanol:acetic acid mix (3:1), both for 10 min at room temperature. Cells were then stained with ORO as described in methods section *"3.2.5 Staining of slides for LSC"* but with Fast Green initially and counter stained with DAPI. ORO and DAPI staining were detected by fluorescence microscopy and ORO was also visualised by brightfield microscopy. When the negative control cell line 3T3-L1 was fixed with either ethanol:acetic acid (Figure 31Ai, Aii) or formaldehyde (Figure 31Ci, Cii), cells did not exhibit ORO staining. However 3T3-L1 differentiated (adipocytes) showed a strong ORO staining after fixation in formaldehyde (Figure 31Di, Dii) while only a very weak red staining could be observed under brightfield when fixed with ethanol:acetic acid mix (Figure 31Bi, Bii), (red arrows). It also appeared that ORO stain displayed a stronger signal when observed under brightfield microscopy (Figure 31Dii) when compared with

fluorescence (Figure 31Di) and that only intensely stained lipid droplets were detected under fluorescence. The absorbance and fluorescence properties of the dye were therefore compared with LSC. ORO staining in adipocytes was detected with LSC either by the use of 488 absorbance, with grey (Figure 32A) or with a background converted to black to improve contrast (Figure 32B), or 633 laser excitation with fluorescence collected in the long red (Figure 32C). ORO staining was again observed to be stronger when detected with absorbance compared with fluorescence. A contour was set to detect ORO droplets and their signal intensity was collected and displayed on scattergrams for absorbance (Figure 33A) and fluorescence (Figure 33B). The number of droplets contoured using absorbance as the parameter was greater than that for fluorescence indicating that fluorescence did not easily detect lightly stained ORO droplets. Moreover the maximum intensity of the signal quantified in droplets was found to be higher with absorbance detection when compared to fluorescence (see magenta square). Therefore all further analyses of buccal cells were therefore performed using the absorbance properties of the ORO stain.

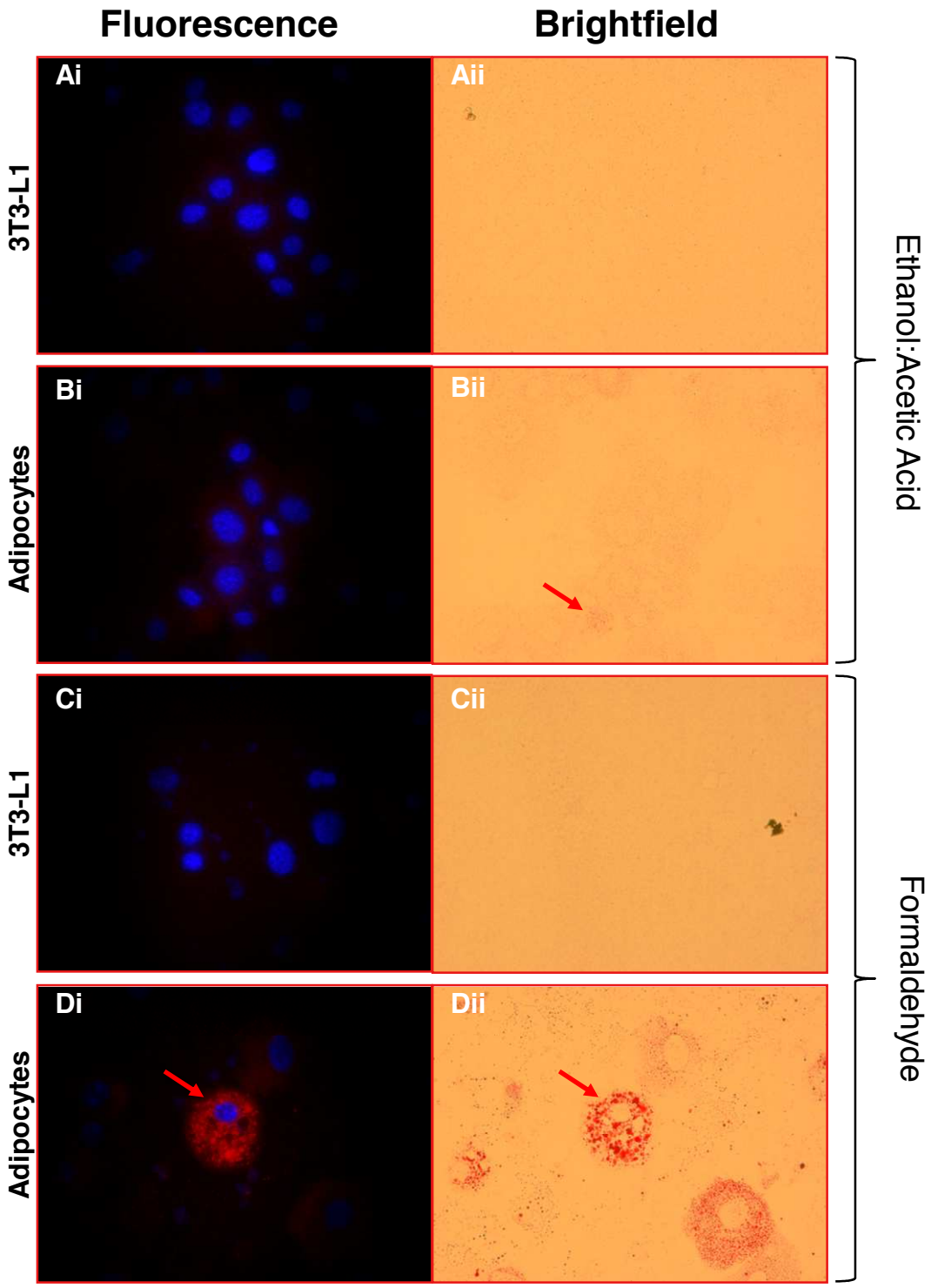

Figure 31: ORO staining of 3T3-L1 cells and adipocytes.
ORO staining was compared using two different cell fixative methods. Cells were observed using a fluorescence microscope (left panels Ai, Bi, Ci, Di), (using DAPI filter) or under brightfield illumination (right panels Aii, Bii, Cii, Dii).

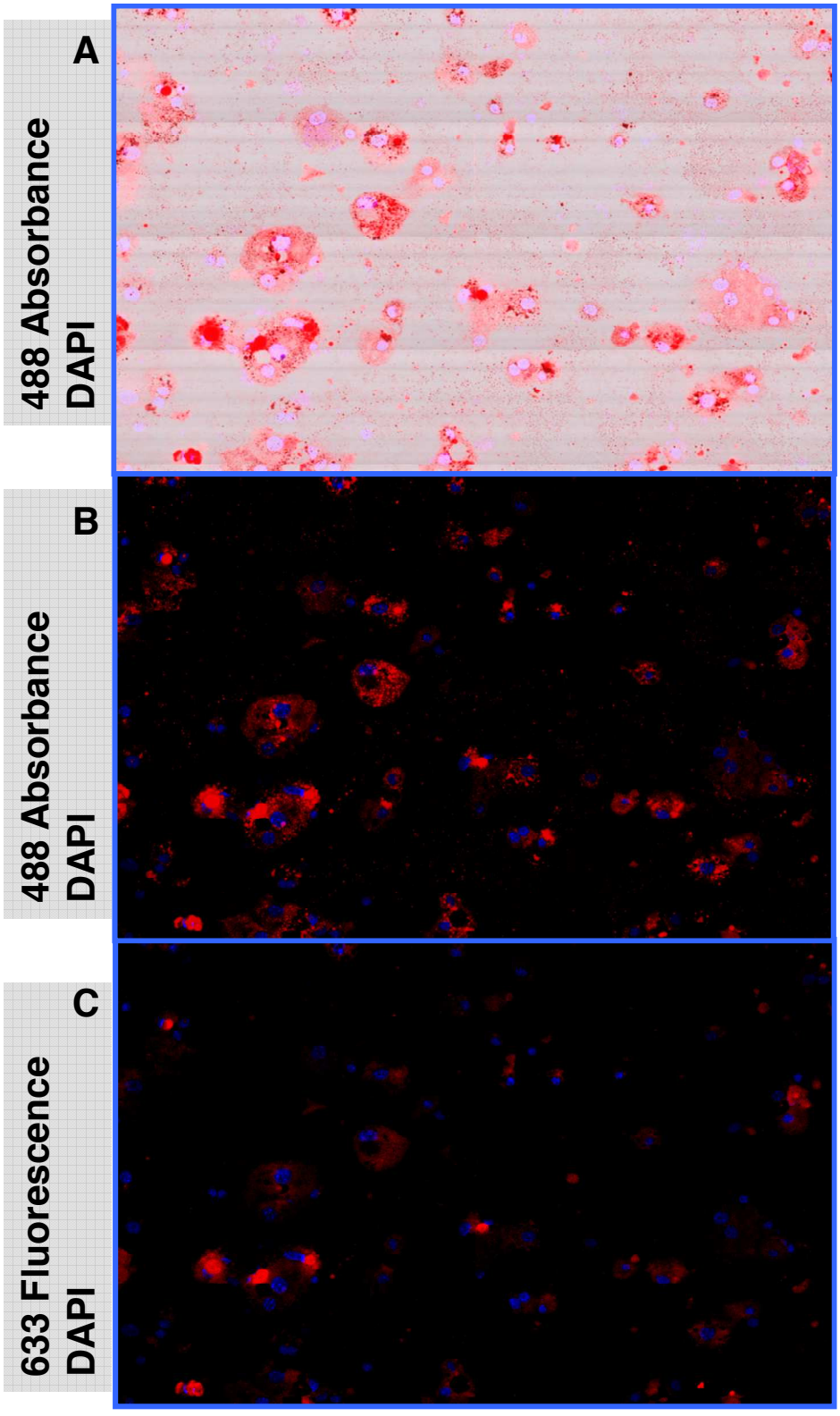

Figure 32: Comparison of absorbance and fluorescence signals of ORO by LSC.
(A) ORO (red) was detected by absorbance at 488 nm combined with DAPI detection (blue). (B) The same representation than A with a background converted to black to improve contrast and for better comparison with C. (C) ORO (red) was detected by fluorescence at 633 nm in the long red channel combined with DAPI detection (blue). Abbreviations; DAPI, 4',6-diamidino-2-phenylindole; LSC, Laser scanning cytometry; ORO, Oil Red O.

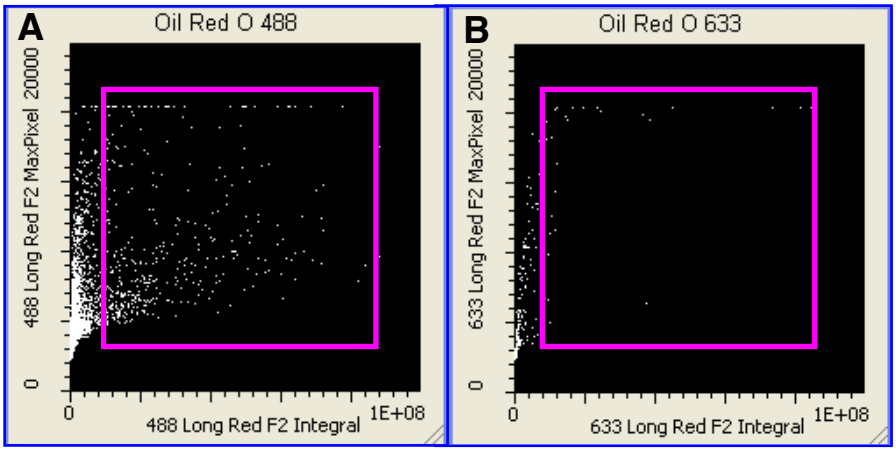

Figure 33: Comparison of absorbance and fluorescence intensity of neutral lipid droplets in adipocytes by LSC.

Scattergrams showing ORO staining quantified using (A) absorbance at 488 nm or (B) fluorescence at 633 nm in the Long Red channel.

3.3.1.3 Washing conditions

As suggested in the protocol developed by Koopman and Schaart (Koopman, et al. 2001), deionised water was used to wash cells before and after incubation with ORO working solution. However when washes with Milli-Q water were applied in this protocol, numerous non-specific ORO binding was detected after scanning with LSC (Figure 34A). Therefore, several washing conditions were tested; i.e. with 1%, 5% and 37% triethyl phosphate. Images obtained by LSC for each of the conditions can be seen in Figure 34 (B, C, and D). When washes were carried out in 37% triethyl phosphate (Figure 34D), most of the ORO staining was removed from the cells while 1% and 5% triethyl phosphate was less stringent and appeared to only remove non-specific binding from the slides (Figure 34B and C). Since small aggregates remaining could easily be excluded from analysis with the use of LSC software, 1% triethyl phosphate solution was preferred to 5% triethyl phosphate for the washing steps to avoid losing cytoplasmic ORO signal.

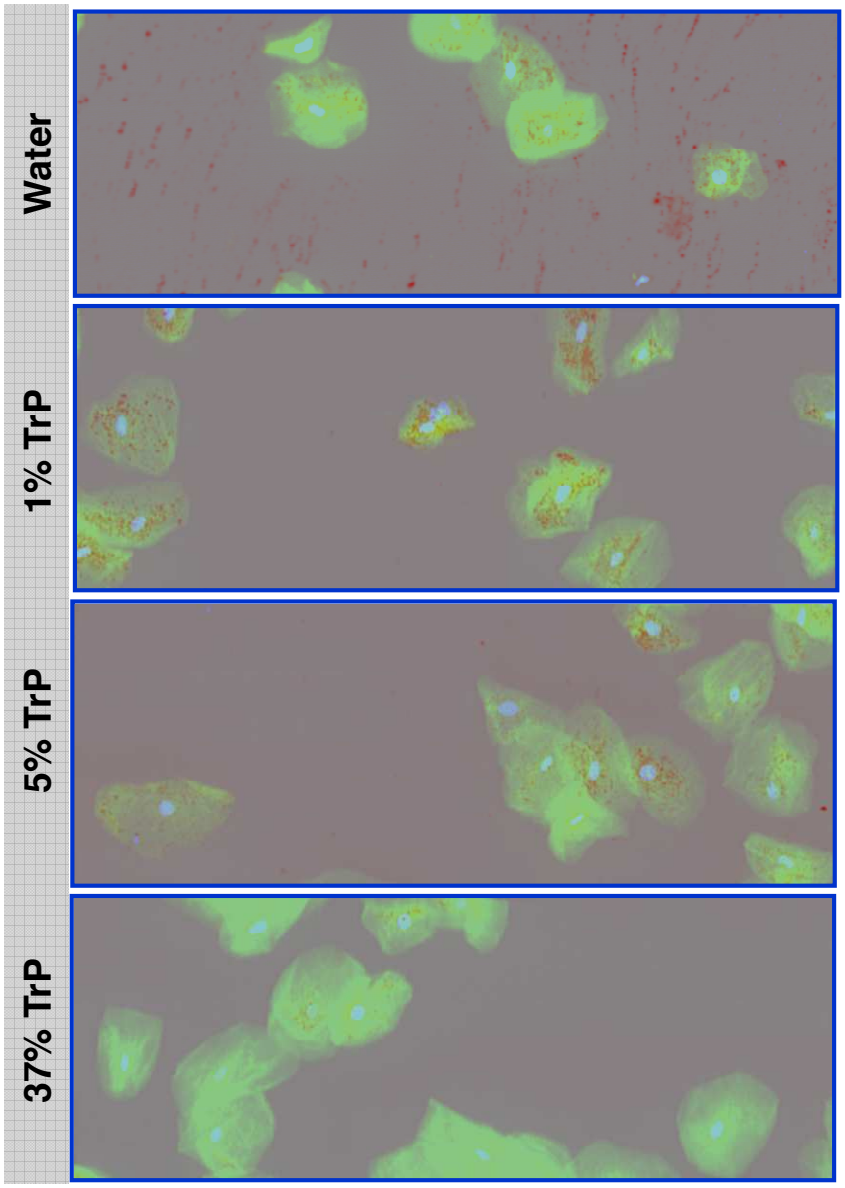

Figure 34: Washing conditions and their effect on ORO staining on buccal cells.
The effect of four different washing conditions (A) water, (B) 1%TrP, (C) 5%TrP and (D) 37%TrP on ORO staining in buccal cells were tested. Abbreviations; Trp, Triethyl phosphate.

3.3.1.4 Mounting medium

Finally, the last issue in the development of the protocol was the choice of the mounting medium. Originally DePeX was used for buccal cells as in chapter 2, section *"2.2.4 Buccal cell fixation and staining"*. However when DePeX was applied on stained cytospots it could be visually seen that DePeX was removing the stain instantly. Therefore, PBS:glycerol mix (1:1) was tested and found to not remove the ORO staining on cells.

3.3.2 Laser scanning cytometry analysis

3.3.2.1 Buccal cytome

In previous studies from our group it was showed that the buccal cytome assay could be used for identifying changes in buccal cell morphology and nuclear parameters in age-related disease such as AD and DS (Thomas, et al. 2007; Thomas, et al. 2008a; Thomas, et al. 2009). Although our previous studies used a visual scoring with different staining conditions, our aim here was to automate the buccal cytome scoring using LSC and to include high-content analysis with a protocol including Fast Green (cytoplasm), DAPI (nuclei) and ORO staining (neutral lipids). Using the protocol as described in section *"3.2.7.5 Automation of the buccal cell cytome"*, single cells were scored based on several cytoplasmic and nuclear staining parameters. We first identified and classified the buccal cytome with the following cell types; basal (Figure 35Ai), transitional (Figure 35Aii), differentiated (Figure 35Aiii) and karyolytic cells (Figure 35Aiv). The distribution of the various cell types was first investigated in the control group and was 13%, 34%, 27%, 26% for basal, transitional, differentiated and karyolytic cells, respectively (Figure 35B). There was a significantly lower percentage of basal cells compared to the other cell types ($P<0.001$) as well as a higher percentage of transitional cells compared to differentiated, karyolytic and basal cells ($P<0.01$). Basal cells are the cells from the basal layer which are smaller in size when compared to differentiated buccal cells and have a nuclear to cytoplasm ratio that is larger than in differentiated buccal cells. According to the classification criteria used here basal cell frequency was 13%, 15% and 17% for control, MCI and AD, respectively (Figure 36A; not significantly different). Transitional cells were classified as a group of cells that were neither large fully differentiated cells nor small basal cells. Transitional cells showed a larger cytoplasm than basal cells and occurred with a frequency of 34%, 29% and 30% for control, MCI and AD, respectively (Figure 36B; not significantly different). Differentiated cells were distinguished from basal cells and transitional cells by their larger size and by a smaller nuclear to cytoplasmic ratio (Figure 36C). These cells are considered to be terminally differentiated relative to basal cells. Figure 36C shows the differentiated cell frequency was 27% for control, 30% for MCI and 29% for AD group. Karyolytic cells were another group of cells scored characterised by absence of a nucleus (completely depleted of DNA) and therefore showed no DAPI staining (Figure 35Aiv). These cells represent a very late stage in the cell death process. Figure 36D

shows the karyolytic cell frequency was not significantly different between groups with 26% for control, 26% for MCI and 24% for AD.

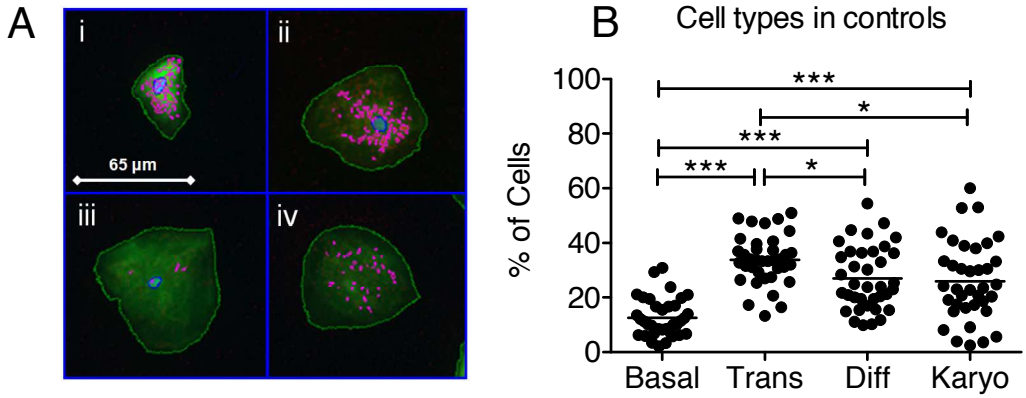

Figure 35: Buccal cell types scored in controls by LSC.
(A) LSC images of different cell types. (Ai) basal, (Aii) transitional, (Aiii) differentiated and (Aiv) karyolytic cells are shown. (B) Scores for each of these cell types were determined in the control group (n=37). Abbreviations; Diff, Differentiated cells; Karyo, Karyolytic cells; Trans, Transitional cells; *, P<0.05; ***, P<0.001.

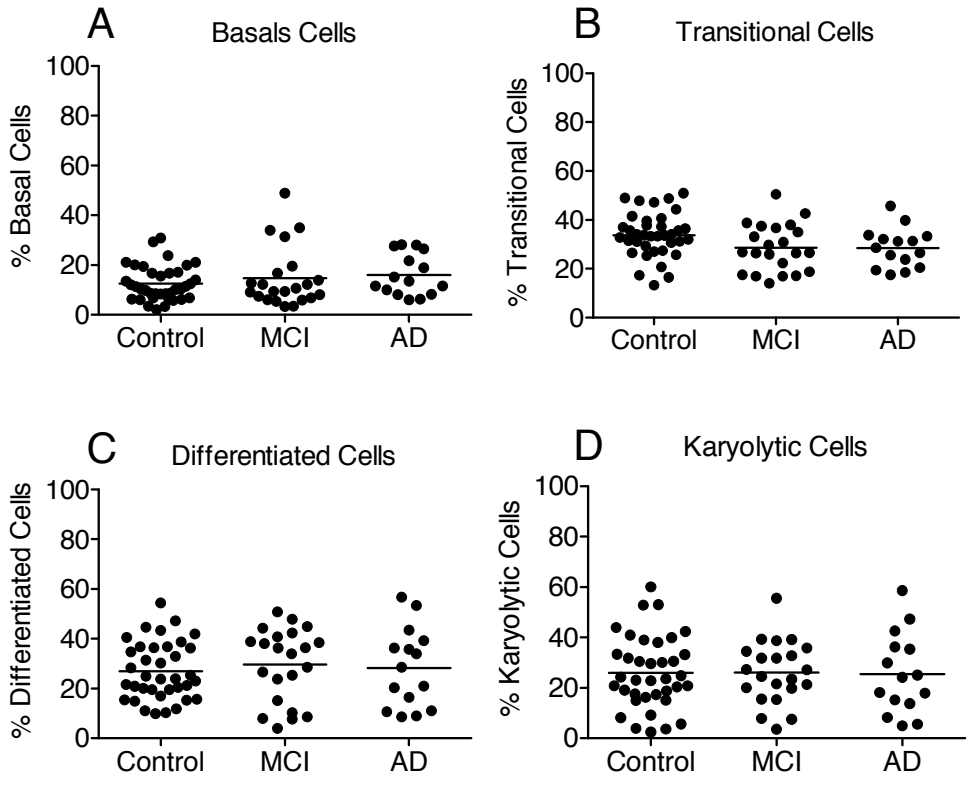

Figure 36: Buccal cell cytome in control, MCI and AD.
Single isolated buccal cells were scored with the parameters defined in the section *"3.2.7.5 Automation of the buccal cell cytome"* and scored as different cell types using the iCyte software. Cell types were compared in buccal cells from controls (n=37), MCI (n=22) and AD (n=15). The frequency of each of the cell types analysed (A) basal, (B) transitional, (C) differentiated and (D) karyolytic was obtained and plotted as a percentage of single cells. No significant differences were observed between groups. Abbreviations; AD, Alzheimer's disease; MCI, Mild cognitive impairment.

3.3.2.2 DNA content

To determine nuclear DNA content of all buccal cells on the microscope slides within the cytospots, the DNA Integral of all nuclei was calculated. Figure 37A shows that there was a significantly higher DNA content in buccal cells from the MCI group ($P<0.01$) compared with the control group whilst there was no significant difference between the MCI and AD groups. Furthermore, when only single cells were analysed (i.e. those not in groups), similar DNA content values were observed and were 1.6×10^6 a.u., 2.8×10^6 a.u. and 2.6×10^6 a.u. for control, MCI and AD, respectively, with a significant higher DNA content in MCI ($P<0.01$) and AD ($P<0.05$) when compared to controls, as shown in Figure 37B. Therefore, the values obtained from the single cell analyses were comparable to those obtained from all cells including those in small groups with a higher DNA content appearing in AD when compared to controls. As a next step in the analysis of individual buccal cells by LSC, the DNA content of the different cell types that contained nuclei i.e. basal, transitional and differentiated buccal cells was investigated. Both MCI and AD groups had a significantly higher DNA content in basal buccal cells (Figure 37C) compared with controls ($P<0.001$ and $P<0.01$, respectively). In transitional cells (Figure 37D) there was a significantly higher DNA content in MCI ($P<0.01$) group compared with controls. Additionally, in fully differentiated buccal cells there was a significantly higher DNA content in both MCI and AD ($P<0.05$) groups compared with controls (Figure 37E). Finally, it should be noted that there was no significant difference between the MCI and AD groups for the DNA content of basal, transitional and differentiated cell types.

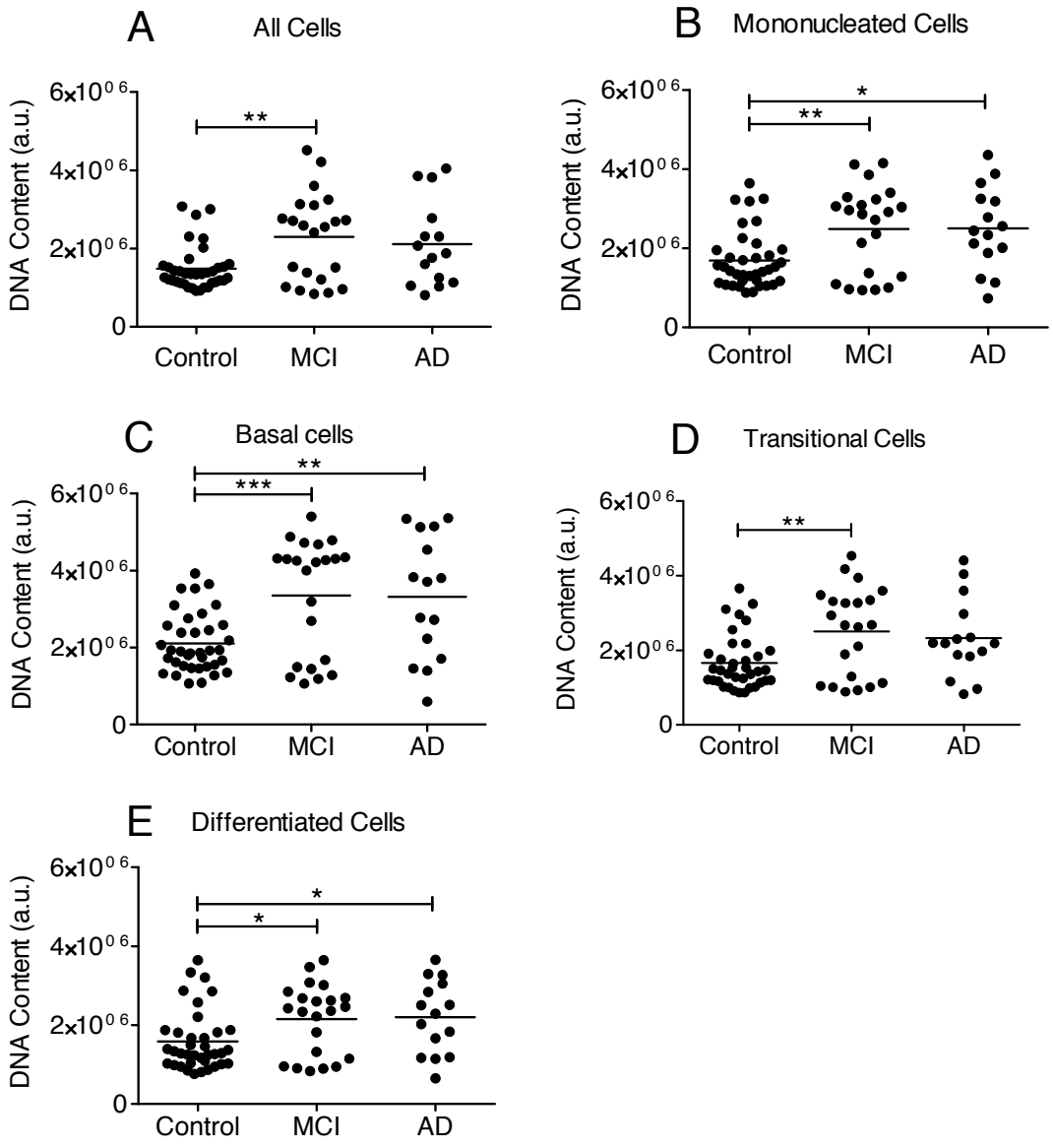

Figure 37: DNA content in buccal cells and their different cell types.
DNA content was measured with blue Integral (DAPI signal). DNA content of each nucleus was recorded and the mean value was obtained from two cytospots for control (n=37), MCI (n=22) and AD (n=15) groups in (A) all cells, (B) single mononucleated cells, (C) basal, (D) transitional and (E) differentiated cells. Karyolytic cells do not have nuclei and therefore DNA content was not scored for those cells. Abbreviations; a.u., Arbitrary units; AD, Alzheimer's disease; MCI, Mild cognitive impairment; *, P<0.05; **, P<0.01; ***, P<0.001.

3.3.2.3 DNA content / Cell cycle.

DNA content was analysed in greater detail to determine the ploidy of nuclei as in section *"3.2.7.6 Measurement of DNA content"*. Peaks of <2N, 2N and >2N nuclei were defined and regions were selected to obtain the percentage of nuclei in each of these categories (Figure 38). An example of a DNA histogram and scattergram for one participant from each of the groups; i.e. control, MCI and AD are shown in Figure 38A, Figure 38B and Figure 38C, respectively. DNA content from all individuals were then analysed in greater detail and is summarised in Figure 39.The results demonstrate that the frequency of nuclei that were <2N was similar for control, MCI and AD (Figure 39A). There was a significant decrease in 2N nuclei scored for MCI and AD ($P<0.01$) compared with controls (Figure 39B), which resulted in there being a significant increase of >2N nuclei in MCI ($P<0.01$) and AD ($P<0.05$) compared with controls (Figure 39C). These differences are summarised in Figure 39D.

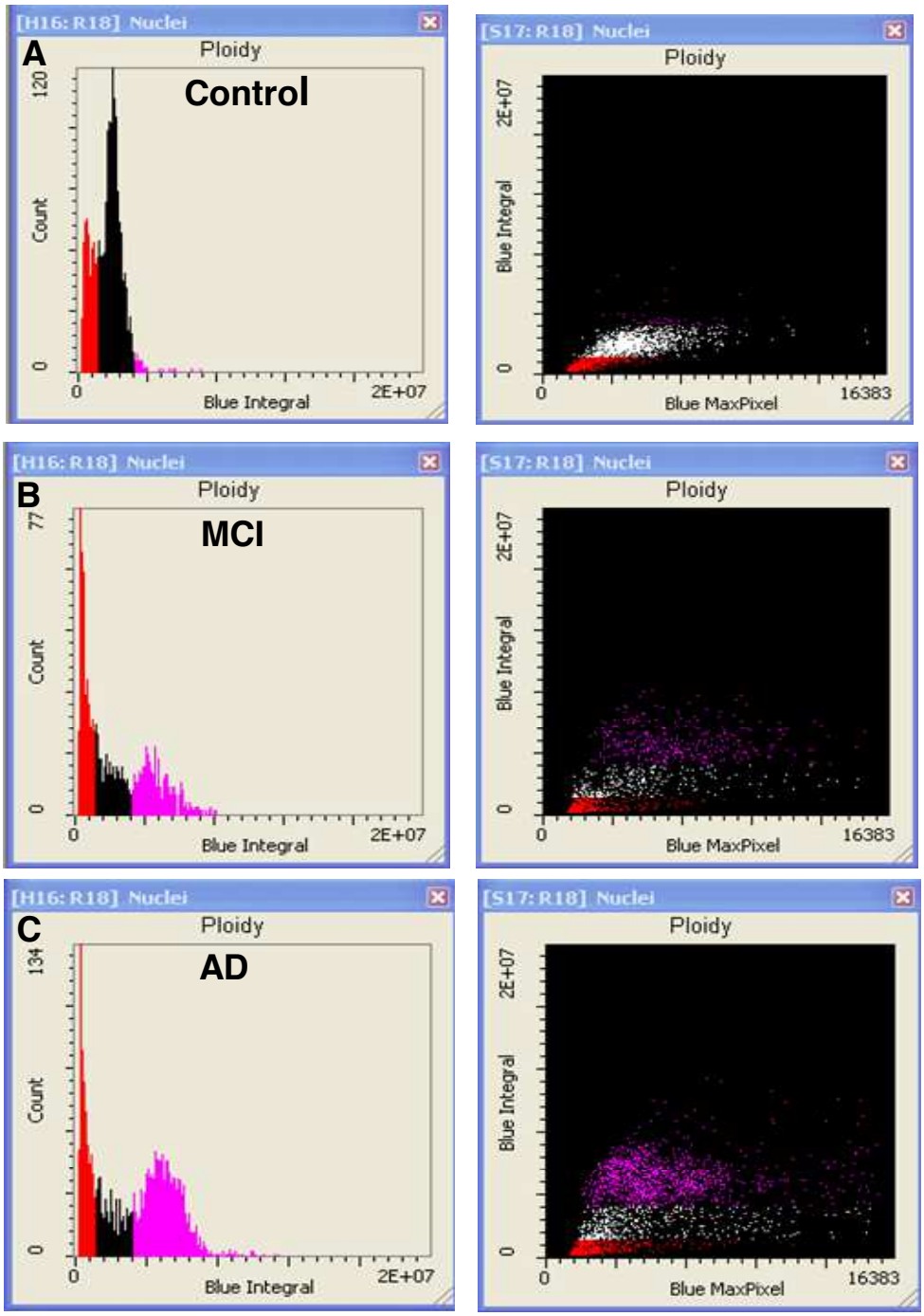

Figure 38: Representative examples of DNA content histogram and scattergram for controls, MCI and AD.

Ploidy histogram and scattergram were created and one representative example is given for (A) controls, (B) MCI and (C) AD. <2N, 2N and >2N peaks were represented in red, black and magenta, respectively.

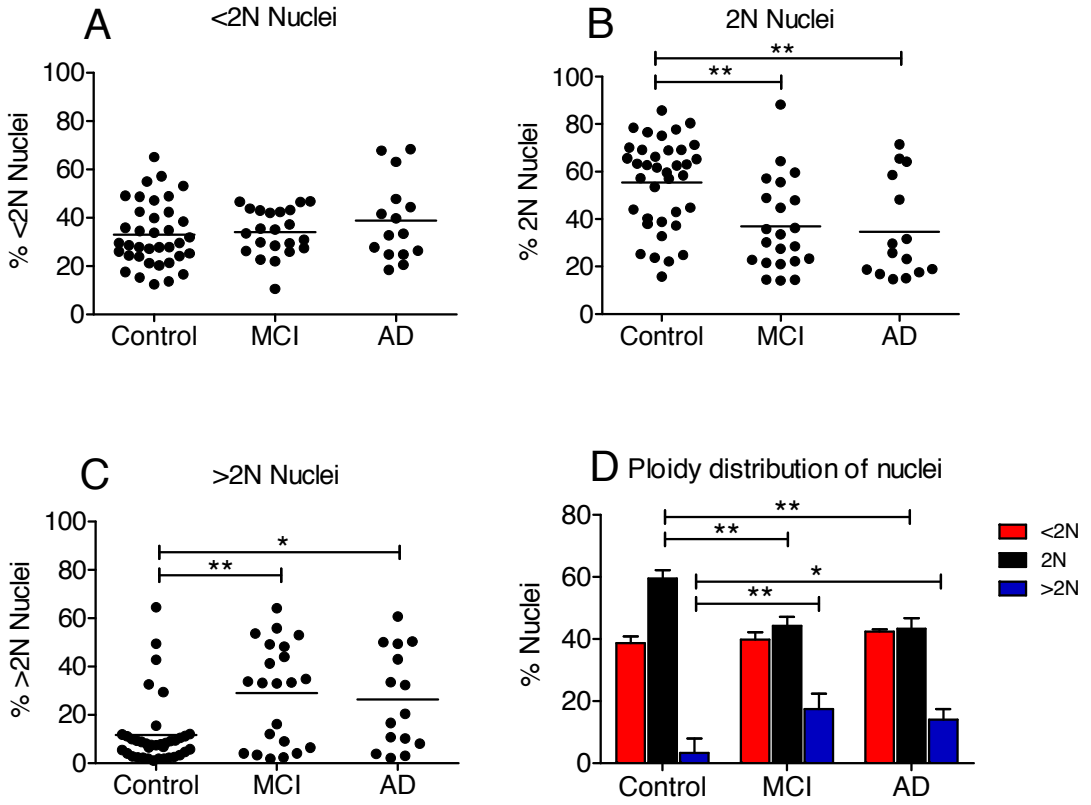

Figure 39: DNA content distribution.
The percentage of (A) <2N nuclei, (B) 2N nuclei and (C) >2N nuclei was assessed in control (n=37), MCI (n=22) and AD (n=15) groups. (D) The distribution of the three peaks, <2N, 2N or >2N is shown for controls, MCI and AD. Abbreviations; AD, Alzheimer's disease; MCI, Mild cognitive impairment; *, P<0.05; **, P<0.01.

3.3.2.4 Circularity

The "circularity" feature in iCyte is a measure of irregular shape so that a high circularity value indicates an increasing degree of non-circular shape. The circularity of nuclei was also measured in buccal cells (Figure 40). The results indicated a significantly increased circularity in all nuclei of AD cases relative to controls (P<0.01); (Figure 40A). Circularity has also been investigated in the different cell types. Figure 40B shows an increased circularity value in nuclei from single cells of MCI and AD compared to controls (P<0.01). Figure 40C shows no significant differences in circularity in nuclei of basal cells between groups whilst a significant increase was observed in transitional cells of MCI and AD relative to controls (Figure 40D; P<0.001). Nuclei of differentiated cells also exhibited higher irregular shapes between AD and controls (Figure 40E; P<0.05).

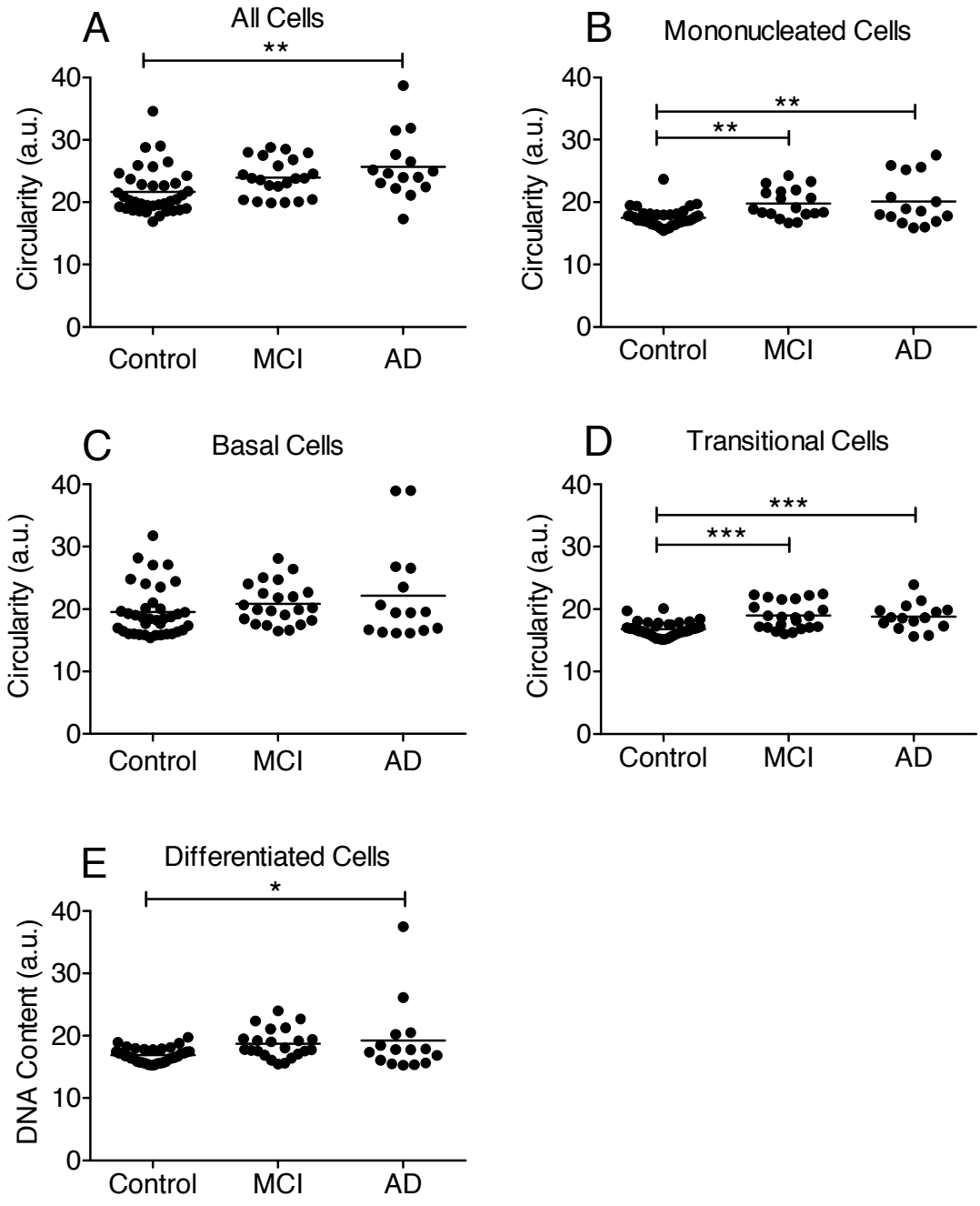

Figure 40: Circularity of nuclei measured in buccal cells and the different cell types.

Circularity of nuclei was measured in buccal cells of control (n=37), MCI (n=22) and AD (n=15) groups in (A) all cells, (B) single mononucleated cells, (C) basal, (D) transitional and (E) differentiated cells. Abbreviations; a.u., Arbitrary units; AD, Alzheimer's disease; MCI, Mild cognitive impairment; *, P<0.5; **, P<0.01; ***, P<0.001.

3.3.2.5 Nuclei area and DNA MaxPixel

Nuclei area was also measured in buccal cells by LSC, with MCI showing a significantly increased nuclear area compared with controls (P<0.001); (Figure 41A). Another useful feature of the laser scanning cytometer is the capability to measure the highest pixel value (MaxPixel) within a defined event. For example the MaxPixel within nuclei provides detail on the level of chromatin condensation (Bingham, et al. 2006). Figure 41B shows DNA MaxPixel of all nuclei between groups. It seemed that an increase exists in MCI and AD when compared to controls but this did not reach statistical significance.

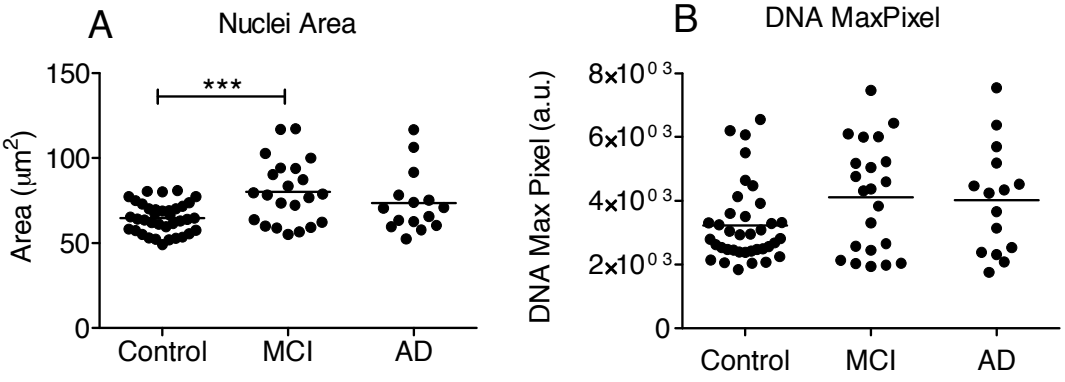

Figure 41: Nuclei area and DNA MaxPixel in buccal cells.
(A) Nuclei area and (B) DNA MaxPixel is shown for control (n=37), MCI (n=22) and AD (n=15). LSC carried out on all nuclei on the cytospots as described in the LSC schematic for buccal cell analysis (Figure 26). Abbreviations; a.u., Arbitrary units; AD, Alzheimer's disease; MCI, Mild cognitive impairment; ***, P<0.001.

3.3.2.6 Neutral lipids

LSC was used to determine the cellular content of neutral lipids in buccal cells from controls, MCI and AD patients by staining cells with ORO. ORO is a lysochrome fat-soluble dye which has been used for demonstrating the presence of neutral lipids such as cholesteryl esters and triglycerides in cells (Pani, et al. 2009a; Pani, et al. 2009b). Upon staining, the neutral lipids appear as bright red spots in the cytoplasm, as shown in Figure 42A (inset). When all cells were examined (including groups of cells), there was a significantly lower (P<0.01) ORO content in the MCI group compared with the controls and there was no significant difference between controls and AD (Figure 42A). Similarly, Figure 42B shows a significant decrease (P<0.05) in ORO between MCI and controls when all the single isolated buccal cells were analysed. ORO content in the

specific buccal cell types was further investigated. Figure 42C demonstrates that ORO staining was significantly lower in the MCI group compared with the control group in the basal cells ($P<0.05$), transitional cells (Figure 42D; $P<0.05$), differentiated cells and karyolytic cells (Figure 42F; $P<0.05$), whilst no significant difference was observed in differentiated cells (Figure 42E). Additionally, there was no significant difference between either the control and AD groups or the MCI and AD groups for any of the buccal cell types.

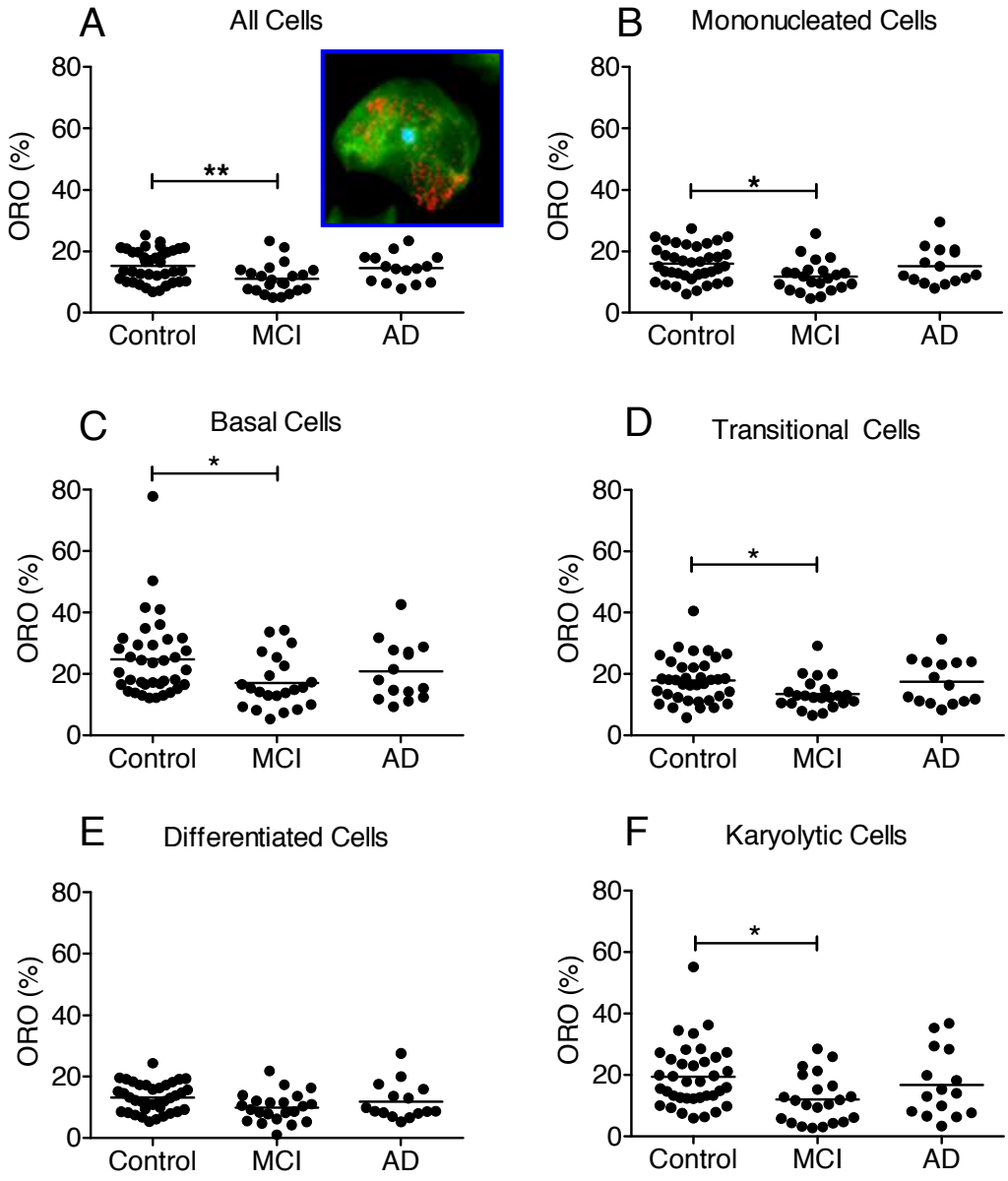

Figure 42: Neutral lipid content in buccal cells and their different cell types.
The area of the ORO staining was divided by the cytoplasm area of cells for a whole cytospot to obtain an ORO content ratio for each individual from control (n=37), MCI (n=22) and AD (n=15) groups. ORO was assessed in (A) all cells, (B) single mononucleated cells, (C) basal, (D) transitional, (E) differentiated and (F) karyolytic cells. Abbreviations; AD, Alzheimer's disease; MCI, Mild cognitive impairment; ORO, Oil Red O; *, $P<0.05$; **, $P<0.01$.

Triglyceride, cholesterol, low-density lipoprotein cholesterol (LDL-C) and high-density lipoprotein cholesterol (HDL-C) levels were measured in blood plasma as described in section "*3.2.6 Lipid analysis in plasma*". No significant differences were found between groups. Results are reported in Table 6.

Table 6: Lipid levels in plasma between controls, MCI and AD.
Abbreviations; AD, Alzheimer's disease; HDL-C, High-density lipoprotein cholesterol; LDL-C, Low-density lipoprotein cholesterol; MCI, Mild cognitive impairment.

	Control	MCI	AD	
	(n=37)	(n=22)	(n=15)	P-Value
Triglyceride (mM)	1.55 ± 0.12	1.75 ± 0.15	1.56 ± 0.2	0.5991
Cholesterol (mM)	5.64 ± 0.17	5.64 ± 0.29	4.96 ± 0.24	0.1259
HDL-C (mM)	1.73 ± 0.06	1.7 ± 0.1	1.52 ± 0.15	0.35
LDL-C (mM)	3.2 ± 0.14	3.14 ± 0.27	2.75 ± 0.23	0.3055

Correlation analyses were further carried out between these different lipid levels measured in plasma and ORO content measured in buccal cells by LSC (Figure 43). No correlation was observed between triglyceride, cholesterol, LDL-C and HDL-C levels in plasma when compared to neutral lipids measured by LSC in buccal cells, with the exception of a significant negative correlation between plasma HDL-C and ORO content of cells in AD cases ($r = -0.56$, $P=0.027$).

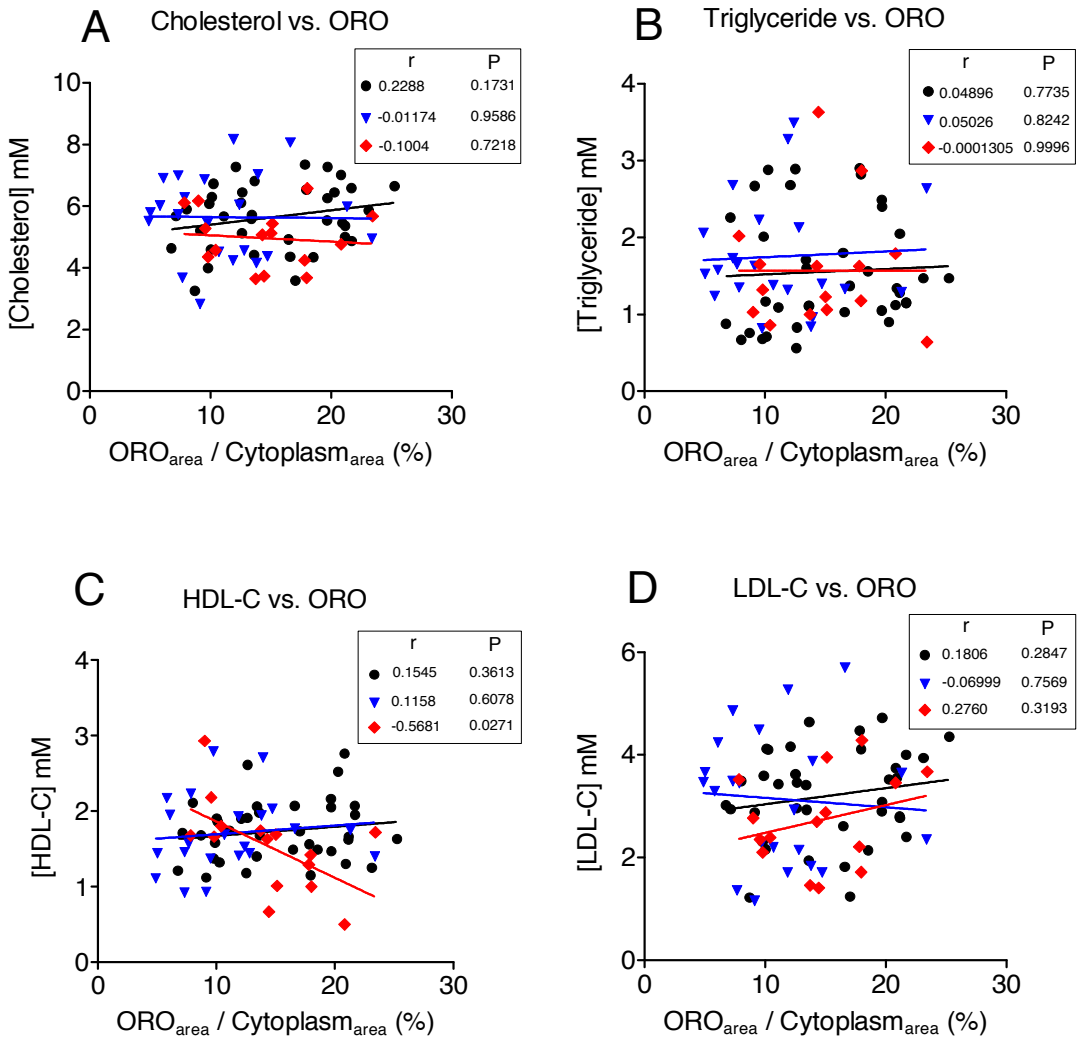

Figure 43: Correlation between ORO content and lipid levels.
Neutral lipid content measured in all buccal cells by LSC is compared to concentration of (A) cholesterol, (B) triglyceride, (C) HDL-C and (D) LDL-C. Abbreviations; HDL-C, High-density lipoprotein cholesterol; LDL-C, Low-density lipoprotein cholesterol; ORO, Oil Red O; ●=Control, ▼=MCI, ♦=AD.

3.3.2.7 DNA/ORO ratio

DNA content was increased in the MCI and AD groups compared with the control group, and ORO content was lower in the AD group and significantly lower in the MCI group compared with the control group. Therefore we investigated whether applying a DNA content/ORO content ratio would amplify the differences observed in the buccal cells. Figure 44A shows the DNA/ORO ratios in all buccal cell types examined (single cells and cells in small groups). Interestingly, the DNA/ORO ratio was significantly higher (3-fold) in the MCI group compared with control group ($P<0.01$) and the AD

group ($P<0.05$). To further identify the cell types contributing to these differences in DNA/ORO ratios, the DNA/ORO ratio was analysed in the individual cells containing nuclei, i.e. basal, transitional and differentiated buccal cells. For all single cells (Figure 44B) there was a significantly higher DNA/ORO ratio in MCI ($P<0.001$) buccal cells compared with control buccal cells. On further analysis of the individual cell types, there was a significantly higher DNA/ORO ratio for MCI compared with control in basal cells (Figure 44C; $P<0.001$) and transitional cells (Figure 44D; $P<0.01$). Additionally, there was a significantly higher DNA/ORO ratio in differentiated cells for MCI ($P<0.01$) and AD ($P<0.05$) compared with control (Figure 44E). To further investigate the differences observed the potential for a correlation between DNA content and ORO content in all buccal cells was investigated. Interestingly, when all cell types (including groups of cells) were examined, there was a significant negative correlation of DNA content with ORO content in the AD group only (Figure 45A; $r = -0.8572$; $P<0.0001$). This strong correlation was also apparent in individual single cells (collectively; basal, transitional, differentiated) from the AD group (Figure 45B; $r = -0.8403$; $P<0.0001$). Similar strong negative correlations were observed in basal ($P<0.001$), as well as in transitional and differentiated cells ($P<0.0001$) of AD cases but not for MCI or controls (Figure 45C, Figure 45D and Figure 45E).

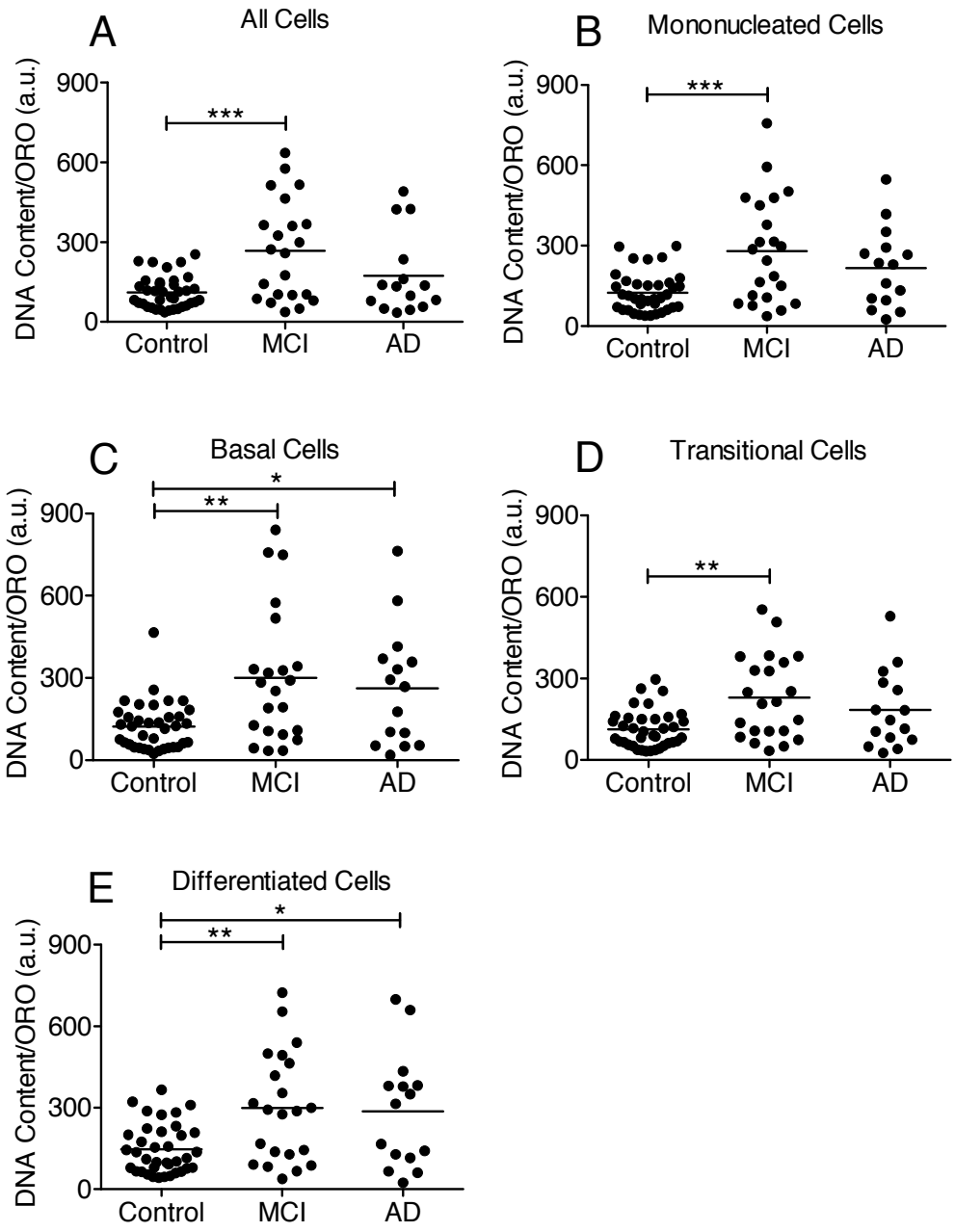

Figure 44: DNA/ORO ratio in buccal cells and their different cell types.
DNA/ORO ratio was calculated for each of the cytospots scanned by LSC for control (n=37), MCI (n=22) and AD (n=15) in (A) all cells, (B) single mononucleated cells, (C) basal, (D) transitional and (E) differentiated cells. Abbreviations; a.u., Arbitrary units; AD, Alzheimer's disease; MCI, Mild cognitive impairment; *, P<0.05; **, P<0.01; ***, P<0.001.

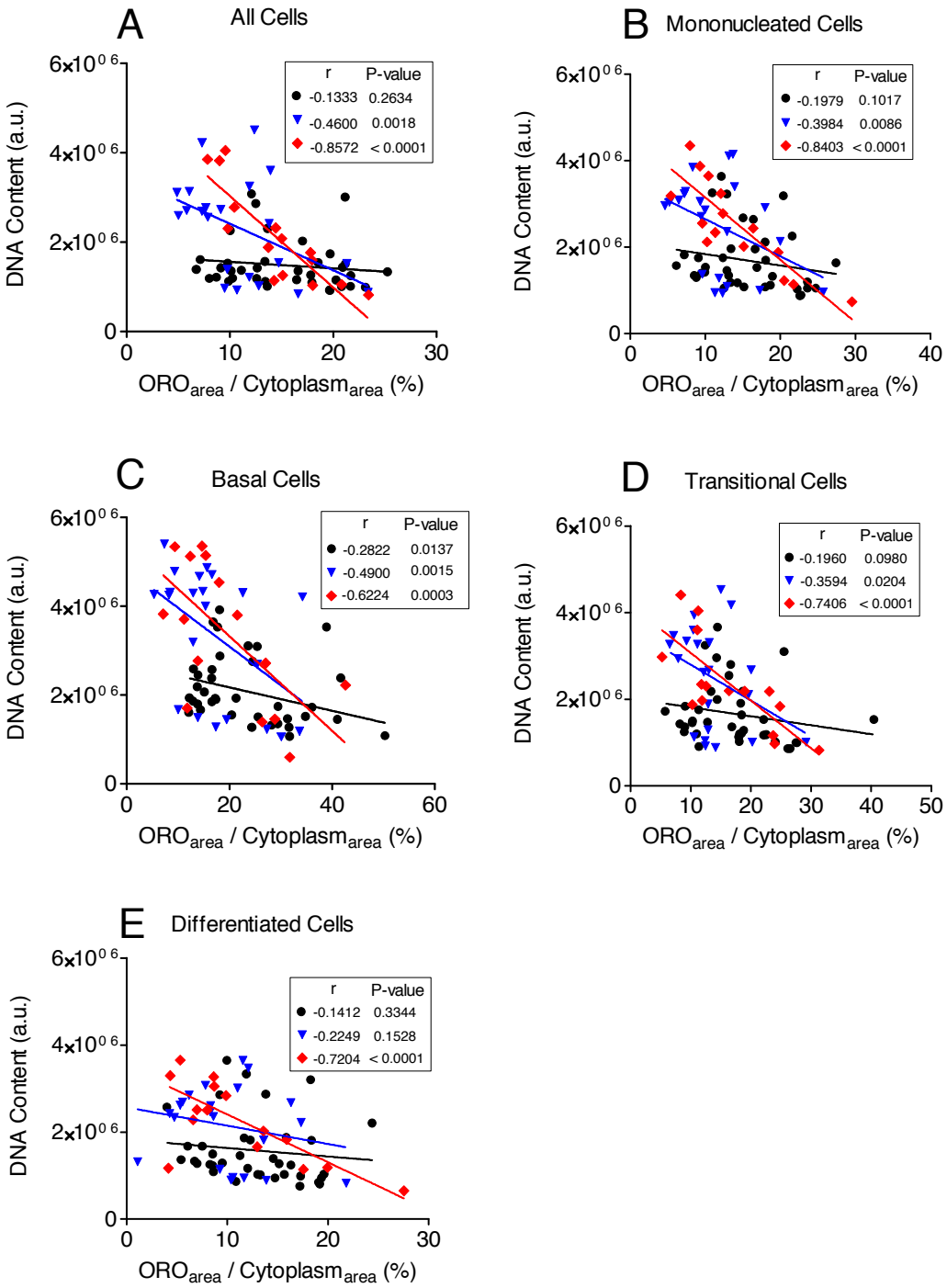

Figure 45: Correlation between DNA content and ORO content.
DNA content and ORO content values were plotted on graphs to observe potential correlations in each groups, control (n=37), MCI (n=22) and AD (n=15). (A) When a whole tissue section was analysed a strong correlation was observed within the AD group. A strong correlation was also observed in AD in (B) single cells only, (C) basal, (D) transitional and (E) differentiated cells. Abbreviations; a.u., Arbitrary units; ORO, Oil Red O; ●=Control, ▼=MCI, ♦=AD.

3.3.2.8 Gender

Data are shown in Table 7 which summarise the results when separated by gender for each of the parameters analysed in all cells (i.e. ORO content, DNA content, DNA/ORO ratio, circularity, % of >2N nuclei). The mean and SEM is reported for each group as well as the significance for the parameters that are significantly different. Since there were only 3 males in the AD cohort, analyses for the AD group should be considered preliminary.

Table 7: Parameters in all cell types for control, MCI and AD groups by gender.
Means and SEM are reported for each group. Means with no associated letters are not significantly different from other means. Means with different letters are significantly different from each others. Significance is accepted at P<0.05. Abbreviations; AD, Alzheimer's disease; F, Female; M, Male; MCI, Mild cognitive impairment; ORO, Oil Red O.

	Control		**MCI**		**AD**	
	M (n=11)	**F (n=26)**	**M (n=15)**	**F (n=7)**	**M (n=12)**	**F (n=3)**
ORO Content	16.6 ± 0.9	12 ± 1.4 **(a)**	12.4 ± 1.3 **(b)**	8.4 ± 1.1	14.7 ± 1.4	13.7 ± 2.4
DNA Content	$1.4e^{+06}$ ± $11e^{+04}$	$1.5e^{+06}$ ± $15e^{+04}$	$2.2e^{+06}$ ± $33e^{+04}$	$2.4e^{+06}$ ± $26e^{+04}$	$2e^{+06}$ ± $30e^{+04}$	$2.5e^{+06}$ ± $77e^{+04}$
DNA/ORO Ratio	97.9 ± 10.8 **(ac)**	139.8 ± 18.7 **(a)**	235.6 ± 48.6 **(b)**	338 ± 67.1 **(bc)**	165.3 ± 42.7	201.4 ± 114
Circularity	21.5 ± 0.8	22 ± 0.8 **(a)**	23.8 ± 0.8	24.3 ± 1.1	26.2 ± 1.4	23.3 ± 4.2 **(b)**
%>2N Nuclei	11.1 ± 2.8	13 ± 4.2 **(a)**	26.2 ± 5.9 **(b)**	34.8 ± 5.8	26.4 ± 6.1	25.9 ± 12.2

3.3.2.9 Fast Green – Cytoplasmic stain

The Integral of Fast Green staining over the whole slide (cytospots) was determined (Figure 46) and was compared between groups. Interestingly, the AD group had a significantly lower Fast Green Integral compared with MCI (P<0.05) whilst there was no significant differences between MCI and AD when compared to controls.

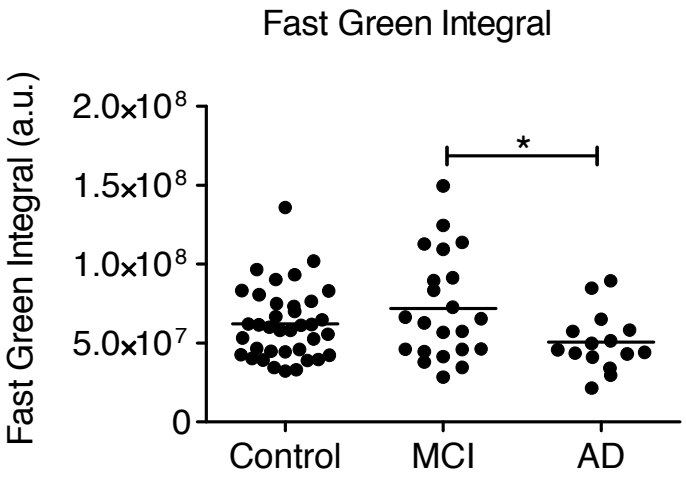

Figure 46: Fast Green Integral measured in all cell types.
Fast Green Integral was measured on the whole tissue sections and compared between control (n=37), MCI (n=22) and AD (n=15) groups. Abbreviations; a.u., Arbitrary units; AD, Alzheimer's disease; MCI, Mild cognitive impairment.

3.3.2.10 Circularity correlations

The circularity results described in section "*3.3.2.4 Circularity*" were compared to ORO results from section "*3.3.2.6 Neutral lipids*" and DNA content results from section "*3.3.2.2 DNA content*" in order to investigate if any correlations existed in all cells as well as within the different cell types for control, MCI and AD groups. Circularity was not found to be correlated with ORO content or DNA content, in all cells or the individual cell types.

3.3.2.11 Receiver-operating characteristic curves

3.3.2.11.1 Single biomarkers

When evaluating a diagnostic test, it is often difficult to determine the threshold value that separates a clinical diagnosis of "normal" from one of "abnormal." A ROC curve helps to visualise and understand the trade-off between high sensitivity and high specificity when discriminating between clinically normal and clinically abnormal values. Therefore to investigate the potential power of the biomarkers investigated in this study, ROC curves were generated for each of the parameters analysed. ROC values are reported in Table 8 for AUC, CI, P-value and selected best pairs of sensitivity and

specificity. Sensitivity and specificity scores vary depending on the cut-off value. Therefore for each cut-off value, sensitivity and specificity were added together and the combination giving the highest score was reported in Table 8. The AUC quantifies the overall ability of the test to discriminate between those individuals from the control group and those from the MCI or AD group. A low efficiency test would have an AUC of 0.5 while a perfect test would have an AUC equal to 1.0. For each graph generated, an identity line (black dashed-line) is shown that represents a ROC curve for a fully random classification (test with an AUC of 0.5); any improvement over random classification would result in a ROC curve at least partially above this straight line. The CI provides a data range that contains the true area with 95% certainty if the patient and control groups would represent a random sampling of a larger population. The P-value obtained tests the null hypothesis that the AUC really equals 0.5 and therefore provides us with information on the test discriminating capacity between controls and MCI or AD. Sensitivity represents the fraction of people within the MCI or AD group that the test correctly identifies as positive. Specificity on the other hand represents the fraction of people from the control group that the test correctly identifies as negative. Sensitivity and specificity were calculated for each value from the data table automatically set as a cut-off value; therefore many pairs of sensitivity and specificity were generated to create a ROC curve. For each category of parameters analysed (i.e. % Cell type, ORO content, DNA content, DNA Content/ORO Ratio, 2N nuclei, >2N nuclei and circularity) the ROC curves with the best AUC values (highlighted in yellow in Table 8) when comparing control versus MCI and control versus AD are shown in Figure 47.

Table 8: Scores obtained from ROC curves generated for the different parameters analysed in buccal cells.

These scores include AUC, CI, P-value, sensitivity and specificity. For each category of parameters analysed (i.e. % Cell type, ORO content, DNA content, DNA Content/ORO Ratio, ploidy and circularity) the ROC curves with the best AUC values when comparing control versus MCI and control versus AD are highlighted in yellow. Abbreviations; AD, Alzheimer's disease; AUC, Area under the curve; CI, Confidence interval; MCI, Mild cognitive impairment; ORO, Oil Red O; *, P<0.05; **, P<0.01; ***, P<0.001.

Parameter	Group	AUC	CI	P-Value	Sensitivity	Specificity
% Basals	MCI	0.5055	35-66	0.9438	50	59
	AD	0.6126	44-79	0.2069	67	57
% Transitionals	MCI	0.6523	50-80	0.0519	55	81
	AD	0.6865	53-84	0.0366*	67	65
% Differentiated	MCI	0.5713	40-74	0.3633	41	81
	AD	0.5027	31-70	0.9758	47	57
% Karyolytics	MCI	0.5160	37-67	0.8385	55	54
	AD	0.5171	34-70	0.8478	47	70
ORO Content (All cells)	MCI	0.7199	58-86	0.005**	68	68
	AD	0.5387	37-71	0.6641	67	49
ORO Content (Mononucleated)	MCI	0.7076	57-84	0.008**	82	57
	AD	0.5613	39-74	0.4923	53	73
ORO Content (Basals)	MCI	0.7101	57-85	0.0073**	64	73
	AD	0.6	42-78	0.2623	47	78
ORO Content (Transitionals)	MCI	0.6794	54-82	0.0221*	73	68
	AD	0.5207	34-70	0.8163	45	73
ORO Content (Differentiated)	MCI	0.6849	54-83	0.0183*	73	62
	AD	0.6	42-78	0.2623	60	70
ORO Content (Karyolytics)	MCI	0.7260	59-86	0.0039**	68	70
	AD	0.5766	39-77	0.3907	40	84
DNA Content (All cells)	MCI	0.6855	52-85	0.0179*	59	92
	AD	0.6703	48-89	0.0563	60	84
DNA Content (Mononucleated)	MCI	0.6806	52-84	0.0212*	68	81
	AD	0.7423	58-91	0.0066**	73	78
DNA Content (Basals)	MCI	0.7101	54-88	0.0073**	59	100
	AD	0.7243	54-91	0.0119*	53	97
DNA Content (Transitionals)	MCI	0.6830	52-84	0.0195*	59	86
	AD	0.7045	53-88	0.0219*	80	70
DNA Content (Differentiated)	MCI	0.6560	50-81	0.0465*	64	84
	AD	0.6955	53-86	0.0284	67	76
DNA/ORO Ratio	MCI	0.7518	61-89	0.0013**	55	100

(All cells)	AD	0.5748	38-76	0.4020	53	68
DNA/ORO Ratio (Mononucleated)	MCI	0.7432	60-89	0.0019**	64	78
	AD	0.6775	50-86	0.0467*	53	86
DNA/ORO Ratio (Basals)	MCI	0.7248	58-87	0.0041**	55	95
	AD	0.6901	50-88	0.0331*	53	97
DNA/ORO Ratio (Transitionals)	MCI	0.7224	58-86	0.0045**	50	92
	AD	0.6162	42-91	0.1927	47	86
DNA/ORO Ratio (Differentiated)	MCI	0.7322	59-87	0.003**	59	86
	AD	0.7027	52-89	0.0231*	53	95
% 2N Nuclei	MCI	0.7727	65-90	0.0005***	64	84
	AD	0.7676	62-92	0.0027**	67	86
% >2N Nuclei	MCI	0.7273	58-87	0.0037**	68	81
	AD	0.7297	57-89	0.01*	60	86
Circularity (All cells)	MCI	0.7303	60-86	0.0033**	64	76
	AD	0.7658	62-91	0.0029**	73	76
Circularity (Mononucleated)	MCI	0.8161	69-94	0.0001***	78	81
	AD	0.6955	52-87	0.0284*	73	59
Circularity (Basals)	MCI	0.6536	51-79	0.0501	64	70
	AD	0.5982	43-77	0.271	60	65
Circularity (Transitionals)	MCI	0.8034	69-92	0.0001***	82	68
	AD	0.8081	66-96	0.0005***	67	92
Circularity (Differentiated)	MCI	0.7445	61-88	0.0018**	73	70
	AD	0.6018	40-80	0.2538	53	76

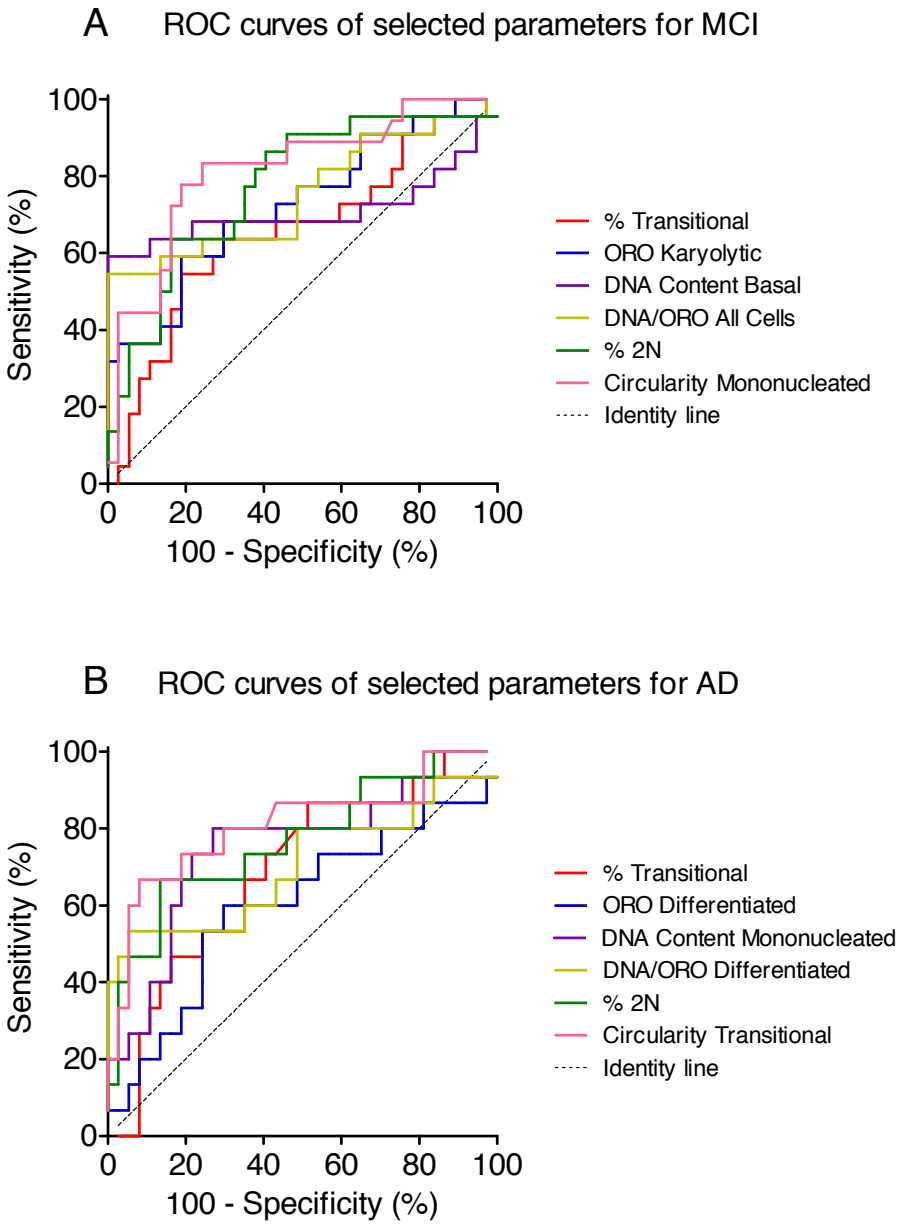

Figure 47: Selection of best ROC curves for different parameters for MCI and AD.
An example of selected ROC curves for (A) MCI vs. control and (B) AD vs. control. Abbreviations; AD, Alzheimer's disease; MCI, Mild cognitive impairment; ORO, Oil Red O; ROC, Receiver-operating characteristic.

3.3.2.11.2 Combination of biomarkers

From the ROC curves data (section "*3.3.2.11.1 Single biomarkers*") it was shown that the biomarkers in our study have a substantial power of diagnostic separation (sensitivity and specificity) between controls and MCI compared with controls and AD. Therefore to further investigate the power of these biomarkers for the MCI group specifically, each parameter analysed in all cells (i.e. DNA Content, ploidy, ORO Content, circularity) was combined with another and new ROC curves generated are shown in Table 9.

Table 9: ROC Curve parameters for a selected set of biomarker combinations comparing MCI and controls.

Data obtained from the combination of biomarkers were used to generate ROC curves to separate MCI from controls. Abbreviations; AUC, Area under the curve; CI, Confidence interval; ORO, Oil Red O; %>2N, % of >2N nuclei; **, P<0.01; ***, P<0.001.

Parameter	AUC	CI	P-Value	Sensitivity	Specificity
DNA Content + %>2N	0.7113	56-87	0.007**	59	92
DNA Content + Circularity	0.71	54-88	0.007**	59	92
DNA Content + ORO	0.7518	61-89	0.0013**	55	100
%>2N + Circularity	0.7408	60-88	0.0021**	59	92
%>2N + ORO	0.7580	62-89	0.001**	59	95
Circularity + ORO	0.7678	64-90	0.0006***	59	84
DNA Content + %>2N + Circularity	0.7260	58-87	0.0039**	68	81
DNA Content + %>2N + ORO	0.7383	59-88	0.0023**	59	92
DNA Content + Circularity + ORO	0.7531	61-89	0.0012**	55	100
%>2N + Circularity + ORO	0.7592	62-90	0.0009***	59	92
DNA Content + %>2N + Circularity + ORO	0.7420	60-89	0.002**	59	95

As previously shown in Table 8 section “3.3.2.11.1 Single biomarkers”, the AUC, CI, P-value, sensitivity and specificity scores were reported for each of the combinations. Biomarkers selected were % of >2N nuclei, circularity, DNA content and ORO content. Biomarker combinations were made by expressing each data point as a percentage of the control group mean. Since ORO content was shown to decrease in MCI compared to controls, the data for this parameter was converted to an absolute value by taking the inverse of the value ORO before being expressed as a percentage of the control group inverse of the mean. These results shown in Table 9 indicated that the combinations of these biomarkers have a substantial diagnostic value for predicting MCI from controls.

3.4 DISCUSSION

The objective of the present study was to adapt the buccal cytome assay (Thomas, et al. 2009) to an automated high-content analysis assay using LSC and to allow simultaneous investigation of aneuploidy and neutral lipid content in buccal cells of MCI and AD relative to controls. This study demonstrated significant changes in buccal cells isolated from MCI and AD subjects including the buccal cell type ratio, increased nuclear DNA content and nuclear circularity as well as the DNA content/neutral lipid ratio in both MCI and AD subjects.

In the present study Feulgen (DNA) and Light Green (cytoplasm) stains from the buccal cytome assay have been replaced with DAPI (DNA) and Fast Green (cytoplasm). Preliminary results demonstrated these changes were necessary to improve the sensitivity of the signals measured by LSC. An advantage of LSC scoring of buccal cells is that all the microscope slides are scanned in the exact same manner i.e. the software is set up in such a manner that all slides are examined using identical parameters and the numerical values obtained by the quantitative imaging allows for the separation of cell types, thus removing the potential for subjectivity existing from one individual scorer to another. Our current results also support our previous observations of substantial differences in frequency of the cell types between the control and Alzheimer's group when visual analysis is used. A previous study which used a Papanicolaou staining method also examined cytometric aspects of buccal cells in AD (de Oliveira, et al. 2008). The terms and criteria for cell types used in that method differs to ours based on the cell staining methods used. For example "parabasal" and "intermediate" cell types may possibly relate to our specified definitions of "basal" and "transitional", respectively. In the study by de Oliveira et al. (de Oliveira, et al. 2008) imaging software ("ImageJ") was used to measure cytometric nuclear and cytoplasmic areas and were found to be respectively increased and decreased ($P<0.01$) in intermediate cells of AD patients when compared to controls. Additionally, they found a significantly lower percentage of intermediate cells in AD when compared to controls ($P<0.05$) (de Oliveira, et al. 2008). The differences observed in intermediate cells, even if not directly comparable with those obtained with our method, also indicate that alterations occur in the composition of BM in AD. Since staining procedures and the definitions of cell types from one scoring method to another vary considerably, it will become necessary to standardise the buccal cell classification system in future studies.

For that reason it would be of interest to investigate markers of different stages of buccal cell proliferation. One prime candidate for such markers are the cytokeratin proteins (Anderton. 1981). A validation of these markers associated with the LSC automated cell separation may offer a very convenient and useful tool for future investigations of biomarkers of AD in BM.

When scoring the various cell types present, no significant difference was found in MCI and AD groups compared to the control group. To define the cell types present we aimed to classify the cells depending on their developmental stage based upon some of the visual scoring criteria previously used by our group (Thomas, et al. 2007). Previously, these criteria when combined with a visual scoring method suggested that the cell composition of the BM was significantly altered in Alzheimer's patients i.e. significant reduction in basal, karyorrhectic and condensed chromatin cells, the latter two being biomarkers of cell death. These changes were possibly explained by a decrease in the regenerative potential of the BM in AD. The frequency of different cell types obtained in our current study using LSC was somewhat different than the previous visual scoring method and this may be partly explained by the different staining procedures used in both studies. Our previous visual scoring study showed that basal and karyorrhectic cells were significantly decreased in AD relative to healthy controls.

In this study aneuploidy was measured by quantitating the fluorescent Integral of the DAPI signal, providing data on nuclear DNA content as shown previously with DAPI staining (Pozarowski, et al. 2004). Results showed a significantly higher DNA content in buccal cells from the MCI group ($P<0.01$) and AD group ($P<0.05$) compared with the control group. However the ploidy distribution of nuclei showed that MCI and AD cases presented a decrease in the frequency of 2N nuclei which was accompanied by an increase in hyperdiploid nuclei as well as nuclear circularity. Therefore, the higher DNA content observed in MCI and AD cases might be partly explained by the accumulation of buccal cells in the S and G2 phase of the cell cycle. The observed hyperdiploidy may be due to cell cycle checkpoint arrest due to mitotic defect leading to mitotic slippage which can lead to generation of 4N cells (Kirsch-Volders, Fenech. 2001). Another possibility is malsegregation of chromosomes leading to trisomic and monosomic cells assuming that the former are more likely to survive. An increase in trisomy 21 and trisomy 17 has been reported in buccal cells in AD and DS compared to their respective

controls (Thomas, Fenech. 2008). Furthermore the MN frequency is a biomarker of chromosome malsegregation and tends to be elevated in lymphocytes, fibroblasts and buccal cells of AD cases (Migliore, et al. 1997; Trippi, et al. 2001; Thomas, et al. 2007). Therefore, the genomic instability events observed previously may partly explain the results of increased DNA content observed in this study when measured quantitatively by LSC.

Other DNA damage markers such as γH2AX (DNA double strand breaks) also were found to be linked with AD, in astrocytes of AD hippocampal regions (Myung, et al. 2008). γH2AX was successfully detected (post-mortem) in human buccal cells using an immunofluorescent antibody against γH2AX (Gonzalez, et al. 2010), which make it an ideal DNA damage marker to be further investigated in the oral mucosa of AD patients in future studies. Oxidative stress has also been studied in exfoliated BM using HPLC after DNA isolation (Borthakur, et al. 2008) and since the association between accumulated oxidative DNA damage and ageing is well documented, it is possible that the BM may show changes in 8-OHdG levels from AD buccal samples, but this is yet to be tested. A study investigating oxidative DNA damage in peripheral leukocytes of MCI and AD patients reported a significantly higher level of oxidised DNA pyrimidines ($p<0.002$) and purines ($p<0.001$) in MCI and AD compared to the control group (Migliore, et al. 2005). Additionally, oxidative damage has been found to increase in the olfactory epithelium of AD cases (Perry, et al. 2003). Thus, confirming the presence of oxidative damage at a peripheral level in AD and therefore oxidative stress could be included as a potential marker of AD to be investigated in the oral mucosa.

Changes in lipid composition in the brain have been reported in AD, for example both membrane cholesterol and phospholipids were found to be significantly reduced in the cortex of AD mice (Yao, et al. 2009), and the lipid composition of different regions in the human brain has been shown to change with ageing as well as in AD (Soderberg, et al. 1990; Soderberg, et al. 1992). Since AD is a systemic disorder, peripheral tissues such as BM might also exhibit changes in their lipid composition. Therefore the lysochrome lipid soluble stain "ORO" was included in our LSC protocol to quantify neutral lipids in buccal cells. This study demonstrates for the first time that ORO content decreases in the oral mucosa of MCI in all cell types examined ($P<0.05$) when compared to controls. The ORO content also tends to decrease in AD but this did not

reach statistical significance. Thus it is possible that changes in neutral lipid accumulation in buccals precedes AD and is elevated at an early stage of AD pathogenesis. Furthermore, it was noted that the DNA content/ORO ratio was significantly elevated compared with controls in both the MCI and AD group in all cell types scored. Additionally we observed a strong negative correlation between DNA content and ORO in the AD group in all cell types but this type of correlation was not observed in controls or MCI suggesting a link between hyperdiploidy and lipid content in cells as progression from MCI to AD occurs. However we have no explanation for this finding unless cell cycle arrest is caused by lack of lipid derived energy required for mitotic activity due to malnutrition. Lipid metabolism has also been studied in fibroblasts from AD patients whereby the cholesterol esterification rate was reported to increase after 48 hours of culture ($P<0.05$) (Pani, et al. 2009a). This level of cholesteryl ester synthesis was linked to an expanded cytoplasmic pool of neutral lipid measured using the ORO staining procedure. The differences of cholesteryl ester synthesis rate in the fibroblasts reported (Pani, et al. 2009a) were accompanied by an increase in mRNA levels of ACAT-1 (Acetyl-Coenzyme A acetyltransferase 1) and a decrease in ABCA1 (ATP-binding cassette transporter) indicating an increased esterification rate and decreased cholesterol efflux, respectively. The protein levels of ACAT-1 and ABCA1 could therefore be explored in buccal cells to help in the understanding of reduced neutral lipid accumulation in MCI as measured in this study. In a microarray study involving mouse cortical neurons, the gene expression profiles were examined by qPCR in response to Aβ42 and a down-regulation of genes involved in the biosynthesis of cholesterol and lipids was observed (i.e. Fdft1, Fdps, Idi1, Ldr, Mvd, Mvk, Nsdhl, Sc4mol) (Malik, et al. 2012). The decrease in ORO content observed in buccal cells of MCI in this study could be due to such genes being down-regulated in buccal cells at the onset of the disease which would result in a decrease in neutral lipid synthesis. This hypothesis could potentially be investigated in buccal cells since mRNA material has previously been extracted from buccal cells for RT-PCR (Michalczyk, et al. 2004). In a second study, Pani et al. (Pani, et al. 2009b) also investigated the DNA synthesis of lymphocytes after growth-stimulation with phytohemagglutinin and found that neutral lipid content increased in parallel with the rate of cell growth *in vitro*, supporting the possibility that the optimal nutrition in culture medium restored the capacity of cells to maintain cholesteryl ester synthesis. We previously hypothesised that the regenerative potential of the BM was reduced with development of AD (Thomas, et al. 2007;

Thomas, et al. 2008a), and therefore it is possible that the rate of regeneration and proliferation of buccal cells influences the cytoplasmic accumulation of neutral lipids *in vivo*; this may partly explain why a decrease of neutral lipid content in buccal cells occurs in the early stage of the disease.

To-date there has been no simple, inexpensive and minimally invasive procedure available to confirm the early diagnosis of AD. Therefore, if screening of populations of individuals is to be performed, more suitable, easily accessible tissues would need to be used, also using diagnostic tests at much lower costs as compared to brain imaging and cerebrospinal fluid diagnostics of Aβ and Tau (Blennow, Zetterberg. 2009; Thambisetty, Lovestone. 2010; Hampel, Prvulovic. 2012). This need for minimally invasive tests could be achieved by targeting surrogate tissues, since it is now well recognised that AD is not a disorder restricted to pathology and biomarkers within the brain only. Combining neutral lipid accumulation, DNA content with other potential more specific protein markers such as Aβ and Tau may substantially increase the likelihood of better predictive markers for AD. Such a combined protocol would provide a high-content, automated assay capable of measuring multiple parameters in human buccal cells which can be easily and painlessly collected.

CHAPTER 4

4. AUSTRALIAN IMAGING, BIOMARKERS AND LIFESTYLE STUDY OF AGING (AIBL)

4.1. INTRODUCTION

The previous chapter "SAND Study" demonstrated the utility of using buccal cells as a peripheral tissue to investigate biomarkers of mild cognitive impairment (MCI) and AD risk. The protocol used in that instance was aimed at the analysis of the buccal cytome, DNA content, ploidy and neutral lipids; however this study aimed to incorporate additional protein biomarkers that are known to be altered in AD. For example, Amyloid-β (Aβ) and Tau proteins are the two main hallmark of AD, known to aggregate in the brain and lead to neurodegeneration (Grundke-Iqbal, et al. 1986; Selkoe. 2001). Elevated Tau and changes in amyloid-β in the cerebrospinal fluid (CSF) remain (to date) the main biological markers to identify AD patients from healthy individuals (Blennow, Zetterberg. 2009; Prvulovic, Hampel. 2011). However, since obtaining CSF is an invasive medical procedure, more easily accessible tissues that reflect the AD pathology have previously been considered in the research for biomarkers of AD. Platelets, lymphocytes, nasal cells and buccal mucosa (BM) for instance have all been previously utilised for investigation of Tau (Hattori, et al. 2002; Arnold, et al. 2010; Armentero, et al. 2011; Neumann, et al. 2011), whilst plasma, nasal cells and fibroblast have been used for amyloid detection with "limited" success (Schupf, et al. 2008; Pani, et al. 2009; Arnold, et al. 2010).

The emphasis of this chapter was utilising buccal samples from control, MCI or AD individuals from the AIBL (Ellis, et al. 2009). This cohort is one of the most well characterised and largest studies of AD involving multi-research centres all over Australia. Therefore buccal cells were collected from this cohort and were analysed by laser scanning cytometry (LSC) with the aim to quantify Tau and amyloid within buccal cells.

The LSC protocol previously developed in chapter 3 allowed high-content analysis of several parameters in buccal cells. However, during the course of this project an

extended knowledge of the software and artificial features was gained, and allowed the protocols to be further developed to incorporate the quantification of protein markers in buccal cells. Since the LSC technology has the capability to combine detection of fluorescent dyes with chromatic stains by the simultaneous use of photomultiplier tubes (PMTs) and photo detectors (PDs), respectively (Luther, et al. 2004; Pozarowski, et al. 2006); the protocol previously developed in chapter 3 was adapted and combined with a protocol aiming to detect Tau and Aβ proteins by immunocytochemistry techniques. The creation of such a protocol was carried out with the intention to extend the high-content analysis capacity of LSC to a higher level with detection of many different biomarkers within an individual cell. Thus, allowing potential correlations of biomarkers within subsets of cell types which could increase the diagnostic power of these biomarkers.

4.2 MATERIAL AND METHODS

4.2.1 Human ethics

Approval for the AIBL was obtained from CSIRO Animal, Food and Health Sciences (Adelaide), University of Melbourne, Hollywood Private Hospital (Perth), Mental and Health Research Institute (Melbourne), St Vincent Hospital (Melbourne) Ethics Committee's. Diagnosis of AD was made by clinicians according to the criteria outlined by the National Institute of Neurological and Communicative Disorders and Stroke-Alzheimer's Disease and related Disorders Association (NINCDS–AD&DA) (McKhann, et al. 1984). Three groups were investigated as follow; Control Group (n=20), MCI (n=20) and AD (n=20). Age, sex, Mini-mental State Examination (MMSE) scores and APOE ε4 genotype information for each group are shown in Table 10. An individual is considered APOE ε4 positive if he has at least one APOE ε4 allele.

Table 10: Clinical characteristics.

Means and SEM are reported for each group (95% CI in parenthesis). Means with no associated letters are not significantly different from other means. Means with different letters are significantly different from each others. Significance is accepted at $P<0.05$. Abbreviations; AD, Alzheimer's disease; APOE, Apolipoprotein E; F, Female; M, Male; MCI, Mild cognitive impairment; MMSE, Mini mental test examination.

	Control	MCI	AD
Sex (M:F)	8:12	11:9	11:9
Age (year)	72.8 ± 1.5 (69.6-75.9) **(a)**	77.8 ± 1.6 (74.4-81.1)	80.6 ± 1.5 (77.3-83.8) **(b)**
MMSE score	28.8 ± 0.2 (28.4-29.2) **(ab)**	26.3 ± 0.7 (24.8-27.7) **(ab)**	13.9 ± 1.6 (10.5-17.2) **(c)**
APOE ε4 positive	6	9	12

4.2.2 Chemicals and Reagents

ELISA INNOTEST® hTAU Ag was purchased from INNOGENETICS® (Hannover, Germany). BCA Kit was from Sigma. All chemicals were of the highest quality grade: NaCl, Tris(hydroxymethyl)aminomethanehydrochloride (Tris), ethylenediaminetetraacetic acid (EDTA), sodium citrate, 4',6-diamidino-2-phenylindole (DAPI), formaldehyde, glycerol, 1-[2,5-Dimethyl-4-(2,5-dimethylphenylazo)phenylazo]-2-naphthol (Oil Red O), triethyl-phosphate and Fast

Green were from Sigma-Aldrich (Castle Hill, NSW, Australia). Phosphate buffered saline (PBS) was from Invitrogen (Mulgrave, Victoria, Australia).

4.2.3 The australian imaging, biomarkers and lifestyle study of aging (AIBL) cohort

The AIBL study of aging is a multi-centre multidisciplinary study of AD and ageing funded by the CSIRO Flagship Initiative, involving research centres in both Western Australia and Victoria; Edith Cowan University, University of Western Australia, University of Melbourne, Neurosciences Australia Ltd, Centre for Positron Emission Tomography (PET), Austin Health, Mental Health Research Institute of Victoria, Monash University, Cosgate Ltd, CSIRO Preventative Health (P-Health) Flagship. Its' aim was to assemble a cohort of individuals who could be assessed and followed at regular intervals and whose tissues, amyloid brain load, and lifestyle factors could be compared in relation to their cognitive function (especially with respect to the presence or absence of AD symptoms) and risk factors. The AIBL cohort is composed of 1112 volunteers aged over 60 and aims to assist with prospective research into AD (Ellis, et al. 2009). The groups characterised in this cohort are presented in Figure 48. When individuals presented with a diagnosis of AD or MCI that had already been made by a treating clinician, this diagnosis was reviewed by a clinical review panel, in order to ensure that diagnoses were made in a consistent manner according to internationally agreed criteria. Volunteers underwent a screening interview and tests to assess their cognitive function were performed. Some tests were selected on the basis of their internationally acknowledged utility and their ubiquity in the research literature (e.g. the MMSE and Geriatric Depression Scale). The tests comprising the neuropsychological battery were selected on the basis that together they covered the main domains of cognition that are affected by AD and other dementias. These tests were chosen so that results from the participants were comparable with those from other similar large studies, and all cognitive tests are internationally recognised as having good evidence of their reliability and validity. MCI diagnoses were made according to a protocol based on the criteria of Winblad et al. 2004. Consistent with Winblad criteria, all participants classified with MCI had either personally, or through an informant, reported memory difficulties. A baseline testing which included full blood examination was also performed by a clinical pathology laboratory. The medication profile of each of the

participants was assessed and its impact on the analysis can be evaluated as all data and information are stored in a database. The AIBL initiative includes a brain imaging study involving only a subset (287) of the 1112 participants, as the cost of such a study is very high. Those selected participants underwent Magnetic Resonance Imaging (MRI) and PET imaging with PiB. This cohort also provides information on health and lifestyle for each participant as all were asked to complete two questionnaires, the International Physical Activity Questionnaire (IPAQ) (Craig, et al. 2003) and the Food Frequency Questionnaire (FFQ) developed by CSIRO (Hodge, et al. 2000). Data and results accumulated for the last four years are stored in a data base which was constantly updated. Ethical clearance was obtained to sample buccal cells from participants and results from this study will be included in the AIBL data base and can be further correlated to all other parameters listed as above and investigated in this cohort. Sixty individuals were chosen for this study from the three groups, control (n=20), MCI (n=20), AD (n=20). Each individual was chose based on several criteria listed below.

(1) PET imaging or brain was or will be completed.
(2) A high yield of buccal cells was sufficient to allow both LSC analyses as well as protein (Tau) ELISA measurements to be carried out.
(3) Buccal cells were stored up to 10 days in Saccomano's solution.

Patient numbers were provided by the Mental Health Research Institute "in a coded manner" so that it was not possible to decipher each patient sample group ID as well as their group affiliation. Therefore the study was completed in a blinded fashion. Samples were "decoded" by matching patient and group numbers by the Mental Health Research Institute Melbourne group at the completion of all assays and after data analysis was performed in this study to prevent any possible bias.

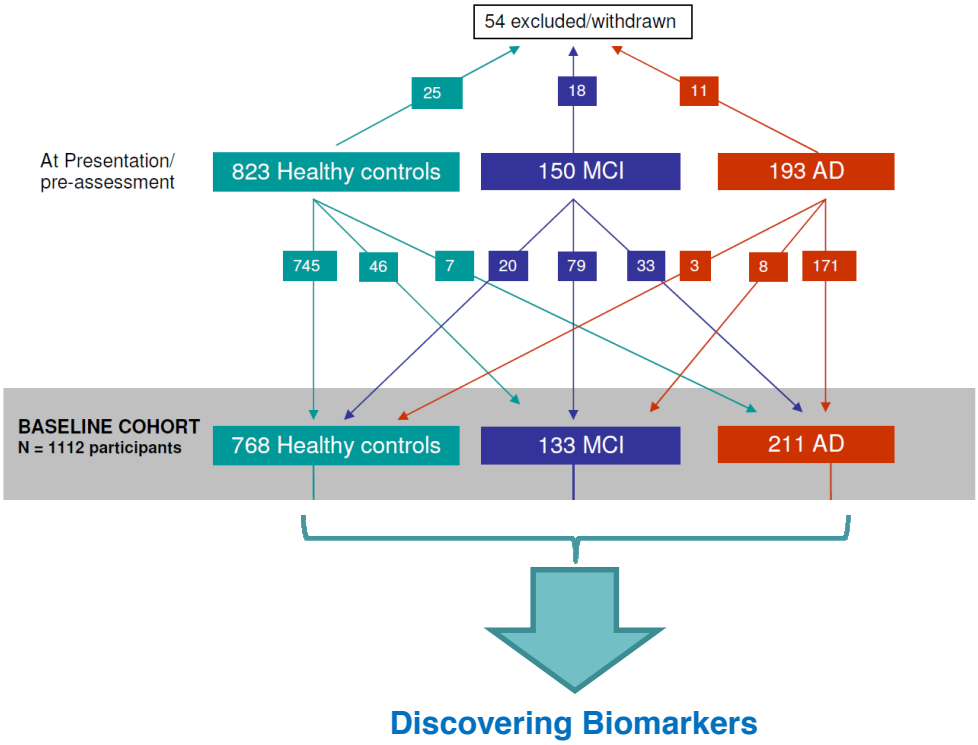

Figure 48: Composition of the AIBL cohort: screening, assessment and cohort subgroups.
Adapted from Ellis et al. 2009.

4.2.4 Buccal cell isolation

Consented participants had a one-off buccal cell sample collected after the brief information session outlining the purpose of the study. Study participants were interviewed at either Mental Health Research Institute (Melbourne) or Hollywood Private Hospital (Perth). Buccal cells were collected by the same individual for the duration of the study. Buccal cells were collected by placing a small flat-headed toothbrush against the inner part of the cheek and rotated 20 times in a circular motion. Both left and right cheeks were sampled separately and then the toothbrushes containing cells were placed into a yellow-cap tube containing 20 mL of Saccomano's fixative solution and agitated vigorously to transfer the cells into solution. Lids of tubes were wrapped in parafilm to avoid spillage during transport and buccal cell samples were then placed in a refrigerator at 4°C for up to a week before being sent to CSIRO Animal, Food and Health Sciences (Adelaide) via Toll Priority courier (www.tollpriority.com.au) at 4°C. Buccal cells were then stored at 4°C and processed

within one week. After centrifugation at 1000 xg for 10 min, the supernatant was removed and the cells were resuspended in 5 mL of buccal buffer as defined in chapter 2, section "*2.2.3 Buccal cell sampling and preparation*". The cell suspension was drawn up into a 10 mL syringe using a 21G needle and resuspended by drawing the suspension up and down 5 times to assist separating large clumps of cells into single cells in suspension. Cells were then passed through a 100 μm filter in a swinex filter holder (Millipore) to further remove large aggregates of cells. The concentration was measured using a haemocytometer and cells were transferred to a microscope slide using a Shandon Cytospin 4 (600 rpm) at a concentration of 30,000 cells/mL to obtain a final cell density of approximately 1500 cells per cytospot done in duplicate. Remaining cells were aliquoted into 1.5 mL eppendorf tubes containing 10% DMSO (final concentration) and frozen at -80°C for further ELISA and/or Western analyses. Slides were then air-dried for 1 h and subsequently transferred to 0.4% formaldehyde in PBS or ethanol:acetic acid (3:1) for 10 min. Slides fixed in 0.4% formaldehyde were rinsed 1 min with ultra pure water. All slides were air-dried for 1 h and then stored in sealed microscope slide boxes with desiccant at -80°C until the staining procedure was performed. Details were recorded in an Excel file and backed up with the following information recorded (i.e. coded participant ID number, initials of sampler, day of sampling, day of processing, days of storage, cell concentration, number of slides, number of eppendorf tubes, box number, information on where tubes and slides were stored, including and other notes and comments).

4.2.5 Protein analysis methods

4.2.5.1 Sample lysates preparation

Aliquots of buccal cells were centrifuged 5 min at 1500 xg and supernatant was removed. Cells were then resuspended in 75 μL to 250 μL (depending on the initial cell concentration) of RIPA lysis buffer (with protease and phosphatase inhibitors diluted at 1/100) for 2 h on ice. Aliquots were then stored in cardboard boxes at -80°C until analysis by BCA, ELISA or Westerns.

4.2.5.2 BCA Kit

Total protein concentration was determined by QuantiPro BCA Assay Kit from SIGMA®. The first step was to mix 2 mL of a solution consisting of sodium carbonate, sodium tartrate and sodium bicarbonate in 0.2 M NaOH, pH 11.25 with 2 mL of 4% (w/v) bicinchoninic acid solution, pH 8.5. To this new solution, 4 mL of a 4% (w/v) copper(II) sulfate (pentahydrate solution) was added to make up the working solution. A standard curve was made by using a protein standard solution consisting of 1 mg/mL bovine serum albumin in 0.15 M NaCl with 0.05% sodium azide as a preservative. This solution was diluted with sample buffer (RIPA buffer with 1/00 protease inhibitor and 1/100 phosphatase inhibitor cocktails) to obtain protein standard concentrations of 0, 0.5, 5, 10, 20 and 30 µg/mL. Two 96 well plates were used to determine the protein concentration of samples. To each well, 100 µL of each sample (previously diluted at ½ in sample buffer) or 100 µL of each protein standard concentrations was added to 100 µL of working solution in duplicates. Wells were sealed with an adhesive plate sealer and samples were incubated at 60°C for 1 h. The 96 well plates were allowed to cool to room temperature and the absorbance of the reaction solution was measured at 562 nm with a spectra MAX 250 (Molecular Devices, USA). The protein concentration of samples was determined by reading absorbance from the standard curve and corrected for the dilution factor (x2).

4.2.5.3 ELISA Kit

Tau was measured following the manufacturer's instructions (ELISA INNOTEST®, hTau, Germany). Each well of the plate was antibody-coated with Anti-TAU AT120 clone. A conjugate working solution 1 was made up by diluting two monoclonal anti-hTAU antibodies (HT7 and BT2 clones) at 1/100. Then, 75 µL of conjugate working solution 1 was added to each well plate. Standards and samples were prepared by diluting them into sample diluent (RIPA buffer + protease and phosphatase inhibitor cocktails). Different concentrations of standards were made up by reconstitution of the lyophilized recombinant hTAU provided with the kit by adding 500 µL of sample diluent and left to stand 15 min before being mixed on a vortex mixer for 15 sec. Concentrations used for the standard curves were expressed in pg/mL (75, 150, 300, 600, 1200 pg/mL). 25 µL of each standard dilution (including the blank made of 25 µL of sample diluent) and the selected AIBL samples were added to duplicate wells of the

antibody-coated plate. The plate was mixed for 1 min at 1000 rpm in a plate shaker and wells were covered with an adhesive sealer to avoid evaporation. The plate was then incubated overnight at 25°C with gentle shaking. The wells were aspirated and then washed with 400 µL of phosphate buffer containing 0.15% Proclin 300 diluted 25x with distilled water. This washing procedure was repeated 4 times and 100 µL of conjugate working solution 2 diluted at 1/100 was then added to each well. Wells were covered with adhesive sealer and incubated for 30 min at 25°C under gentle shaking. Wells were washed with the washing procedure detailed previously and 100 µL substrate working solution (tetramethyl benzidine (TMB) dissolved in dimethyl sulfoxide (DMSO) diluted 100x in phosphate-citrate buffer containing 0.02% hydrogen peroxide) was added to each well and incubated for 30 min at room temperature (RT) in the dark. The enzymatic reaction was stopped by adding 100 µL of 2 M sulphuric acid to each well in the same sequence and the same time intervals as the substrate solution. The plate was gently mixed and absorbance at 450 nm and 620 nm was read by using a spectra MAX 250 within 15 min after the reaction was stopped.

4.2.5.4 ELISA Plates set up and test

Since the ELISA Kit was originally designed for measuring Tau in CSF samples, the standard curve had to be tested when the sample diluents solution provided by the Kit was replaced with the lysis buffer solution used to prepare our buccal cell protein samples. Therefore, the Tau protein standard provided with the kit to generate the standard curve was used with sample diluents or RIPA buffer plus anti-phosphatase and anti-protease cocktails. With each condition a human Tau recombinant protein at a known concentration of 500 pg/mL was also assayed in duplicate. Figure 49 shows the standard curve generated with the kit sample diluents solution (blue curve) or with RIPA buffer plus anti-phosphatase and –protease cocktails (red curve) when plotted on the same graph. It was observed that the standard curve obtained with Tau protein standards diluted in RIPA buffer instead of sample diluent solution was slightly different; however it did not affect the detection of Tau protein since the human Tau recombinant was detected at the same concentration with both standard curves.

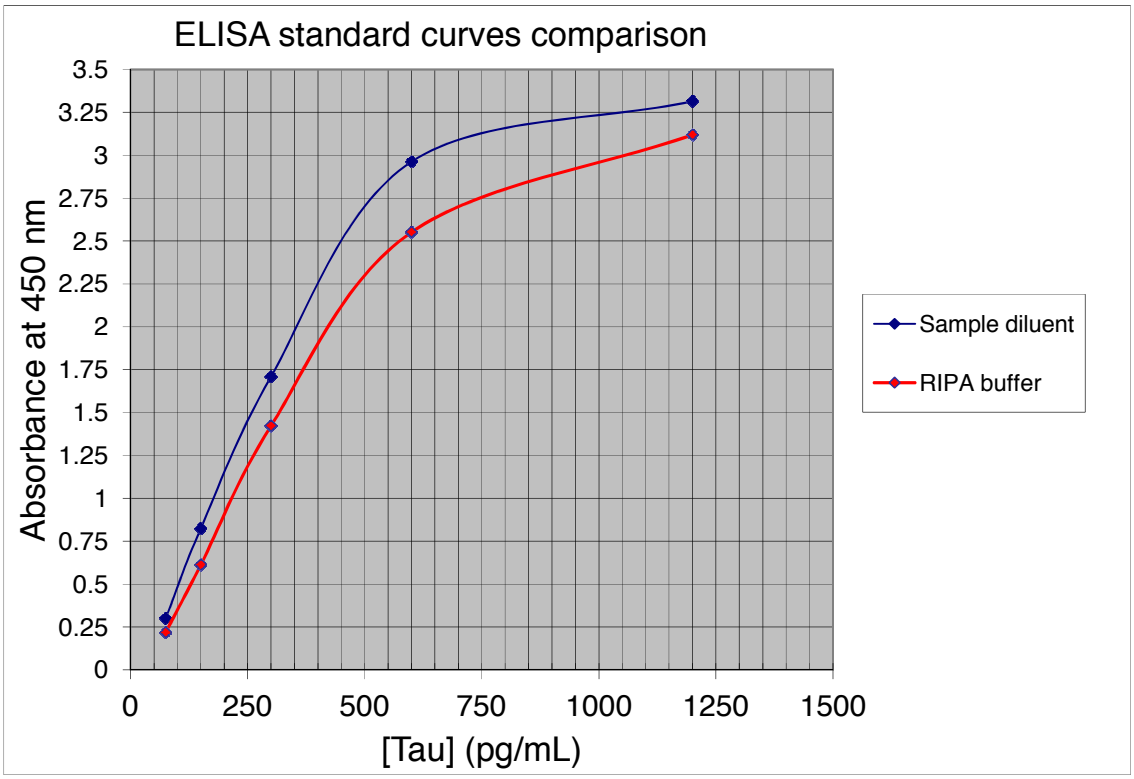

Figure 49: Standard curves comparison of kit sample diluents with RIPA buffer.
Tau protein standards provided with the ELISA kit were tested with the sample diluents solution provided by the kit or with RIPA buffer used to prepare buccal cell protein samples.

To investigate at what protein concentration buccal cell samples should be added to the ELISA wells for proper Tau detection, a first test was run with two samples (one control and one AD) of known total protein concentration at different dilutions (1, 1/2, 1/10 and 1/20). Tau was best detected within the standard curve range for both samples when no dilutions were performed. It was not possible to assay all cell samples on a single ELISA plate; therefore to ensure that the two ELISA plates used provided comparable results, the same human Tau recombinant protein at a known concentration of 500 pg/mL was assayed on both plates. No difference was observed between the two ELISA plates.

4.2.5.5 Western blots

Cells were centrifuged 5 min at 1500 xg and incubated with 500 µL of RIPA lysis buffer containing phosphatase and protease inhibitors for 2h at 4°C. Cells were diluted 1:2 with Laemmli Sample Buffer containing β-Mercapto Ethanol at a ratio of 1:20 and

then heated at 95°C for 3 min to denature proteins. Up to 30 µL of sample was loaded on each lane, 10 µL of ladder protein was also added to one lane to follow migration and provide details about molecular weight of bands observed. Samples for polyacrylamide gel electrophoresis were run on BioRad "TGX Any Kd" gels or Invitrogen "Novex 16% Tricine" gels. Typically, samples were electrophoresed for up to 1 h at 150-200V. Proteins were then transferred to nitro cellulose 0/45 µm membranes (BioRad system) or PVDF membranes 0.2 µm (Invitrogen system). Membranes were washed 5 min in TBST (Tris-buffered saline, 0.1% Tween) prior to the blocking step and placed in 20 mL of Blocking Solution (2 % BSA dissolved in TBST) for 1 h. The membranes were incubated overnight at RT with primary antibodies. The membranes were washed 3 times for 5 min with TBST and secondary antibody conjugated horseradish peroxidise (PerkinElmer) added to the membranes in blocking solution and incubated for 2 h at RT. The membranes were washed 3 times for 5 min with TBST prior to imaging by enhanced chemiluminescence (Western Lightning®Plus-ECL, PerkinElmer) using an Image Quant LAS 4000 imager (GE Health Care).

4.2.6 Staining procedures of slides

4.2.6.1 Staining procedure for visual scoring

Microscope slides containing buccal cells previously fixed with ethanol:acetic acid (3:1) were defrosted and stained for visual scoring of the buccal cytome as described in chapter 2, section "*2.2.4 Buccal cell fixation and staining*".

4.2.6.2 Staining procedures for LSC

Microscope slides containing buccal cells previously fixed with 0.4% formaldehyde were defrosted and stained in small batches of 8 including a control slide to ensure proper staining. Microscope slides were washed 5 min in TBS and incubated for 10 min in 5% Triton X-100 in PBS at RT in Coplin Jars. 25 µL of 88% formic acid in RO water was added to each cytospot and covered with parafilm for 5 min. Slides were then washed with TBS 2 times for 5 min in Coplin Jars. Each cytospot was covered with 25 µL of blocking solution (1.5% BSA in TBS) and was gently shaken in a humidified box for 30 min at 37°C. Blocking solution was gently removed by the use of absorbing paper. The primary antibodies mix solution, composed of Anti-Aβ1-42 Rabbit

monoclonal and Anti-Tau BT2 Mouse monoclonal antibodies at a dilution of 1/50 and 1/100, respectively in blocking solution, was added to the cytospots and covered with parafilm in a humidified box at 4°C overnight under gentle mixing. Slides were washed 5 min in TBS in Coplin Jars and then washed 3 times for 30 sec each in 1% triethyl-phosphate in ultra pure water and then incubated with Oil Red O (ORO) staining working solution (3 mg/mL ORO in 36% triethyl-phosphate) for 45 min in the dark, to stain for neutral lipids. From this point onwards all steps were undertaken in the dark. Slides were then washed 3 times for 30 sec with 1% triethyl-phosphate and then slides were further stained in 0.2% (w/v) Fast Green for 30 min, to stain cytoplasm. The excess of Fast Green was removed by rinsing the slides for 1 min with running tap water. Remaining water on the slides was gently removed with absorbing paper. Then, 25 µL of secondary antibody mix solution, composed of Alexa Fluor 488 Anti-Mouse and Alexa Fluor 568 Anti-Rabbit both diluted at 1/100 in blocking solution, was added on the cytospots and covered with parafilm in a humidified box for 1.5 h at 37°C. Slides were washed 5 min in TBS in Coplin Jars. Nuclei were stained with DAPI (0.2 µg/mL) for 5 min. The excess of DAPI was removed by rinsing the slides in 300 mM NaCl, 34 mM sodium citrate. Slides were then mounted with coverslips and PBS:glycerol (1:1) mounting medium. To avoid drying, the coverslips were sealed around the edge with nail polish and slides were kept in the dark in a microscope box with desiccant at -20°C for up to 2 days until analysed by LSC. All incubation steps of slides in Coplin Jars were carried out with gentle mixing motion to ensure adequate solution movement over the samples.

4.2.7 Laser scanning cytometry

4.2.7.1 Lasers and detectors

Microscope slides containing freshly stained buccal cells were inserted into a 4 slide carrier and analysed by iCyte® Automated Imaging Cytometer (CompuCyte Corporation, Westwood, MA). Lasers selected for the high-content assays were 405 nm, 488 nm, 561 nm and 633 nm to detect DAPI, ORO and Tau as well as Aβ, and Fast Green respectively. The blue, green, red and long red PMTs were used to collect fluorescence from DAPI, Tau, Aβ and Fast Green respectively. As ORO is a chromatic stain, the 488 PD was set up to quantify its absorbance properties (Table 11).

Table 11: Laser and detector selection for buccal cells.

Target	Dyes	Excitation Lasers (nm)	Detectors
Cytoplasm	Fast Green	633	Long Red (Fluorescence)
Nuclei	DAPI	405	Blue (Fluorescence)
Neutral Lipids	Oil Red O	488	488 LL (Absorbance)
Amyloid-β 1-42	488 Alexa Fluor	488	Green (Fluorescence)
Tau BT2	568 Alexa Fluor	561	Red (Fluorescence)

Abbreviations; LL, light loss (absorption)

4.2.7.2 Low and high resolution scans

The low resolution scan and high resolution scan settings regarding objectives, laser increment steps and rectangular regions were as described in chapter 3, section "*3.2.7.2 Low and high resolution scans"*.

4.2.7.3 Setting up the dynamic range

In this modified LSC protocol the lasers and detector settings were as shown in Figure 50. Two paths were used to avoid unnecessary overlapping of fluorescence. In the first path (upper panel) violet and yellow lasers were used simultaneously while in the second path (lower panel) blue and red lasers were selected. It would have been possible to set the instrument to scan slides using three paths but this would have been very time consuming as each scan field would have been scanned three times. In the same manner as described in chapter 3, section "*3.2.7.3 Setting up the dynamic range*", Voltage, Gain and Offset values were set for optimal collection of emission signals from dyes.

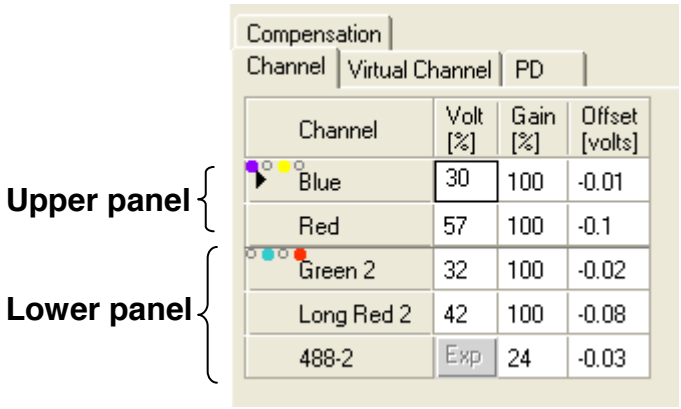

Figure 50: Detector module used for this study.

405 and 561 nm lasers were used in the upper panel for the first path and fluorescence was collected in the Blue and Red Channels. In the second path (lower panel) 488 and 633 nm lasers were selected and fluorescence was collected in the Green and Long Red channels while blue laser absorbance was collected with a 488 PD.

Absorbance obtained with 488 PD was inverted by creating a virtual channel "Blue I" and focus was adjusted as in chapter 3, Figure 23 of section "*3.2.7.3 Setting up the dynamic range"* by manually generating a "profile line" (magenta) other cell images to ensure the resolution and intensity of the ORO signal were optimal.

4.2.7.4 Virtual channels and compensation

4.2.7.4.1 Spectra viewer

Before setting up virtual channels for compensation it was essential to determine what compensation would be needed. For that the visual spectra viewer tool from the invitrogen website was used as a guide (Figure 51). Excitation wavelengths could be selected and overlapping of their emission wavelengths be seen on the bandpass emission filter region selected (grey shadow). Compensation would only be needed for the first path where signals collected from DAPI and secondary antibody conjugate Alexa Fluor 568 should only be detected. Emission (dashed line) and excitation (solid line) wavelengths were selected for DAPI (blue), Alexa Fluor 568 (Green) and Fast Green (Red). As Fast Green was not available in the list of dyes provided by invitrogen, its' closest in terms of fluorescence properties was selected (Alexa Fluor 633). The 561 nm laser selected to excite Alexa Fluor 568 can be viewed as the yellow vertical line and the emitted filter bandpass region where the subsequent emitted fluorescence was collected by the Red PMT can be viewed in grey shadow. The first fluorescence overlap

that occurs in that grey region can be seen where the emission curve of DAPI crosses the grey region, meaning that the Red PMT collects a small amount of DAPI fluorescence at the same time Alexa Fluor 568 dye fluorescence is being collected. In this compensation set-up the DAPI signal collected within that channel was therefore subtracted from the Alexa Fluor 568 signal. The second overlap was minimal and involved fluorescence emitted from Fast Green (red curve). It can be viewed that the 561 excitation laser line (yellow) crosses the excitation curve of the antibody conjugate dye (green dashed line) but also the excitation curve of Fast Green (red dashed line). No compensation would be needed if the Fast Green emission curve (solid line) was located out of the emission filter bandpass region. However, with the settings used, Alexa Fluor 568 signal was collected at the same time as the Fast Green signal, and therefore Fast Green was subtracted from the total signal collected within the Red channel.

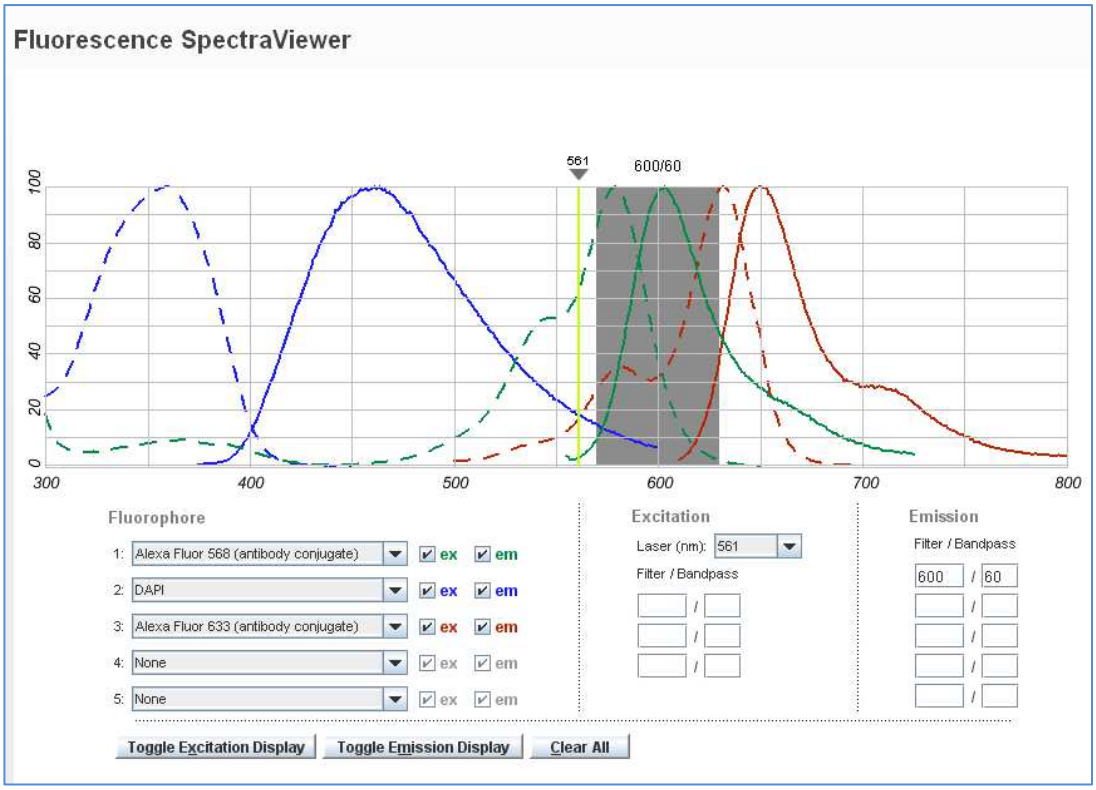

Figure 51: Fluorescence spectra viewer tool from invitrogen website.
Fluorophores were selected as follows; DAPI (blue), Alexa Fluor 568 (Green), Alex Fluor 633 (red) and their excitation and emission patterns can be seen in dashed and solid curves, respectively. The excitation laser selected is 561 nm (yellow vertical line) and the emission filter representing the Red channel is viewed (grey region). Overlapping and compensation needed can then be assessed.

4.2.7.4.2 Virtual channels

With the aid of the spectra viewer, compensation of several virtual channels was created as shown in Table 12.

Table 12: Creation of virtual channels to compensate for non-specific fluorescence.

Virtual Channel	Input Channel	Operator	Purpose
488 Inv	488 LL	Invert	Convert from brightfield to darkfield
Blue M	Blue	Multiply 0.28	Adjustment factor for DAPI compensation
Red C	Red	Subtract Blue M	Compensated for DAPI stain
Long Red M	Long Red	Multiply 0.08	Adjustment factor for Fast Green compensation
Red C Final	Red C	Subtract Long Red M	Compensated for Fast Green stain

4.2.7.4.3 Random segmentation and compensation

In a similar way as it was done in chapter 2, section *"2.2.5.3 Virtual channels and compensation";* the random segmentation "phantom" feature was used to properly define and evaluate the compensation settings by monitoring the distribution of events in scattergrams. Compensation scattergrams can be seen in Figure 52. The first level of compensation involved subtracting DAPI signal (Blue Integral) from Red Integral, when proper compensation is reached the uncompensated events (Figure 52A) moves towards a more vertical position as shown by the cyan line in the compensated events scattergram (Figure 52B). The first level compensated virtual channel named "Red C" was then used in the second level of compensation where Fast Green signal (Long Red 2 Integral) was subtracted from Red C Integral. In the same manner compensation was properly achieved when the uncompensated events (Figure 52C) have moved towards a more vertical position (Figure 52D) as shown by the cyan line. The channel obtained after final compensation is named "Red C Final" and was used for contouring and analysis of the signal obtained from Alexa Fluor 568 antibody conjugate.

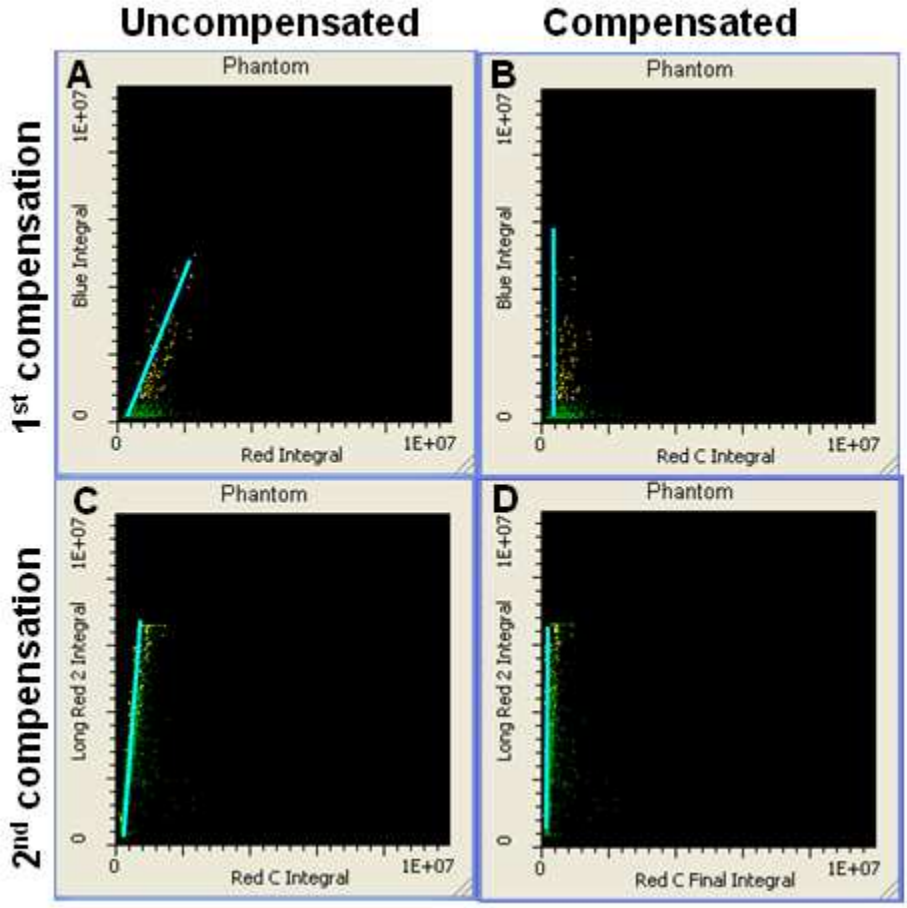

Figure 52: "Phantom" events plotted on scattergrams for compensation.
(A-B) First level of compensation subtracts DAPI signal received in the Red channel from the Alexa Fluor 568 signal. When compensated events moves towards a more vertical position. (C-D) Second level of compensation, which involves subtracting Fast Green from the Alexa Fluor 568 signal.

The different levels of compensation can be visualised in the images generated by LSC with examples of a field image shown in Figure 53. Fast Green, DAPI, Alexa Fluor 488 and Alexa Fluor 568 can be respectively seen in green, blue, yellow and magenta. Originally, signals for each dye were separately generated in black and white. Since the PMTs quantify the intensity of light (photons) but do not detect the color, the use of the "CompuColor" feature to allocate colors of preference to each signal was applied. In this manner the most contrasted colors could be selected for better appreciation of intensity and localisation of dyes on a single image (Figure 53A). To observe the effect of compensation of fluorescence for Alexa Fluor 568 signal, the original black and white images were used. Prior to any compensation, nuclei (blue arrows) could be partly distinguished (Figure 53B) in the red channel, however the nuclei signal was

decreased at the first level of compensation when subtracting the overlapping DAPI signal (Figure 53C). Further compensation completely removed the background (non-specific) cytoplasm (long red) signal from the red signal (magenta arrows); (Figure 53D).

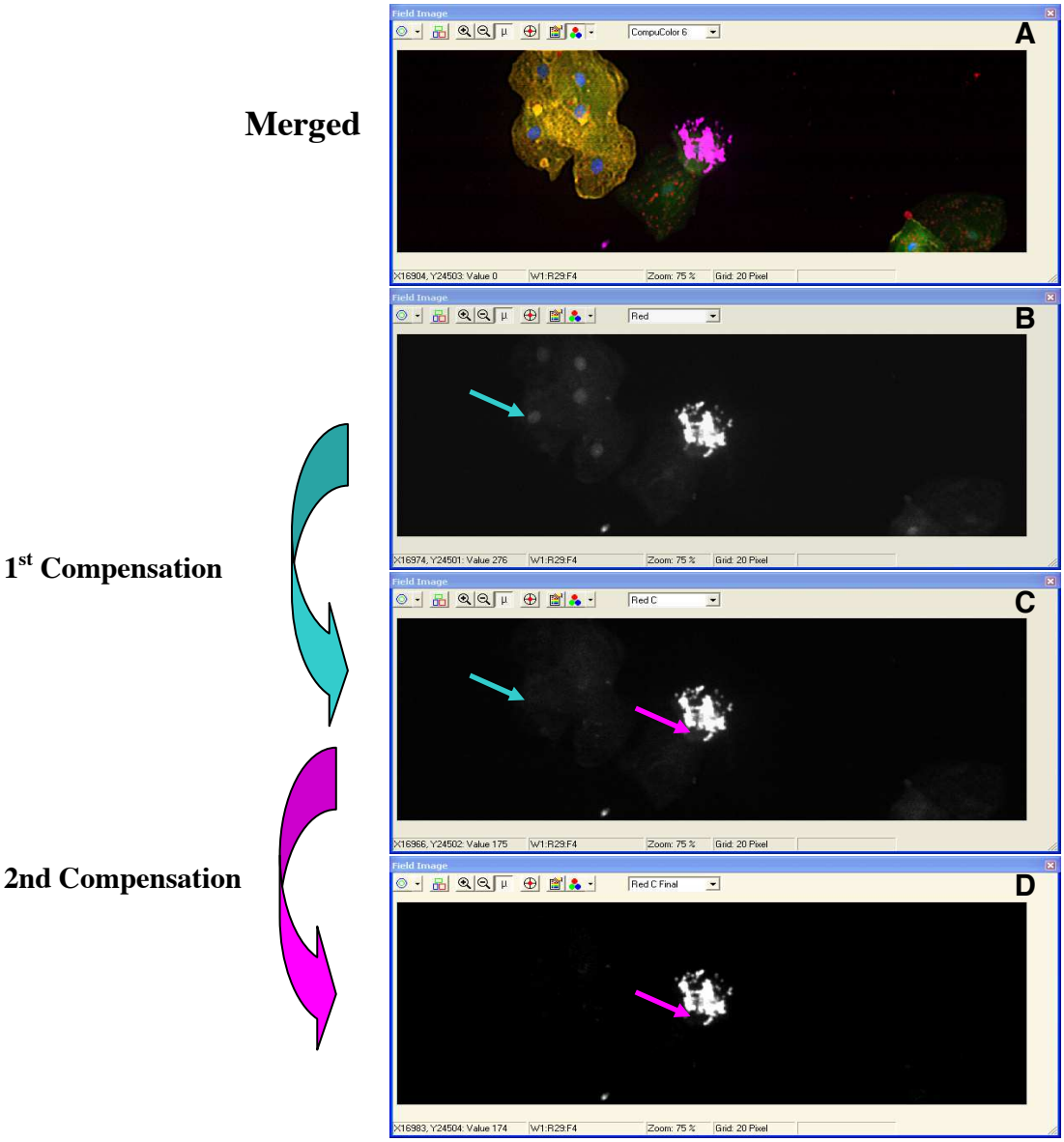

Figure 53: Visualisation of compensation effects on field images.
(A) Merged color field image where all final signals are shown prior to compensation. (B) Red signal before first compensation. (C) Red C signal after first level compensation. (D) Red C Final signal after second level compensation.

4.2.7.5 LSC protocol and segmentation of events

To analyse these five dyes in a combined manner and reach a higher content analysis level it was necessary to upgrade the LSC protocol developed previously in chapter 3, section "*3.2.7.4 LSC protocol and segmentation of events*". Therefore a new LSC protocol was designed (Figure 54). The first part (Figure 54A) of the protocol was similar to that in the previous protocol developed. One difference was to be noted, the color of contour for neutral lipids was changed from magenta to red to help visualising contours. An add-on to this protocol was developed for the detection of the antibody conjugates, Alexa Fluor 488 and 568 (Figure 54B).

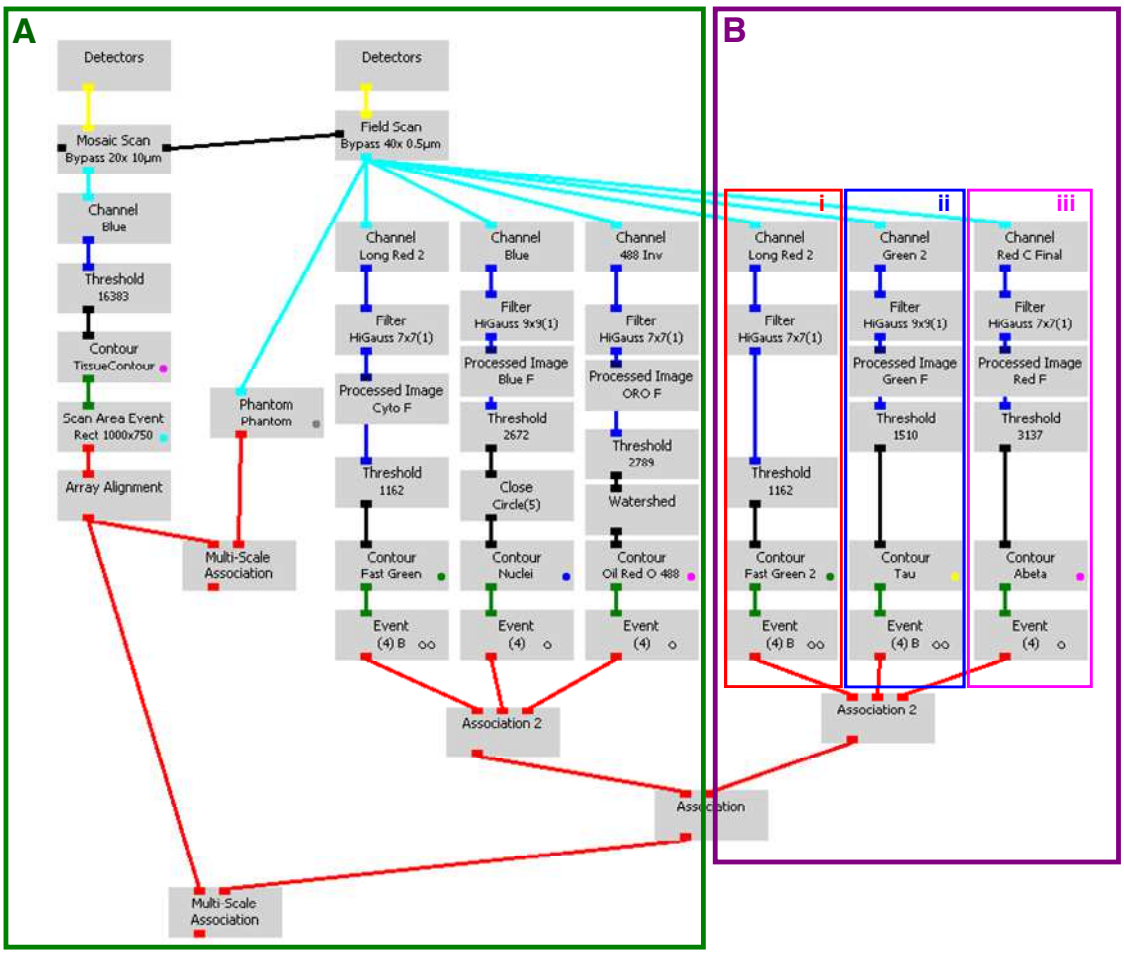

Figure 54: LSC protocol designed for this study.
(A) Contains first resolution scan settings which was similar to the LSC protocol used previously with one difference, the color of neutral lipids contour being red. (B) The second half of the high resolution scan was added to detect, contour and analyse signals obtained from Alexa Fluor 488 and 568.

Since the “Association 2” module has only three inputs available and they were already utilised (Figure 54A), it was then necessary to create a duplicate scale of the primary event Fast Green (Figure 54Bi). This allowed the new data for Aβ and Tau to link to Fast Green 2. The second scale (Figure 54Bii) shows settings used for detection of signal obtained from Alexa Fluor 488 in the Channel “Green 2”. A filter “HiGauss 9x9” was applied to improve contrast followed by a threshold set at a value of 1510. This value was observed to optimally separate Tau signal from background. Contour was set as yellow with a minimum area of 10 μm^2 to improve small false positives exclusion in the “Event” module. The third scale measured signal collected from Alexa Fluor 568 (Figure 54Biii) and termed “Red C Final” which represented the final compensated signal. A filter “Hi-Gauss 7x7” was applied to the “Red C Final” to increase detection of Aβ spots within the cells. Since most of the “Red C Final” signal observed was intense it was necessary to set a high value threshold of 3137 for proper contouring. A magenta color was selected and it was noted that events could reach a small size; therefore the minimal area detection was set at 1 μm^2. An example of a field image can be seen without (Figure 55A) or with the five events (cytoplasm, nuclei, neutral lipids, Tau and Aβ) contoured (Figure 55B).

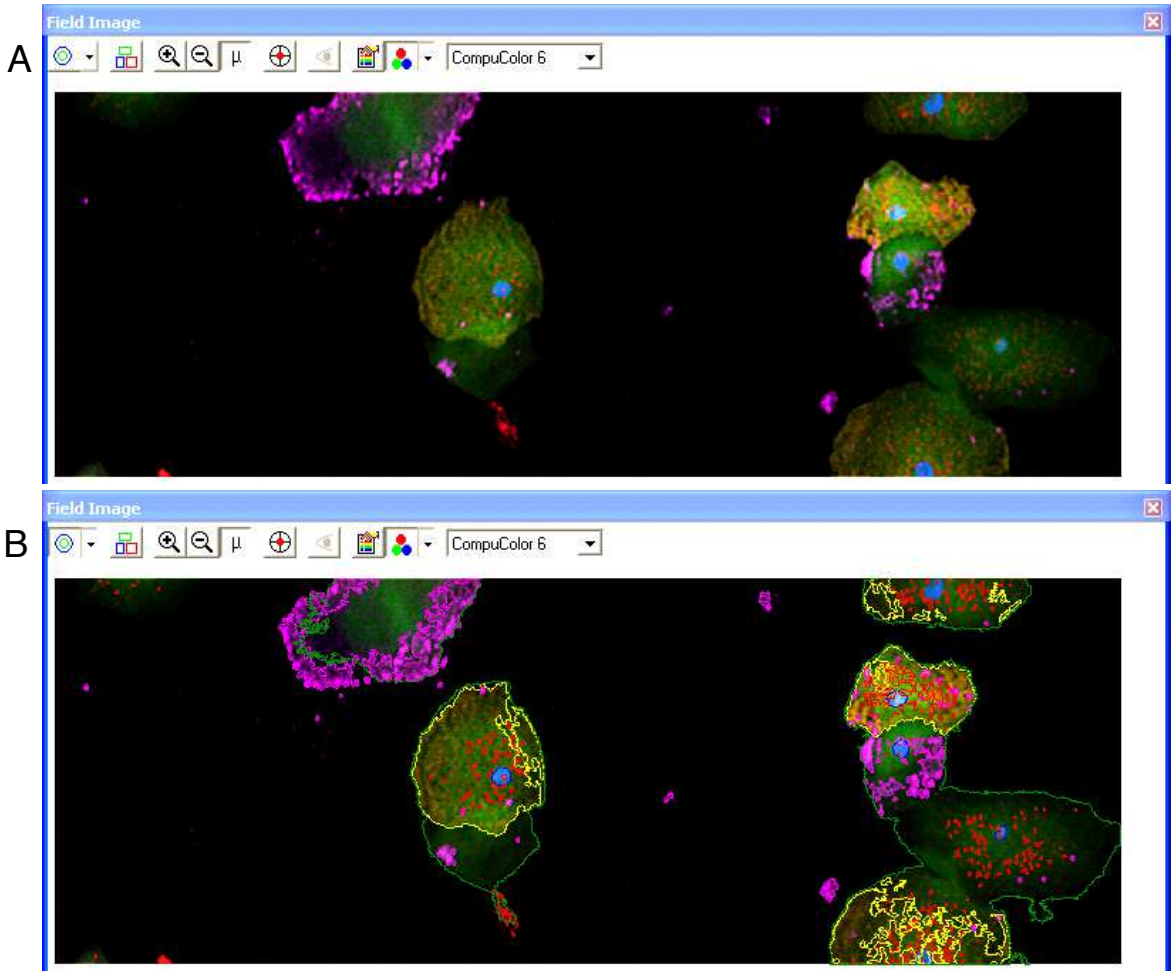

Figure 55: Field images generated by LSC.
Field image generated by LSC, (A) without and (B) with the contour feature activated; a green, blue, red, yellow and magenta contour is automatically drawn (by the mean of the settings previously selected in the LSC protocol; see Figure 54) around cytoplasm, nuclei, neutral lipids, Tau and Aβ respectively.

Prior to each scan the same region from a control slide of buccal cells stained with Feulgen was scanned with a 488 laser to ensure that the signal collected with the 488 PD was constant over the study (no variations were observed). Prior to each batch scan, a control slide containing buccal cells sampled from the same individual (healthy male aged 69) was used to ensure that all settings and measurements had not drifted and to confirm proper staining. There was no measurable drift over the course of the study. The fluorescence (and absorbance where appropriate) of events were recorded as follows: area, count, circularity, maximum pixel, fluorescence or inverted absorbance Integral.

4.2.7.6 Automation of the buccal cell cytome

Identification of cell types for scoring in the automated buccal cytome assay was made by the use of scattergrams as described in chapter 3, section "*3.2.7.5 Automation of the buccal cell cytome"*.

4.2.7.7 Ploidy measurements

DNA content was measured as described in chapter 3, section "*3.2.7.6 Measurement of DNA content"*.

4.2.7.8 Data and statistics

4.2.7.8.1 Generation of Data

Statistics were generated as described in chapter 3, section "*3.2.7.7.1 Generation of data"*. In addition new parameters were investigated and therefore additional statistics were generated.

4.2.7.8.2 Statistical analysis

One-way analysis of variance (ANOVA) and linear correlation analyses were carried out to determine the significance of the cellular parameters measured between the control, MCI and AD groups. Pairwise comparison of significance between these groups was determined using Tukey's test. Post test for linear trend were carried out across the groups (control, MCI and AD) when appropriate. ANOVA and correlation values were calculated using GraphPad Prism 5 (GraphPad Software Inc., San Diego, CA, USA). Significance was accepted at $P<0.05$. When no significance was found, P-values were not shown on the graphs. Column statistics were generated and receiver-operating characteristic (ROC) curves were carried out for selected parameters and their combinations between the control and MCI groups as well as AD groups to obtain area under the curve (AUC), and P-values.

4.3 RESULTS

4.3.1 Saccomano's fixative effect on ORO staining

Since it was not practical to process buccal cells on the day of collection, the cells needed to be stored in a mild fixative medium that would not impact on downstream analyses. Therefore Saccomano's fixative was chosen and is composed of polyethylene glycol, ethanol and water, and is used to store cells collected from the AIBL cohort participants. There is no data available in the literature on the effect of Saccomano's solution on neutral lipid content. Therefore the hypothesis that Saccomano's solution might have an effect on ORO staining in buccal cells was tested. Buccal cells were sampled from a healthy individual aged 42, split into 4 tubes containing 20 mL of Saccomano's each and stored at 4°C. Different incubation times were tested, each of the tubes was removed at different times (i.e. after 1, 8, 15 and 28 days). Because 1 day is a minimal time of storage of buccal cells in Saccomano's due to sampling and shipping from Melbourne and Perth to Adelaide the first time point selected was 1 day. Cells were processed as described in chapter 3, section "*3.2.3 Buccal cell isolation*" and microscope slides for each time condition were stained in triplicates as described in chapter 3, section "*3.2.5 Staining of slides for LSC*". Figure 56A shows ORO content for each of the six cytospots analysed. A decrease in ORO content was observed after 15 days and 28 days of incubation of buccal cells in Saccomano's ($P<0.05$ and $P<0.001$, respectively), however no significant decrease was measured after 8 days and between 8 and 15 days of incubation times. Buccal cells also exhibited a significantly lower ORO content at 8 days compared to 28 days of incubation in Saccomano's.

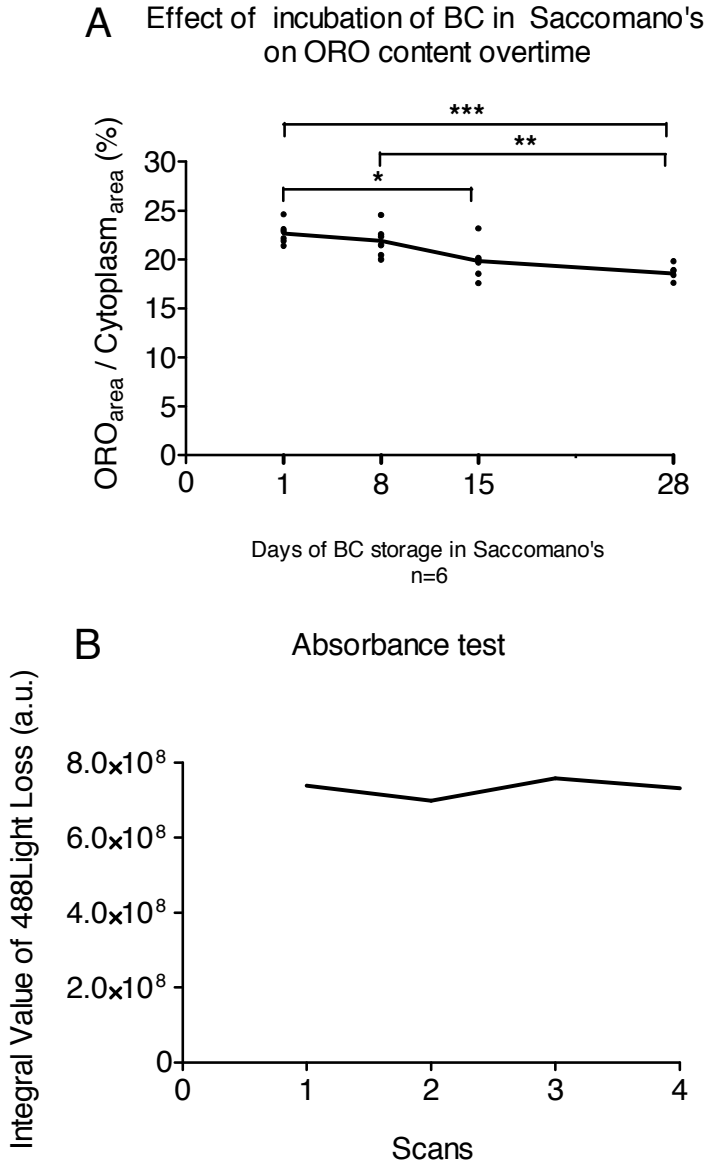

Figure 56: Effect of storage in Saccomano's on neutral lipid content of buccal cells. (A) After 15 and 28 days of storage the ORO content significantly decreased ($P<0.05$ and $P<0.001$, respectively). No significant variations can be observed between 1 and 8 days as well as 8 and 15 days of storage. A significant decrease is shown between 8 and 28 days of storage ($P<0.01$). (B) No differences were measured in the absorbance of the internal control slide over the experiment. Abbreviations; a.u., Arbitraty units; BC, Buccal cells; ORO, Oil Red O; *, $P<0.05$; **, $P<0.01$; ***, $P<0.001$.

To ensure that no drift in the absorbance detected by 488 PD detector (absorbance used to measure ORO staining) as well as no drop in the 488 nm laser power occurred during the experiment that would affect its' final outcome, a standard slide was scanned before each scan. This internal control slide contained buccal cells stained with Feulgen, a chromatic stain of nuclei that can also be quantified by 488 nm absorbance. The exact same region on that slide was scanned with the same settings, and the Integral value of Feulgen measured was reported on a graph (Figure 56B). No shift of the PD detector or drop of the 488 laser power occurred over the experiment which therefore confirms that the small decrease of neutral lipid content in buccal cells was due to their storage in Saccomano's overtime. To remove this potential bias from the analysis, one of the criteria for selection of the 60 AIBL samples analysed in this study was that the storage of buccal cells in Saccomano's did not exceed a duration interval of 10 days.

4.3.2 Western blots

One of the aims of this study was to detect and quantify putative Aβ and Tau by LSC in buccal cells. Since Aβ (amyloid) and Tau have been reported to be expressed in the BM previously (Hattori, et al. 2002; Ko, et al. 2007), Western blotting on buccal cell samples was carried out to detect putative Aβ and Tau prior to measurement by high-content LSC analyses. The Western blotting preliminary tested antibodies on buccal cell samples but were not undertaken for quantitative purposes between samples, since a large quantity of cellular material was required and does not provide any information of localisation or presence in particular buccal cell types. For Western blots a secondary antibody control was run in the absence of a primary antibody to ensure the high specificity of the secondary antibody used. An example of such a secondary control is shown in Figure 60B.

4.3.2.1 Amyloid

Amyloid is known to spontaneously form oligomers and makes the detection of Aβ peptides arduous. Two antibodies were initially chosen, one that reportedly is specific for Aβ1-42 (rabbit polyclonal; Abcam, ab10148) and the other that detects amyloid oligomers (Clone A11, rabbit polyclonal; Millipore). Pure Aβ1-42 peptides are known to form oligomers and can be detected with an anti-oligomeric antibody (Figure 57A). Figure 57B shows the same anti-oligomeric antibody when tested on buccal cell

samples from two healthy participants of different ages (41 and 66 years old) to investigate if amyloid was present. The total cell lysate as well as centrifuged cell lysate (cleared) were loaded to investigate if amyloid was detectable in the soluble protein fraction. In all samples, a band around 70 kDa was similarly detected, in both total and centrifuged cell lysates, as when pure Aβ was loaded (Figure 57A). The monomer of Aβ42 could not be detected on these gels since the resolving molecular weight was only 10 kDa, additionally the gel system used in this example was not strongly denaturing, which would be required to resolve the Aβ42 monomer (see later).

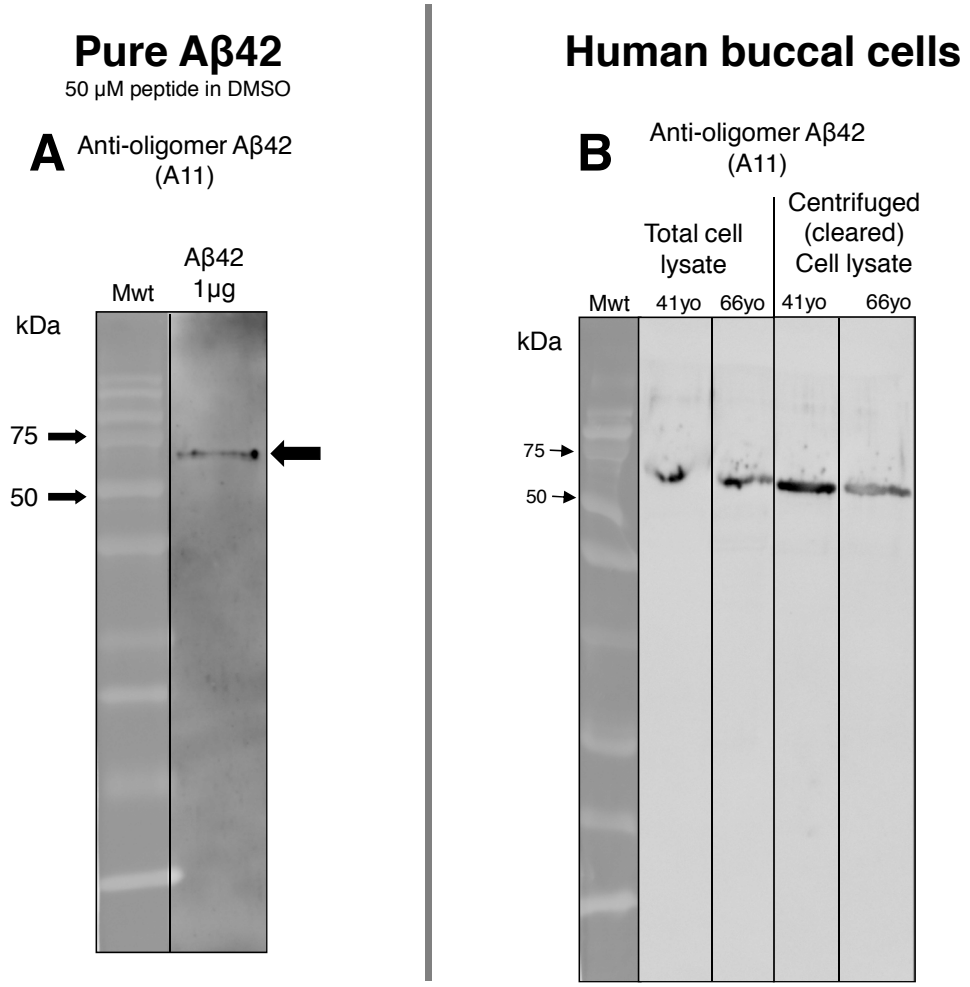

Figure 57: Pure Aβ42 and human buccal cells amyloid detection by Western blot.
(A) An anti-oligomer Aβ42 antibody used to detect the pure Aβ1-42 form. (B) The anti-oligomer Aβ42 antibody was also tested on human buccal cells. Abbreviations; Aβ, Amyloid-β; Mwt, Molecular weight; yo, Years old.

The antibody anti-Aβ1-42 (ab10148) that targets the aminoacids 33-42 of Aβ42 at the end of the peptide, was tested on the same total human buccal cell lysates from the two individuals aged 41 and 66 years (Figure 58). A band appeared around 45 kDa for both wells (41 and 66yo) with two extra bands appearing around 35 kDa for the 66 years old individual. Since the band around 45 kDa appeared to be stronger in the older subject, a reprobing of the strip to detect β-actin was performed to ensure that this difference was not due to less protein being loaded for the younger subject. In fact, the opposite was true because the β-actin signal was stronger for this younger individual, verifying that the more intense 45 kDa signal in the older subject was correct.

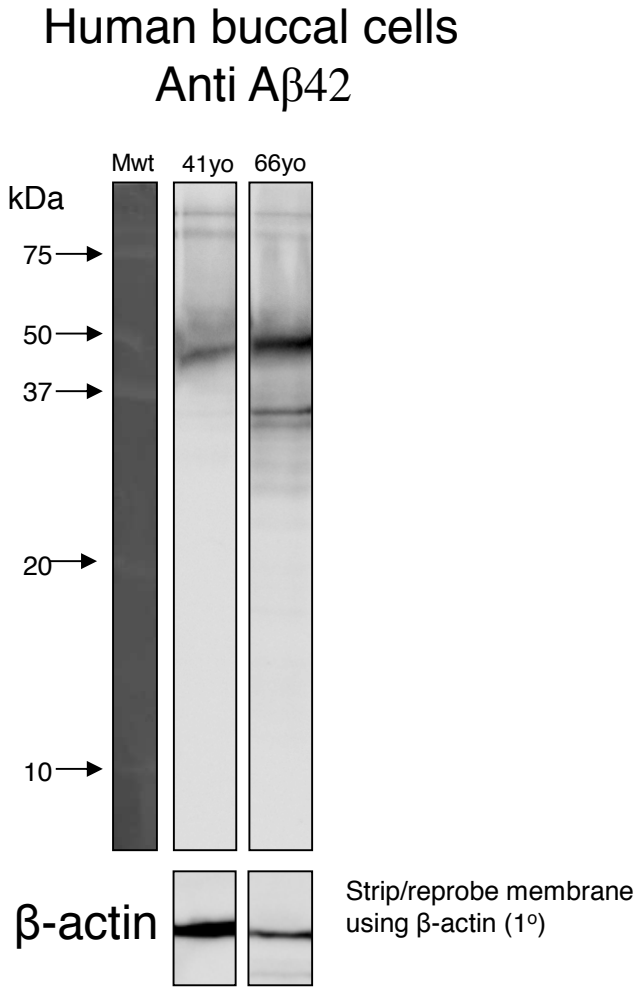

Figure 58: Anti-Aβ42 antibody tested on human buccal cell samples.
Buccal cells from two healthy individuals (41 and 66 years old) were tested on Western. Abbreviations; Aβ, Amyloid-β; Mwt, Molecular weight; yo, Years old.

Another antibody that is commonly used for detection of amyloid is WO2 (mouse monoclonal; provided by Rebecca Nisbet, CSIRO Parkville) that recognises amino acid residues 4-10 of human Aβ and that was provided by colleagues at CSIRO (Melbourne), was also tested on human buccal cells of the same 66 years old subject. Figure 59 shows a Western blot result when WO2 was tested however using more "denaturing" conditions in this example (Tricine gels and running buffers) with the aim to detect Aβ42 monomer. With 30 sec exposure (Figure 59A) a strong band appeared at 4.5 kDa in the well of the pure Aβ. A weak band corresponding to 45 kDa that could also be observed in the sample from a brain lysate of an Alzheimer's mouse model is shown. Therefore to better visualise potential bands in both samples containing the human buccal cells and AD mouse brain lysates (female APP/PSEN1 mouse's hippocampus), the time of membrane exposure was increased to 20 min (Figure 59B). A strip of paper was used to cover the pure Aβ sample that would saturate at such extended exposure time. When 20 min exposure was set, a weak and strong band appeared at 4.5 kDa in wells containing human buccal cells and AD mouse brain lysates, respectively (Figure 59B).

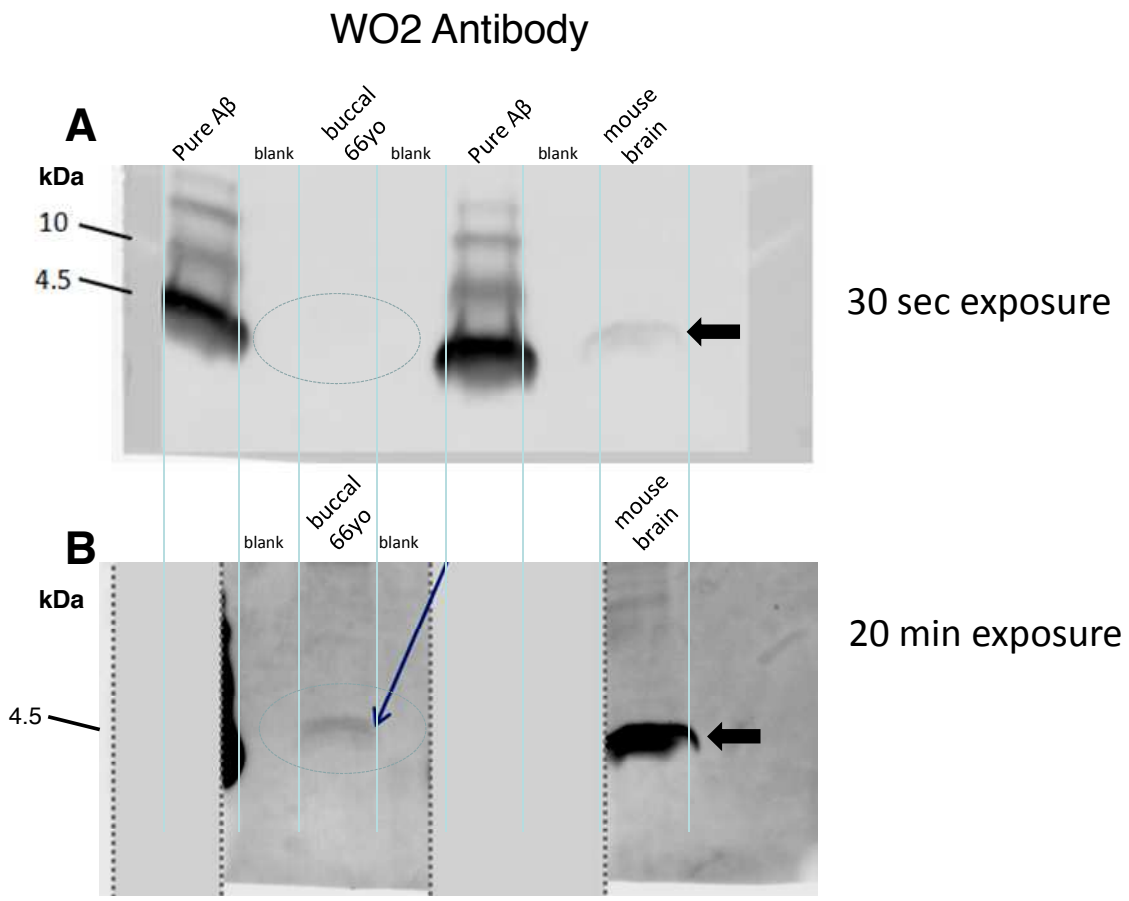

Figure 59: WO2 Antibody tested on human buccal cells, pure Aβ and AD mouse brain sample.
The membrane was exposed first (A) at 30 sec exposure time and then (B) at 20 min exposure time. The blue arrow shows the "putative" Aβ band. Abbreviations; Aβ, Amyloid-β; yo; Years old.

The WO2 antibody was further tested, this time by testing buccal cells from another subject (41 years old) and pure Aβ. Figure 60 shows the results obtained with this Western. At 3 min exposure time (Figure 60A), a band was observed at 20-25 kDa in the AD mouse brain lysate. A band was observed at 4.5 kDa in the buccal cell lysate of the 41yo individual, whilst stronger bands were detected for the AD mouse brain lysate as well as the three wells containing pure Aβ in different conditions. A secondary antibody control was tested (Figure 60B) to ensure the signal observed was not due to non-specific binding of the secondary antibody (no signal was observed).

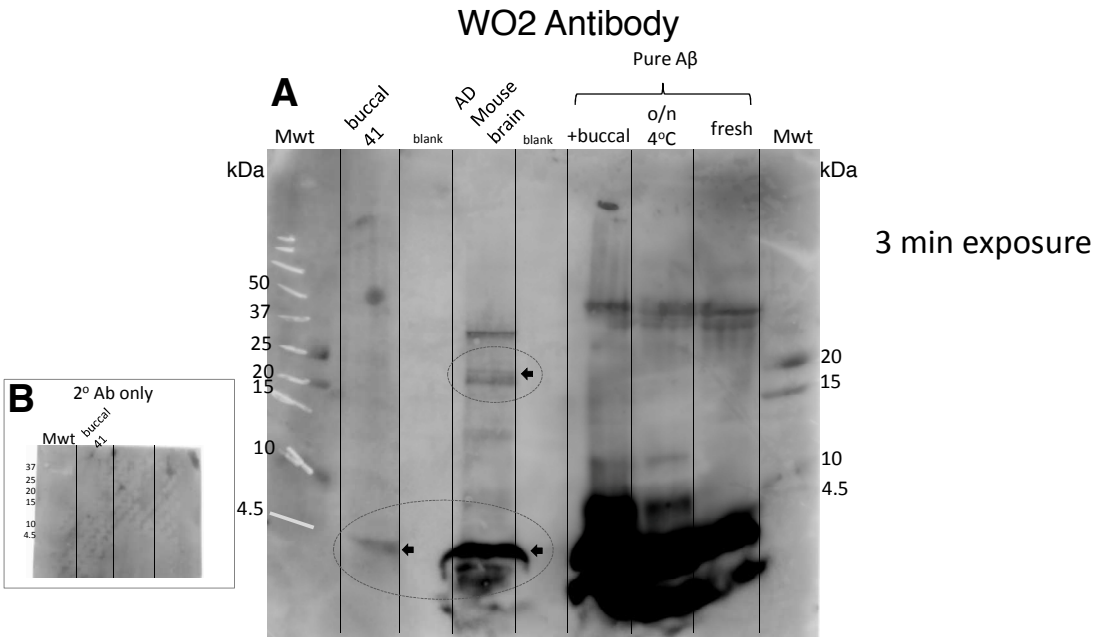

Figure 60: WO2 Antibody tested on human buccal cells, different pure Aβ conditions and AD mouse brain sample.
The membrane was exposed at (A) 3 min exposure time. (B) A control for the secondary antibody. Abbreviations; Aβ, Amyloid-β; Mwt, Molecular weight.

To further confirm whether buccal cells express Aβ42, samples were subjected to PAGE in a different lab (Professor Andy Hill from the department of Biochemistry and Molecular Biology, University of Melbourne, Australia). Samples from the same individual as well as the mouse brain lysate and pure Aβ were examined using WO2 antibody under denaturing conditions. Figure 61 shows results obtained from Prof Hill's lab. It was shown that a band at 4.5 kDa similarly appeared in the wells containing buccal cell lysate from a 66yo subject and from pure Aβ. A 110 kDa band was also seen in the buccal sample from the 66yo subject. Additionally, it appeared there was a large amount of amyloid detected in the AD mouse brain lysate.

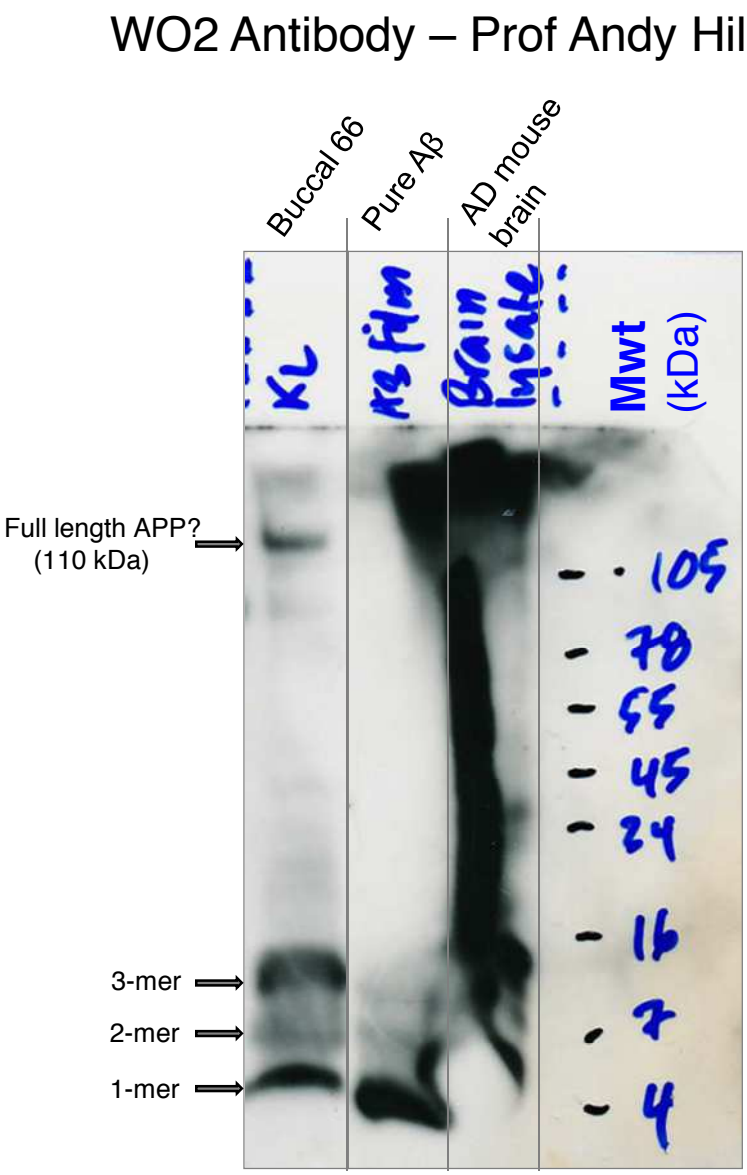

Figure 61: WO2 Antibody tested on human buccal cell samples, pure Aβ and AD mouse brain lysate at Prof Hill's laboratory.
"KL" is a buccal sample from 66 years old healthy male. Possible multimer combinations of Aβ1-42 are labeled on the left side. Abbreviations; Aβ, Amyloid-β; APP, Amyloid precursor protein; Mwt, Molecular weight.

4.3.2.2 Tau

Two different antibodies were tested on Western for detection of Tau in buccal cell lysate from a 66 years old subject and AD mouse brain lysate. When DAKO A0024 Tau was used, a significant background was visible (Figure 62A). Additionally, numerous light bands appeared in the buccal cell total lysate when compared to the soluble fraction. This antibody did not seem to detect any clean bands in the AD mouse brain

lysate. However, a second antibody BT-2 Tau (an antibody that is used in the Innotest ELISA Kit) was utilised on a total buccal cell lysate and AD mouse brain sample (Figure 62B). This antibody showed several bands in the buccal cell lysate appearing below 10 kDa, around 21 kDa and 50 kDa. A strong band can also be seen between 50 and 75 kDa. It is therefore plausible that different forms of Tau (isoforms) are present in buccal cells. The AD mouse brain lysate showed bands localised at different molecular weights with a strong band around 24 kDa.

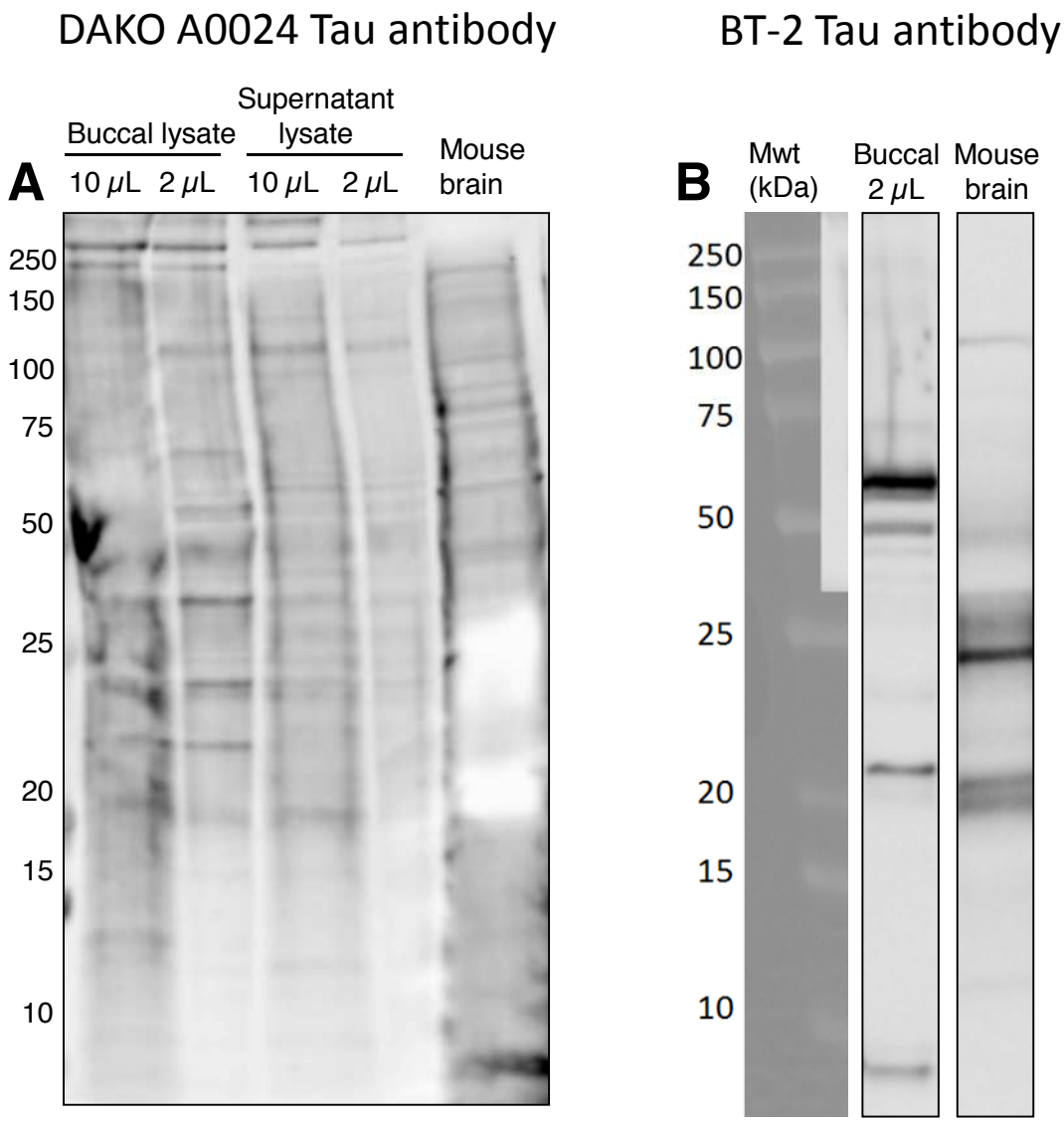

Figure 62: DAKO A0024 Tau and BT-2 Tau antibody tested on human buccal cell and mouse brain lysates.
Buccal cell and AD mouse brain lysates were run on Western blot with (A) DAKO A0024 Tau antibody or (B) BT-2 Tau antibody. Abbreviation; Mwt, Molecular weight.

4.3.3 Immunocytochemistry

4.3.3.1 Testing amyloid antibodies

Thioflavin T (a common but relatively non-specific stain used to detect amyloid) was tested on buccal cells. After 1 h incubation, no signal was detected. Several other antibodies (i.e. anti-4G8 Aβ, anti-6E10 Aβ) were tested by immuncytochemistry using two fixation methods (formaldehyde 0.4% and Ethanol:Acetic acid 3:1 mix). Each antibody was tested separately on buccal cells sampled from the same healthy male individual aged 66 also sampled previously for Western blots. Buccal cells were additionally counterstained with DAPI to localise nuclei and adjust focus under fluorescence microscopy. The starting dilution for antibodies tested was 1:50. If signal was detected dilutions of 1:100 and 1:200 were then tested to see if any improvement in clarity of the signal could be made. Different antibody incubation conditions were also tested, 1 h, 2 h at 37°C or overnight at 4°C. The secondary antibodies used for detection of all tested primary antibodies binding were Alexa Fluor 488 or 568. Other secondary antibodies were also tested such as Alexa Fluor 633 and Phycoerytrhin (PE) but did not provide a cleaner and stronger signal compared to Alexa Fluor 488 when scanned by LSC. Moreover PE showed to be less stable under fluorescence excitation as it bleached more rapidly. To ensure that the signal obtained was not induced by non-specific binding of secondary antibodies, a negative control slide was run through the immunocytochemistry protocol without the primary antibody incubation step. No signal was detected. Figure 63 shows signal detected by fluorescence microscopy with a 40x objective in buccal cells, when anti-amyloid oligomeric (Clone A11) and Alexa Fluor 568 were used as a primary and secondary antibody, respectively. A lot of background on the microscope slide and false negatives were detected and did not disappear when more numerous and stringent washes (TBS with 0.1% Tween) were used or when lower primary and secondary antibody dilutions were used.

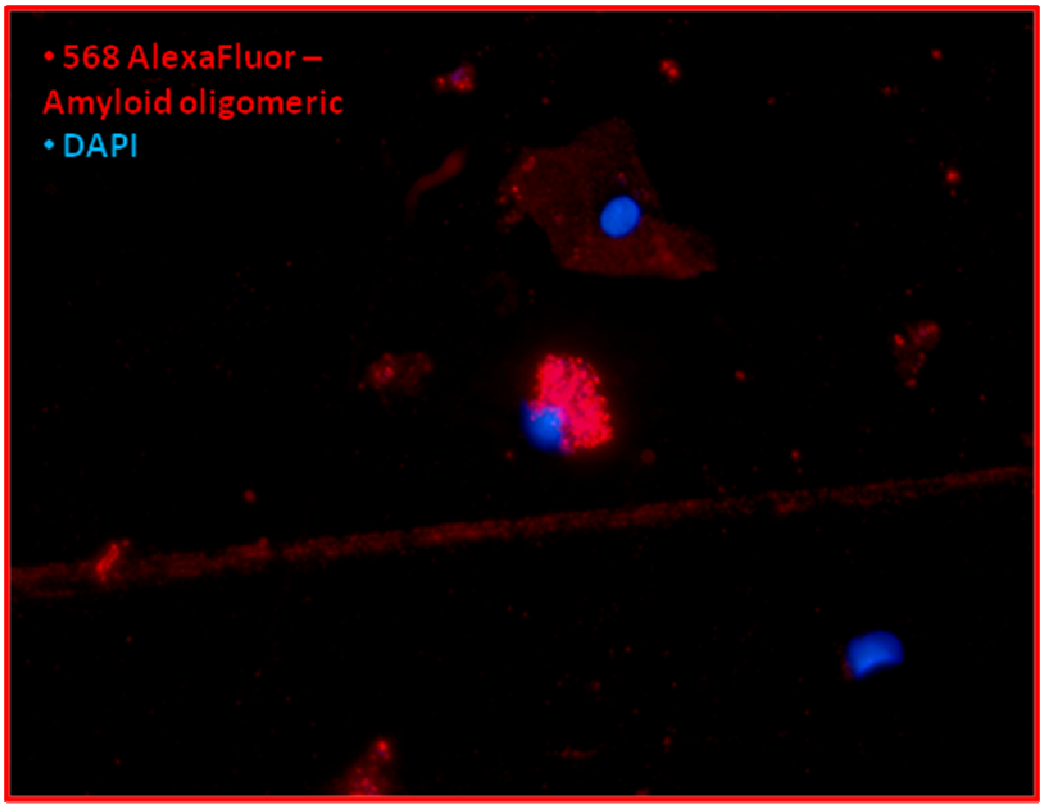

Figure 63: Detection of amyloid oligomeric and nuclei in buccal cells by fluorescence microscopy (40x).
Anti-amyloid oligomeric antibody was bound by a fluorescent Alexa Fluor 568 secondary antibody (red), while nuclei were counterstained with DAPI (blue). A lot of background staining as well as non-specific binding was detected.

Detection of Anti-Aβ1-42 (ab10148) antibody by fluorescence with secondary antibody Alexa Fluor 488 is shown in Figure 64. A 40x image obtained by fluorescence microscopy shows a clean signal in green with no subsequent background that is localised around nuclei and within the cytoplasm (Figure 64A). No cytoplasm stains were used at first to avoid any possible interference with the Alexa Fluor 488 dye. The blue rectangular region was viewed using a 100x oil objective and showed that Aβ-1-42 protein seemed to aggregate (Figure 64B).

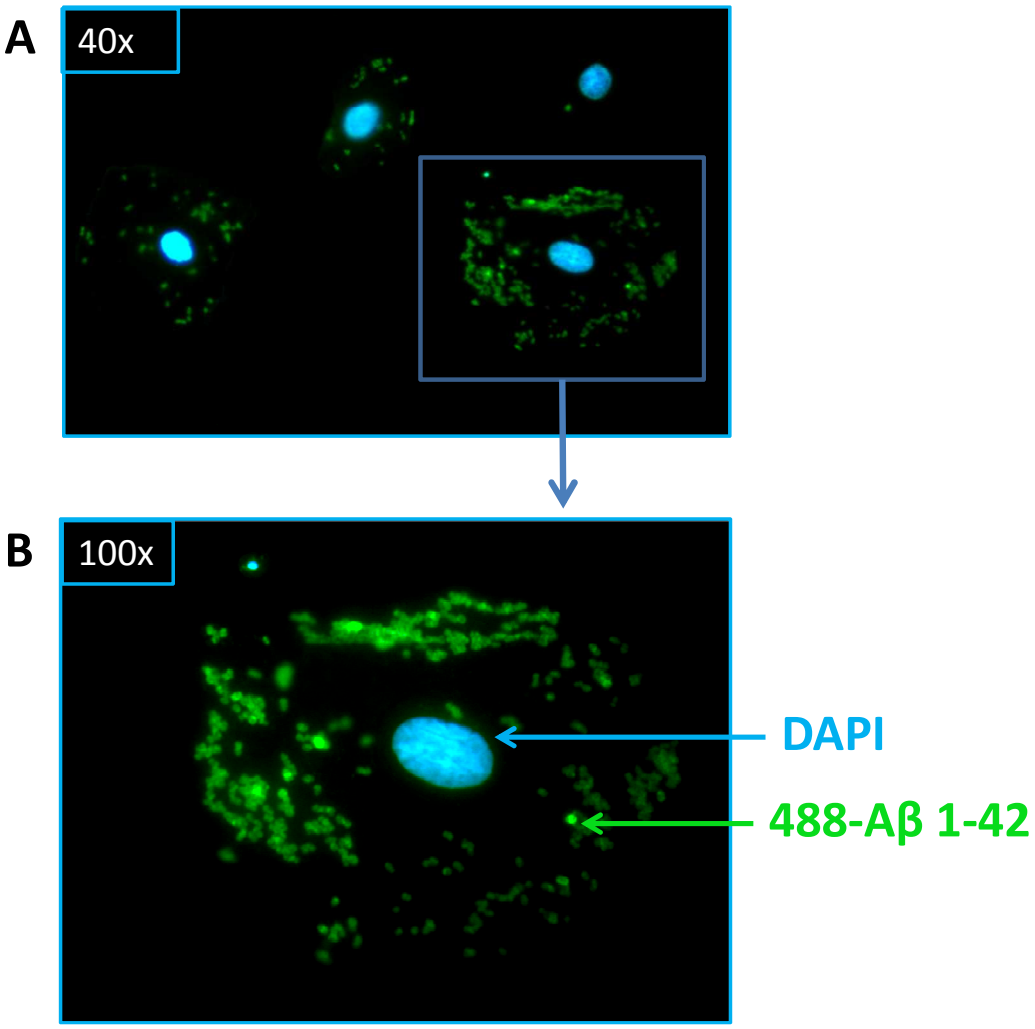

Figure 64: Detection of Aβ1-42 and nuclei in buccal cells by fluorescence microscopy.
(A) A 40x objective picture shows DAPI staining (blue) and Aβ1-42 detected by Alexa Fluor 488 secondary antibody (green). (B) The blue rectangle region was viewed with a 100x objective which shows DAPI and Alexa Fluor 488.

The same slide was then scanned by LSC to ensure that fluorescence could be detected and contoured. Figure 65 shows DAPI and Alexa Fluor 488 signals separately in black and white (Figure 65A and Figure 65B, respectively). In Figure 65C, when both signals were merged with a "shaded relief" feature (offering a view in relief of the cells by using their natural absorbance when exposed to a 488 nm laser) it could be seen that DAPI (blue) and Aβ1-42 (green) were detectable and localised in the cytoplasm of cells. A contour was set up in the LSC protocol and the same picture can be seen with magenta contour around Aβ1-42 and a blue contour around nuclei (Figure 65D). It should be noted that even if the "shaded relief" feature allows visualisation of buccal

cells it does not permit cytoplasm contouring. Therefore a cytoplasm stain was required in the staining protocol.

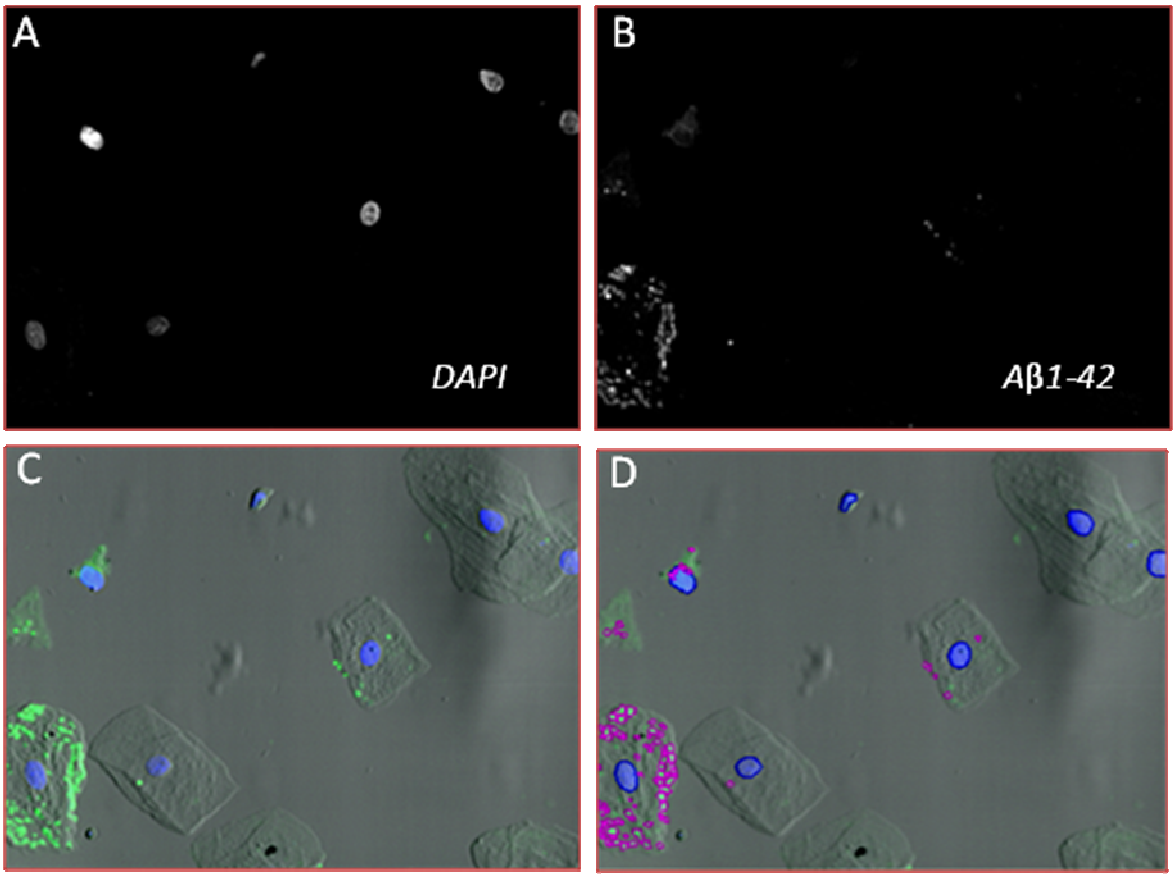

Figure 65: Aβ 1-42 detection in buccal cells by LSC.
This first LSC test shows (A) DAPI and (B) Aβ1-42 signals separately in black and white. (C) Both DAPI (blue) and Aβ1-42 (green) signals were then merged and cells could be localised by the use of the "shaded relief" feature. (D) Contours were defined in the LSC workspace to set a magenta and blue contour around Aβ1-42 and nuclei, respectively.

4.3.3.2 Testing tau antibodies

Antibodies Anti-Tau 93, DAKO A0024 and Anti-Tau BT2 were tested by immunocytochemistry. As in section "*4.3.3.1 Testing amyloid antibodies*" different antibody dilution and incubation conditions were tested. No signal could be obtained with Anti-Tau 93 and DAKO A0024. However Figure 66 shows fluorescence detected with Anti-BT2 antibody (green) and DAPI (blue). The Anti-BT2 signal though present, did not seem very strong (Figure 66A) so antigen revealing techniques were utilised such as heating or acid treatment. Only acid treatment with 88% formic acid for 5 min

considerably improved the signal (Figure 66B). A longer acid treatment up to 10 min did not further improve the signal detected. Since a cytoplasmic stain was necessary for cytoplasmic contouring and therefore high-content analysis by LSC, a Fast Green staining step was added to this immucytochemistry protocol for detection of Tau BT2 and is shown in Figure 67. Three fluorescent wavelengths for DAPI, Fast Green and Alexa Fluor 488 were detected under fluorescence microscopy and shown in Figure 67A. Since adding an extra staining step (Fast Green) might have affected the Alexa Fluor 488 antibody signal, the fluorescent microscope's filters were then set (to capture blue and green only) to demonstrate that there was no loss of Tau signal (Figure 67B).

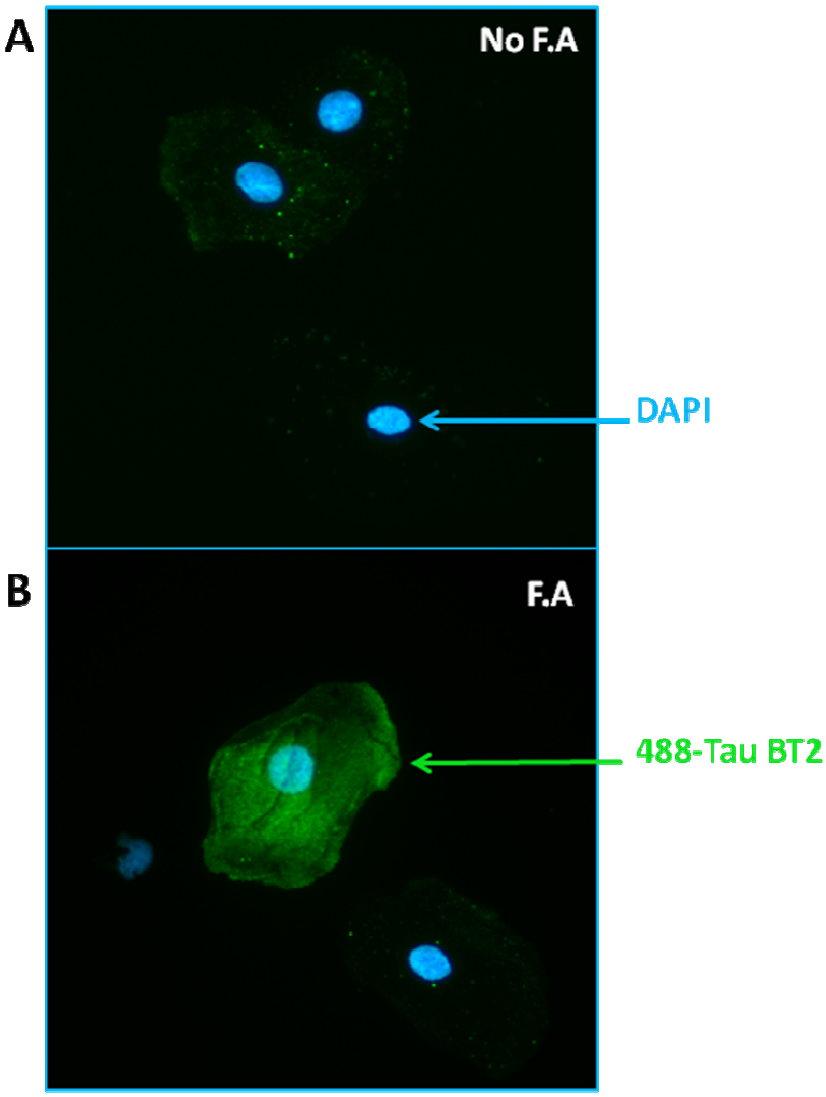

Figure 66: Tau BT2 antibody detected by Alexa Fluor 488 under fluorescence microscopy with or without formic acid treatment.
DAPI (blue) and Anti-Tau BT2 (green) signals can be seen (A) without or (B) with antigen revealing by formic acid treatment. Abbreviation; F.A, Formic acid.

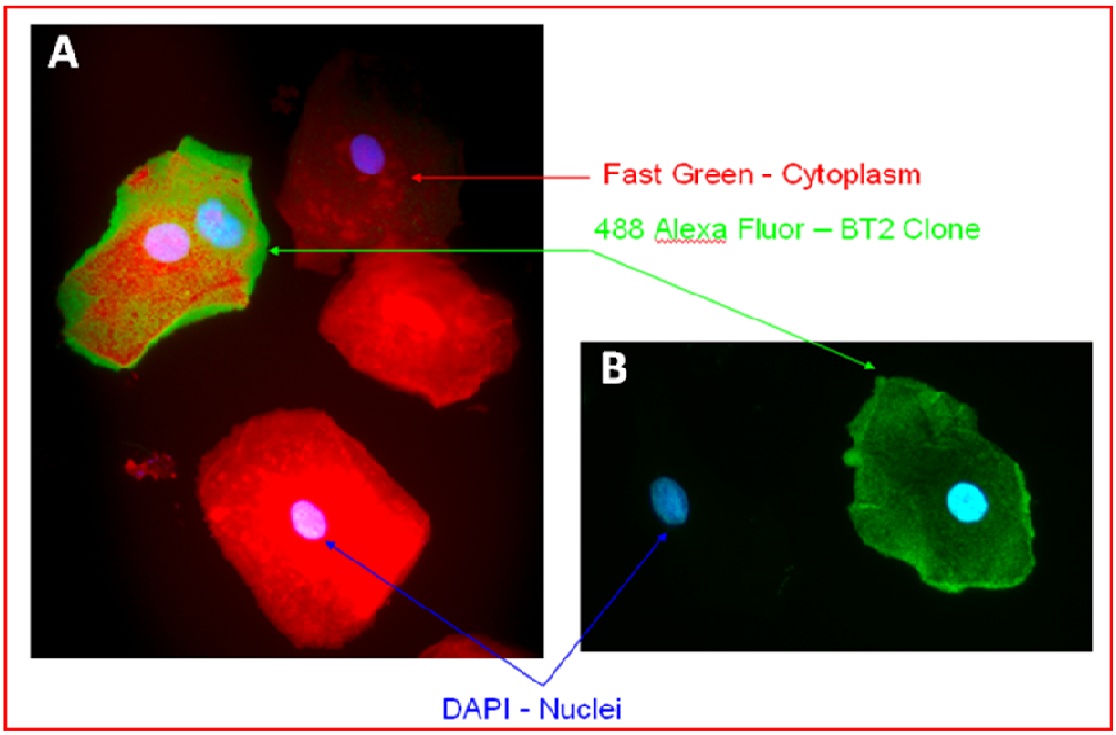

Figure 67: DAPI, Fast Green and Tau BT2 detection in buccal cells by immunofluorescence.
Fluorescence shows (A) simultaneous detection of Fast Green (red), DAPI (blue) and Tau BT2 (green) and (B) buccal cells with Tau BT2 and DAPI signals without Fast Green staining.

The same microscope slides were then scanned with LSC to ensure, that proper detection and contouring could be achieved, as done previously with Aβ1-42. Figure 68 shows a region image of several buccal cells stained with Fast Green (red), DAPI (blue) and Alexa Fluor 488 (green) with a clear cytoplasmic signal and no background. A field image is also shown in Figure 69 with proper contouring of nuclei (blue), Tau BT2 (magenta) and cytoplasm (green). Some small contoured false positives (red crosses), being cell debris, were then excluded from the analysis by using their small size as an exclusion criteria.

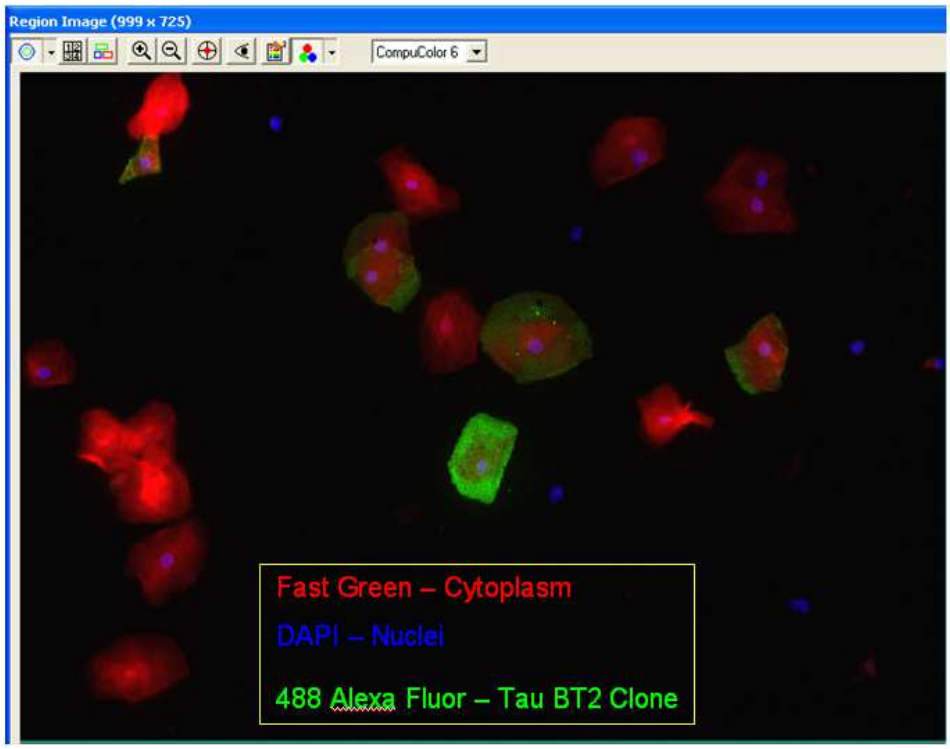

Figure 68: Region image of buccal cells scanned by LSC.
Buccal cells were stained with Fast Green (cytoplasm), DAPI (blue) and 488 Alexa Fluor (green), then scanned by LSC.

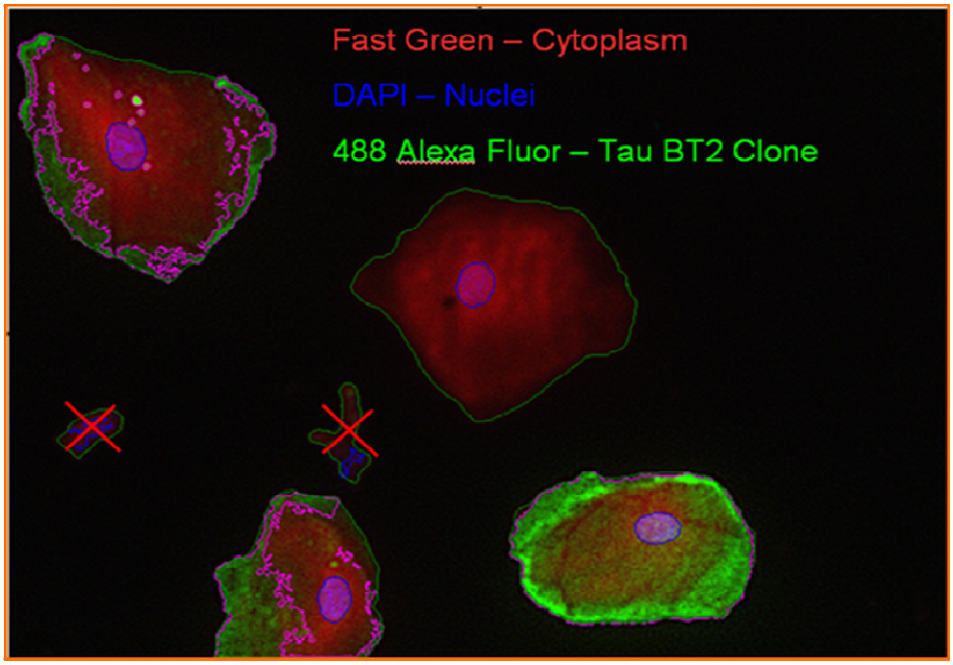

Figure 69: Field image of buccal cells scanned by LSC.
Buccal cells were stained with Fast Green (cytoplasm), DAPI (blue) and 488 Alexa Fluor (green), then scanned by LSC. Contours were then defined for nuclei (blue), Tau BT2 (magenta) and cytoplasm (green).

4.3.3.3 Testing dual antibodies staining

To detect two different proteins with antibodies it was necessary to ensure that no cross-reactivity was occuring. Therefore both of the secondary antibodies used were raised in goat and both were directed against different species. Alexa Fluor 488 was directed against mouse antibodies while Alexa Fluor 568 was directed against rabbit antibodies. To avoid any interference and properly assess both signals, buccal cells were only counterstained with DAPI and no cytoplasm stain was used in the first instance. Figure 70 shows buccal cells after a dual staining immunocytochemistry protocol.

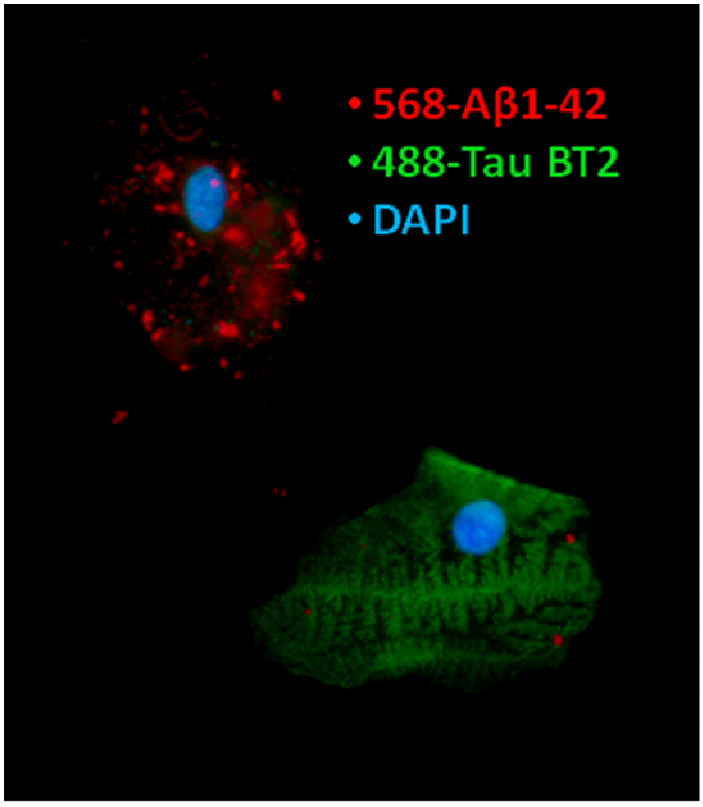

Figure 70: Detection of Tau BT2, Aβ1-42 and DAPI simultaneously in buccal cells. Alexa Fluor 568 Anti-Rabbit (red) bound to rabbit Anti-Aβ1-42 while Alexa Fluor 488 Anti-Mouse bound to mouse Anti-Tau BT2. Cells were counterstained with DAPI (blue). Both signals were specific to the buccal cell cytoplasm and exhibit very low background.

4.3.3.4 Testing dual antibodies staining combined with ORO protocol

Both antibodies (anti-Tau BT2 and anti-Aβ1-42) could be used simultaneously and the next aim was to combine this protocol with that used for neutral and cell type detection (previously used in chapter 3). To test this combination it was first attempted to stain

buccal cells with the ORO protocol from chapter 3, section "*3.2.5. Staining of slides for LSC*", after the dual antibody protocol was applied. A microscope slide was used at the same time without the added ORO protocol as a control. While the signal from the antibodies was evident in the control slide, it was difficult to detect a signal from the new protocol which combined antibody and ORO staining methods. ORO, Fast Green and DAPI stains were however stained intensely. Therefore four new conditions were tested to optimise the staining method so that all parameters could be measured simultaneously by LSC. The order of cell treatment conditions are summarised below:

1. Triton/Acid → Primary Ab → Secondary Ab → ORO → DAPI
2. Triton/Acid →Primary Ab → Secondary Ab → DAPI → Fast Green
3. ORO → Fast Green → Triton/Acid → Primary Ab → Secondary Ab → DAPI
4. Triton/Acid → ORO → Fast Green → Primary Ab → Secondary Ab → DAPI

Conditions 1 and 2 were aimed at ensuring that the decrease in the intensity of the dual antibody signal was due to ORO step only. Conditions 3 and 4 tested the hypothesis that the high-content protocol could be achieved if the ORO protocol could be included as a first step. For this sequence to be properly tested, the timing of the detergent (triton) and acid (formic) treatments had to also be tested, being either after (condition 3) or before (condition 4) ORO and Fast Green. In condition 1, ORO signal was intense but resulted in a strongly decreased intensity of both Alexa Fluor 488 and 568. Condition 2 resulted in a weak intensity of the two (secondary) antibodies. In condition 3 the secondary antibody signals were very adequate, however no ORO stain was observed. Condition 4 showed that when detergent and acid treatments were applied at the beginning of the protocol ORO and Fast Green signals were strong, and Alexa Fluor 568 binding to Anti-AB1-42 antibody was detectable, however there was little to none of the Alexa Fluor 488 binding to Anti-Tau BT2 observed. At this point the next combination tested was formic acid treatment just prior to incubation with the primary antibodies for Tau BT2 detection. The following order was tested:

Triton → ORO → Fast Green → Acid → Primary Ab → Secondary Ab → DAPI

In this new protocol tested, ORO stain was still not detectable and therefore removed by the formic acid treatment. However Alexa Fluor 488 green signal was observed. The next step was to test if a longer acid treatment of up to 10 min, allow for the Alexa Fluor 488 signal as well as allowing for the detection of neutral lipids with ORO. Therefore, the final step for development of the high-content protocol was to test whether that the primary antibody incubation step, if applied after the acid treatment, and prior to the ORO incubation step, would allow simultaneous detection of both Alexa Fluor antibodies and the other stains (ORO, Fast Green and DAPI):

Titron → Acid → Primary Ab → ORO → Fast Green → Secondary Ab → DAPI

For the purposes of demonstrating some of the staining results, both brightfield and fluorescence microscopy images were taken. Figure 71 and Figure 72 show staining of buccal cells obtained when the above sequence of steps was performed and then visualised with a 20x or 40x objective, respectively. In Figure 71A, ORO signal could be visualised under brightfield. The same field of cells can also be seen under fluorescence (Figure 71B) where a clear detection of cytoplasm (Fast Green), nuclei (DAPI), Tau (Alexa Fluor 488) and Aβ (Alexa Fluor 568) could be observed and co-localised within cells with ORO signal detected under brightfield (Figure 71A). A picture taken under fluorescence microscopy with a 40x objective is shown in Figure 72A. Since the fluorescence microscope used a single beam to excite dyes it was difficult to visually identify ORO from Aβ and Fast Green signals. However these signals were easily quantified and separated using the LSC protocols described earlier. Fast green appeared as a uniform cytoplasmic stain and by combining fluorescence with brightfield (Figure 72B) it was then possible to compare red signals obtained from Alexa Fluor 568 (Aβ) under fluorescence with ORO chromatic stain (Figure 72B).

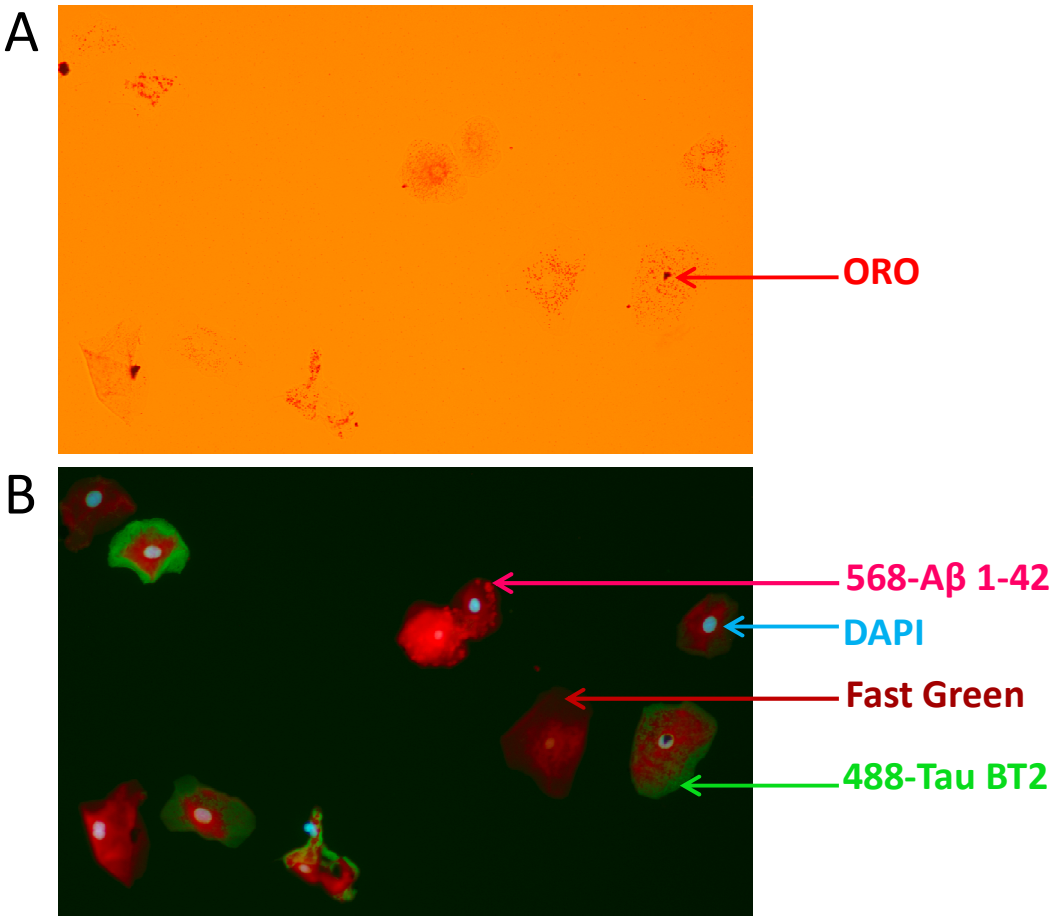

Figure 71: Buccal cells viewed with 20x objective; fluorescence microscope images. (A) Shows a brightfield image of buccal cells with ORO staining in red. (B) Shows the same image under fluorescence with DAPI (blue), Fast Green (red), Tau (green) and Aβ (intense red). Fast green and Aβ (both red) could not be easily distinguished in this fluorescence picture, however the LSC protocols could separate and quantify each of the signals easily.

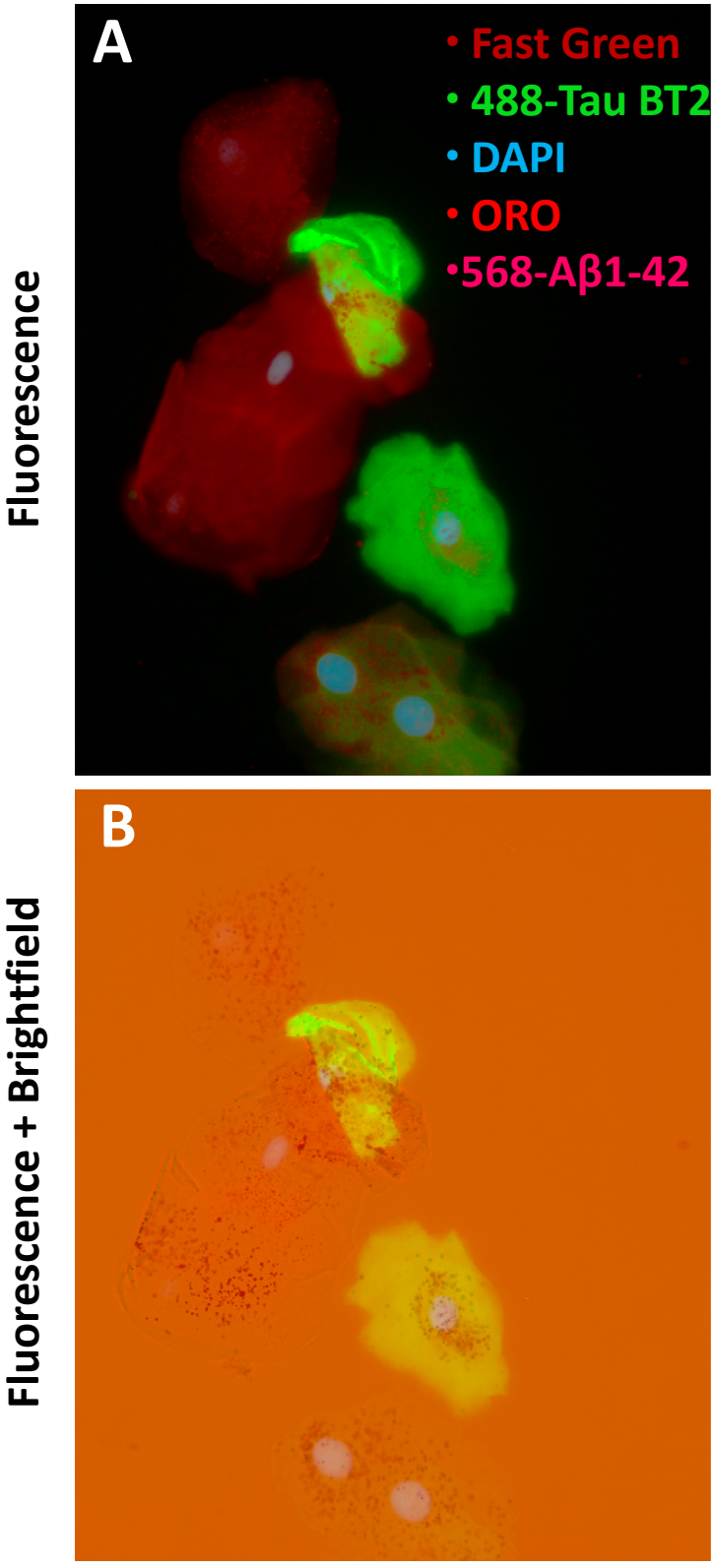

Figure 72: Buccal cells visualised under fluorescence and brightfield microscopy with a 40x objective.
(A) Buccal cells viewed with fluorescence and (B) under brightfield.

It is important to note that fluorescence microscopy was not aimed at quantifying signals within cells but simply used to assess the effectiveness of the high-content immunocytochemistry protocol. Therefore the same slide visually assessed by fluorescence microscopy was then analysed by LSC which allowed the use of excitation lasers for proper separation of signals. A region image is shown in Figure 73 for overall visualisation of the different dyes simultaneously in buccal cells with DAPI (blue), Fast Green (green), ORO (red), Aβ (magenta) and Tau (yellow).

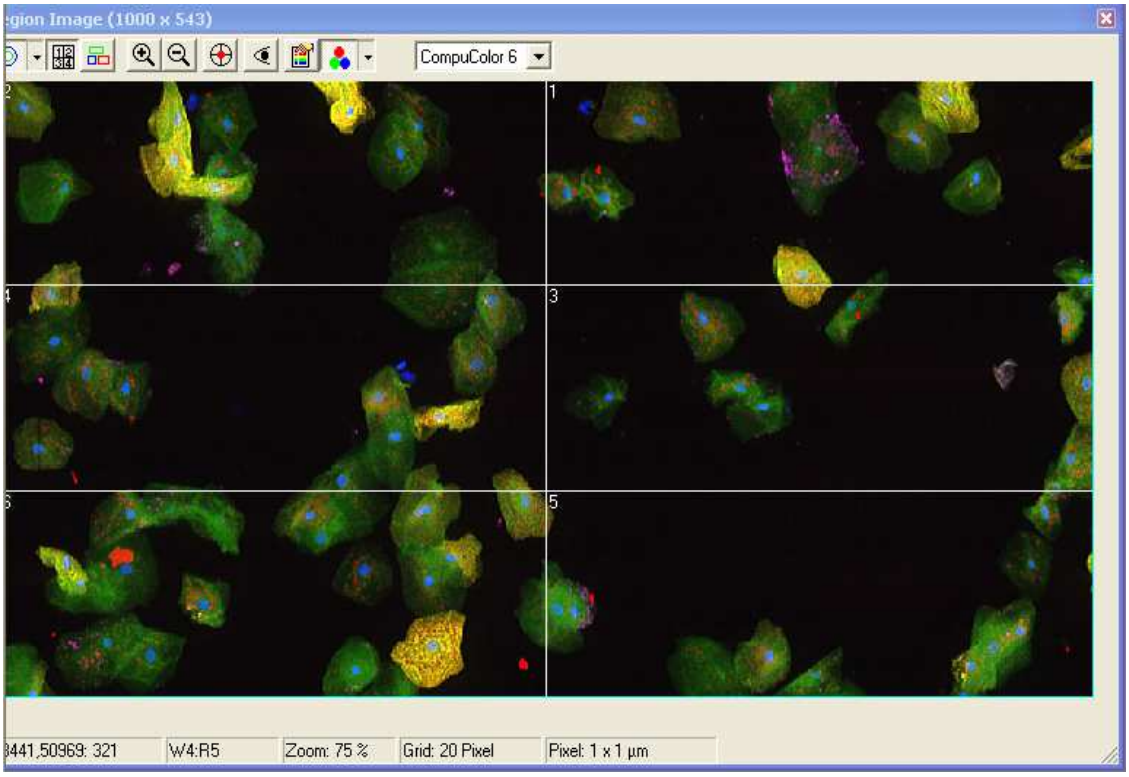

Figure 73: Region image of buccal cells scanned by LSC.
Five simultaneous signals could be visualised, DAPI (blue), Fast Green (green), ORO (red), Aβ (magenta) and Tau (yellow).

The high-content detection protocol that was developed for LSC was then applied to buccal cells of participants from the AIBL cohort for LSC analysis.

4.3.4 Laser scanning cytometry – High-content analysis

4.3.4.1 Buccal cytome

In this study the buccal cytome was also examined as in chapter 3, section "*3.3.2.1 Buccal cytome*" to investigate if this newly developed high-content protocol allowed similar separation of cell types. Figure 74 shows the frequency of the different buccal cell types. There was no significant difference observed in the several cell types scored by LSC (i.e. basal, transitional, differentiated and karyolytic cells) between control, MCI and AD groups.

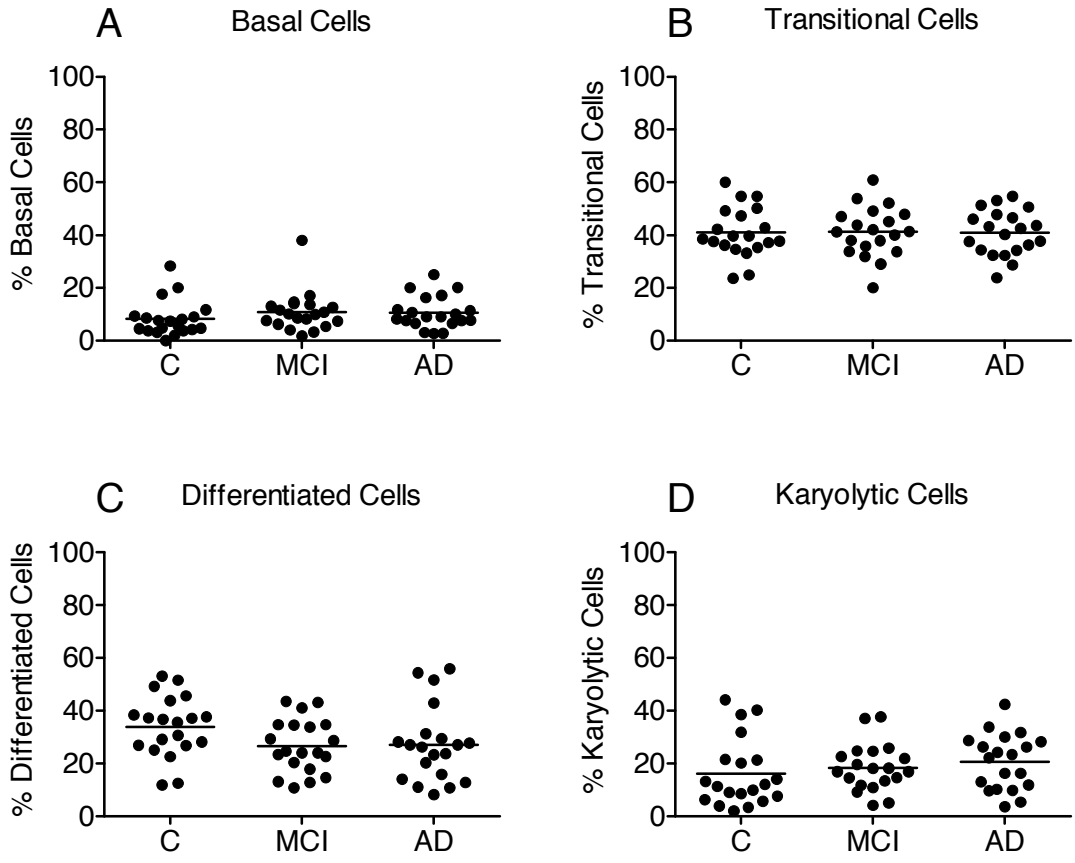

Figure 74: Buccal cytome in controls, MCI and AD.
The frequency of each of the cell types was scored for control (n=20), MCI (n=20) and AD (n=20) groups. It was then reported as a percentage of isolated single buccal cells analysed for (A) basal, (B) transitional, (C), differentiated and (D) karyolytic cells. Abbreviations; AD, Alzheimer's disease; C, Control; MCI, Mild cognitive impairment.

4.3.4.2 DNA content

DNA content was measured in all cells as well as in the different cell types, as described in chapter 3, section "*3.3.2.2 DNA content*". This high-content protocol did not show significant differences for DNA content when compared between controls, MCI and AD in all buccal cells as well as in the different cell types (Figure 75).

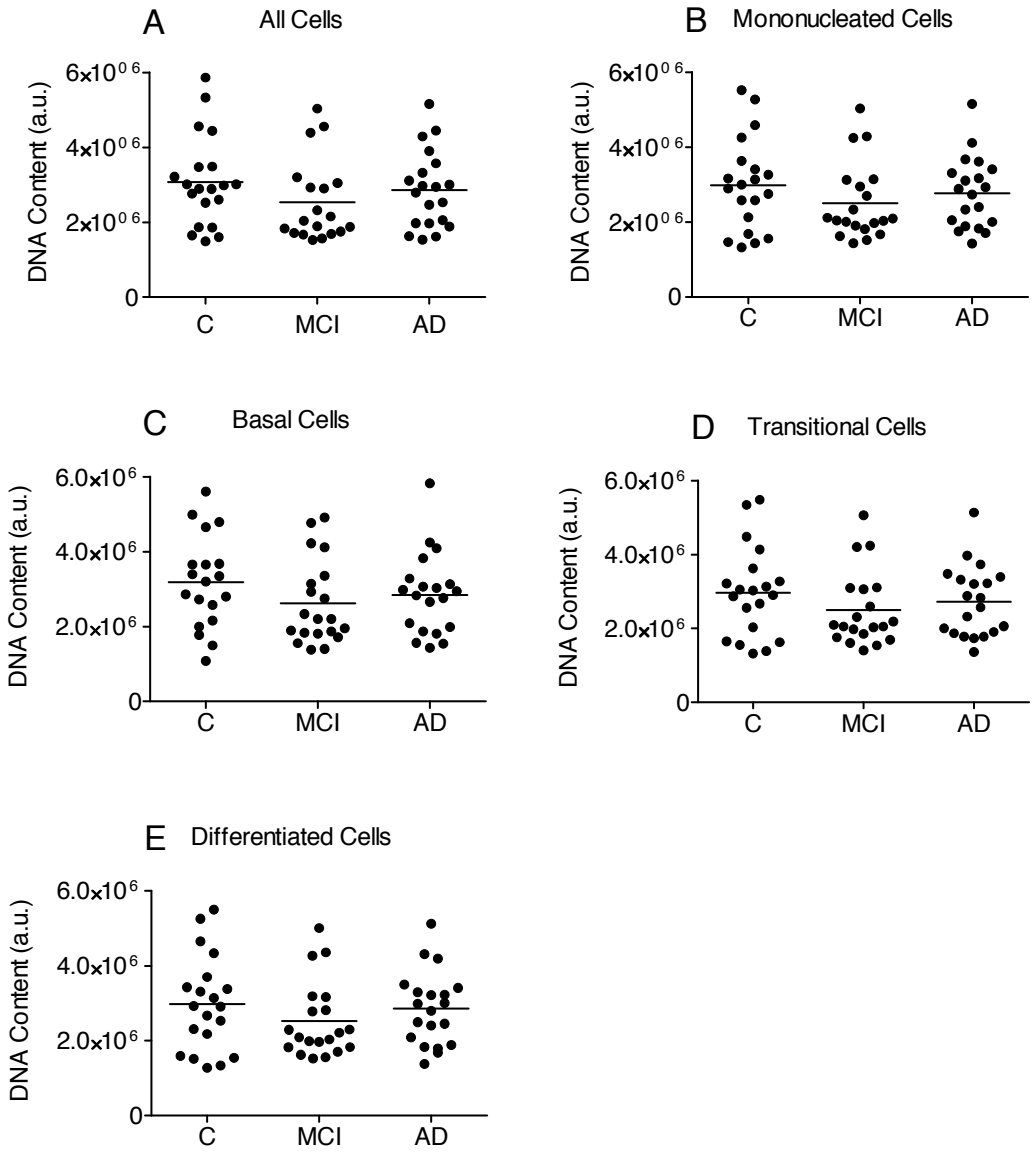

Figure 75: DNA content between control, MCI and AD groups.
DNA content was measured for control (n=20), MCI (n=20) and AD (n=20) groups in (A) all cells, (B) all isolated single cells with a nucleus, (C) basal, (D) transitional and (E) differentiated cells. Abbreviations; a.u., Arbitrary units; AD, Alzheimer's disease; C, Control; MCI, Mild cognitive impairment.

4.3.4.3 DNA content / Cell cycle

DNA content was analysed as previously carried out in chapter 3, section "*3.3.2.3 DNA Content / Cell cycle*". The percentage of nuclei in each of these peaks, i.e. <2N, 2N and >2N nuclei are shown in Figure 76. No significant difference in the percentage of nuclei within these three peaks was observed between groups. However it seems that a higher percentage of >2N nuclei compared to <2N and 2N nuclei appeared in the three groups. These percentages were summarised in Figure 76D.

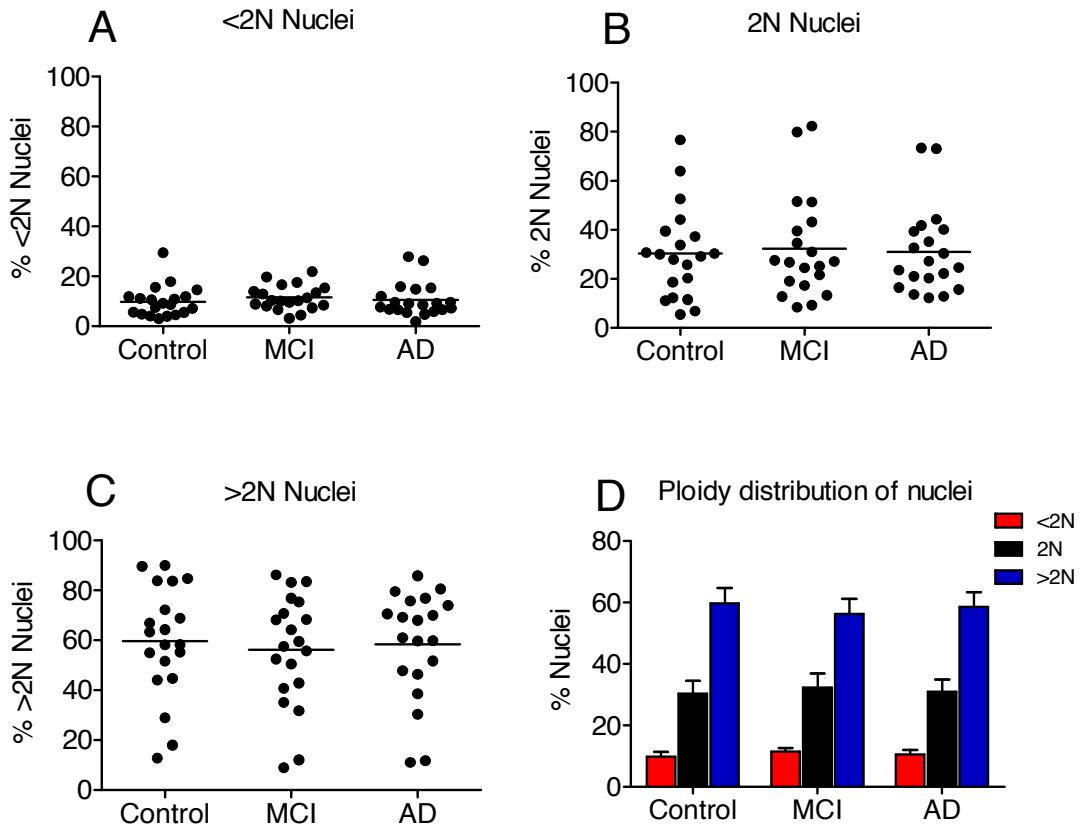

Figure 76: DNA content distribution.
The percentage of (A) <2N nuclei, (B), 2N nuclei and (C) >2N nuclei was assessed in control (n=20), MCI (n=20) and AD (n=20) groups. (D) The distribution of the three peaks, <2N, 2N or >2N is shown for controls, MCI and AD. Abbreviations; AD, Alzheimer's disease; C, Control; MCI, Mild cognitive impairment.

4.3.4.4 Circularity

Circularity of nuclei, a measure of irregular nuclear shape was also analysed with LSC as in chapter 3, section "*3.3.2.4 Circularity*". Circularity of nuclei was reported for all buccal cells as well as the different cell types as shown in Figure 77. There was no significant difference between the three groups. A linear trend test was also applied on this data set but no significance was observed.

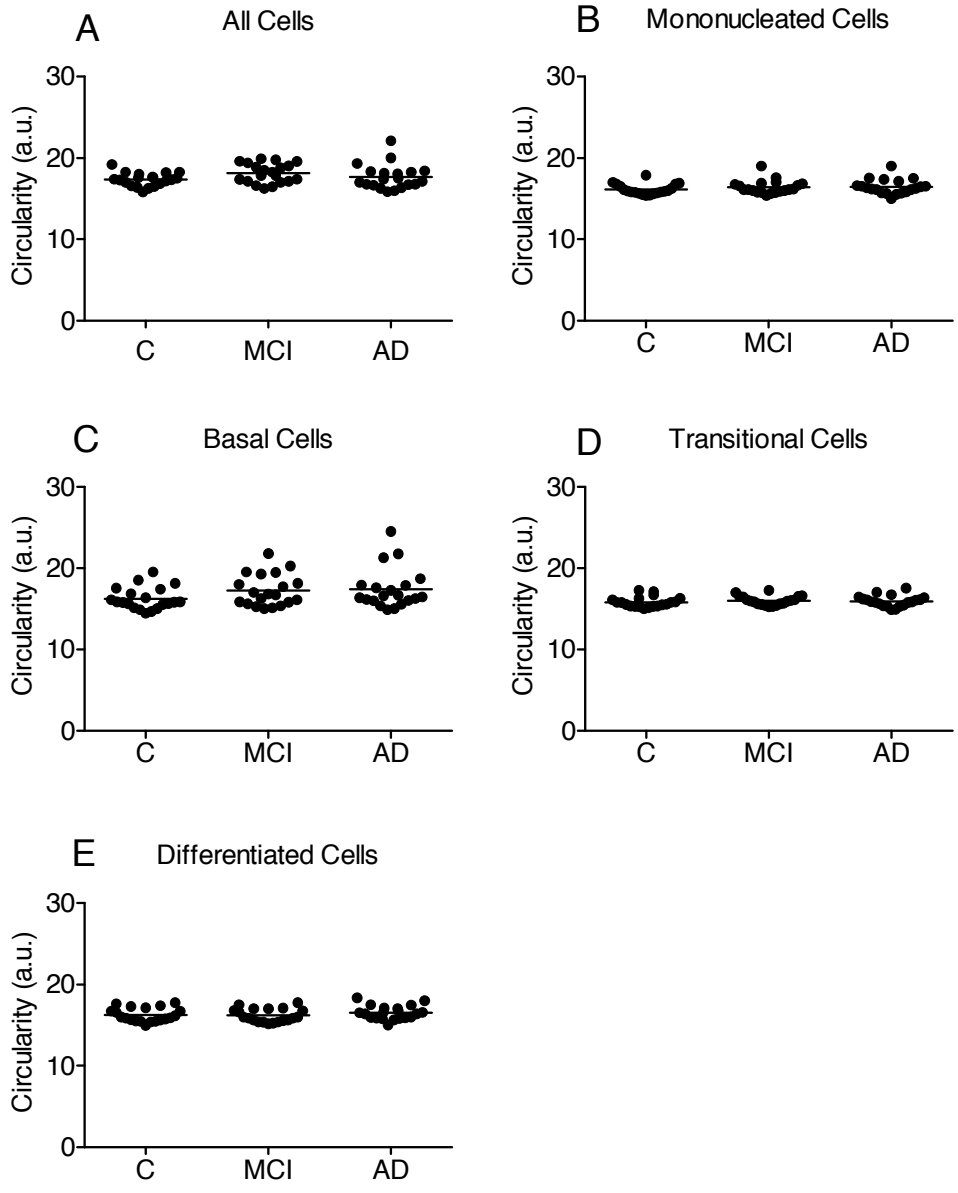

Figure 77: Circularity of nuclei measured in buccal cells between controls, MCI and AD.

Circularity of nuclei was measured for control (n=20), MCI (n=20) and AD (n=20) groups in (A) all cells, (B) all isolated single cells with a nucleus, (C) basal, (D) transitional and (D) differentiated. Abbreviations; a.u., Arbitrary units; AD, Alzheimer's disease; C, Control; MCI, Mild cognitive impairment.

4.3.4.5 Fast Green Integral and DNA MaxPixel

Fast Green Integral and DNA MaxPixel were measured as in chapter 3, section "*3.3.2.9 Fast Green – Cytoplasmic stain*" and section "*3.3.2.5 Nuclei Area and DNA MaxPixel*", respectively. The total amount of Fast Green fluorescence (Fast Green Integral) was quantified by LSC and shown in Figure 78A. No significant difference was observed, however a slight decrease of the Fast Green signal measured in buccal cells was observed in AD when compared to controls and MCI. Figure 78B shows the mean highest pixel values of nuclei (MaxPixel) measured by LSC between control, MCI and AD groups. No significant differences were observed between the three groups.

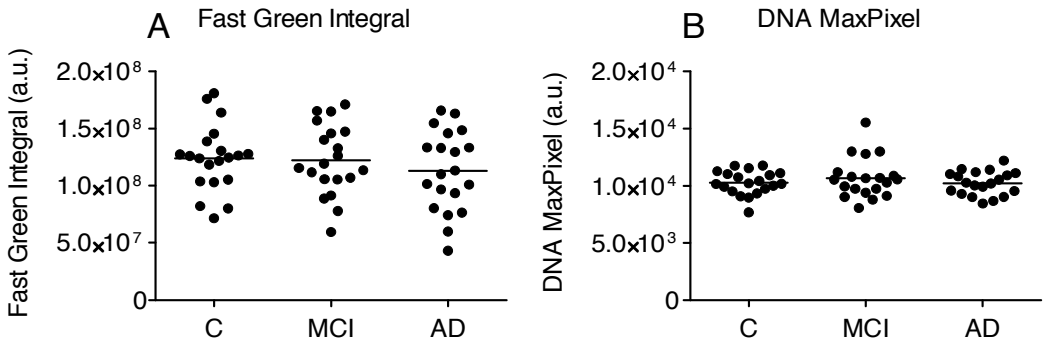

Figure 78: Fast Green Integral and DAPI MaxPixel between control, MCI and AD groups.

(A) Fast Green Integral and (B) DNA MaxPixel were measured by LSC for control (n=20), MCI (n=20) and AD (n=20) groups. Abbreviations; a.u., Arbitrary units; AD, Alzheimer's disease; C, Control; MCI, Mild cognitive impairment.

4.3.4.6 Neutral lipids

ORO staining was quantified as in chapter 3, section "*3.3.2.6 Neutral lipids*" by measuring the ORO_{Area} / $Cytoplasm_{Area}$ expressed in percentage for all cells as well as the different isolated cell types. This ratio was compared between control, MCI and AD groups and is shown in Figure 79. There was no significant difference observed between the three groups in all buccal cells as well as the different cell types. However basal cells had the highest proportion of ORO staining compared with the other cell types and mean values were marginally higher for MCI and AD relative to controls (Figure 79C).

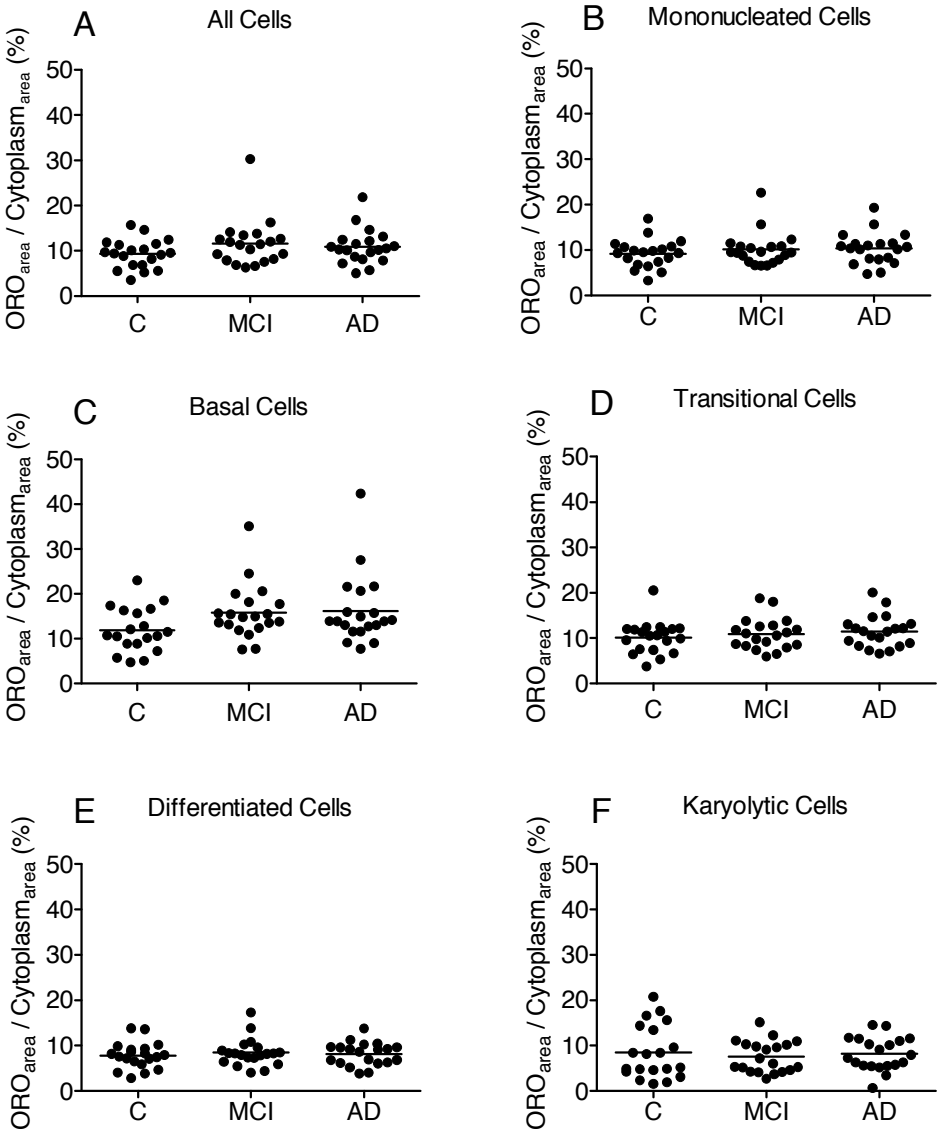

Figure 79: Neutral lipid content in buccal cells and their different cell types.
Neutral lipid content was measured for control (n=20), MCI (n=20) and AD (n=20) groups in (A) all cells, (B) all isolated single cells with a nucleus, (C) basal, (D) transitional, (E) differentiated and (F) karyolytic cells. Abbreviations; AD, Alzheimer's disease; C, Control; MCI, Mild cognitive impairment.

4.3.4.7 Amyloid-β

Aβ1-42 was measured in buccal cells by immunocytochemistry with a labeling secondary antibody Alexa Fluor 568 as described in section "*4.2.6.2 Staining procedures for LSC*". Several different Aβ parameters were measured by LSC (including % cells with Aβ, Aβ Area, Aβ signal Integral (intensity of the signal) and Count (frequency of signals)) in all cell types (All cells) and/or in all single isolated cells with a nucleus (mononucleated cells), basal, transitional, differentiated and karyolytic cells.

4.3.4.7.1 Distribution of Aβ in buccal cells

Buccal cells were separated between those with Aβ signal and those absent of Aβ signal. The percentage of cells with Aβ was then reported for all single cells as well as each cell type analysed (Figure 80). There was a significant increase of Aβ in buccal cells from AD compared with controls ($P<0.05$) in all nucleated single cells (Figure 80A). Similarly, an increase of Aβ was observed in transitional (Figure 80C) and differentiated cells (Figure 80D). No significant difference between AD and controls was observed in basal (Figure 80B) and karyolytic cells (Figure 80E). Additionally, a significant increase in the linear trend across the groups (i.e. AD>MCI>control) was observed in mononucleated, transitional and karyolytic cells ($P<0.05$) as well as in differentiated cells ($P<0.01$).

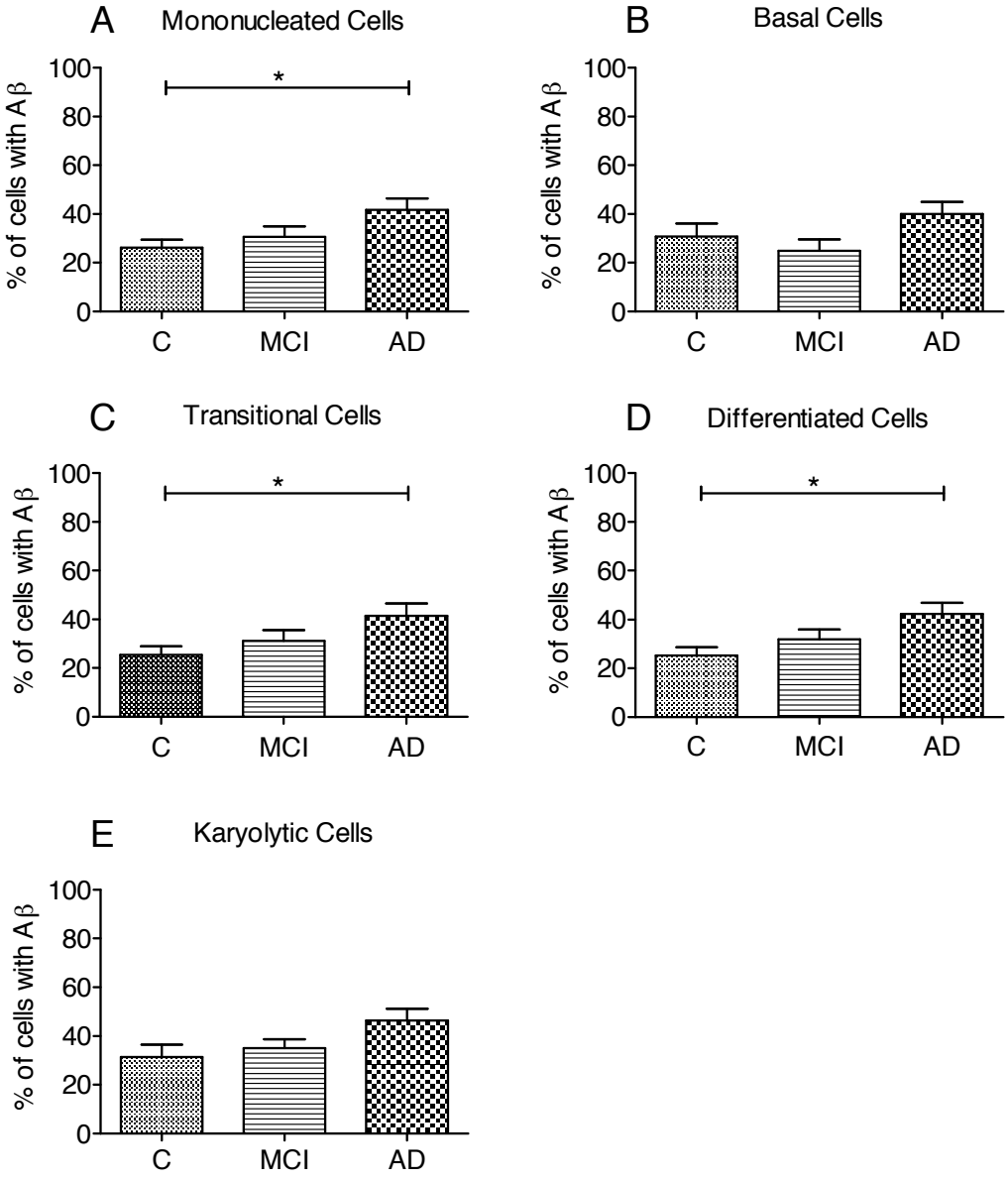

Figure 80: Frequency of buccal cells with Aβ signal in control, MCI and AD groups.

The percentage of cells exhibiting Aβ signals was reported for control (n=20), MCI (n=20) and AD (n=20) groups in (A) all isolated single cells with a nucleus, (B) basal, (C) transitional, (D) differentiated and (E) karyolytic cells. Data are mean ± SEM. Abbreviations; Aβ, Amyloid-β; AD, Alzheimer's disease; C, Control; MCI, Mild cognitive impairment; *, $P<0.05$.

4.3.4.7.2 Count/number

The percentage of cells with Aβ signal was observed to significantly increase in AD compared to controls. Therefore a further investigation was required to determine whether there was more Aβ signal present within cells by quantifying the average "count" (number) of Aβ events (foci) per cell. There was a significant higher quantity of Aβ events scored in all cells (Figure 81A), mononucleated cells (Figure 81B) and transitional cells (Figure 81D) when comparing AD versus controls ($P<0.05$) with a concomitant increase in the linear trend across the groups, i.e. AD>MCI>control ($P<0.01$). When examining basal cells (Figure 81C), a significant (2-fold) difference was found between MCI and AD groups ($P<0.05$) whilst no difference was found when comparing AD with controls. Differentiated cells (Figure 81E) from the AD group had a significantly higher (approximately 2-fold) Aβ count compared with controls ($P<0.05$) with a linear trend for an increase across the groups, i.e. AD>MCI>control ($P<0.05$). However karyolytic cells (Figure 81F) did not show significant differences or linear trend between the three groups for number of Aβ events per cell.

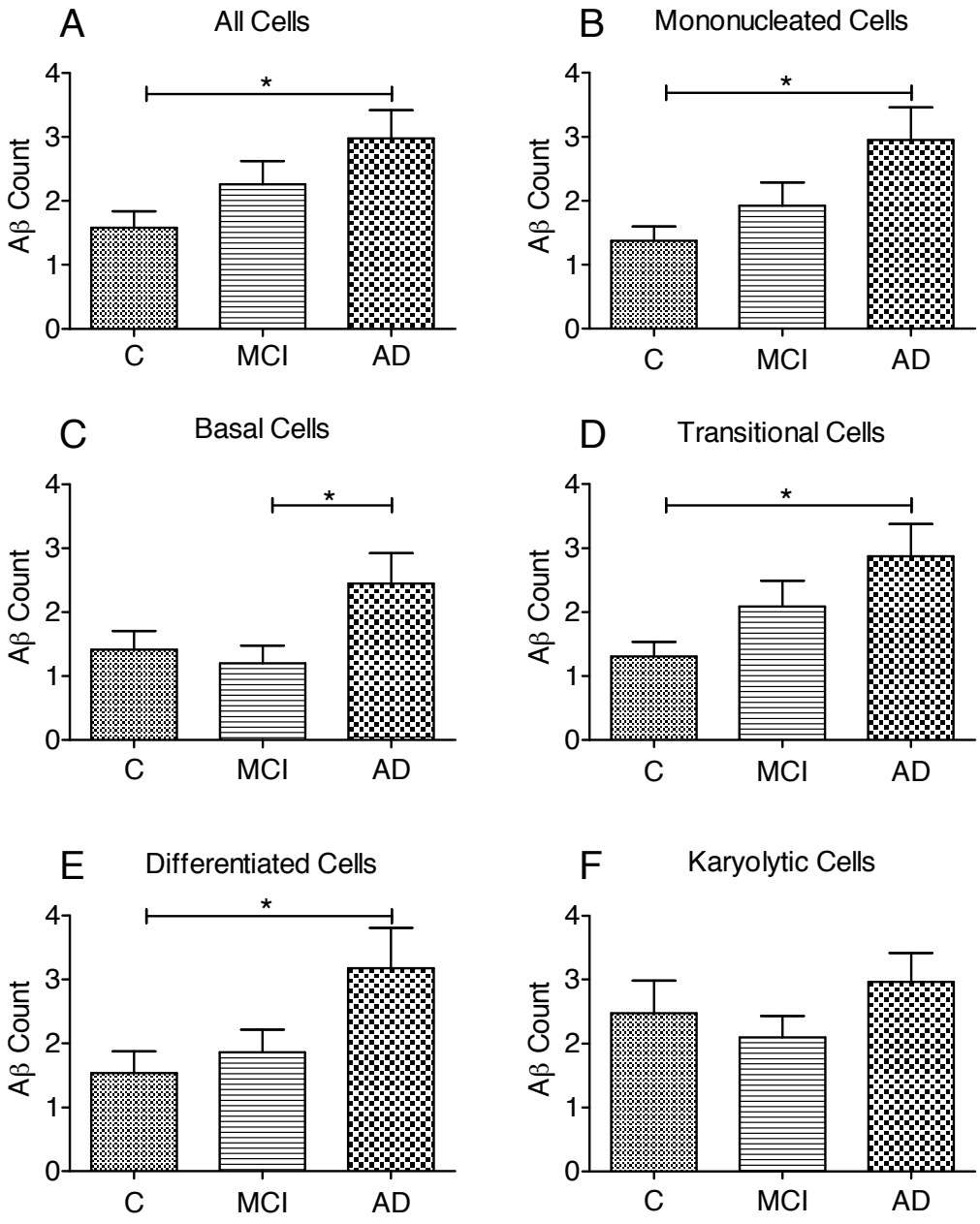

Figure 81: Average number of Aβ events scored in all buccal cells and different cell types.

The frequency of Aβ events is reported for control (n=20), MCI (n=20) and AD (n=20) groups in (A) all cells, (B) all isolated single cells with a nucleus, (C) basal, (D) transitional, (E) differentiated and (F) karyolytic cells. Abbreviations; Aβ, Amyloid-β; AD, Alzheimer's disease; C, Control; MCI, Mild cognitive impairment; *, $P<0.05$.

4.3.4.7.3 Integral of Aβ in buccal cells

To investigate if Aβ signals were in fact more intense in buccal cells of MCI and AD compared to controls, the Integral (total amount of fluorescence) of Aβ events per cell was quantified by LSC and reported in Figure 82. The Aβ Integral when measured in all cells (Figure 82A) or mononucleated cells (Figure 82B) was found to be significantly higher (approximately 3- and 4.5-fold, respectively) in AD compared to controls ($P<0.01$) and associated with a linear trend for an increase across groups, i.e. AD>MCI>controls ($P<0.01$). Although basal cells (Figure 82C) and karyolytic cells (Figure 82F) had a higher Aβ Integral in AD compared with controls, there was no statistically significant difference in Aβ Integral in these cell types between groups , but an increase in the linear trend was observed in basal cells ($P<0.05$). Figure 82D and Figure 82E shows a significant (approximately 3.5- and 4.5-fold, respectively) higher Aβ Integral between AD and controls ($P<0.05$) in transitional and differentiated cells, respectively. A linear trend across groups was also observed in these two cell types (transitional and differentiated) between the three groups ($P<0.05$).

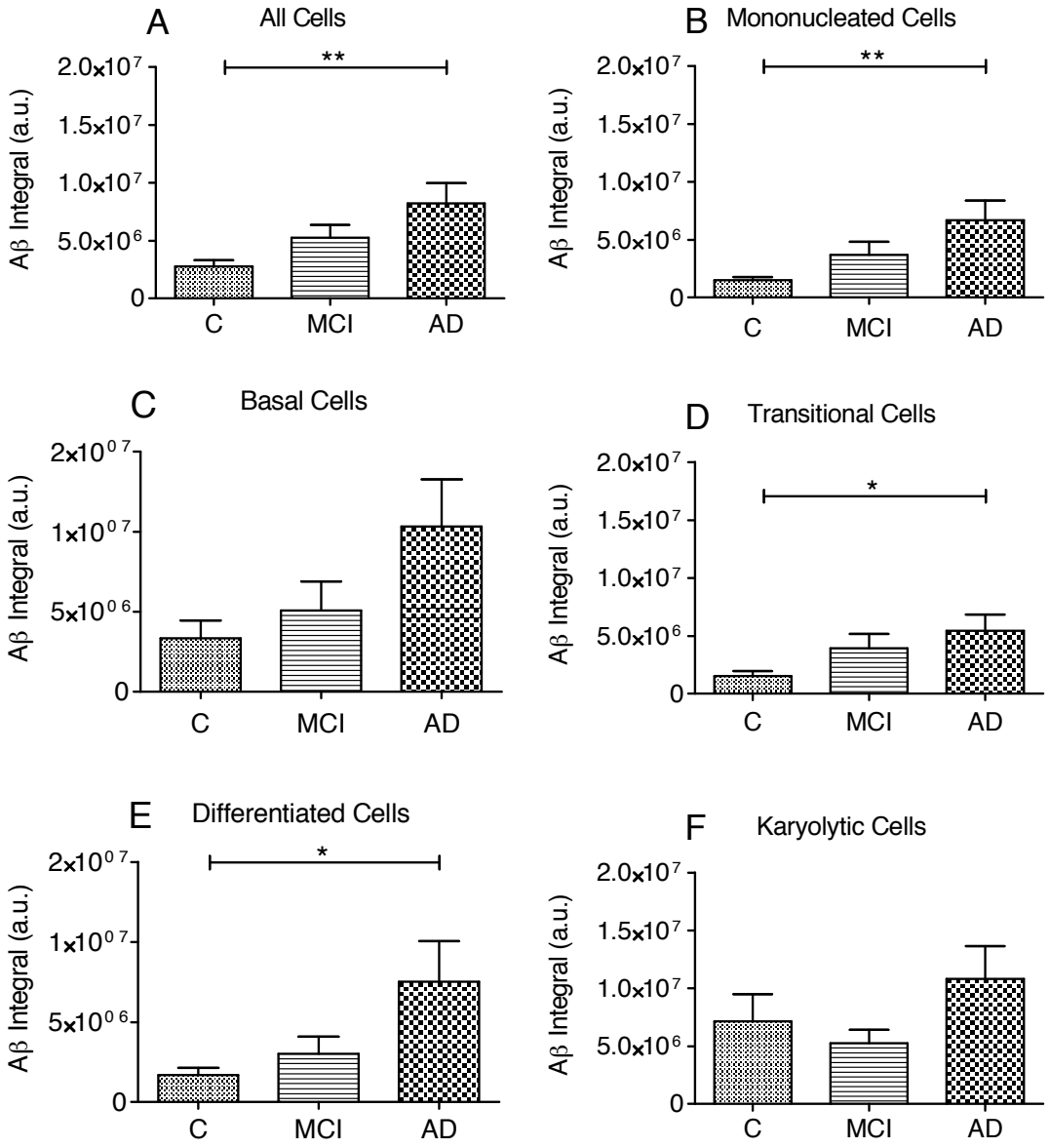

Figure 82: Total fluorescence Integral of Aβ events quantified in buccal cells between control, MCI and AD groups.

The total amount of fluorescence of Aβ events was obtained by measuring the fluorescence Integral for control (n=20), MCI (n=20) and AD (n=20) groups in (A) all cells, (B) all isolated single cells with a nucleus, (C) basal, (D) transitional, (E) differentiated and (F) karyolytic cells. Abbreviations; a.u., Arbitrary unit; Aβ, Amyloid-β; AD, Alzheimer's disease; C, Control; MCI, Mild cognitive impairment; *, P<0.05; **, P<0.01.

4.3.4.7.4 Area of Aβ in buccal cells

To test whether the higher number of Aβ events (foci) observed in buccal cells of AD compared to controls (as shown in section "*4.3.4.7.2 Count/number*") was not due to larger but less frequent Aβ signals in controls than AD; the average area of each Aβ signal was quantified within cells (Figure 83). There was a significantly higher area of events in AD compared to controls ($P<0.05$) when observed in all cells (2.5-fold), isolated single cells with one nucleus (3.5-fold), basal cells (4-fold), transitional cells (3-fold) and differentiated cells (3.5-fold) as shown in Figure 83. However, karyolytic cells (Figure 83F) did not exhibit a significant difference in Aβ area between groups. When tested, an increase in the linear trend was observed across the groups (i.e. AD>MCI>control) in all cells and mononucleated cells ($P<0.001$) as well as in basal, transitional and differentiated cells ($P<0.05$), whilst no linear trend was found in karyolytic cells.

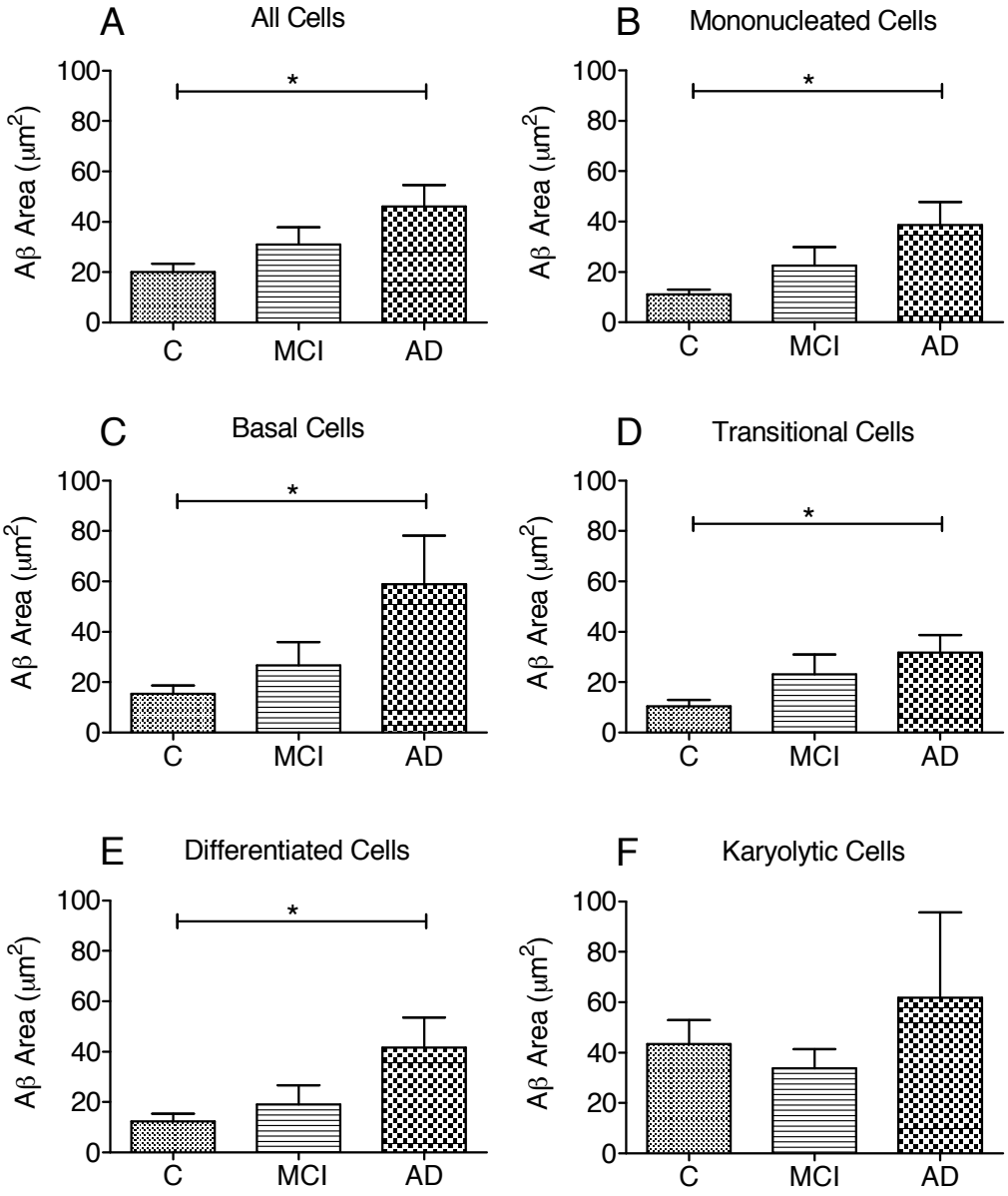

Figure 83: Area of Aβ events in all cells and different cell types.
Area of Aβ events was measured for control (n=20), MCI (n=20) and AD (n=20) groups in (A) all cells, (B) all isolated single cells with a nucleus, (C) basal, (D) transitional, (E) differentiated and (F) karyolytic cells. Abbreviations; Aβ, Amyloid-β; AD, Alzheimer's disease; C, Control; MCI, Mild cognitive impairment; *, $P<0.05$.

4.3.4.7.5 Receiver-operating characteristic curves

Since the Aβ signal was significantly higher in AD compared with controls groups, ROC curves were generated, as described in chapter 3, section "*3.3.2.11 Receiver-operating characteristic curves*", to determine the diagnostic value of this parameter to distinguish AD from controls. ROC curves were generated for the following parameters analysed; Aβ area, Aβ Integral and Aβ count. Figure 84 shows the different ROC curves. P-values and AUC were for Aβ Area (P=0.023; AUC = 0.71), Aβ Integral (P=0.008; AUC = 0.74) and Aβ Count (P=0.017; AUC = 0.72).

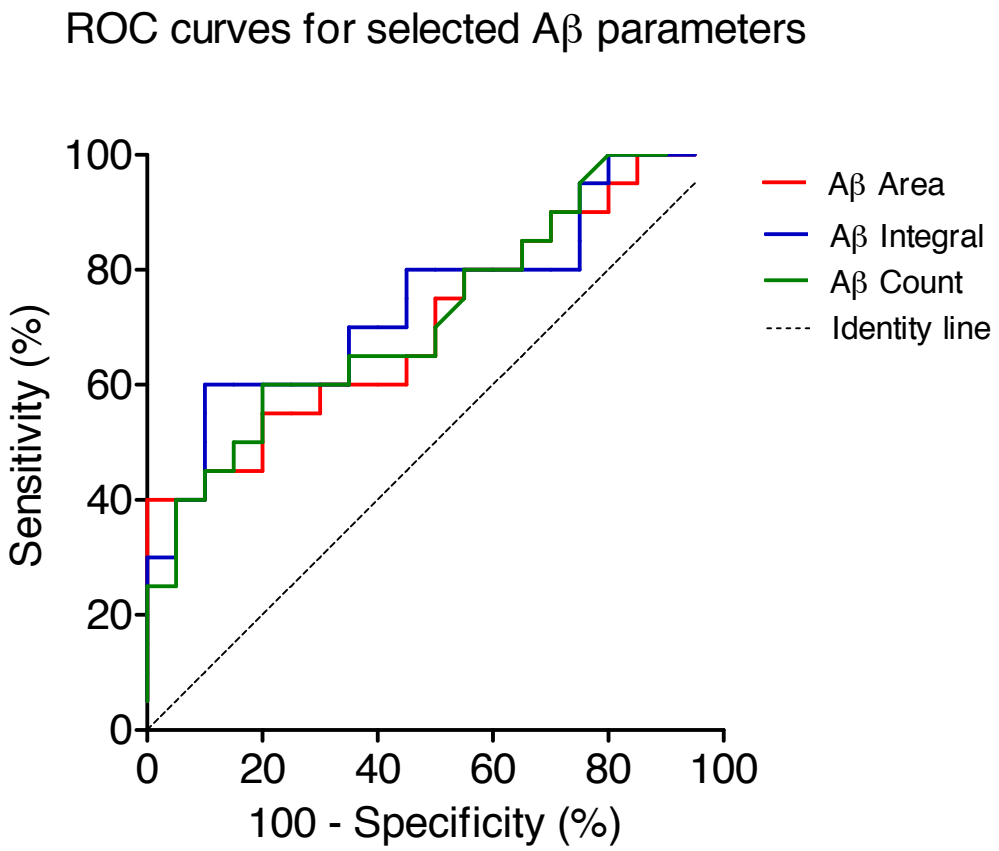

Figure 84: ROC curves for selected Aβ parameters for controls and AD.
The ROC curves were generated for Aβ area, Aβ Integral and Aβ count parameters analysed in buccal cells between control and AD groups. Abbreviations; Aβ, Amyloid-β; ROC, Receiver-operating characteristic.

4.3.4.7.6 Amyloid-β and AIBL parameters

To ensure that differences observed in Aβ were not due to the age difference between control and AD groups (see section "*4.2.1 Human ethics*", Table 10), a correlation test was performed between age of participants and Aβ Integral measured in all cells and no correlation was observed (r = 0.127, P=0.331). To investigate if Aβ measurements in buccal cells were related to the advancement in cognitive decline of subjects, correlations were tested between Aβ Integral and MMSE scores (Figure 85). Since from the Aβ parameters measured by LSC, Aβ Integral reached the strongest significant difference between AD and controls (P<0.01) and that Aβ Integral directly relates to the total quantity of Aβ in buccal cells, therefore Aβ Integral in all cells was selected for investigating correlations with MMSE scores.

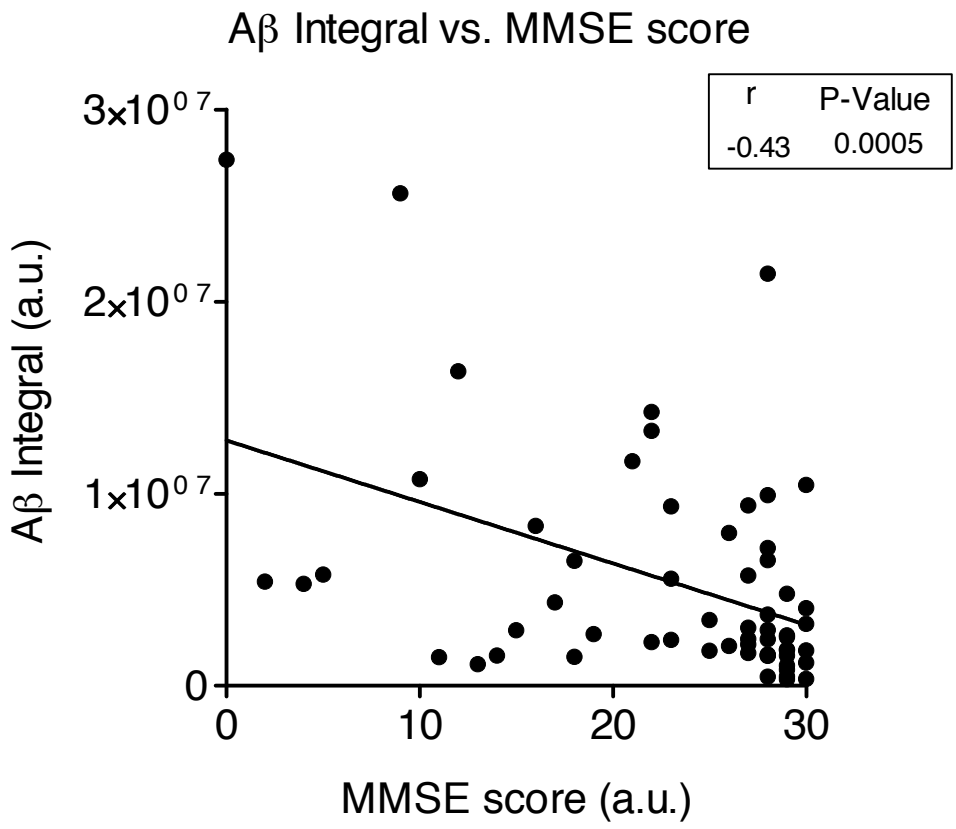

Figure 85: Correlation between Aβ Integral in all buccal cells and MMSE scores for all 60 subjects.

When both Aβ Integral in all cells and MMSE scores are plotted on a graph a weak correlation is observed (r = -0.43, P=0.0005). Abbreviations; a.u., Arbitrary units; Aβ, Amyloid-β; MMSE, Mini mental state examination.

Additionally, many parameters have been analysed on the AIBL cohort in previous studies and stored in the AIBL database. Data available for these 60 participants have been extracted from the database and correlation tests were carried out between each of these parameters and Aβ Integral measurements in buccal cells obtained in this study. Table 13 summarises the r and P-values obtained for each of the parameters examined and the following were found to be correlated with Aβ in buccal cells i.e. MMSE, Homocysteine, Pl Calcium, Pl HDL, Pl Urea, Creatinine, Pl Albumin, White cell count, Monocyte count, and Eosinophil count.

Table 13: Summary of correlations tested between Aβ Integral in buccal cells and measurements available from the AIBL database.
P-Value was accepted at P<0.05.

Parameter	Pearson r	CI	P-value
Age	0.127	-0.13 to 0.369	ns
MMSE	-0.434	-0.619 to -0.202	0.0005 ***
BMI	0.058	-0.223 to 0.331	ns
Pl Albumin	-0.374	-0.591 to -0.107	0.0075 **
Pl Total protein	0.059	-0.223 to 0.332	ns
Homocysteine	0.284	0.006 to 0.521	0.045 *
Serum Folate	-0.052	-0.326 to 0.229	ns
Red Blood Cell Folate	0.005	-0.283 to 0.273	ns
Serum B12	0.059	-0.222 to 0.332	ns
Insulin	0.116	-0.382 to 0.167	ns
Pl Glucose	-0.098	-0.185 to 0.366	ns
Pl Cholesterol	-0.154	-0.414 to 0.130	ns
Pl Triglyceride	-0.121	-0.386 to 0.163	ns
Pl HDL	-0.301	-0.535 to -0.025	0.033 *
Pl LDL	-0.013	-0.298 to 0.266	ns
Pl Bilirubin	0.016	-0.263 to 0.293	ns
Pl Urea	0.333	0.060 to 0.559	0.018 *
Pl Creatinine	0.430	0.173 to 0.633	0.0018 **

eGFR	-0.221	-0.470 to 0.061	ns
Pl Calcium	0.368	0.188 to 0.587	0.0085 **
Pl Mg	-0.083	-0.353 to 0.200	ns
Pl Fe	-0.148	-0.409 to 0.135	ns
Tansferrin	-0.241	-0.487 to 0.039	ns
Trf sat	-0.051	-0.325 to 0.230	ns
Serum Ferritin	0.199	-0.083 to 0.453	ns
Cer	-0.273	-0.513 to 0.005	ns
ALT	-0.079	-0.352 to 0.287	ns
AP	0.038	-0.251 to 0.306	ns
GGT	-0.094	-0.363 to 0.189	ns
Testosterone	0.215	-0.069 to 0.468	ns
LH	-0.062	-0.334 to 0.220	ns
FT3	-0.039	-0.314 to 0.241	ns
FT4	-0.053	-0.327 to 0.228	ns
AST	0.065	-0.217 to 0.337	ns
TSH	-0.044	-0.3186 to 0.237	ns
PCV	0.133	-0.148 to 0.394	ns
Haemoglobin	0.108	-0.172 to 0.373	ns
RCC	0.132	-0.149 to 0.393	ns
MCV	-0.055	-0.326 to 0.223	ns
MCH	-0.105	-0.369 to 0.176	ns
MCHC	-0.104	-0.369 to 0.176	ns
RDW	0.021	-0.256 to 0.294	ns
ESR	0.224	-0.057 to 0.473	ns
Plt	0.071	-0.208 to 0.340	ns
MPV	0.097	-0.183 to 0.362	ns
WCC	0.309	0.036 to 0.539	0.027 *
Neutrophils	0.245	-0.032 to 0.488	ns
Lymphocytes	0.067	-0.212 to 0.336	ns

Monocytes	0.375	0.111 to 0.590	0.006 **
Eosinophils	0.385	0.122 to 0.597	0.005 **
Basophils	0.021	-0.256 to 0.295	ns

Abbreviations:
ALT, Alanine aminotransferase; **AP**, Alkaline phosphatase; **AST**, Aspartate aminotransferase; **BMI**, Body mass index; **Cer**, Ceruloplasmin; **CI**, Confidence interval; **eGFR**, Estimated glomerular filtration rate; **ESR**, Erythrocyte sediment rate; **Fe**, Iron; **FT3**, Free thyroxine; **FT4**, Free triodothyronine; **GGT**, Gamma-glutamyl transferase; **HDL**, High-density lipoprotein; **LDL**, Low-density lipoprotein; **LH**, Leutenizing hormone; **MCH**, Mean cell hematocrit; **MCHC**, Mean corpuscular haemoglobin concentration; **MCV**, Mean corpuscular volume; **Mg**, Magnesium; **MMSE**, Mini mental state examination; **MPV**, Mean platelet volume; **ns**, Not significantly different; **PCV**, Pack cell volume; **Pl**, plasma; **Plt**, Platelet count; **RCC**, Red blood cell count; **RDW**, Red cell volume distribution; **Trf sat**, Tranferrin saturation; **TSH**, Thyroid stimulation hormone; **WCC**, White cell count.

4.3.4.8 Tau in buccal cells

As described in chapter 3, section "*4.2.6.2 Staining procedures for LSC*", Tau protein within buccal cells was measured with LSC by quantifying the fluorescence emitted from Alexa Fluor 488 secondary antibody. The following parameters were reported; i) the percentage of cells with Tau signal, ii) the area (μm^2) iii) the Integral of Tau events within all buccal cells. Since Tau events were large and often covering the entire cytoplasm area as opposed to Aβ spots which were typically smaller spots, the number of Tau events was not considered relevant and therefore not reported here.

4.3.4.8.1 Distribution of Tau in buccal cells

Figure 86 shows the percentage of buccal cells with Tau signal detected within them in the different cell types. No significant difference was found between control, MCI and AD groups.

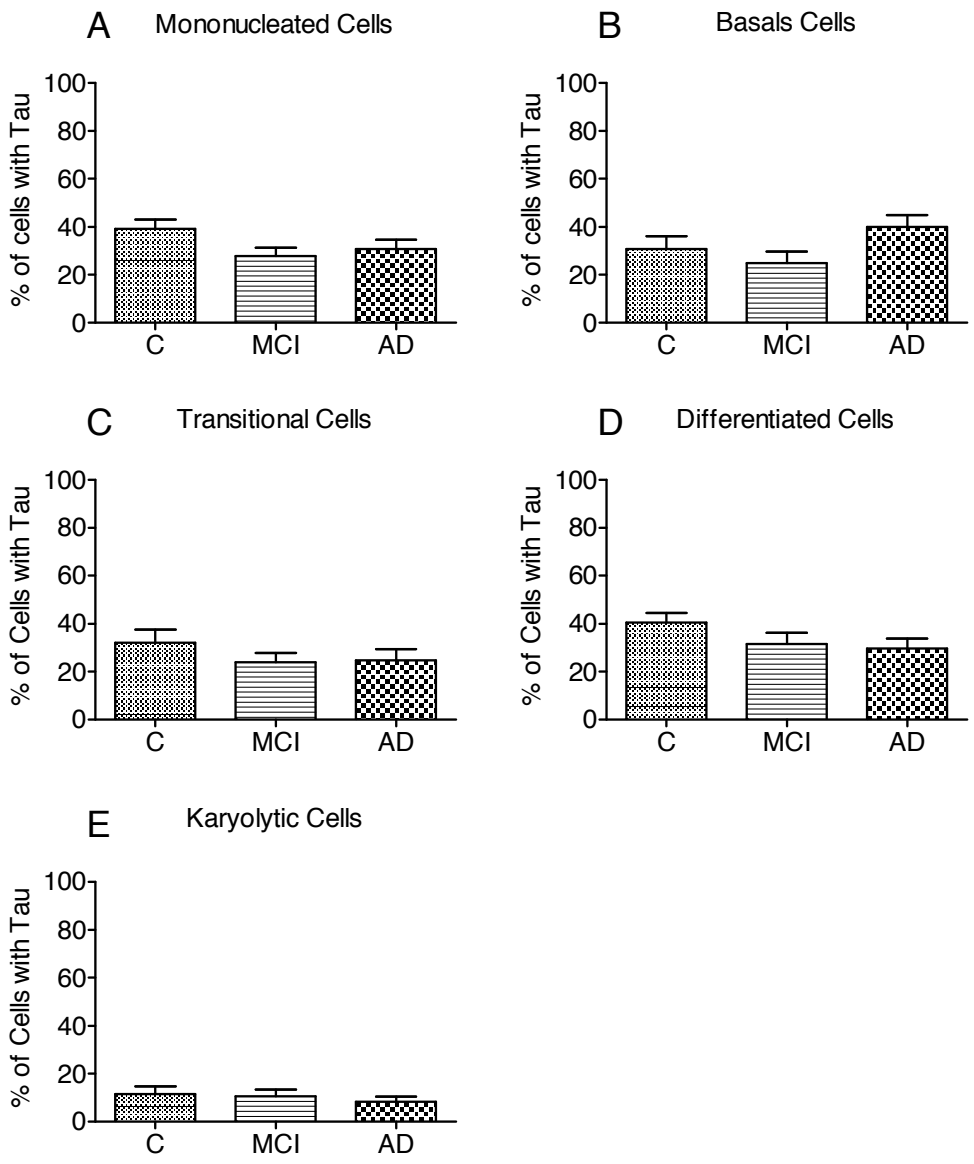

Figure 86: Percentage of cells with Tau signal between controls, MCI and AD.
Percentages were reported for control (n=20), MCI (n=20) and AD (n=20) groups in (A) all isolated single cells with a nucleus, (B) basal, (C) transitional, (D) differentiated and (E) karyolytic cells. Abbreviations; AD, Alzheimer's disease; C, Control; MCI, Mild cognitive impairment.

4.3.4.8.2 Integral

The average total amount of fluorescence for Tau signal was measured with the Tau Integral and reported in Figure 87. A significant increase in Tau Integral was observed in transitional cells (Figure 87D) between MCI and AD ($P<0.05$). However no significant difference was observed between groups in all cells as well as in the different cell types (i.e. mononucleated, basal, differentiated and karyolytic cells). It should be noted though, that karyolytic and basal cells had significantly lower Tau compared with differentiated cells ($P<0.001$).

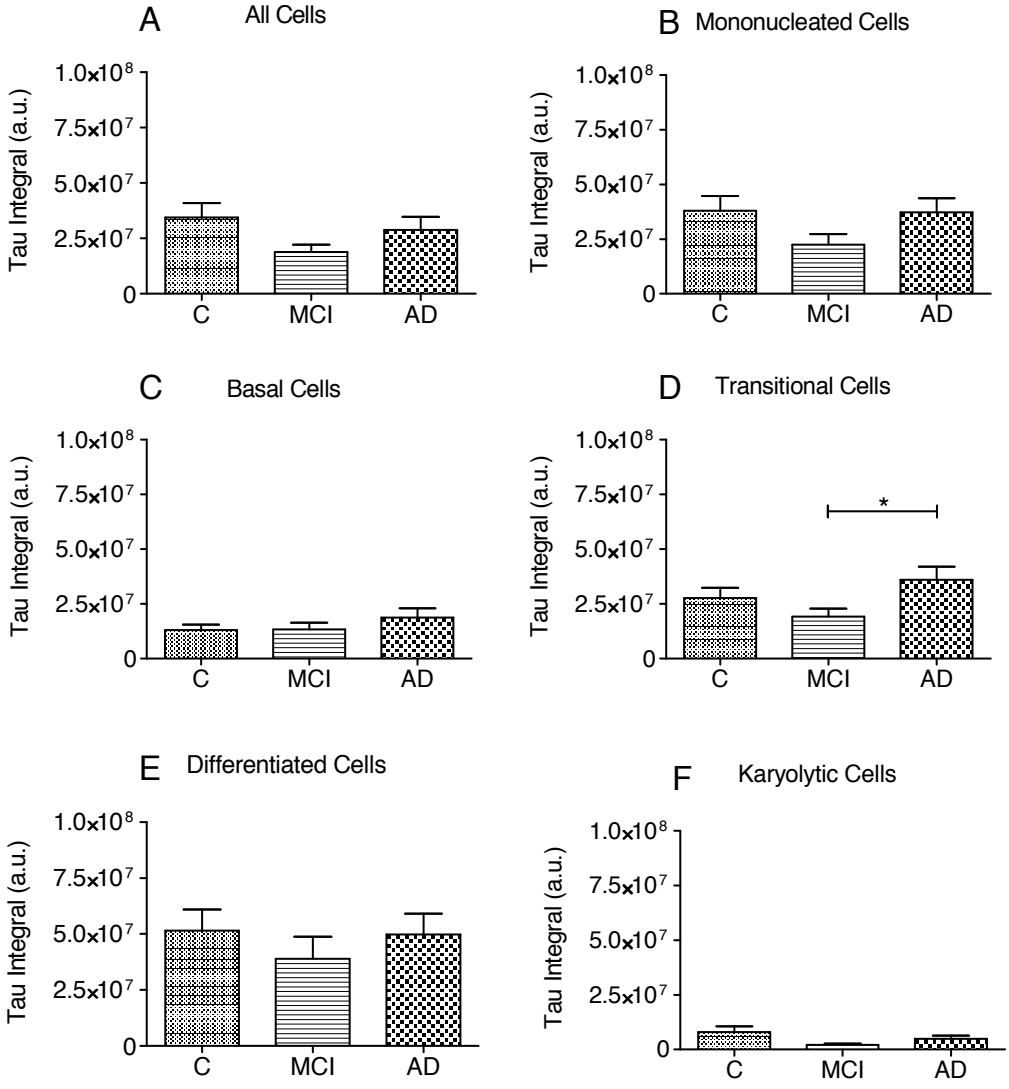

Figure 87: Total fluorescence of Tau events quantified in buccal cells between control, MCI and AD groups.

Total fluorescence was reported as Tau Integral and measured for control (n=20), MCI (n=20) and AD (n=20) groups in (A) all cells, (B) all isolated single cells with a nucleus, (C) basal, (D) transitional, (E) differentiated and (F) karyolytic cells. Abbreviations; a.u., Arbitrary unit; AD, Alzheimer's disease; C, Control; MCI, Mild cognitive impairment.

4.3.4.8.3 Area

The average area of Tau events detected in buccal cells was also measured and shown in Figure 88. Measurements were carried out in all cells as well as in the different cell types. There was a significant difference observed in karyolytic cells (Figure 88F) between controls and MCI ($P<0.05$), otherwise no significant difference was found in the other cell types (i.e. mononucleated, basal, transitional and differentiated cells) as well as all cells between groups. Also, karyolytic cells in all three groups had significantly lower ($P<0.05$) Tau area compared with transitional and differentiated cells.

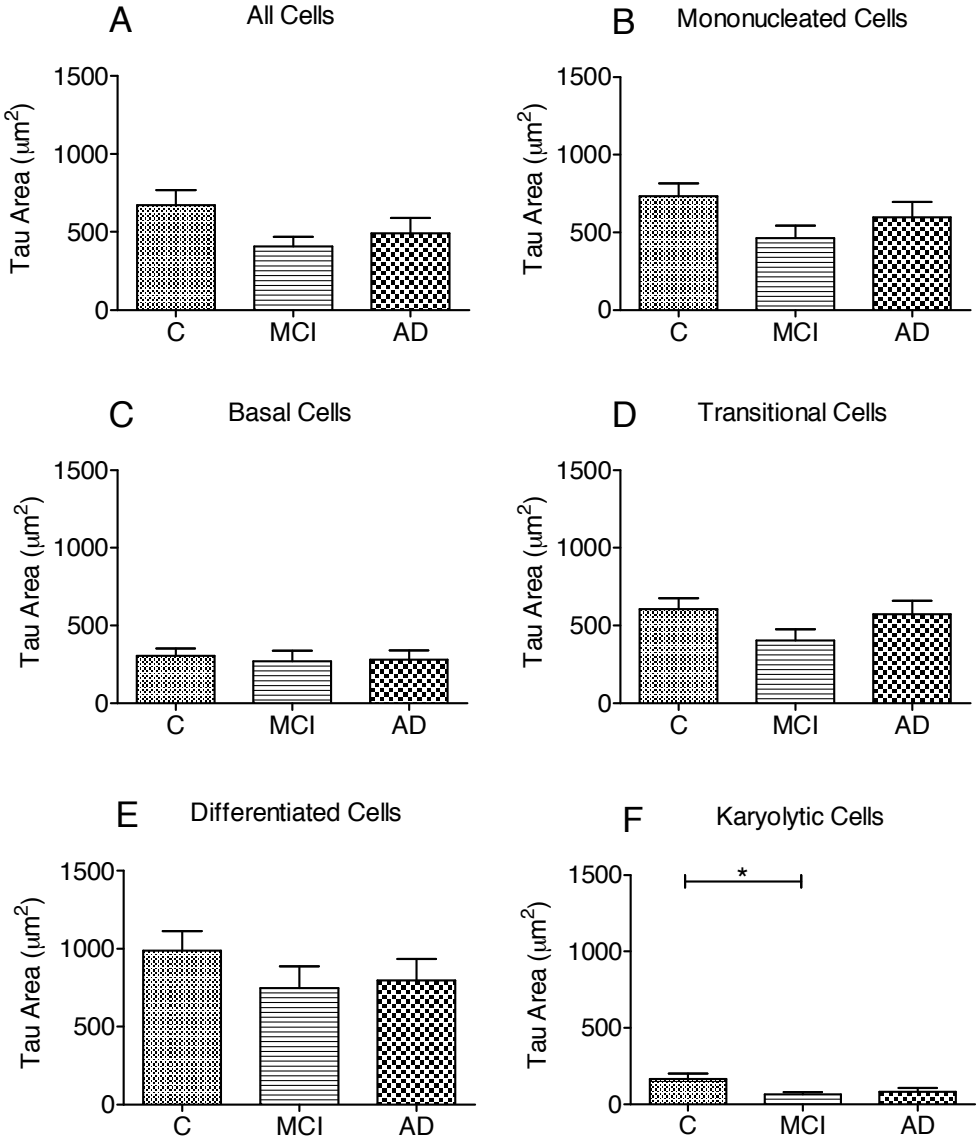

Figure 88: Area of Tau events in all cells and different cell types.
Area of Tau was reported for control (n=20), MCI (n=20) and AD (n=20) groups in (A) all cells, (B) isolated single cells with a nucleus, (C) basal, (D) transitional, (E) differentiated and (F) karyolytic cells. Abbreviations; AD, Alzheimer's disease; C, Control; MCI, Mild cognitive impairment; *, $P<0.05$.

4.3.5 Enzyme-linked immunosorbent assay

4.3.5.1 Tau measurements

Tau concentration in buccal cells was also determined by ELISA as described in section "*4.2.5.3 ELISA Kit*". For three samples, the protein concentration was too low due to a low cell concentration after sampling and processing. Therefore, these samples could not be included in the ELISA test and the analysis was carried out on the remaining samples available for the control (n=19), MCI (n=18) and AD (n=20) groups. The quantity of Tau for each sample was reported in pg of Tau per µg of total protein and is shown in Figure 89. There was no significant difference between groups, although a slight increase in the AD group relative to MCI and controls was observed.

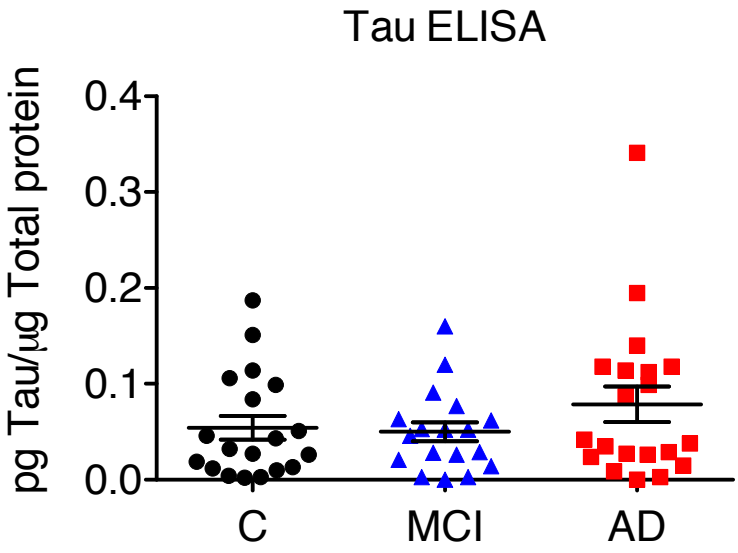

Figure 89: Tau protein measured in buccal cell samples between controls, MCI and AD.
Data are mean ± SEM. Abbreviations; AD, Alzheimer's disease; C, Control; MCI, Mild cognitive impairment.

4.3.5.2 ELISA vs. LSC

To investigate if Tau measurements obtained with an ELISA platform were comparable with Tau measurements determined by LSC, the three measures of Tau analysed with LSC (i.e. distribution of cells with Tau, Tau Integral and Tau Area) were plotted against the quantity of Tau measured by ELISA and P-values and r were reported (Figure 90). It appeared that quantity of Tau protein measured by ELISA did not correlate with Tau protein quantified by LSC.

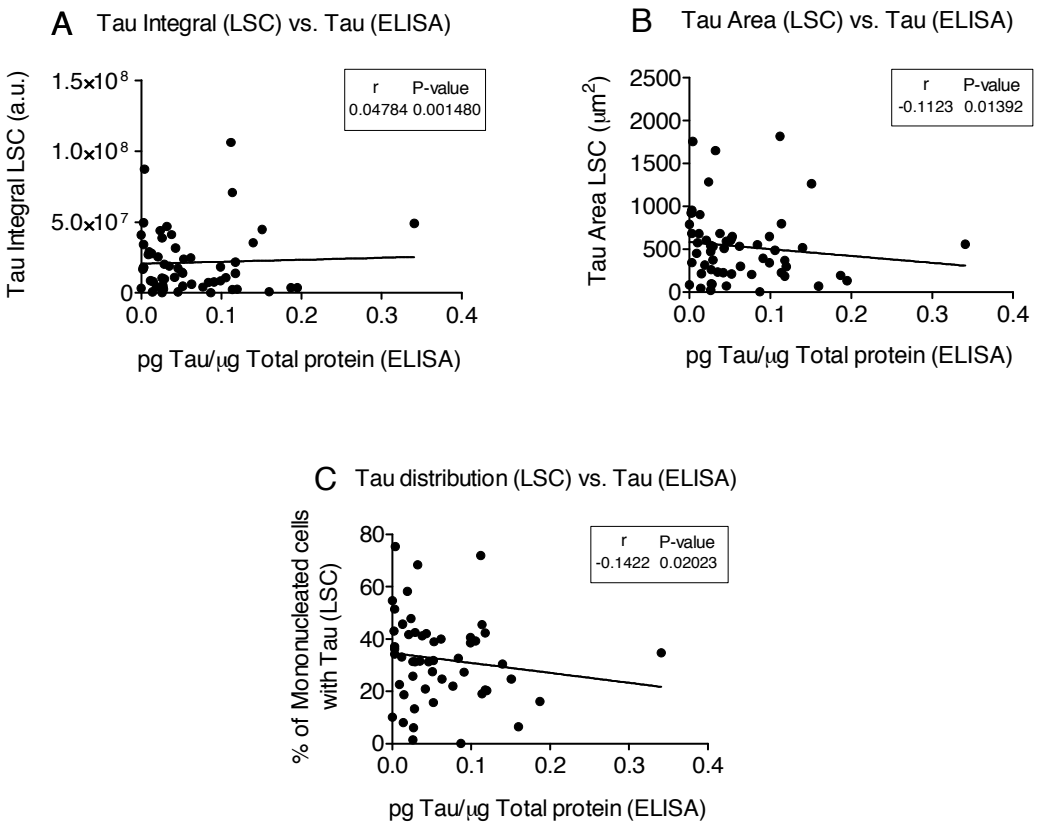

Figure 90: Tau measured by LSC vs. Tau measured by ELISA.
Tau measured by ELISA was compared with Tau measurements by LSC (n=57), (A) Tau Integral, (B) Tau Area and (C) Tau distribution in cells. Abbreviation; a.u., Arbitrary units.

4.3.6 Correlation of Tau and Aβ

To investigate if correlations existed between Tau and Aβ in buccal cells, the quantity of Aβ measured by LSC was compared to the quantity of Tau measured by ELISA (Figure 91A and B) as well as by LSC (Figure 91C and D). These measurements were compared when no distinction was made between control, MCI and AD groups (Figure 91A and C) as well as when these three groups were separated (Figure 91B and D). There was no strong correlation observed between Tau and Aβ.

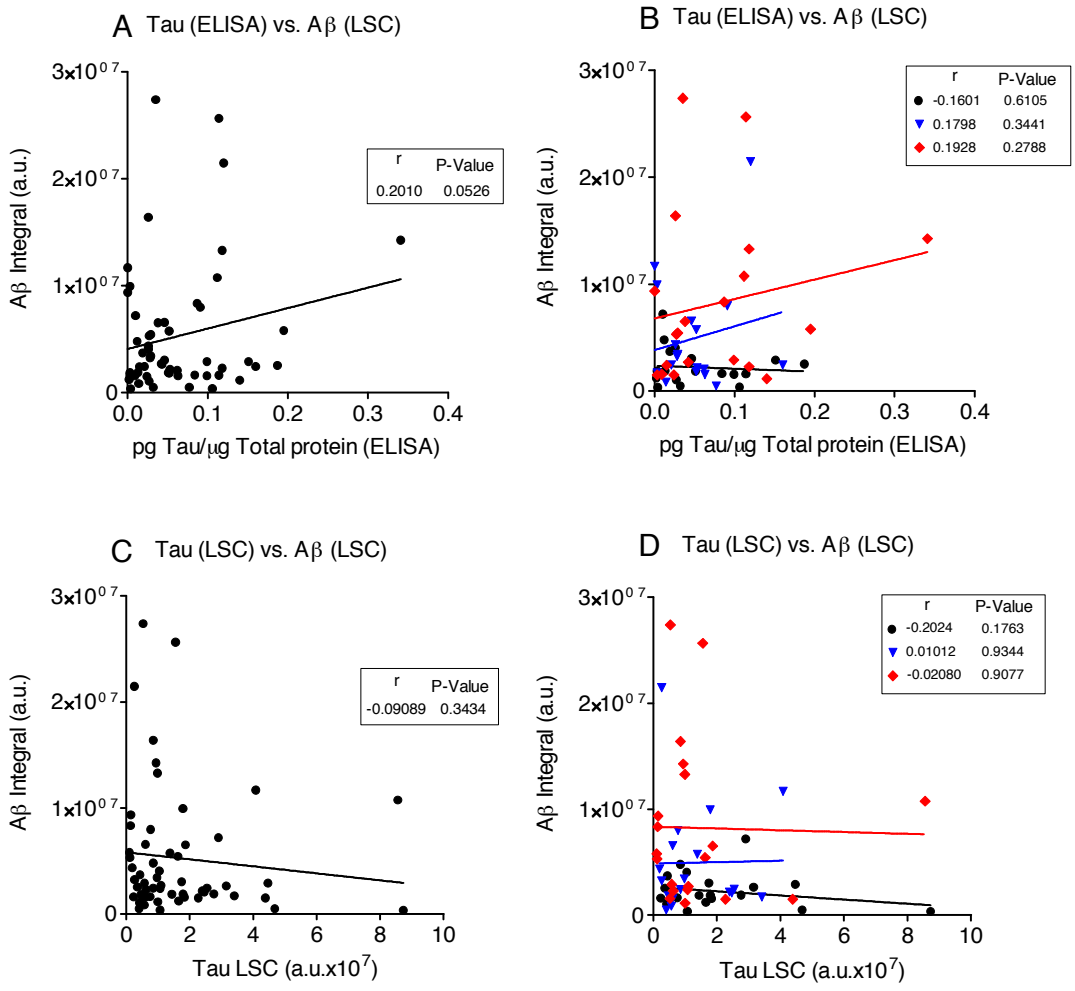

Figure 91: Aβ vs. Tau in buccal cells.
Aβ Integral measured by LSC was compared in buccal cells with (A) Tau measured by ELISA and (C) Tau measured by LSC when all data from the groups of control, MCI, AD were plotted together. Aβ Integral was also compared in buccal cells with (B) Tau measured by ELISA and (D) Tau measured by LSC between control (n=19), MCI (n=18) and AD (n=20) groups. Abbreviations; a.u., Arbitrary units; Aβ, Amyloid β; ●=Control, ▼=MCI, ♦=AD.

4.3.7 Visual scoring of buccal cytome parameters

4.3.7.1 Visual scoring

Microscope slides containing buccal cells that were stained as described in section "*4.2.6.1 Staining procedure for visual scoring*" were visually assessed using the buccal cytome assay (Thomas, et al. 2009). The frequency of the different cell types (i.e. basal, differentiated, binucleated, karyolytic, karyorrhectic, pyknotic cells and cells with condensed chromatin) were reported for each participant from the control, MCI and AD groups (Figure 92). No significant differences were observed between the three groups for each of the different cell types scored, however when scores for basal and karyorrhectic cells were combined (Figure 92H), a significant decrease was observed in MCI when compared to controls ($P<0.01$).

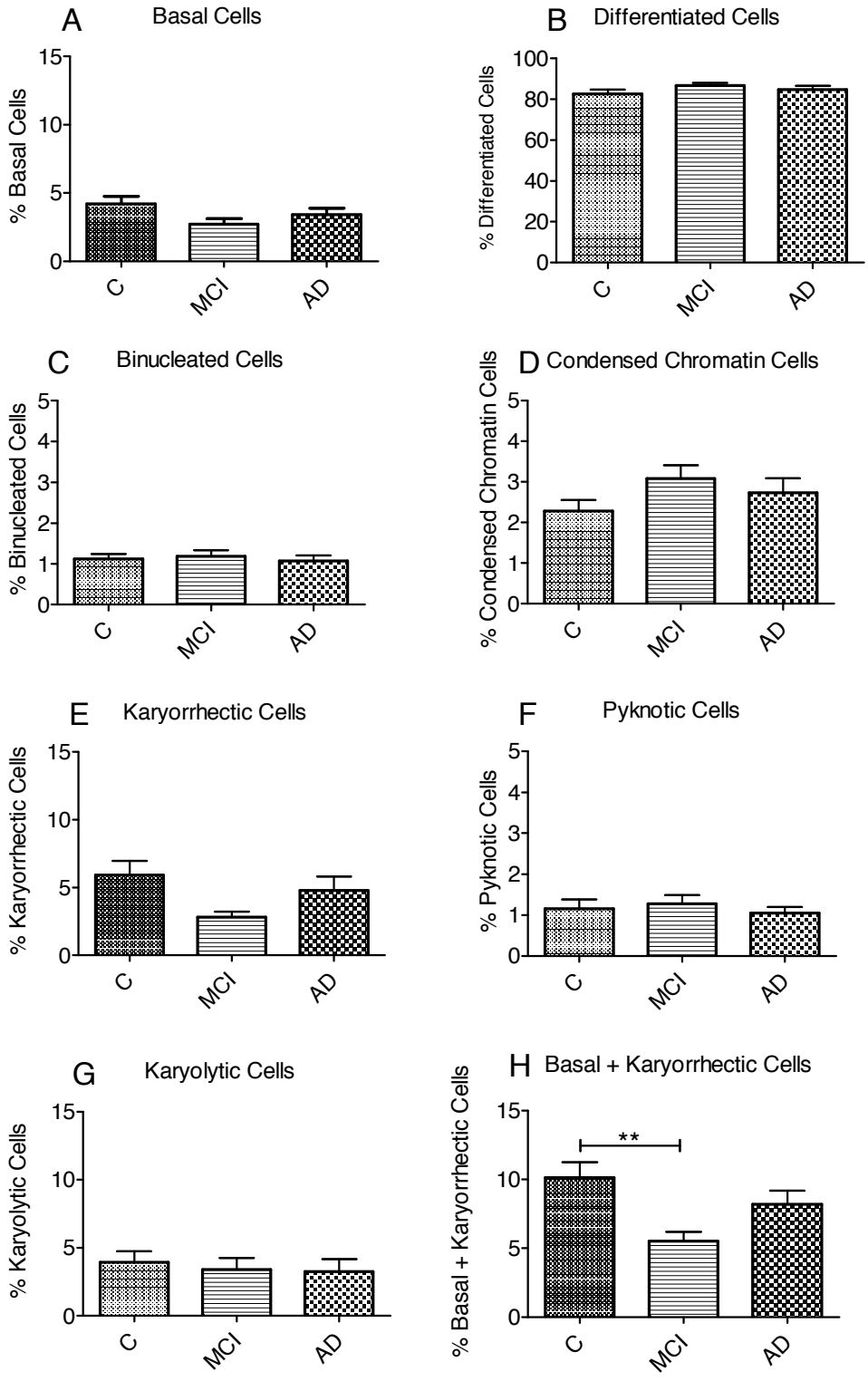

Figure 92: Buccal cell cytome scored visually in controls, MCI and AD.
The frequency of cell types was reported for control (n=20), MCI (n=20) and AD (n=20) groups for (A) basal, (B), differentiated, (C) binucleated, (D) condensed chromatin, (E) karyorrhectic, (F) pyknotic, (G) karyolytic cells and for (H) basal and karyorrhectic cells combined. Abbreviations; AD, Alzheimer's disease; C, Control; MCI, Mild cognitive impairment **, P<0.01.

4.3.7.2 Visual vs. LSC scoring

The percentage of cell types scored visually was compared to the percentage obtained by LSC scoring when possible (i.e. basal, differentiated and karyolytic cells). Figure 93 shows the comparison of scoring between the visual and LSC method. No correlation was observed between percentages obtained for basal and differentiated cells (Figure 93A and B, respectively). However, a positive correlation was shown between the percentage of karyolytic cells ($r = 0.51$, $P<0.0001$) obtained by LSC and visual scoring (Figure 93C). To compare these two methods no distinction was made between control, MCI and AD groups. However, the same comparisons were also made when the three groups were analysed individually (data not shown) and there was no significant difference. However, there was a positive correlation of the two methods (in basal cells) observed between LSC and visual scoring methods in the AD group only ($r = 0.523$, $P=0.0180$).

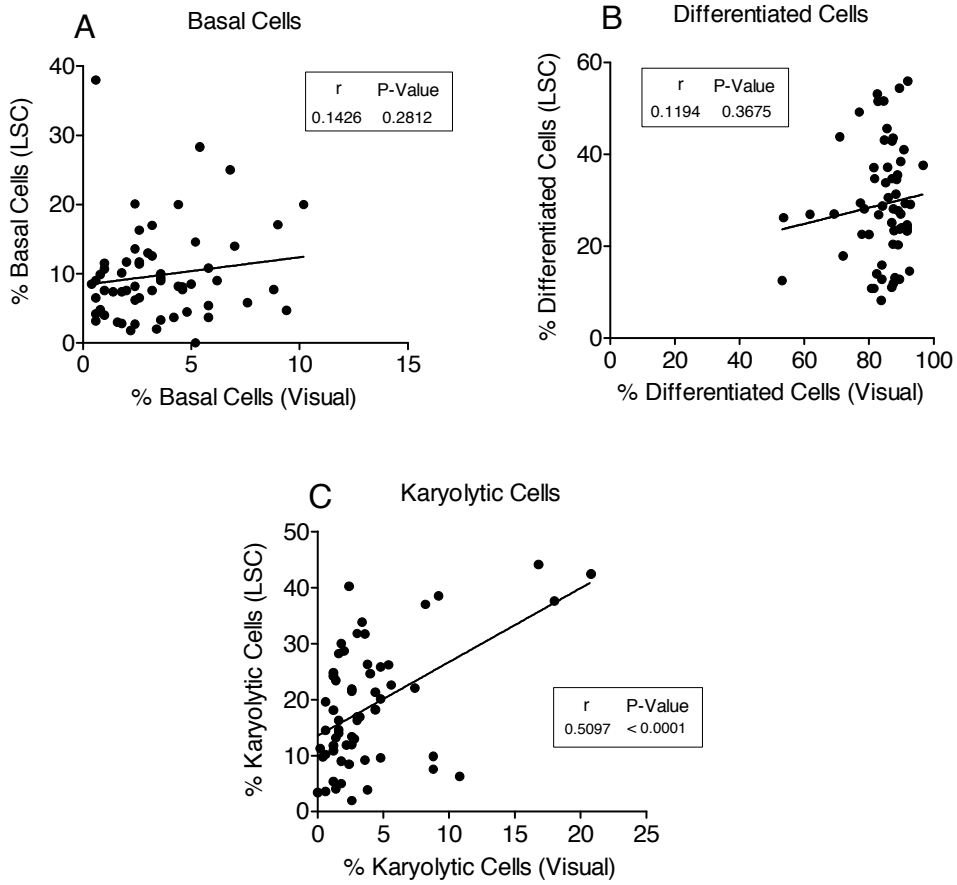

Figure 93: Visual scoring vs. LSC scoring.
Percentages of (A) basal, (B) differentiated and (C) karyolytic cells were compared when scored by LSC or visually for all participants (n=60).

4.4 DISCUSSION

The first objective of this chapter was to demonstrate the utility of LSC for high-content (multiple parameters) analysis. A protocol was successfully developed to quantify amyloid, Tau, DNA content, aneuploidy and neutral lipids simultaneously in individual buccal cells.

There were no differences found between control, MCI and AD groups in the DNA content measurements. Similarly no differences were observed when circularity and ploidy were assessed by LSC. However, this newly developed protocol involved an intensive staining procedure including an acid treatment for necessary antigen revealing and it has been suggested that acid treatment initiates DNA denaturation (Darzynkiewicz, et al. 1977; Shapiro, et al. 1978), as well as to affect DNA structure and therefore accessibility of DNA by fluorochromes (Darzynkiewicz, et al. 1984; Evenson, et al. 1986). For instance it has been shown *in situ* that DNA accessibility to dyes (e.g. DAPI, Hoechst 33342, Acridine Orange, Propidium Iodide) restricted by nuclear proteins, was increased after 0.1M HCl acid treatment leading to removal of histones (Darzynkiewicz, et al. 1984). Furthermore, formaldehyde fixation was used in this chapter which generates cross-links with chromatin constituents and may further affect DNA staining with intercalating fluorochromes (Darzynkiewicz, et al. 2010). It is therefore plausible that the strong formic acid treatment applied to buccal cells for antigen revealing as well as the formaldehyde fixation step had an effect on the DNA staining with DAPI, which may partially explain the lack of significant differences of DNA content between the AD and control groups as measured in this AIBL study protocol.

There were also no significant differences observed in neutral lipids content between control, MCI and AD groups when measured by LSC. However, it was shown in this study as described in this chapter that incubation of buccal cells in Saccomano's was a critical step of the protocol affecting neutral lipid staining. Since there have been no prior studies investigating short-term storage and transport conditions of buccal cells, Saccomano's medium was chosen as the medium to collect buccal cell samples into, immediately after isolation. It was not practical in the AIBL study to assay buccal cells on fresh samples since buccal cells needed to be collected at two locations (Melbourne and Perth) then transported to Adelaide.

Quantification of Tau protein in buccal cells was tested by the commercially available ELISA kit (INNOTEST®, Germany) and no significant differences were observed between control, MCI and AD groups. Although there was significant "putative" Tau protein in all samples, these results should be considered with caution since the ELISA kit used was specifically designed for measurements of Tau in CSF samples, and not necessarily tissue or cellular lysates. Moreover, phosphorylated Tau is the main component of neurofibrillary tangles (NFTs) in AD (Spires-Jones, et al. 2009), and is the toxic form detected in CSF samples for diagnostics (Blennow, Zetterberg. 2009; Prvulovic, Hampel. 2011). The form of Tau measured by ELISA and LSC was "total" Tau (regardless of phosphorylation levels) which did not provide direct information on the quantity of phosphorylated Tau in buccal cells. The kit that was chosen for this study was the same as that used by Hattori et al. 2002, and the aim here was to determine whether total Tau was elevated in AD of buccal cells, as in the Hattori paper. Even though there were no significant differences between controls, MCI and AD for total Tau, no correlations were observed when comparing Tau measurements between the ELISA and LSC methods. This lack of correlation may be partly explained by the combination of three antibodies included in the ELISA kit to measure Tau protein in samples (i.e. AT120, HT7 and BT2 clones), in contrast with the LSC method which used the anti-BT2 antibody only.

Amyloid signal was determined by quantitation with LSC and was found to be higher in buccal cells of AD with a concomitant increase linear trend observed from controls to MCI to AD. The LSC results showed an increase in the frequency of cells with Aβ1-42, but also the number, size, and intensity of Aβ1-42 signals were increased in buccal cells of AD. Additionally, several significant correlations were observed between buccal cell Aβ Integral and other biological parameters that were available from the AIBL database on the same subjects (i.e. Plasma homocysteine, calcium, HDL, urea, creatinine, albumin as well as white cell, monocyte, and eosinophil counts). These correlations suggest a possible link between Aβ in buccal cells and the other biological markers measured in AIBL. Although amyloid is a main hallmark of AD that accumulates within the brain (Selkoe. 1991; De-Paula, et al. 2012), it has also previously been detected in non-neural tissues such as liver, skeletal muscle, platelets, vascular walls, fibroblasts, olfactory epithelium and plasma (Schupf, et al. 2008; Pani, et al. 2009; Roher, et al. 2009; Arnold, et al. 2010), further suggesting that AD pathology may be

exhibited in peripheral tissues other than the brain. Therefore Aβ levels can be measured in peripheral tissues and as such, these Aβ reservoirs might affect exchanges of Aβ between the brain and periphery. Moreover, since the BM and the brain are both derived from differentiated ectodermal tissue, it could be postulated that there exists a link of brain and BM, and increased levels of Aβ in buccal cells in MCI and AD.

The buccal cell cytome assay which identifies the different cell types present was performed by visual scoring. A significant decrease in the frequency of karyorrhectic and basal cells when combined was observed between MCI and controls. This combination of cell types confirms its' potential as a AD risk biomarker as observed previously (Thomas, et al. 2007). LSC was also used for identifying some of the cell types (i.e. basal, transitional, differentiated and karyolytic cells) but no significant differences were observed between groups. Correlations between visual scoring and LSC scoring were investigated for cell types where possible, and a positive correlation was found for karyolytic cells when control, MCI and AD groups were combined. The separation of karyolytic cells by LSC does not take into account either the cytoplasmic area or the nucleus/cytoplasm area ratio since these cells are depleted of nuclei. According to this positive correlation observed, LSC can separate karyolytic cells from other cell types. The visual buccal cytome assay does not include a category for transitional cells (Thomas, et al. 2009) in contrast with LSC scoring, which explains the higher percentage of differentiated cells when scored visually. Basal buccal cells scored by LSC did positively correlate with visual scoring but only in the AD group, which indicates that although scores for basal cells differ from both methods, they remain close since both these methods are based on the same main criteria for basal cell identification. This may be explained by the quantitative nature of measurements for the $Area_{Nuclei}/Area_{Cytoplasm}$ ratio and the cytoplasm area of cells obtained by LSC that cannot be precisely obtained by visual assessment. Nevertheless correlation factors between LSC and visual scoring of cell types were generally weak and further improvements in the LSC protocol could be required if it is to be used as a substitute to visual scoring.

CHAPTER 5

5. CONCLUSION AND FUTURE DIRECTIONS

Aim

The broad aim of this study was to investigate buccal cells as a peripheral tissue source for biomarkers of MCI and AD using laser scanning cytometry (LSC). Several potential biomarkers were chosen, based on previous findings in studies on AD. High-content analyses were developed for Aβ, Tau, neutral lipids and DNA content. A total of 60 samples were assayed from the highly characterised AIBL cohort.

Advantage of LSC

LSC imaging and analysis are non-confocal by design. This resulting in a very high depth of focus (20 μm) that allows collection of the total signal through the depth of cells. This in turn, provides precise quantification of the measured signals (DNA content, for example), which is superior to many alternative technologies such as camera-based microscopy imaging systems and (to a much greater extent) confocal imaging systems which collect data from a very narrow plane through the sample and therefore do not provide the level of complete quantification available using LSC. LSC has the advantage to be versatile in the choice of sample it can analyse. It has previously been utilised in investigations on several types of tissue and cells such as brain tissue sections (Mosch, et al. 2006; Mosch, et al. 2007), macrophages (Coelho, et al. 2012), buccal cells (Darzynkiewicz, et al. 2011), pancreas (Peterson, et al. 2008), breast tissue (Tulchin, et al. 2010), neurons (Bingham, et al. 2006), fine-needle aspirate biopsies (Gerstner, Tarnok. 2002; Juan, et al. 2011), adipocytes (Lin, et al. 2004), laryngeal mucosa (Gerstner, et al. 2005) and bone marrow (Tsujioka, et al. 2008). The LSC has been used previously in many different approaches, and has been a convenient tool for high-content analysis. For instance in DNA damage investigations, LSC has been used for detection of γH2AX, a phosphorylated histone protein marker of DNA double strand breaks (Huang, et al. 2004a; Huang, et al. 2004b; Huang, et al. 2005; Kurose, et al. 2005; Tanaka, et al. 2009; Zhao, et al. 2009a) that forms foci in nuclei. LSC multi parameter analysis was used in a previous study and showed that drug induced γH2AX could be separated from apoptosis-associated γH2AX by dual detection of

immunofluorescent γH2AX and caspase-3 activation (Huang, et al. 2004b). Furthermore, detection of these two parameters associated with a nuclear stain (PI) allowed their association to specific cell cycle stages and chromatin condensation levels of nuclei. Therefore LSC offers a higher sensitivity in DSB detection than the traditional single cell DNA electrophoresis (comet) assay, and more importantly offers the possibility to immunocytochemically co-detect DNA damage with expression of any other protein with association to the cell cycle, within the same individual cells. It was therefore considered in this thesis to further investigate DNA damage and cell cycle in buccal cells from SAND and AIBL studies by the use of LSC. A study on drug discovery also demonstrated the high-content automated potential of LSC in tissue section analysis (Krull, Peterson. 2011). Pancreas from a rat model of type 2 diabetes mellitus (Zucker diabetic rat) were analysed with five different dyes for simultaneous detection of nuclear DNA, Ki67 (cell proliferation marker), insulin, glucagon and voltage-dependent anion channel, while preserving the tissue architecture of samples analysed (Krull, Peterson. 2011). The LSC methods presented in this study showed promise in the automation and high-content analyses of single buccal cells for neutral lipids, DNA content and protein detection as well as quantitation. In contrast with flow cytometry, LSC opened up the possibility to work on fixed samples with archiving of scanned data for future reanalysis (Pozarowski, et al. 2006; Mach, et al. 2010). Moreover, the adaptation of the buccal cytome assay using LSC as described in this thesis, allowed to a certain extent an automated cell sorting (identification and quantification of cell types) simultaneously with quantitation of markers of interest. However, the large size of buccal cells and the high number of dyes and fluorescent labelled antibodies utilised to reach a high-content analysis protocol weakened the high-throughput potential of this technology for this assay. Nevertheless, for high-content investigation studies such as this one, the access to information in such detail at a cellular level makes the LSC a tremendously efficient tool for quantitative imaging and understanding the biology of cells in greater depth.

DNA content / Cell cycle

Measurement of DNA content can be easily determined in most LSC protocols by the incorporation of common dyes (e.g. DAPI, PI) into the immunocytochemistry technique (Darzynkiewicz, et al. 2010), and offers valuable information on aneuploidy in cells. In chapter 3, an increase in DNA content was observed in fixed buccal cells of MCI and

AD subjects of the SAND study, in all isolated single cells when compared to controls ($P<0.05$ and $P<0.01$, respectively). This increase was accompanied with a similar increase in percentage of >2N nuclei between MCI, AD and control groups. Since the percentage of 2N nuclei decreased in parallel, it indicates that buccal cells tend to exhibit hyperdiploidy genotype in MCI and AD compared with controls. Although the cell cycle was significantly different it would be valuable if information on specific proteins involved in cell cycle regulation could be collected simultaneously for each of the cell types. The cell cycle is typically divided into four phases: S-phase, during which DNA replication occurs, M-phase, where mitosis takes place and the two gap phases (G_1 and $G_{2)}$ that separate S- and M-phase. The transition between those different phases is mainly regulated by cyclin/cyclin-dependent kinase complexes (Pines. 1994; Grana, Reddy. 1995; Pines. 1995). The first checkpoint is located at the end of the cell cycle's G_1 phase, just before entry into S-phase, making the key decision of whether the cell should divide, delay division, or enter a resting stage called G_0. However the presence of several factors such as mitotic growth factors can induce the re-entry of resting cells into the cell cycle (Sherr. 1994) and increasing evidence indicates that via this mechanism, neurons in AD are forced through a cell cycle that they are no longer equipped to complete (Zhu, et al. 1999; McShea, et al. 2007; Zhu, et al. 2007; Lee, et al. 2009) and therefore leads to cell death and neurodegeneration (Wang, et al. 2009). AD pathology has also been linked to proteins that are involved in maintaining the cell cycle. For example hyperphosphorylated Tau is linked to the activity of cyclin-dependent protein kinases (Brion, et al. 1994; Brion. 2006); amyloid precursor protein (APP) metabolism is monitored by cell cycle dependent changes and is also up-regulated by mitogenic stimulation (Iqbal, et al. 1984; Grundke-Iqbal, et al. 1986; Copani, et al. 1999); and finally Aβ (a product of APP processing) has been identified as mitogenic in *in vitro* studies (Schubert, et al. 1989; Milward, et al. 1992). These studies suggest that altered cell cycle mechanisms may be indirectly involved in the process of AD onset and development. Moreover, a recent study using lymphocytes from AD patients demonstrated the potential of G1/S checkpoint proteins as biomarkers of AD. In that study, Cyclin E, Rb, CDK2 and E_2F-1, gave specificity/sensitivity scores of 84/81%, 74/89%, 80/78% and 85/85%, respectively (Song, et al. 2012). Studies with LSC have previously identified the cell cycle stage by measuring the “DNA index”, which was calculated by MaxPixel vs. Integral of the signal collected from the nuclear dye, which allowed further separation of nuclei with high or low condensed chromatin

(Pozarowski, et al. 2006; Kuliffay, et al. 2010). Therefore it would be of particular interest to investigate cell cycle characteristics and protein checkpoints of targeted cells in AD by LSC if appropriate methods could be applied to isolated peripheral cells such as buccal cells and/or lymphocytes from blood.

Proteomic studies

Although well characterised antibodies were used in this study to detect putative "Tau" and "Aβ42" in buccal cells, more effort is required to confirm these proteins conclusively. Putative "Tau" protein was detected by the BT2 antibody using LSC and this same antibody is used within the Tau ELISA kit (INNOTEST®, Germany). A study by Hattori et al. 2002 demonstrated that buccal cells from AD contain on average 0.93 ± 0.11 pg of Tau/μg of total protein in buccal cell lysates using the same ELISA kit compared to 0.53 ± 0.06 pg/μg for age-matched controls (P=0.0034). Using the same ELISA kit in this study (AIBL), a small increase in Tau was observed in AD compared to controls but was not significantly different. However this may be partly explained by the differences in the cohorts investigated and batches of ELISA kit used as well as the differences in buccal cell processing (Hattori, et al. 2002). This particular ELISA kit which uses the antibodies (AT120, HT7 and BT2) measures "total" Tau. However, Tau protein is a phosphoprotein with 79 potential Ser and Thr phosphorylation sites; with at least 6 isoforms of Tau known to exist. Therefore it is possible that Tau would show multiple molecular weights when Western blots are carried out (e.g. Figure 2C and Figure 4 from Crouch et al. 2009). A study from Sjögren et al. 2001 detected Tau in Rotofor fractions of cerebrospinal fluid (CSF) by Western blotting at 25 kDa and 52 kDa with several antibodies, i.e. HT7, AT120, BT2, AT270 and AT8. However all antibodies (HT7, AT120, AT270 and AT8) excluding BT2 antibody also detected immunoreactive bands in the range of 65 to 80 kDa (Sjogren, et al. 2001). The bands observed in Sjögren et al. 2001 study using BT2 antibody correlated with bands (around 21 kDa and 50 kDa) observed in buccal cells when the same BT2 antibody was used (see chapter 4, section "*4.3.2.2 Tau*"). However, the method applied by Sjögren et al. 2001 did not provide information on Tau detection at lower molecular weights and therefore, no comparison could be made in regard to the band observed below 10 kDa in buccal cells. Furthermore, different isoforms of Tau in human platelets detected by Western have also been shown to differ from AD disease state to controls (Neumann, et

al. 2011). Stronger bands at higher molecular weights (150-250 kDa) were observed in parallel with weaker bands of low molecular weights (50-75 kDa) in AD compared with controls ($P<0.001$). This variation in the molecular weight ratio of Tau may indicate that Tau aggregates to form multimers at a higher occurrence in AD. The detection of Tau has also been shown in human blood lymphocytes by immunocytochemistry, although no distinction between both Tau and phosphorylated Tau were made (Kvetnoy, et al. 2000). This suggests that Tau is present in peripheral tissues in different isoforms and therefore a precise identification of Tau and phosphorylated Tau isoforms, as well as their quantification in buccal cells would be valuable if correlated with measurements of Tau in CSF and other peripheral tissues.

Similarly, Aβ42 appeared in different forms; the well characterised antibody for Aβ42 (WO2) demonstrated a clear band at 4.5 kDa and molecular weights corresponding to multimers of this size, as well as another band at approximately 110 kDa which may represent APP. Similar bands were observed with WO2 antibody in a study investigating amyloid in brain (cerebellum) and retina lysates from a transgenic mice *Tg2576* (Dutescu, et al. 2009). A strong band at 4.5 kDa was detected in the brain lysates whilst APP full length was detected both in the retina and brain lysates at around 110 kDa. A band could also be observed around 20-25 kDa in retina samples which seems to match the band observed in the mouse brain lysates as shown in chapter 4, section "*4.3.2.1 Amyloid*", Figure 60. In this study, a band at approximately 65 kDa was also seen in buccal cells when detected with the antibody anti-oligomer (A11) and this band matched the molecular weight of a band that corresponded to pure Aβ42 as detected with the anti-oligomer antibody. A study on identification of amyloid in brain cell lysates of transgenic *Tg2576* mice by Western, showed presence of bands, possibly 12-mer of Aβ, around 56 kDa in soluble mouse brain lysates, when detected with the same antibody anti-oligomer (A11) (Lesne, et al. 2006). Additionally, the A11 antibody specificity towards oligomers detection has previously been demonstrated (Zhao, et al. 2009b). Full length hI-APP_{1-37} peptides of known concentration were incubated at different times immediately after dissolving to generate oligomers of increasing concentration. The antibody A11 was then confirmed by a dot blot assay and the increased binding of A11 was found to be proportional to the quantity of oligomers present. Furthermore, APP expression has been demonstrated previously in oral mucosa of hamsters (Ko, et al. 2007), which was reduced by green tea extracts in their diet.

These previous findings and the similarity of bands observed in Western blots with this study support the notion of putative "amyloid" and "APP" being detected in buccal cells. However, an ELISA for Aβ42 was not carried out as it was for Tau due to lack of time available as well as sample availability. Samples were therefore prioritised for ELISA assay detection of Tau, since it was previously shown that changes in total Tau concentration appeared in buccal cells (Hattori, et al. 2002).

The identification and quantification of multimeric Aβ species is essential in Alzheimer's research, although difficult to undertake. Antibodies aiming at detecting amyloid have different binding sites along the length of the peptide and therefore might differ from one another depending on the type of tissue analysed and the method of detection used (e.g. ELISA, Western, immunocytochemistry). The main antibodies used in the cited literature and the ones used in this study are shown in Figure 94. It would be necessary for further studies to confirm the presence of Aβ42 in buccal cells. Different methods have been proposed aiming at improving detection of amyloid. For instance, using heat-induced antigen-epitope retrieval technique combined with separation of protein by SDS-PAGE and immunoblotting with 6E10 antibody was shown to efficiently detect Aβ monomers and multimers of low and high molecular weights in human brain tissue (Rosen, et al. 2010). Superior sensitivity to detect isoform specific peptides can be obtained with combination of immunoprecipitation, 2D-gel electrophoresis, Western blotting and liquid chromatography-mass spectrometry (LC-MS) techniques (Newton, et al. 2006). Applying such intensive proteomic procedures for instance, would allow clear characterisation of the "putative" amyloid detected in buccal cells.

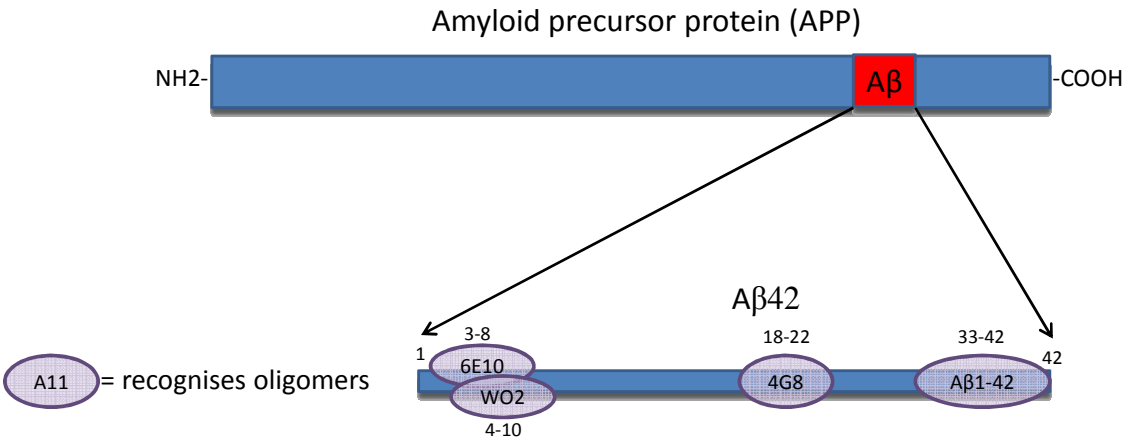

Figure 94: Antibody sites for amyloid detection.

Comparison of protocols

Chapter 3, Table 9 showed that the significant differences in DNA content and neutral lipids observed in the SAND study had a potential diagnostic value when combined for separating MCI from controls (AUC = 0.7518). It was possible from the results from AIBL study samples (chapter 4) to further include measurements of these two parameters into a new protocol for higher content analysis including the simultaneous detection of Tau and Aβ. In chapter 4, the main target was to detect and investigate if differences existed in Aβ and Tau protein levels in buccal cells between control, MCI and AD groups. A second objective was to combine successfully 5 fluorochromes in one protocol for detection by LSC since a protocol for detection of lipids and DNA content was already established (chapter 3). However since the two cell preparation and staining methods were very different it was difficult to directly compare their results. Figure 95 summarises the main differences and the critical steps (violet) that potentially affected the outcomes of the assays. Incubation of buccal cells in Saccomano's fixative was shown to be a critical step with small but significant effect on ORO staining detection. Additionally, the acid treatment and fixation method may have had an effect on the DNA structure modifying the nuclear dye binding and accessibility to the DNA and therefore affecting the staining and nuclear measurements. These differences in sample fixation, treatment and processing may partly explain why no change in DNA content was observed between controls, MCI and AD in the AIBL study compared with the SAND study which used freshly isolated buccal cells and a simplified staining method. Although the AIBL study samples were processed in a very different manner to the SAND study buccals, every attempt was made to ensure that there was no loss of

fluorescence (or absorbance) of the parameters measured. Furthermore, since the AIBL study samples were not collected locally it was not practical within the budgetary limitations to process and fix buccal cells freshly onto microscope slides as in the SAND study. Nevertheless, a future protocol defined in a way that each step would have no negative effects on the efficiency of the dyes would be robust, and if combined with LSC would facilitate the detection for simultaneous biomarkers of disease. A newly developed LSC protocol should therefore be considered as a tool in future biomarker research.

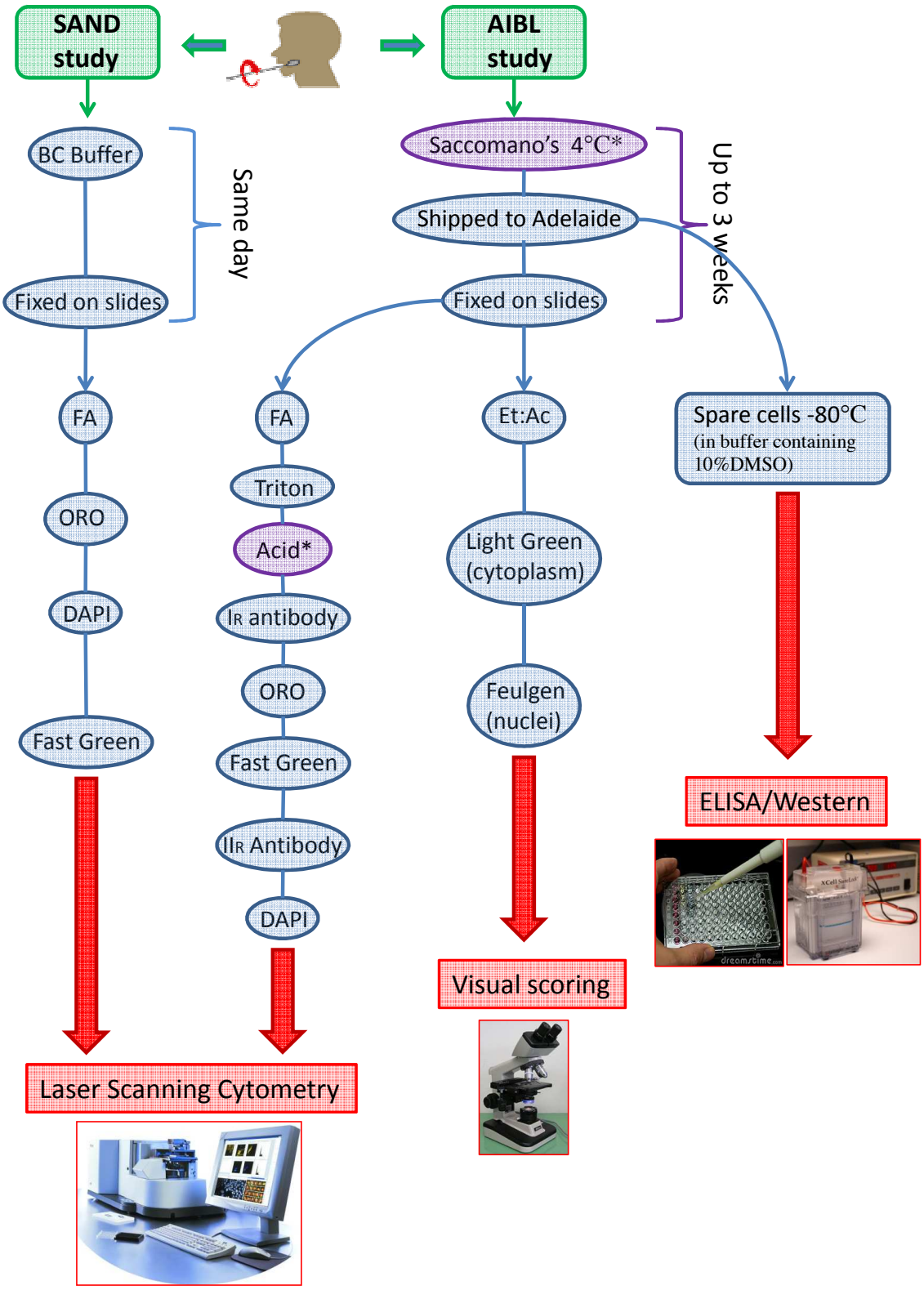

Figure 95: Differences in protocol between SAND and AIBL study.
Abbreviations: BC Buffer, Buccal Cell Buffer; Et:Ac, Ethanol:Acetic Acid; FA, Formaldehyde; Ir antibody, Primary Antibody; IIr antibody, Secondary Antibody; ORO, Oil Red O.

Visual scoring

A previous study by Thomas et al. 2007 demonstrated the value of scoring the different cell types in the buccal mucosa (BM) of AD by the use of the "buccal cytome assay", which showed a strong diagnostic value of the combined frequencies of karyorrhectic and basal cells to separate AD from controls, with specificity and sensitivity scores obtained of 97% and 82%, respectively (Thomas, et al. 2007). Therefore, in chapter 4 (AIBL study) visual scoring was carried out in parallel to LSC scoring on the buccal cell slides from participants, to investigate if differences could be observed in the frequency of cell types and if both scoring methods were correlated. No difference in the frequency of cell types was observed between groups when LSC scoring was performed. However, visual scoring of cell types which allows for a more in depth description of cell types based on several morphological features, showed a significant decrease ($P<0.01$) of both karyorrhectic and basal cell frequencies in MCI when compared to control. Both methods were compared but did not show correlations in the scoring of basal and differentiated cells between participants, although a weak correlation for karyolytic cells could be observed. In this study, the issue of visual scoring not perfectly aligning with LSC scoring was mainly due firstly, to the difference of staining methods utilised and secondly, the objectivity residing within both methods. Visual scoring for instance defines some categories of cell types that could not be scored with LSC (e.g. condensed chromatin and karyorrhectic cells). Moreover, there likely exists an underlying variability between visual scorers as well as a physical limitation caused by the inability of a scorer to accurately measure the size of nuclei or the $Area_{Nuclei}/Area_{Cytoplasm}$ ratio by visual scoring. LSC is limited by the difficulty of identifying cell boundaries in cell clumps or overlapping cells. The LSC however sets exact values and defined gating regions to separate cell types that will be consistent over the study. Nevertheless, the choice of such values and regions also implies a level of subjectivity from the LSC user since these have to be set manually by pre-determining the set values empirically. Ideally, a comparison study of both methods should be undertaken. To align both scoring methods, identical slides should be scored and percentage of cells obtained must be compared. Scoring must also include collection of pictures for each cell scored by LSC with determination of false and true positives by an expert scorer. If possible, the buccal cytome assay by LSC should be upgraded in a way that it will also include segregation of the other cell types scored visually (i.e. pyknotic, karyorrhectic, binucleated and condensed chromatin cells). However with that said, it is

highly unlikely and impractical for that approach to be successful, since the current buccal micronucleus cytome assay uses Light Green/Feulgen stains which are permanent stains and ideal for light microscopy, whilst the LSC assay described in this thesis necessitates the use of fluorescent probes such as Fast Green/DAPI, which cannot be visualised with light microscopy. An LSC method for scoring biomarkers of the buccal cytome assay in Light Green/Feulgen stained slides was described previously (Darzynkiewicz, et al. 2011; Leifert, et al. 2011) but was not validated against visual scoring. If both methods could be more precisely aligned, it would then be valuable to reduce subjectivity resulting from these scoring methods possibly by also comparing LSC scoring with a biochemical marker of buccal cell distribution by the use of antibodies that bind to cytokeratin proteins. As discussed in chapter 1 section "*1.2.3 Cytokeratins – Biochemical cell type segregation*", different types of cytokeratin are expressed in BM depending on the cell differentiation stage. Preliminary results showed that it was possible to separate cell populations by immunocytochemistry in a robust manner with LSC. Defining regions for cell type characterisation will therefore not only be guided by criteria of cytoplasm size and nuclei structure, but also by the direct protein expression subsequent to the differentiation stage of cells. Such a further study would be greatly beneficial to the current and limited knowledge of buccal cells available in the literature.

Novel biomarkers

This study has demonstrated the practical use of buccal cells in the search for biomarkers of AD. The Integral of Aβ was found to be significantly increased in buccal cells of AD when compared to controls ($P<0.01$), and a negative significant correlation was observed between buccal cell Aβ Integral and MMSE scores ($r = -0.43$, $P=0.0005$). Additionally, as described in chapter 4 correlations between Aβ Integral and several other biomarkers (e.g. Plasma homocysteine, albumin and calcium) available in the AIBL database for the same 60 participants were observed. Interestingly, in the whole AIBL cohort homocysteine ($P=0.002$), albumin and calcium ($P<0.0001$) levels in blood were also found to be significantly altered in AD compared to controls (Doecke, et al. 2012). The Aβ results obtained in this study are not sufficient to be proposed as a diagnostic tool for identification of AD sufferers or determining those at risk of developing AD such as MCI; however this correlation indicates that Aβ loading in buccal cells increases with cognitive decline. The quantitation of Aβ loading in buccal

cells if used properly with combination of the MMSE mental test could help improve the accuracy of the diagnosis of AD or identify those at increased risk for AD. Moreover, if further investigation in AIBL project shows that Aβ accumulation in the brain detected with positron emission tomography (PET)-scan correlates with Aβ loading in buccal cells, a buccal cell assay aimed at quantifying Aβ in the BM in a robust and high throughput manner should be considered because such an assay could be used to provide information on likelihood of Aβ accumulation in the brain and cognitive decline, in a minimally invasive and less expensive manner.

The APOE ε4 allele is a strong genetic risk factor for AD (Strittmatter, et al. 1993) with APOE ε4 heterozygous and homozygous individuals being more susceptible to develop AD at an earlier age. APOE genotyping cannot predict AD with certainty; however novel biomarkers have been recently associated with AD and could be investigated in buccal cells in combination with genotype information. For instance, following completion of a genome-wide association study (Alzheimer's Disease Neuroimaging Initiative) (Potkin, et al. 2009), TOMM40 (translocase of outer mitochondrial membrane 40) was found to be a potential gene associated with AD (TOMM40 risk alleles were two times more frequent than in controls) and therefore an additional risk for developing AD (Potkin, et al. 2009). The expression of this gene has been found to be significantly down-regulated in blood from AD compared to controls (Lee, et al. 2012). Chitotriosidase (chitinase), a chitinolytic enzyme secreted by activated mononucleated cells, showed increased level and activity in macrophages and plasma from AD, respectively (Di Rosa, et al. 2006; Sotgiu, et al. 2007). A significant increase in chitotriosidase activity has also been observed in CSF sampled from AD patients when compared to controls (Mattsson, et al. 2011; Watabe-Rudolph, et al. 2012). YKL-40, a homolog to chitotriosidase was recently described in early stage of AD with significantly higher protein levels found in CSF ($P<0.0001$) as well as in plasma ($P=0.014$) compared to controls (Craig-Schapiro, et al. 2010; Choi, et al. 2011), and more importantly, presented a strong ability to predict onset and progression of dementia (Craig-Schapiro, et al. 2010). For instance, it was found that a high YKL-40/Aβ42 ratio in CSF demonstrated strong predictive values of a faster cognitive decline, and that levels of YKL-40 correlated ($r = 0.5948$, $P<0.0001$) with levels of phosphorylated Tau in CSF (Craig-Schapiro, et al. 2010). Stathmin, a ubiquitous phosphoprotein highly expressed in neurons was also investigated in adult human brains

(post-mortem) of AD and found to exhibit a significant decrease ($P<0.05$) in protein levels from the temporal and frontal cortex regions when analysed by 2D-gel images (Cheon, et al. 2001). It would be interesting to know how those novel biomarkers vary within buccal cells and whether they are associated with MCI and AD.

Other tissues

Although much biomarker work has been achieved using plasma as a source of peripheral tissue, plasma analyses have brought several contradictory results to light. For instance, plasma levels of Aβ in AD were found to vary in different studies (Schupf, et al. 2008; Schneider, et al. 2009; Song, et al. 2011). Therefore more focus should be intended on peripheral tissues (i.e. lymphocytes, olfactory epithelium, buccal cells, and fibroblasts) by the use of a similar high-content LSC protocol. Additionally, it would be worth considering the measurement of Aβ42 protein levels in buccal cells by ELISA on available SAND and AIBL study samples and to further investigate potential correlations with other results obtained in these studies (chapter 3 and 4). Moreover, studies investigating brain tissue should also be considered in application with LSC since this technology is very suitable for tissue section analysis (Peterson, et al. 2008; Henriksen, et al. 2011; Fueldner, et al. 2012) and has previously been used with human brain slices (Mosch, et al. 2006). Therefore, a detailed assessment of brain tissue sections from post-mortem examination of humans or AD model mice in parallel with peripheral tissues by LSC could be considered in future studies.

General conclusion

In order to treat AD early before the neurodegeneration has progressed to a widespread and irreversible stage of the disease process, there is need for a biomarker or combination of biomarkers that enable early presymptomatic and predementia diagnosis, at least at the symptomatic stage of MCI. Additionally, a strong biomarker for early diagnostics of AD is needed to help differentiating with certainty AD from other forms of dementia at its' early stage. As populations throughout the world continue to age, the prevalence of AD will increase dramatically with a predicted increase of 300% in the next thirty years, becoming a global concern threatening to impact heavily on both social and economic levels (Sloane, et al. 2002; Ferri, et al. 2005; Smith. 2008). The BM is an easily accessible non neuronal tissue, which offers a simple, painless and non-expensive sampling procedure involving rotations of a

toothbrush against the inner cheeks of patients. Previous findings suggest that the regenerative potential of the BM varies and cytological changes occur within buccal cells following AD appearance, but the knowledge gap in this area is important. Only some studies have investigated changes in the oral mucosa in AD involving cytological parameters, cell types composition, increase of Tau and micronuclei, telomere shortening and chromosome 17 and 21 aneuploidy (see chapter 1, Table 1). Results obtained from this thesis confirm the hypothesis that BM is a legitimate tissue of interest in the search for AD diagnostic biomarkers. This is the first time that these parameters, examined in this study either individually or in combination, were investigated in buccal cells, therefore the interindividual variability of the different biomarkers in the studied group has to be further investigated. Furthermore, research must be undertaken for a better understanding of the biology of buccal cells, to replicate such studies and investigate other potential markers of AD. Those potential biomarkers, hence proven to be detectable in buccal cells, as well as those already investigated in buccal cells should be examined in cross sectional studies to seek differences in MCI and AD. Longitudinal studies can then be applied to capture their variation with the progression of the disease and cognitive decline. In terms of prevention, such markers should be targeted to help differentiation between MCI from controls in a follow-up study, and the rate of conversion from MCI to AD should be compared with changes in those markers in order to select which ones would predict conversion and onset of the disease with the highest accuracy. Investigation work on those knowledge gaps would greatly improve the potential for buccal cells to be a peripheral tissue in future AD diagnosis research. If combined with results from other peripheral tissue investigations, new biomarker sets could emerge that may identify individuals who are at increased risk or are at an early stage of AD with much higher certainty to be clinically useful. Such a diagnostic allied with a minimally invasive approach would also be valuable to the community, since it would be possible to monitor the progress of the disease but also determine the effectiveness of potential therapeutic or lifestyle intervention strategies.

CHAPTER 6

6. CITED REFERENCES

Abe, T., Tohgi, H., Isobe, C., Murata, T., Sato, C., 2002. Remarkable Increase in the Concentration of 8-Hydroxyguanosine in Cerebrospinal Fluid from Patients with Alzheimer's Disease. *J. Neurosci. Res.* **70** (3), 447-450.

Albert, S., Oguntayo, O., Samaila, M., 2012. Comparative Study of Visual Inspection of the Cervix using Acetic Acid (VIA) and Papanicolaou (Pap) Smears for Cervical Cancer Screening. *Ecancermedicalscience* **6** 262.

Alzheimer, A., Stelzmann, R.A., Schnitzlein, H.N., Murtagh, F.R., 1995. An English Translation of Alzheimer's 1907 Paper, "Uber Eine Eigenartige Erkankung Der Hirnrinde". *Clin. Anat.* **8** (6), 429-431.

Alzheimer's Association, Thies, W., Bleiler, L., 2011. 2011 Alzheimer's Disease Facts and Figures. *Alzheimers Dement.* **7** (2), 208-244.

Anderton, B.H., 1981. Intermediate Filaments: A Family of Homologous Structures. *J. Muscle Res. Cell. Motil.* **2** (2), 141-166.

Antoccia, A., Tanzarella, C., Modesti, D., Degrassi, F., 1993. Cytokinesis-Block Micronucleus Assay with Kinetochore Detection in Colchicine-Treated Human Fibroblasts. *Mutat. Res.* **287** (1), 93-99.

Armentero, M.T., Sinforiani, E., Ghezzi, C., Bazzini, E., Levandis, G., Ambrosi, G., Zangaglia, R., Pacchetti, C., Cereda, C., Cova, E., Basso, E., Celi, D., Martignoni, E., Nappi, G., Blandini, F., 2011. Peripheral Expression of Key Regulatory Kinases in Alzheimer's Disease and Parkinson's Disease. *Neurobiol. Aging* **32** (12), 2142-2151.

Armstrong, R.A., 2006. Plaques and Tangles and the Pathogenesis of Alzheimer's Disease. *Folia Neuropathol.* **44** (1), 1-11.

Arnold, S.E., Lee, E.B., Moberg, P.J., Stutzbach, L., Kazi, H., Han, L.Y., Lee, V.M., Trojanowski, J.Q., 2010. Olfactory Epithelium Amyloid-Beta and Paired Helical Filament-Tau Pathology in Alzheimer Disease. *Ann. Neurol.* **67** (4), 462-469.

Artandi, S.E., Chang, S., Lee, S.L., Alson, S., Gottlieb, G.J., Chin, L., DePinho, R.A., 2000. Telomere Dysfunction Promotes Non-Reciprocal Translocations and Epithelial Cancers in Mice. *Nature* **406** (6796), 641-645.

Ayyad, S.B., Israel, E., El-Setouhy, M., Nasr, G.R., Mohamed, M.K., Loffredo, C.A., 2006. Evaluation of Papanicolaou Stain for Studying Micronuclei in Buccal Cells Under Field Conditions. *Acta Cytol.* **50** (4), 398-402.

Banks-Schlegel, S.P., 1982. Keratin Alterations during Embryonic Epidermal Differentiation: A Presage of Adult Epidermal Maturation. *J. Cell Biol.* **93** (3), 551-559.

Barger, S.W., Harmon, A.D., 1997. Microglial Activation by Alzheimer Amyloid Precursor Protein and Modulation by Apolipoprotein E. *Nature* **388** (6645), 878-881.

Bedner, E., Melamed, M.R., Darzynkiewicz, Z., 1998. Enzyme Kinetic Reactions and Fluorochrome Uptake Rates Measured in Individual Cells by Laser Scanning Cytometry. *Cytometry* **33** (1), 1-9.

Beer, J., Masters, C.L., Beyreuther, K., 1995. Cells from Peripheral Tissues that Exhibit High APP Expression are Characterized by their High Membrane Fusion Activity. *Neurodegeneration* **4** (1), 51-59.

Binder, L.I., Frankfurter, A., Rebhun, L.I., 1985. The Distribution of Tau in the Mammalian Central Nervous System. *J. Cell Biol.* **101** (4), 1371-1378.

Bingham, B., Kotnis, S., McHendry-Rinde, B., Shen, R., Wood, A., Kennedy, J.D., 2006. Laser Scanning Cytometry in the Characterization of the Proapoptotic Effects of Transiently Transfected Genes in Cerebellar Granule Neurons. *Cytometry A.* **69** (11), 1114-1122.

Blennow, K., Zetterberg, H., 2009. Cerebrospinal Fluid Biomarkers for Alzheimer's Disease. *J. Alzheimers Dis.* **18** (2), 413-417.

Borroni, B., Agosti, C., Marcello, E., Di Luca, M., Padovani, A., 2010. Blood Cell Markers in Alzheimer Disease: Amyloid Precursor Protein Form Ratio in Platelets. *Exp. Gerontol.* **45** (1), 53-56.

Borthakur, G., Butryee, C., Stacewicz-Sapuntzakis, M., Bowen, P.E., 2008. Exfoliated Buccal Mucosa Cells as a Source of DNA to Study Oxidative Stress. *Cancer Epidemiol. Biomarkers Prev.* **17** (1), 212-219.

Bowden, P.E., Wood, E.J., Cunliffe, W.J., 1983. Comparison of Prekeratin and Keratin Polypeptides in Normal and Psoriatic Human Epidermis. *Biochim. Biophys. Acta* **743** (1), 172-179.

Braak, H., Braak, E., 1991. Demonstration of Amyloid Deposits and Neurofibrillary Changes in Whole Brain Sections. *Brain Pathol.* **1** (3), 213-216.

Brecht, W.J., Harris, F.M., Chang, S., Tesseur, I., Yu, G.Q., Xu, Q., Dee Fish, J., Wyss-Coray, T., Buttini, M., Mucke, L., Mahley, R.W., Huang, Y., 2004. Neuron-Specific Apolipoprotein e4 Proteolysis is Associated with Increased Tau Phosphorylation in Brains of Transgenic Mice. *J. Neurosci.* **24** (10), 2527-2534.

Breitkreutz, D., Bohnert, A., Herzmann, E., Bowden, P.E., Boukamp, P., Fusenig, N.E., 1984. Differentiation Specific Functions in Cultured and Transplanted Mouse

Keratinocytes: Environmental Influences on Ultrastructure and Keratin Expression. *Differentiation* **26** (2), 154-169.

Brion, J.P., 2006. Immunological Demonstration of Tau Protein in Neurofibrillary Tangles of Alzheimer's Disease. *J. Alzheimers Dis.* **9** (3 Suppl), 177-185.

Brion, J.P., Octave, J.N., Couck, A.M., 1994. Distribution of the Phosphorylated Microtubule-Associated Protein Tau in Developing Cortical Neurons. *Neuroscience* **63** (3), 895-909.

Bull, C.F., O'Callaghan, N.J., Mayrhofer, G., Fenech, M.F., 2009. Telomere Length in Lymphocytes of Older South Australian Men may be Inversely Associated with Plasma Homocysteine. *Rejuvenation Res.* **12** (5), 341-349.

Burns, T., Breathnack, S., Cox, N. (Eds.), 2004. Rook's Textbook of Dermatology. Blackwell publishing, Oxford (UK).

Buttini, M., Yu, G.Q., Shockley, K., Huang, Y., Jones, B., Masliah, E., Mallory, M., Yeo, T., Longo, F.M., Mucke, L., 2002. Modulation of Alzheimer-Like Synaptic and Cholinergic Deficits in Transgenic Mice by Human Apolipoprotein E Depends on Isoform, Aging, and Overexpression of Amyloid Beta Peptides but Not on Plaque Formation. *J. Neurosci.* **22** (24), 10539-10548.

Buttini, M., Orth, M., Bellosta, S., Akeefe, H., Pitas, R.E., Wyss-Coray, T., Mucke, L., Mahley, R.W., 1999. Expression of Human Apolipoprotein E3 Or E4 in the Brains of Apoe-/- Mice: Isoform-Specific Effects on Neurodegeneration. *J. Neurosci.* **19** (12), 4867-4880.

Cairns, N.J., Ikonomovic, M.D., Benzinger, T., Storandt, M., Fagan, A.M., Shah, A.R., Reinwald, L.T., Carter, D., Felton, A., Holtzman, D.M., Mintun, M.A., Klunk, W.E., Morris, J.C., 2009. Absence of Pittsburgh Compound B Detection of Cerebral Amyloid Beta in a Patient with Clinical, Cognitive, and Cerebrospinal Fluid Markers of Alzheimer Disease: A Case Report. *Arch. Neurol.* **66** (12), 1557-1562.

Cawthon, R.M., Smith, K.R., O'Brien, E., Sivatchenko, A., Kerber, R.A., 2003. Association between Telomere Length in Blood and Mortality in People Aged 60 Years Or Older. *Lancet* **361** (9355), 393-395.

Ceppi, M., Biasotti, B., Fenech, M., Bonassi, S., 2010. Human Population Studies with the Exfoliated Buccal Micronucleus Assay: Statistical and Epidemiological Issues. *Mutat. Res.* **705** (1), 11-19.

Cheng, N., Cai, H., Belluscio, L., 2011. In Vivo Olfactory Model of APP-Induced Neurodegeneration Reveals a Reversible Cell-Autonomous Function. *J. Neurosci.* **31** (39), 13699-13704.

Cheon, M.S., Fountoulakis, M., Cairns, N.J., Dierssen, M., Herkner, K., Lubec, G., 2001. Decreased Protein Levels of Stathmin in Adult Brains with Down Syndrome and Alzheimer's Disease. *J. Neural Transm. Suppl.* **(61)** (61), 281-288.

Choi, J., Lee, H.W., Suk, K., 2011. Plasma Level of Chitinase 3-Like 1 Protein Increases in Patients with Early Alzheimer's Disease. *J. Neurol.* **258** (12), 2181-2185.

Christensen, D.Z., Schneider-Axmann, T., Lucassen, P.J., Bayer, T.A., Wirths, O., 2010. Accumulation of Intraneuronal Abeta Correlates with ApoE4 Genotype. *Acta Neuropathol.* **119** (5), 555-566.

Clausen, H., Moe, D., Buschard, K., Dabelsteen, E., 1986. Keratin Proteins in Human Oral Mucosa. *J. Oral Pathol.* **15** (1), 36-42.

Clausen, H., Vedtofte, P., Moe, D., Dabelsteen, E., 1983. Keratin Pattern in Human and Buccal and Hard Palate Mucosa. *Scand. J. Dent. Res.* **91** (5), 411-413.

Coelho, C., Tesfa, L., Zhang, J., Rivera, J., Goncalves, T., Casadevall, A., 2012. Analysis of Cell Cycle and Replication of Mouse Macrophages After in Vivo and in Vitro Cryptococcus Neoformans Infection using Laser Scanning Cytometry. *Infect. Immun.* **80** (4), 1467-1478.

Copani, A., Condorelli, F., Caruso, A., Vancheri, C., Sala, A., Giuffrida Stella, A.M., Canonico, P.L., Nicoletti, F., Sortino, M.A., 1999. Mitotic Signaling by Beta-Amyloid Causes Neuronal Death. *FASEB J.* **13** (15), 2225-2234.

Cosentino, S.A., Stern, Y., Sokolov, E., Scarmeas, N., Manly, J.J., Tang, M.X., Schupf, N., Mayeux, R.P., 2010. Plasma Ss-Amyloid and Cognitive Decline. *Arch. Neurol.* **67** (12), 1485-1490.

Cossec, J.C., Simon, A., Marquer, C., Moldrich, R.X., Leterrier, C., Rossier, J., Duyckaerts, C., Lenkei, Z., Potier, M.C., 2010. Clathrin-Dependent APP Endocytosis and Abeta Secretion are Highly Sensitive to the Level of Plasma Membrane Cholesterol. *Biochim. Biophys. Acta* **1801** (8), 846-852.

Craig, C.L., Marshall, A.L., Sjostrom, M., Bauman, A.E., Booth, M.L., Ainsworth, B.E., Pratt, M., Ekelund, U., Yngve, A., Sallis, J.F., Oja, P., 2003. International Physical Activity Questionnaire: 12-Country Reliability and Validity. *Med. Sci. Sports Exerc.* **35** (8), 1381-1395.

Craig-Schapiro, R., Perrin, R.J., Roe, C.M., Xiong, C., Carter, D., Cairns, N.J., Mintun, M.A., Peskind, E.R., Li, G., Galasko, D.R., Clark, C.M., Quinn, J.F., D'Angelo, G., Malone, J.P., Townsend, R.R., Morris, J.C., Fagan, A.M., Holtzman, D.M., 2010. YKL-40: A Novel Prognostic Fluid Biomarker for Preclinical Alzheimer's Disease. *Biol. Psychiatry* **68** (10), 903-912.

Crouch, P.J., Hung, L.W., Adlard, P.A., Cortes, M., Lal, V., Filiz, G., Perez, K.A., Nurjono, M., Caragounis, A., Du, T., Laughton, K., Volitakis, I., Bush, A.I., Li, Q.X., Masters, C.L., Cappai, R., Cherny, R.A., Donnelly, P.S., White, A.R., Barnham, K.J., 2009. Increasing Cu Bioavailability Inhibits Abeta Oligomers and Tau Phosphorylation. *Proc. Natl. Acad. Sci. U. S. A.* **106** (2), 381-386.

Cutler, R.G., Kelly, J., Storie, K., Pedersen, W.A., Tammara, A., Hatanpaa, K., Troncoso, J.C., Mattson, M.P., 2004. Involvement of Oxidative Stress-Induced Abnormalities in Ceramide and Cholesterol Metabolism in Brain Aging and Alzheimer's Disease. *Proc. Natl. Acad. Sci. U. S. A.* **101** (7), 2070-2075.

Dalquen, P., Bittel, D., Gudat, F., von Overbeck, J., Heitz, P.U., 1986. Combined Immunoreaction and Papanicolaou's Stain on Cytological Smears. *Pathol. Res. Pract.* **181** (1), 50-54.

Darzynkiewicz, Z., Smolewski, P., Holden, E., Luther, E., Henriksen, M., Francois, M., Leifert, W., Fenech, M., 2011. Laser Scanning Cytometry for Automation of the Micronucleus Assay. *Mutagenesis* **26** (1), 153-161.

Darzynkiewicz, Z., Halicka, H.D., Zhao, H., 2010. Analysis of Cellular DNA Content by Flow and Laser Scanning Cytometry. *Adv. Exp. Med. Biol.* **676** 137-147.

Darzynkiewicz, Z., Huang, X., Okafuji, M., King, M.A., 2004. Cytometric Methods to Detect Apoptosis. *Methods Cell Biol.* **75** 307-341.

Darzynkiewicz, Z., Bedner, E., Li, X., Gorczyca, W., Melamed, M.R., 1999. Laser-Scanning Cytometry: A New Instrumentation with Many Applications. *Exp. Cell Res.* **249** (1), 1-12.

Darzynkiewicz, Z., Traganos, F., Kapuscinski, J., Staiano-Coico, L., Melamed, M.R., 1984. Accessibility of DNA in Situ to various Fluorochromes: Relationship to Chromatin Changes during Erythroid Differentiation of Friend Leukemia Cells. *Cytometry* **5** (4), 355-363.

Darzynkiewicz, Z., Traganos, F., Sharpless, T.K., Melamed, M.R., 1977. Cell Cycle-Related Changes in Nuclear Chromatin of Stimulated Lymphocytes as Measured by Flow Cytometry. *Cancer Res.* **37** (12), 4635-4640.

de Oliveira, R.M., Lia, E.N., Guimaraes, R.M., Bocca, A.L., Cavalcante Neto, F.F., da Silva, T.A., 2008. Cytologic and Cytometric Analysis of Oral Mucosa in Alzheimer's Disease. *Anal. Quant. Cytol. Histol.* **30** (2), 113-118.

de Vries, H.G., Collee, J.M., van Veldhuizen, M.H., Achterhof, L., Smit Sibinga, C.T., Scheffer, H., Buys, C.H., ten Kate, L.P., 1996. Validation of the Determination of deltaF508 Mutations of the Cystic Fibrosis Gene in Over 11 000 Mouthwashes. *Hum. Genet.* **97** (3), 334-336.

De-Paula, V.J., Radanovic, M., Diniz, B.S., Forlenza, O.V., 2012. Alzheimer's Disease. *Subcell. Biochem.* **65** 329-352.

Deptala, A., Bedner, E., Gorczyca, W., Darzynkiewicz, Z., 1998. Activation of Nuclear Factor Kappa B (NF-kappaB) Assayed by Laser Scanning Cytometry (LSC). *Cytometry* **33** (3), 376-382.

Devereux-Graminski, B., Sampugna, J., 1993. Variability in Lipids Isolated from Human Cheek Cells. *The Journal of nutritional biochemistry* **4** (May), 264-267.

Di Rosa, M., Dell'Ombra, N., Zambito, A.M., Malaguarnera, M., Nicoletti, F., Malaguarnera, L., 2006. Chitotriosidase and Inflammatory Mediator Levels in Alzheimer's Disease and Cerebrovascular Dementia. *Eur. J. Neurosci.* **23** (10), 2648-2656.

Doecke, J.D., Laws, S.M., Faux, N.G., Wilson, W., Burnham, S.C., Lam, C.P., Mondal, A., Bedo, J., Bush, A.I., Brown, B., De Ruyck, K., Ellis, K.A., Fowler, C., Gupta, V.B., Head, R., Macaulay, S.L., Pertile, K., Rowe, C.C., Rembach, A., Rodrigues, M., Rumble, R., Szoeke, C., Taddei, K., Taddei, T., Trounson, B., Ames, D., Masters, C.L., Martins, R.N., Alzheimer's Disease Neuroimaging Initiative, Australian Imaging Biomarker and Lifestyle Research Group, 2012. Blood-Based Protein Biomarkers for Diagnosis of Alzheimer Disease. *Arch. Neurol.* **69** (10), 1318-1325.

Dong, L.M., Weisgraber, K.H., 1996. Human Apolipoprotein E4 Domain Interaction. Arginine 61 and Glutamic Acid 255 Interact to Direct the Preference for very Low Density Lipoproteins. *J. Biol. Chem.* **271** (32), 19053-19057.

Dong, L.M., Wilson, C., Wardell, M.R., Simmons, T., Mahley, R.W., Weisgraber, K.H., Agard, D.A., 1994. Human Apolipoprotein E. Role of Arginine 61 in Mediating the Lipoprotein Preferences of the E3 and E4 Isoforms. *J. Biol. Chem.* **269** (35), 22358-22365.

Dutescu, R.M., Li, Q.X., Crowston, J., Masters, C.L., Baird, P.N., Culvenor, J.G., 2009. Amyloid Precursor Protein Processing and Retinal Pathology in Mouse Models of Alzheimer's Disease. *Graefes Arch. Clin. Exp. Ophthalmol.* **247** (9), 1213-1221.

Ellis, K.A., Bush, A.I., Darby, D., De Fazio, D., Foster, J., Hudson, P., Lautenschlager, N.T., Lenzo, N., Martins, R.N., Maruff, P., Masters, C., Milner, A., Pike, K., Rowe, C., Savage, G., Szoeke, C., Taddei, K., Villemagne, V., Woodward, M., Ames, D., AIBL Research Group, 2009. The Australian Imaging, Biomarkers and Lifestyle (AIBL) Study of Aging: Methodology and Baseline Characteristics of 1112 Individuals Recruited for a Longitudinal Study of Alzheimer's Disease. *Int. Psychogeriatr.* **21** (4), 672-687.

Elzay, R.P., 1983. A Modification of the Papanicolaou Exfoliative Cytology Stain to Demonstrate Keratin in Paraffin-Block Tissue Sections. *Oral Surg. Oral Med. Oral Pathol.* **56** (1), 51-53.

Evenson, D., Darzynkiewicz, Z., Jost, L., Janca, F., Ballachey, B., 1986. Changes in Accessibility of DNA to various Fluorochromes during Spermatogenesis. *Cytometry* **7** (1), 45-53.

Feigelson, H.S., Rodriguez, C., Robertson, A.S., Jacobs, E.J., Calle, E.E., Reid, Y.A., Thun, M.J., 2001. Determinants of DNA Yield and Quality from Buccal Cell Samples Collected with Mouthwash. *Cancer Epidemiol. Biomarkers Prev.* **10** (9), 1005-1008.

Fenech, M., Morley, A.A., 1986. Cytokinesis-Block Micronucleus Method in Human Lymphocytes: Effect of in Vivo Ageing and Low Dose X-Irradiation. *Mutat. Res.* **161** (2), 193-198.

Fenech, M., Crott, J.W., 2002. Micronuclei, Nucleoplasmic Bridges and Nuclear Buds Induced in Folic Acid Deficient Human Lymphocytes-Evidence for Breakage-Fusion-Bridge Cycles in the Cytokinesis-Block Micronucleus Assay. *Mutat. Res.* **504** (1-2), 131-136.

Fernandez, M., Gobartt, A.L., Balana, M., COOPERA Study Group, 2010. Behavioural Symptoms in Patients with Alzheimer's Disease and their Association with Cognitive Impairment. *BMC Neurol.* **10** 87.

Ferri, C.P., Prince, M., Brayne, C., Brodaty, H., Fratiglioni, L., Ganguli, M., Hall, K., Hasegawa, K., Hendrie, H., Huang, Y., Jorm, A., Mathers, C., Menezes, P.R., Rimmer, E., Scazufca, M., Alzheimer's Disease International, 2005. Global Prevalence of Dementia: A Delphi Consensus Study. *Lancet* **366** (9503), 2112-2117.

Fraga, C.G., Shigenaga, M.K., Park, J.W., Degan, P., Ames, B.N., 1990. Oxidative Damage to DNA during Aging: 8-Hydroxy-2'-Deoxyguanosine in Rat Organ DNA and Urine. *Proc. Natl. Acad. Sci. U. S. A.* **87** (12), 4533-4537.

Friedewald, W.T., Levy, R.I., Fredrickson, D.S., 1972. Estimation of the Concentration of Low-Density Lipoprotein Cholesterol in Plasma, without use of the Preparative Ultracentrifuge. *Clin. Chem.* **18** (6), 499-502.

Fueldner, C., Mittag, A., Knauer, J., Biskop, M., Hepp, P., Scholz, R., Wagner, U., Sack, U., Emmrich, F., Tarnok, A., Lehmann, J., 2012. Identification and Evaluation of Novel Synovial Tissue Biomarkers in Rheumatoid Arthritis by Laser Scanning Cytometry. *Arthritis Res. Ther.* **14** (1), R8.

Garcia-Closas, M., Egan, K.M., Abruzzo, J., Newcomb, P.A., Titus-Ernstoff, L., Franklin, T., Bender, P.K., Beck, J.C., Le Marchand, L., Lum, A., Alavanja, M., Hayes, R.B., Rutter, J., Buetow, K., Brinton, L.A., Rothman, N., 2001. Collection of Genomic DNA from Adults in Epidemiological Studies by Buccal Cytobrush and Mouthwash. *Cancer Epidemiol. Biomarkers Prev.* **10** (6), 687-696.

Geller, L.N., Potter, H., 1999. Chromosome Missegregation and Trisomy 21 Mosaicism in Alzheimer's Disease. *Neurobiol. Dis.* **6** (3), 167-179.

Gerstner, A.O., Thiele, A., Tarnok, A., Machlitt, J., Oeken, J., Tannapfel, A., Weber, A., Bootz, F., 2005. Preoperative Detection of Laryngeal Cancer in Mucosal Swabs by Slide-Based Cytometry. *Eur. J. Cancer* **41** (3), 445-452.

Gerstner, A.O., Tarnok, A., 2002. Analysis of Fine-Needle Aspirate Biopsies from Solid Tumors by Laser Scanning Cytometry (LSC). *Curr. Protoc. Cytom* **Chapter 7** Unit 7.20.

Giasson, B.I., Ischiropoulos, H., Lee, V.M., Trojanowski, J.Q., 2002. The Relationship between oxidative/nitrative Stress and Pathological Inclusions in Alzheimer's and Parkinson's Diseases. *Free Radic. Biol. Med.* **32** (12), 1264-1275.

Gibson, G.E., Haroutunian, V., Zhang, H., Park, L.C., Shi, Q., Lesser, M., Mohs, R.C., Sheu, R.K., Blass, J.P., 2000. Mitochondrial Damage in Alzheimer's Disease Varies with Apolipoprotein E Genotype. *Ann. Neurol.* **48** (3), 297-303.

Gong, C.X., Shaikh, S., Wang, J.Z., Zaidi, T., Grundke-Iqbal, I., Iqbal, K., 1995. Phosphatase Activity Toward Abnormally Phosphorylated Tau: Decrease in Alzheimer Disease Brain. *J. Neurochem.* **65** (2), 732-738.

Gong, C.X., Singh, T.J., Grundke-Iqbal, I., Iqbal, K., 1993. Phosphoprotein Phosphatase Activities in Alzheimer Disease Brain. *J. Neurochem.* **61** (3), 921-927.

Gonzalez, J.E., Roch-Lefevre, S.H., Mandina, T., Garcia, O., Roy, L., 2010. Induction of Gamma-H2AX Foci in Human Exfoliated Buccal Cells After in Vitro Exposure to Ionising Radiation. *Int. J. Radiat. Biol.* **86** (9), 752-759.

Gorczyca, W., Davidian, M., Gherson, J., Ashikari, R., Darzynkiewicz, Z., Melamed, M.R., 1998. Laser Scanning Cytometry Quantification of Estrogen Receptors in Breast Cancer. *Anal. Quant. Cytol. Histol.* **20** (6), 470-476.

Gorczyca, W., Melamed, M.R., Darzynkiewicz, Z., 1996. Laser Scanning Cytometer (LSC) Analysis of Fraction of Labelled Mitoses (FLM). *Cell Prolif.* **29** (10), 539-547.

Goukassian, D., Gad, F., Yaar, M., Eller, M.S., Nehal, U.S., Gilchrest, B.A., 2000. Mechanisms and Implications of the Age-Associated Decrease in DNA Repair Capacity. *FASEB J.* **14** (10), 1325-1334.

Graeber, M.B., Kosel, S., Egensperger, R., Banati, R.B., Muller, U., Bise, K., Hoff, P., Moller, H.J., Fujisawa, K., Mehraein, P., 1997. Rediscovery of the Case Described by Alois Alzheimer in 1911: Historical, Histological and Molecular Genetic Analysis. *Neurogenetics* **1** (1), 73-80.

Grana, X., Reddy, E.P., 1995. Cell Cycle Control in Mammalian Cells: Role of Cyclins, Cyclin Dependent Kinases (CDKs), Growth Suppressor Genes and Cyclin-Dependent Kinase Inhibitors (CKIs). *Oncogene* **11** (2), 211-219.

Grierson, A.M., Mitchell, P., Adams, C.L., Mowat, A.M., Brewer, J.M., Harnett, M.M., Garside, P., 2005. Direct Quantitation of T Cell Signaling by Laser Scanning Cytometry. *J. Immunol. Methods* **301** (1-2), 140-153.

Grosgen, S., Grimm, M.O., Friess, P., Hartmann, T., 2010. Role of Amyloid Beta in Lipid Homeostasis. *Biochim. Biophys. Acta* **1801** (8), 966-974.

Grundke-Iqbal, I., Iqbal, K., Tung, Y.C., Quinlan, M., Wisniewski, H.M., Binder, L.I., 1986. Abnormal Phosphorylation of the Microtubule-Associated Protein Tau (Tau)

in Alzheimer Cytoskeletal Pathology. *Proc. Natl. Acad. Sci. U. S. A.* **83** (13), 4913-4917.

Guangda, X., Bangshun, X., Xiujian, L., Yangzhong, H., 1999. Apovarepsilon(4) Allele Increases the Risk for Exercise-Induced Silent Myocardial Ischemia in Non-Insulin-Dependent Diabetes Mellitus. *Atherosclerosis* **147** (2), 293-296.

Gupta, V.B., Laws, S.M., Villemagne, V.L., Ames, D., Bush, A.I., Ellis, K.A., Lui, J.K., Masters, C., Rowe, C.C., Szoeke, C., Taddei, K., Martins, R.N., AIBL Research Group, 2011. Plasma Apolipoprotein E and Alzheimer Disease Risk: The AIBL Study of Aging. *Neurology* **76** (12), 1091-1098.

Hampel, H., Prvulovic, D., 2012. Are Biomarkers Harmful to Recruitment and Retention in Alzheimer's Disease Clinical Trials? an International Perspective. *J. Nutr. Health Aging* **16** (4), 346-348.

Han, X., 2005. Lipid Alterations in the Earliest Clinically Recognizable Stage of Alzheimer's Disease: Implication of the Role of Lipids in the Pathogenesis of Alzheimer's Disease. *Curr. Alzheimer Res.* **2** (1), 65-77.

Han, X., Holtzman, D.M., McKeel, D.W.,Jr, 2001. Plasmalogen Deficiency in Early Alzheimer's Disease Subjects and in Animal Models: Molecular Characterization using Electrospray Ionization Mass Spectrometry. *J. Neurochem.* **77** (4), 1168-1180.

Harris, F.M., Brecht, W.J., Xu, Q., Tesseur, I., Kekonius, L., Wyss-Coray, T., Fish, J.D., Masliah, E., Hopkins, P.C., Scearce-Levie, K., Weisgraber, K.H., Mucke, L., Mahley, R.W., Huang, Y., 2003. Carboxyl-Terminal-Truncated Apolipoprotein E4 Causes Alzheimer's Disease-Like Neurodegeneration and Behavioral Deficits in Transgenic Mice. *Proc. Natl. Acad. Sci. U. S. A.* **100** (19), 10966-10971.

Harty, L.C., Garcia-Closas, M., Rothman, N., Reid, Y.A., Tucker, M.A., Hartge, P., 2000. Collection of Buccal Cell DNA using Treated Cards. *Cancer Epidemiol. Biomarkers Prev.* **9** (5), 501-506.

Hattori, H., Matsumoto, M., Iwai, K., Tsuchiya, H., Miyauchi, E., Takasaki, M., Kamino, K., Munehira, J., Kimura, Y., Kawanishi, K., Hoshino, T., Murai, H., Ogata, H., Maruyama, H., Yoshida, H., 2002. The Tau Protein of Oral Epithelium Increases in Alzheimer's Disease. *J. Gerontol. A Biol. Sci. Med. Sci.* **57** (1), M64-70.

Hayney, M.S., Poland, G.A., Lipsky, J.J., 1996. A Noninvasive 'Swish and Spit' Method for Collecting Nucleated Cells for HLA Typing by PCR in Population Studies. *Hum. Hered.* **46** (2), 108-111.

Henriksen, M., Miller, B., Newmark, J., Al-Kofahi, Y., Holden, E., 2011. Laser Scanning Cytometry and its Applications: A Pioneering Technology in the Field of Quantitative Imaging Cytometry. *Methods Cell Biol.* **102** 161-205.

Herz, J., Beffert, U., 2000. Apolipoprotein E Receptors: Linking Brain Development and Alzheimer's Disease. *Nat. Rev. Neurosci.* **1** (1), 51-58.

Hill, M.W., Epithelial proliferation and turn over in oral epithelia and epidermis with age. In: The Effect of Ageing in the Oral Mucosa and Skin, Bocca Raton: CRC Press, London (UK), 1994a, pp. 75-83.

Hill, M.W., The structural aspects of ageing in the oral mucosa. In: The Effect of Ageing in the Oral Mucosa and Skin, Bocca Raton: CRC Press, London (UK), 1994b, pp. 65-74.

Hodge, A., Patterson, A.J., Brown, W.J., Ireland, P., Giles, G., 2000. The Anti Cancer Council of Victoria FFQ: Relative Validity of Nutrient Intakes Compared with Weighed Food Records in Young to Middle-Aged Women in a Study of Iron Supplementation. *Aust. N. Z. J. Public Health* **24** (6), 576-583.

Huang, H.C., Jiang, Z.F., 2009. Accumulated Amyloid-Beta Peptide and Hyperphosphorylated Tau Protein: Relationship and Links in Alzheimer's Disease. *J. Alzheimers Dis.* **16** (1), 15-27.

Huang, X., Halicka, H.D., Traganos, F., Tanaka, T., Kurose, A., Darzynkiewicz, Z., 2005. Cytometric Assessment of DNA Damage in Relation to Cell Cycle Phase and Apoptosis. *Cell Prolif.* **38** (4), 223-243.

Huang, X., Halicka, H.D., Darzynkiewicz, Z., 2004a. Detection of Histone H2AX Phosphorylation on Ser-139 as an Indicator of DNA Damage (DNA Double-Strand Breaks). *Curr. Protoc. Cytom* **Chapter 7** Unit 7.27.

Huang, X., Okafuji, M., Traganos, F., Luther, E., Holden, E., Darzynkiewicz, Z., 2004b. Assessment of Histone H2AX Phosphorylation Induced by DNA Topoisomerase I and II Inhibitors Topotecan and Mitoxantrone and by the DNA Cross-Linking Agent Cisplatin. *Cytometry A.* **58** (2), 99-110.

Huang, Y., Liu, X.Q., Wyss-Coray, T., Brecht, W.J., Sanan, D.A., Mahley, R.W., 2001. Apolipoprotein E Fragments Present in Alzheimer's Disease Brains Induce Neurofibrillary Tangle-Like Intracellular Inclusions in Neurons. *Proc. Natl. Acad. Sci. U. S. A.* **98** (15), 8838-8843.

Hull, M.T., Warfel, K.A., 1983. Age-Related Changes in the Cutaneous Basal Lamina: Scanning Electron Microscopic Study. *J. Invest. Dermatol.* **81** (4), 378-380.

Hyman, B.T., Trojanowski, J.Q., 1997. Consensus Recommendations for the Postmortem Diagnosis of Alzheimer Disease from the National Institute on Aging and the Reagan Institute Working Group on Diagnostic Criteria for the Neuropathological Assessment of Alzheimer Disease. *J. Neuropathol. Exp. Neurol.* **56** (10), 1095-1097.

Iqbal, K., Alonso Adel, C., Chen, S., Chohan, M.O., El-Akkad, E., Gong, C.X., Khatoon, S., Li, B., Liu, F., Rahman, A., Tanimukai, H., Grundke-Iqbal, I., 2005.

Tau Pathology in Alzheimer Disease and Other Tauopathies. *Biochim. Biophys. Acta* **1739** (2-3), 198-210.

Iqbal, K., Grundke-Iqbal, I., 1998. Tau Phosphatase Activity as a Therapeutic Target for AD. *Drug News. Perspect.* **11** (1), 10-14.

Iqbal, K., Grundke-Iqbal, I., Smith, A.J., George, L., Tung, Y.C., Zaidi, T., 1989. Identification and Localization of a Tau Peptide to Paired Helical Filaments of Alzheimer Disease. *Proc. Natl. Acad. Sci. U. S. A.* **86** (14), 5646-5650.

Iqbal, K., Zaidi, T., Thompson, C.H., Merz, P.A., Wisniewski, H.M., 1984. Alzheimer Paired Helical Filaments: Bulk Isolation, Solubility, and Protein Composition. *Acta Neuropathol.* **62** (3), 167-177.

Jenkins, E.C., Velinov, M.T., Ye, L., Gu, H., Li, S., Jenkins, E.C.,Jr, Brooks, S.S., Pang, D., Devenny, D.A., Zigman, W.B., Schupf, N., Silverman, W.P., 2006. Telomere Shortening in T Lymphocytes of Older Individuals with Down Syndrome and Dementia. *Neurobiol. Aging* **27** (7), 941-945.

Ji, Z.S., Miranda, R.D., Newhouse, Y.M., Weisgraber, K.H., Huang, Y., Mahley, R.W., 2002. Apolipoprotein E4 Potentiates Amyloid Beta Peptide-Induced Lysosomal Leakage and Apoptosis in Neuronal Cells. *J. Biol. Chem.* **277** (24), 21821-21828.

Johnson, P.L., Klein, M.N., 1956. Application of the Papanicolaou Stain to Paraffin Sections. *Stain Technol.* **31** (5), 223-225.

Jovanovic, S.V., Clements, D., MacLeod, K., 1998. Biomarkers of Oxidative Stress are significantly Elevated in Down Syndrome. *Free Radic. Biol. Med.* **25** (9), 1044-1048.

Juan, G., Zoog, S.J., Ferbas, J., 2011. Leveraging Image Cytometry for the Development of Clinically Feasible Biomarkers: Evaluation of Activated Caspase-3 in Fine Needle Aspirate Biopsies. *Methods Cell Biol.* **102** 309-320.

Kamentsky, L.A., Kamentsky, L.D., Fletcher, J.A., Kurose, A., Sasaki, K., 1997. Methods for Automatic Multiparameter Analysis of Fluorescence in Situ Hybridized Specimens with a Laser Scanning Cytometer. *Cytometry* **27** (2), 117-125.

Kamino, K., Nagasaka, K., Imagawa, M., Yamamoto, H., Yoneda, H., Ueki, A., Kitamura, S., Namekata, K., Miki, T., Ohta, S., 2000. Deficiency in Mitochondrial Aldehyde Dehydrogenase Increases the Risk for Late-Onset Alzheimer's Disease in the Japanese Population. *Biochem. Biophys. Res. Commun.* **273** (1), 192-196.

Kamiya, N., Yokose, T., Kiyomatsu, Y., Fahey, M.T., Kodama, T., Mukai, K., 1999. Assessment of DNA Content in Formalin-Fixed, Paraffin-Embedded Tissue of Lung Cancer by Laser Scanning Cytometer. *Pathol. Int.* **49** (8), 695-701.

Khachaturian, Z.S., 1985. Diagnosis of Alzheimer's Disease. *Arch. Neurol.* **42** (11), 1097-1105.

Kimberly, W.T., Zheng, J.B., Town, T., Flavell, R.A., Selkoe, D.J., 2005. Physiological Regulation of the Beta-Amyloid Precursor Protein Signaling Domain by c-Jun N-Terminal Kinase JNK3 during Neuronal Differentiation. *J. Neurosci.* **25** (23), 5533-5543.

Kimura, M., Stone, R.C., Hunt, S.C., Skurnick, J., Lu, X., Cao, X., Harley, C.B., Aviv, A., 2010. Measurement of Telomere Length by the Southern Blot Analysis of Terminal Restriction Fragment Lengths. *Nat. Protoc.* **5** (9), 1596-1607.

King, I.B., Satia-Abouta, J., Thornquist, M.D., Bigler, J., Patterson, R.E., Kristal, A.R., Shattuck, A.L., Potter, J.D., White, E., 2002. Buccal Cell DNA Yield, Quality, and Collection Costs: Comparison of Methods for Large-Scale Studies. *Cancer Epidemiol. Biomarkers Prev.* **11** (10 Pt 1), 1130-1133.

Kirby, A., Woodward, A., Jackson, S., Wang, Y., Crawford, M.A., 2010a. The Association of Fatty Acid Deficiency Symptoms (FADS) with Actual Essential Fatty Acid Status in Cheek Cells. *Prostaglandins Leukot. Essent. Fatty Acids* **83** (1), 1-8.

Kirby, A., Woodward, A., Jackson, S., Wang, Y., Crawford, M.A., 2010b. Childrens' Learning and Behaviour and the Association with Cheek Cell Polyunsaturated Fatty Acid Levels. *Res. Dev. Disabil.* **31** (3), 731-742.

Kirsch-Volders, M., Fenech, M., 2001. Inclusion of Micronuclei in Non-Divided Mononuclear Lymphocytes and necrosis/apoptosis may Provide a More Comprehensive Cytokinesis Block Micronucleus Assay for Biomonitoring Purposes. *Mutagenesis* **16** (1), 51-58.

Ko, S.Y., Chang, K.W., Lin, S.C., Hsu, H.C., Liu, T.Y., 2007. The Repressive Effect of Green Tea Ingredients on Amyloid Precursor Protein (APP) Expression in Oral Carcinoma Cells in Vitro and in Vivo. *Cancer Lett.* **245** (1-2), 81-89.

Kolsch, H., Heun, R., Jessen, F., Popp, J., Hentschel, F., Maier, W., Lutjohann, D., 2010. Alterations of Cholesterol Precursor Levels in Alzheimer's Disease. *Biochim. Biophys. Acta* **1801** (8), 945-950.

Koo, E.H., 2002. The Beta-Amyloid Precursor Protein (APP) and Alzheimer's Disease: Does the Tail Wag the Dog? *Traffic* **3** (11), 763-770.

Koopman, R., Schaart, G., Hesselink, M.K., 2001. Optimisation of Oil Red O Staining Permits Combination with Immunofluorescence and Automated Quantification of Lipids. *Histochem. Cell Biol.* **116** (1), 63-68.

Krull, D.L., Peterson, R.A., 2011. Preclinical Applications of Quantitative Imaging Cytometry to Support Drug Discovery. *Methods Cell Biol.* **102** 291-308.

Kuliffay, P., Sanislo, L., Galbavy, S., 2010. Chromatin Texture, DNA Index, and S-Phase Fraction in Primary Breast Carcinoma Cells Analysed by Laser Scanning Cytometry. *Bratisl. Lek. Listy* **111** (1), 4-8.

Kummer, C., Wehner, S., Quast, T., Werner, S., Herzog, V., 2002. Expression and Potential Function of Beta-Amyloid Precursor Proteins during Cutaneous Wound Repair. *Exp. Cell Res.* **280** (2), 222-232.

Kurose, A., Tanaka, T., Huang, X., Halicka, H.D., Traganos, F., Dai, W., Darzynkiewicz, Z., 2005. Assessment of ATM Phosphorylation on Ser-1981 Induced by DNA Topoisomerase I and II Inhibitors in Relation to Ser-139-Histone H2AX Phosphorylation, Cell Cycle Phase, and Apoptosis. *Cytometry A.* **68** (1), 1-9.

Kvetnoy, I.M., Hernandez-Yago, J., Kvetnaia, T.V., Khavinson, V.K., Malinin, V.V., Yarilin, A.A., Sharova, N.I., Blesa, J.R., Anisimov, V.N., Lenskaia, L.V., Sluchevskaia, S.F., Chekalina, S.I., Tokarev, O.Y., Yuzhakov, V.V., 2000. Tau-Protein Expression in Human Blood Lymphocytes: A Promising Marker and Suitable Sample for Life-Time Diagnosis of Alzheimer's Disease. *Neuro Endocrinol. Lett.* **21** (4), 313-318.

Le Marchand, L., Lum-Jones, A., Saltzman, B., Visaya, V., Nomura, A.M., Kolonel, L.N., 2001. Feasibility of Collecting Buccal Cell DNA by Mail in a Cohort Study. *Cancer Epidemiol. Biomarkers Prev.* **10** (6), 701-703.

Lee, E.J., Patten, G.S., Burnard, S.L., McMurchie, E.J., 1994. Osmotic and Other Properties of Isolated Human Cheek Epithelial Cells. *Am. J. Physiol.* **267** (1 Pt 1), C75-83.

Lee, H.G., Casadesus, G., Zhu, X., Castellani, R.J., McShea, A., Perry, G., Petersen, R.B., Bajic, V., Smith, M.A., 2009. Cell Cycle Re-Entry Mediated Neurodegeneration and its Treatment Role in the Pathogenesis of Alzheimer's Disease. *Neurochem. Int.* **54** (2), 84-88.

Lee, T.S., Goh, L., Chong, M.S., Chua, S.M., Chen, G.B., Feng, L., Lim, W.S., Chan, M., Ng, T.P., Ranga Krishnan, K., 2012. Downregulation of TOMM40 Expression in the Blood of Alzheimer Disease Subjects Compared with Matched Controls. *J. Psychiatr. Res.* **46** (6), 828-830.

Leifert, W.R., Francois, M., Thomas, P., Luther, E., Holden, E., Fenech, M., 2011. Automation of the Buccal Micronucleus Cytome Assay using Laser Scanning Cytometry. *Methods Cell Biol.* **102** 321-339.

Leinonen, V., Alafuzoff, I., Aalto, S., Suotunen, T., Savolainen, S., Nagren, K., Tapiola, T., Pirttila, T., Rinne, J., Jaaskelainen, J.E., Soininen, H., Rinne, J.O., 2008. Assessment of Beta-Amyloid in a Frontal Cortical Brain Biopsy Specimen and by Positron Emission Tomography with Carbon 11-Labeled Pittsburgh Compound B. *Arch. Neurol.* **65** (10), 1304-1309.

Lesne, S., Koh, M.T., Kotilinek, L., Kayed, R., Glabe, C.G., Yang, A., Gallagher, M., Ashe, K.H., 2006. A Specific Amyloid-Beta Protein Assembly in the Brain Impairs Memory. *Nature* **440** (7082), 352-357.

Lillie, R.D., Conn, H.J. (Eds.), 1969. H. J. Conn's Biological stains. Williams & Wilkins, Baltimore.

Lin, J., Page, K.A., Della-Fera, M.A., Baile, C.A., 2004. Evaluation of Adipocyte Apoptosis by Laser Scanning Cytometry. *Int. J. Obes. Relat. Metab. Disord.* **28** (12), 1535-1540.

Ljungberg, M.C., Dayanandan, R., Asuni, A., Rupniak, T.H., Anderton, B.H., Lovestone, S., 2002. Truncated apoE Forms Tangle-Like Structures in a Neuronal Cell Line. *Neuroreport* **13** (6), 867-870.

Loning, T., Staquet, M.J., Thivolet, J., Seifert, G., 1980. Keratin Polypeptides Distribution in Normal and Diseased Human Epidermis and Oral Mucosa. Immunohistochemical Study on Unaltered Epithelium and Inflammatory, Premalignant and Malignant Lesions. *Virchows Arch. A Pathol. Anat. Histol.* **388** (3), 273-288.

Lovat, L.B., Persey, M.R., Madhoo, S., Pepys, M.B., Hawkins, P.N., 1998. The Liver in Systemic Amyloidosis: Insights from 123I Serum Amyloid P Component Scintigraphy in 484 Patients. *Gut* **42** (5), 727-734.

Lueck, N.E., Robinson, R.A., 2008. High Levels of Expression of Cytokeratin 5 are Strongly Correlated with Poor Survival in Higher Grades of Mucoepidermoid Carcinoma. *J. Clin. Pathol.* **61** (7), 837-840.

Lum, A., Le Marchand, L., 1998. A Simple Mouthwash Method for Obtaining Genomic DNA in Molecular Epidemiological Studies. *Cancer Epidemiol. Biomarkers Prev.* **7** (8), 719-724.

Luther, E., Kamentsky, L.A., 1996. Resolution of Mitotic Cells using Laser Scanning Cytometry. *Cytometry* **23** (4), 272-278.

Luther, E., Kamentsky, L., Henriksen, M., Holden, E., 2004. Next-Generation Laser Scanning Cytometry. *Methods Cell Biol.* **75** 185-218. United States.

Mach, W.J., Thimmesch, A.R., Orr, J.A., Slusser, J.G., Pierce, J.D., 2010. Flow Cytometry and Laser Scanning Cytometry, a Comparison of Techniques. *J. Clin. Monit. Comput.* **24** (4), 251-259.

Mahley, R.W., Weisgraber, K.H., Huang, Y., 2006. Apolipoprotein E4: A Causative Factor and Therapeutic Target in Neuropathology, Including Alzheimer's Disease. *Proc. Natl. Acad. Sci. U. S. A.* **103** (15), 5644-5651.

Mahley, R.W., 1988. Apolipoprotein E: Cholesterol Transport Protein with Expanding Role in Cell Biology. *Science* **240** (4852), 622-630.

Malik, B., Fernandes, C., Killick, R., Wroe, R., Usardi, A., Williamson, R., Kellie, S., Anderton, B.H., Reynolds, C.H., 2012. Oligomeric Amyloid-Beta Peptide Affects the Expression of Genes Involved in Steroid and Lipid Metabolism in Primary Neurons. *Neurochem. Int.* **61** (3), 321-333.

Marin, D.B., Green, C.R., Schmeidler, J., Harvey, P.D., Lawlor, B.A., Ryan, T.M., Aryan, M., Davis, K.L., Mohs, R.C., 1997. Noncognitive Disturbances in

Alzheimer's Disease: Frequency, Longitudinal Course, and Relationship to Cognitive Symptoms. *J. Am. Geriatr. Soc.* **45** (11), 1331-1338.

Martin, V., Fabelo, N., Santpere, G., Puig, B., Marin, R., Ferrer, I., Diaz, M., 2010. Lipid Alterations in Lipid Rafts from Alzheimer's Disease Human Brain Cortex. *J. Alzheimers Dis.* **19** (2), 489-502.

Martins, I.J., Berger, T., Sharman, M.J., Verdile, G., Fuller, S.J., Martins, R.N., 2009. Cholesterol Metabolism and Transport in the Pathogenesis of Alzheimer's Disease. *J. Neurochem.* **111** (6), 1275-1308.

Martins, I.J., Hone, E., Foster, J.K., Sunram-Lea, S.I., Gnjec, A., Fuller, S.J., Nolan, D., Gandy, S.E., Martins, R.N., 2006. Apolipoprotein E, Cholesterol Metabolism, Diabetes, and the Convergence of Risk Factors for Alzheimer's Disease and Cardiovascular Disease. *Mol. Psychiatry* **11** (8), 721-736.

Martins, R.N., Robinson, P.J., Chleboun, J.O., Beyreuther, K., Masters, C.L., 1991. The Molecular Pathology of Amyloid Deposition in Alzheimer's Disease. *Mol. Neurobiol.* **5** (2-4), 389-398.

Masters, B.R., Gonnord, G., Corcuff, P., 1997. Three-Dimensional Microscopic Biopsy of in Vivo Human Skin: A New Technique Based on a Flexible Confocal Microscope. *J. Microsc.* **185** (Pt 3), 329-338.

Matoltsy, A.G., Matoltsy, M.N., Cliffel, P.J., 1983. Characterization of Keratin Polypeptides of Normal and Psoriatic Horny Cells. *J. Invest. Dermatol.* **80** (3), 185-188.

Mattsson, N., Tabatabaei, S., Johansson, P., Hansson, O., Andreasson, U., Mansson, J.E., Johansson, J.O., Olsson, B., Wallin, A., Svensson, J., Blennow, K., Zetterberg, H., 2011. Cerebrospinal Fluid Microglial Markers in Alzheimer's Disease: Elevated Chitotriosidase Activity but Lack of Diagnostic Utility. *Neuromolecular Med.* **13** (2), 151-159.

McKhann, G., Drachman, D., Folstein, M., Katzman, R., Price, D., Stadlan, E.M., 1984. Clinical Diagnosis of Alzheimer's Disease: Report of the NINCDS-ADRDA Work Group Under the Auspices of Department of Health and Human Services Task Force on Alzheimer's Disease. *Neurology* **34** (7), 939-944.

McMurchie, E.J., Margetts, B.M., Beilin, L.J., Croft, K.D., Vandongen, R., Armstrong, B.K., 1984. Dietary-Induced Changes in the Fatty Acid Composition of Human Cheek Cell Phospholipids: Correlation with Changes in the Dietary polyunsaturated/saturated Fat Ratio. *Am. J. Clin. Nutr.* **39** (6), 975-980.

McShea, A., Lee, H.G., Petersen, R.B., Casadesus, G., Vincent, I., Linford, N.J., Funk, J.O., Shapiro, R.A., Smith, M.A., 2007. Neuronal Cell Cycle Re-Entry Mediates Alzheimer Disease-Type Changes. *Biochim. Biophys. Acta* **1772** (4), 467-472.

Michalczyk, A., Varigos, G., Smith, L., Ackland, M.L., 2004. Fresh and Cultured Buccal Cells as a Source of mRNA and Protein for Molecular Analysis. *BioTechniques* **37** (2), 262-4, 266-9.

Migliore, L., Coppede, F., Fenech, M., Thomas, P., 2011. Association of Micronucleus Frequency with Neurodegenerative Diseases. *Mutagenesis* **26** (1), 85-92.

Migliore, L., Fontana, I., Trippi, F., Colognato, R., Coppede, F., Tognoni, G., Nucciarone, B., Siciliano, G., 2005. Oxidative DNA Damage in Peripheral Leukocytes of Mild Cognitive Impairment and AD Patients. *Neurobiol. Aging* **26** (5), 567-573.

Migliore, L., Coppede, F., 2002. Genetic and Environmental Factors in Cancer and Neurodegenerative Diseases. *Mutat. Res.* **512** (2-3), 135-153.

Migliore, L., Botto, N., Scarpato, R., Petrozzi, L., Cipriani, G., Bonuccelli, U., 1999. Preferential Occurrence of Chromosome 21 Malsegregation in Peripheral Blood Lymphocytes of Alzheimer Disease Patients. *Cytogenet. Cell Genet.* **87** (1-2), 41-46.

Migliore, L., Testa, A., Scarpato, R., Pavese, N., Petrozzi, L., Bonuccelli, U., 1997. Spontaneous and Induced Aneuploidy in Peripheral Blood Lymphocytes of Patients with Alzheimer's Disease. *Hum. Genet.* **101** (3), 299-305.

Milward, E.A., Papadopoulos, R., Fuller, S.J., Moir, R.D., Small, D., Beyreuther, K., Masters, C.L., 1992. The Amyloid Protein Precursor of Alzheimer's Disease is a Mediator of the Effects of Nerve Growth Factor on Neurite Outgrowth. *Neuron* **9** (1), 129-137.

Mirra, S.S., Heyman, A., McKeel, D., Sumi, S.M., Crain, B.J., Brownlee, L.M., Vogel, F.S., Hughes, J.P., van Belle, G., Berg, L., 1991. The Consortium to Establish a Registry for Alzheimer's Disease (CERAD). Part II. Standardization of the Neuropathologic Assessment of Alzheimer's Disease. *Neurology* **41** (4), 479-486.

Miyata, M., Smith, J.D., 1996. Apolipoprotein E Allele-Specific Antioxidant Activity and Effects on Cytotoxicity by Oxidative Insults and Beta-Amyloid Peptides. *Nat. Genet.* **14** (1), 55-61.

Moll, R., Franke, W.W., Schiller, D.L., Geiger, B., Krepler, R., 1982a. The Catalog of Human Cytokeratins: Patterns of Expression in Normal Epithelia, Tumors and Cultured Cells. *Cell* **31** (1), 11-24.

Moll, R., Moll, I., Wiest, W., 1982b. Changes in the Pattern of Cytokeratin Polypeptides in Epidermis and Hair Follicles during Skin Development in Human Fetuses. *Differentiation* **23** (2), 170-178.

Mosch, B., Morawski, M., Mittag, A., Lenz, D., Tarnok, A., Arendt, T., 2007. Aneuploidy and DNA Replication in the Normal Human Brain and Alzheimer's Disease. *J. Neurosci.* **27** (26), 6859-6867.

Mosch, B., Mittag, A., Lenz, D., Arendt, T., Tarnok, A., 2006. Laser Scanning Cytometry in Human Brain Slices. *Cytometry A*. **69** (3), 135-138.

Mutoh, M., Komiya, M., Teraoka, N., Ueno, T., Takahashi, M., Kitahashi, T., Sugimura, T., Wakabayashi, K., 2009. Overexpression of Low-Density Lipoprotein Receptor and Lipid Accumulation in Intestinal Polyps in Min Mice. *Int. J. Cancer* **125** (11), 2505-2510.

Myerson, S., Hemingway, H., Budget, R., Martin, J., Humphries, S., Montgomery, H., 1999. Human Angiotensin I-Converting Enzyme Gene and Endurance Performance. *J. Appl. Physiol.* **87** (4), 1313-1316.

Myung, N.H., Zhu, X., Kruman, I.I., Castellani, R.J., Petersen, R.B., Siedlak, S.L., Perry, G., Smith, M.A., Lee, H.G., 2008. Evidence of DNA Damage in Alzheimer Disease: Phosphorylation of Histone H2AX in Astrocytes. *Age (Dordr)* **30** (4), 209-215.

Nelson, P.T., Alafuzoff, I., Bigio, E.H., Bouras, C., Braak, H., Cairns, N.J., Castellani, R.J., Crain, B.J., Davies, P., Del Tredici, K., Duyckaerts, C., Frosch, M.P., Haroutunian, V., Hof, P.R., Hulette, C.M., Hyman, B.T., Iwatsubo, T., Jellinger, K.A., Jicha, G.A., Kovari, E., Kukull, W.A., Leverenz, J.B., Love, S., Mackenzie, I.R., Mann, D.M., Masliah, E., McKee, A.C., Montine, T.J., Morris, J.C., Schneider, J.A., Sonnen, J.A., Thal, D.R., Trojanowski, J.Q., Troncoso, J.C., Wisniewski, T., Woltjer, R.L., Beach, T.G., 2012. Correlation of Alzheimer Disease Neuropathologic Changes with Cognitive Status: A Review of the Literature. *J. Neuropathol. Exp. Neurol.* **71** (5), 362-381.

Neumann, K., Farias, G., Slachevsky, A., Perez, P., Maccioni, R.B., 2011. Human Platelets Tau: A Potential Peripheral Marker for Alzheimer's Disease. *J. Alzheimers Dis.* **25** (1), 103-109.

Newton, J.R., Parkinson, D., Clench, M.R., 2006. Strategies for Examination of Alzheimer's Disease Amyloid Precursor Protein Isoforms. *Anal. Bioanal Chem.* **385** (4), 692-699.

Nunomura, A., Perry, G., Aliev, G., Hirai, K., Takeda, A., Balraj, E.K., Jones, P.K., Ghanbari, H., Wataya, T., Shimohama, S., Chiba, S., Atwood, C.S., Petersen, R.B., Smith, M.A., 2001. Oxidative Damage is the Earliest Event in Alzheimer Disease. *J. Neuropathol. Exp. Neurol.* **60** (8), 759-767.

O'Callaghan, N.J., Fenech, M., 2011. A Quantitative PCR Method for Measuring Absolute Telomere Length. *Biol. Proced. Online* **13** 3.

Ohta, S., Ohsawa, I., Kamino, K., Ando, F., Shimokata, H., 2004. Mitochondrial ALDH2 Deficiency as an Oxidative Stress. *Ann. N. Y. Acad. Sci.* **1011** 36-44.

Oster, T., Pillot, T., 2010. Docosahexaenoic Acid and Synaptic Protection in Alzheimer's Disease Mice. *Biochim. Biophys. Acta* **1801** (8), 791-798.

Oud, P.S., Henderik, J.B., Huysmans, A.C., Pahlplatz, M.M., Hermkens, H.G., Tas, J., James, J., Vooijs, G.P., 1984. The use of Light Green and Orange II as Quantitative Protein Stains, and their Combination with the Feulgen Method for the Simultaneous Determination of Protein and DNA. *Histochemistry* **80** (1), 49-57.

Padovani, A., Borroni, B., Colciaghi, F., Pettenati, C., Cottini, E., Agosti, C., Lenzi, G.L., Caltagirone, C., Trabucchi, M., Cattabeni, F., Di Luca, M., 2002. Abnormalities in the Pattern of Platelet Amyloid Precursor Protein Forms in Patients with Mild Cognitive Impairment and Alzheimer Disease. *Arch. Neurol.* **59** (1), 71-75.

Pani, A., Dessi, S., Diaz, G., La Colla, P., Abete, C., Mulas, C., Angius, F., Cannas, M.D., Orru, C.D., Cocco, P.L., Mandas, A., Putzu, P., Laurenzana, A., Cellai, C., Costanza, A.M., Bavazzano, A., Mocali, A., Paoletti, F., 2009a. Altered Cholesterol Ester Cycle in Skin Fibroblasts from Patients with Alzheimer's Disease. *J. Alzheimers Dis.* **18** (4), 829-841.

Pani, A., Mandas, A., Diaz, G., Abete, C., Cocco, P.L., Angius, F., Brundu, A., Mucaka, N., Pais, M.E., Saba, A., Barberini, L., Zaru, C., Palmas, M., Putzu, P.F., Mocali, A., Paoletti, F., La Colla, P., Dessi, S., 2009b. Accumulation of Neutral Lipids in Peripheral Blood Mononuclear Cells as a Distinctive Trait of Alzheimer Patients and Asymptomatic Subjects at Risk of Disease. *BMC Med.* **7** 66.

Panossian, L.A., Porter, V.R., Valenzuela, H.F., Zhu, X., Reback, E., Masterman, D., Cummings, J.L., Effros, R.B., 2003. Telomere Shortening in T Cells Correlates with Alzheimer's Disease Status. *Neurobiol. Aging* **24** (1), 77-84.

Papanicolaou, G.N., 1948. The Cell Smear Method of Diagnosing Cancer. *Am. J. Public Health Nations Health* **38** (2), 202-205.

Pastorino, L., Lu, K.P., 2006. Pathogenic Mechanisms in Alzheimer's Disease. *Eur. J. Pharmacol.* **545** (1), 29-38.

Patten, G.S., Leifert, W.R., Burnard, S.L., Head, R.J., McMurchie, E.J., 1996. Stimulation of Human Cheek Cell Na+/H+ Antiporter Activity by Saliva and Salivary Electrolytes: Amplification by Nigericin. *Mol. Cell. Biochem.* **154** (2), 133-141.

Perluigi, M., Butterfield, D.A., 2012. Oxidative Stress and Down Syndrome: A Route Toward Alzheimer-Like Dementia. *Curr. Gerontol. Geriatr. Res.* **2012** 724904.

Perry, G., Nunomura, A., Hirai, K., Zhu, X., Perez, M., Avila, J., Castellani, R.J., Atwood, C.S., Aliev, G., Sayre, L.M., Takeda, A., Smith, M.A., 2002. Is Oxidative Damage the Fundamental Pathogenic Mechanism of Alzheimer's and Other Neurodegenerative Diseases? *Free Radic. Biol. Med.* **33** (11), 1475-1479.

Perry, G., Castellani, R.J., Smith, M.A., Harris, P.L., Kubat, Z., Ghanbari, K., Jones, P.K., Cordone, G., Tabaton, M., Wolozin, B., Ghanbari, H., 2003. Oxidative Damage in the Olfactory System in Alzheimer's Disease. *Acta Neuropathol.* **106** (6), 552-556.

Petersen, R.C., Roberts, R.O., Knopman, D.S., Boeve, B.F., Geda, Y.E., Ivnik, R.J., Smith, G.E., Jack, C.R.,Jr, 2009. Mild Cognitive Impairment: Ten Years Later. *Arch. Neurol.* **66** (12), 1447-1455.

Petersen, R.C., 2000. Mild Cognitive Impairment: Transition between Aging and Alzheimer's Disease. *Neurologia* **15** (3), 93-101.

Petersen, R.C., Smith, G.E., Waring, S.C., Ivnik, R.J., Tangalos, E.G., Kokmen, E., 1999. Mild Cognitive Impairment: Clinical Characterization and Outcome. *Arch. Neurol.* **56** (3), 303-308.

Petersen, R.C., Smith, G.E., Ivnik, R.J., Tangalos, E.G., Schaid, D.J., Thibodeau, S.N., Kokmen, E., Waring, S.C., Kurland, L.T., 1995a. Apolipoprotein E Status as a Predictor of the Development of Alzheimer's Disease in Memory-Impaired Individuals. *JAMA* **273** (16), 1274-1278.

Petersen, R.C., Smith, G.E., Ivnik, R.J., Tangalos, E.G., Schaid, D.J., Thibodeau, S.N., Kokmen, E., Waring, S.C., Kurland, L.T., 1995b. Apolipoprotein E Status as a Predictor of the Development of Alzheimer's Disease in Memory-Impaired Individuals. *JAMA* **273** (16), 1274-1278.

Peterson, C., Goldman, J.E., 1986. Alterations in Calcium Content and Biochemical Processes in Cultured Skin Fibroblasts from Aged and Alzheimer Donors. *Proc. Natl. Acad. Sci. U. S. A.* **83** (8), 2758-2762.

Peterson, C., Ratan, R.R., Shelanski, M.L., Goldman, J.E., 1986. Cytosolic Free Calcium and Cell Spreading Decrease in Fibroblasts from Aged and Alzheimer Donors. *Proc. Natl. Acad. Sci. U. S. A.* **83** (20), 7999-8001.

Peterson, R.A., Krull, D.L., Butler, L., 2008. Applications of Laser Scanning Cytometry in Immunohistochemistry and Routine Histopathology. *Toxicol. Pathol.* **36** (1), 117-132.

Pines, J., 1995. Cyclins, CDKs and Cancer. *Semin. Cancer Biol.* **6** (2), 63-72.

Pines, J., 1994. Protein Kinases and Cell Cycle Control. *Semin. Cell Biol.* **5** (6), 399-408.

Potkin, S.G., Guffanti, G., Lakatos, A., Turner, J.A., Kruggel, F., Fallon, J.H., Saykin, A.J., Orro, A., Lupoli, S., Salvi, E., Weiner, M., Macciardi, F., Alzheimer's Disease Neuroimaging Initiative, 2009. Hippocampal Atrophy as a Quantitative Trait in a Genome-Wide Association Study Identifying Novel Susceptibility Genes for Alzheimer's Disease. *PLoS One* **4** (8), e6501.

Pozarowski, P., Holden, E., Darzynkiewicz, Z., 2006. Laser Scanning Cytometry: Principles and Applications. *Methods Mol. Biol.* **319** 165-192.

Pozarowski, P., Huang, X., Gong, R.W., Priebe, W., Darzynkiewicz, Z., 2004. Simple, Semiautomatic Assay of Cytostatic and Cytotoxic Effects of Antitumor Drugs by

Laser Scanning Cytometry: Effects of the Bis-Intercalator WP631 on Growth and Cell Cycle of T-24 Cells. *Cytometry A*. **57** (2), 113-119.

Pruimboom-Brees, I.M., Brees, D.J., Shen, A.C., Keener, M., Francone, O., Amacher, D.E., Loy, J.K., Kerlin, R.L., 2005. Using Laser Scanning Cytometry to Measure PPAR-Mediated Peroxisome Proliferation and Beta Oxidation. *Toxicol. Pathol*. **33** (1), 86-91.

Prvulovic, D., Hampel, H., 2011. Amyloid Beta (Abeta) and Phospho-Tau (p-Tau) as Diagnostic Biomarkers in Alzheimer's Disease. *Clin. Chem. Lab. Med*. **49** (3), 367-374.

Puglielli, L., Tanzi, R.E., Kovacs, D.M., 2003. Alzheimer's Disease: The Cholesterol Connection. *Nat. Neurosci*. **6** (4), 345-351.

Ramirez, M.J., Surralles, J., Galofre, P., Creus, A., Marcos, R., 1999. FISH Analysis of 1cen-1q12 Breakage, Chromosome 1 Numerical Abnormalities and Centromeric Content of Micronuclei in Buccal Cells from Thyroid Cancer and Hyperthyroidism Patients Treated with Radioactive Iodine. *Mutagenesis* **14** (1), 121-127.

Richard, F., Amouyel, P., 2001. Genetic Susceptibility Factors for Alzheimer's Disease. *Eur. J. Pharmacol*. **412** (1), 1-12.

Richards, B., Skoletsky, J., Shuber, A.P., Balfour, R., Stern, R.C., Dorkin, H.L., Parad, R.B., Witt, D., Klinger, K.W., 1993. Multiplex PCR Amplification from the CFTR Gene using DNA Prepared from Buccal brushes/swabs. *Hum. Mol. Genet*. **2** (2), 159-163.

Roher, A.E., Esh, C.L., Kokjohn, T.A., Castano, E.M., Van Vickle, G.D., Kalback, W.M., Patton, R.L., Luehrs, D.C., Daugs, I.D., Kuo, Y.M., Emmerling, M.R., Soares, H., Quinn, J.F., Kaye, J., Connor, D.J., Silverberg, N.B., Adler, C.H., Seward, J.D., Beach, T.G., Sabbagh, M.N., 2009. Amyloid Beta Peptides in Human Plasma and Tissues and their Significance for Alzheimer's Disease. *Alzheimers Dement*. **5** (1), 18-29.

Rosen, R.F., Tomidokoro, Y., Ghiso, J.A., Walker, L.C., 2010. SDS-PAGE/immunoblot Detection of Abeta Multimers in Human Cortical Tissue Homogenates using Antigen-Epitope Retrieval. *J. Vis. Exp*. **(38). pii: 1916. doi** (38), 10.3791/1916.

Runz, H., Rietdorf, J., Tomic, I., de Bernard, M., Beyreuther, K., Pepperkok, R., Hartmann, T., 2002. Inhibition of Intracellular Cholesterol Transport Alters Presenilin Localization and Amyloid Precursor Protein Processing in Neuronal Cells. *J. Neurosci*. **22** (5), 1679-1689.

Samani, N.J., Boultby, R., Butler, R., Thompson, J.R., Goodall, A.H., 2001. Telomere Shortening in Atherosclerosis. *Lancet* **358** (9280), 472-473.

Sampugna, J., Light, L., Enig, M.G., Jones, D.Y., Judd, J.T., Lanza, E., 1988. Cheek Cell Fatty Acids as Indicators of Dietary Lipids in Humans. *Lipids* **23** (2), 131-136.

Schneider, P., Hampel, H., Buerger, K., 2009. Biological Marker Candidates of Alzheimer's Disease in Blood, Plasma, and Serum. *CNS Neurosci. Ther.* **15** (4), 358-374.

Schubert, D., Cole, G., Saitoh, T., Oltersdorf, T., 1989. Amyloid Beta Protein Precursor is a Mitogen. *Biochem. Biophys. Res. Commun.* **162** (1), 83-88.

Schupf, N., Tang, M.X., Fukuyama, H., Manly, J., Andrews, H., Mehta, P., Ravetch, J., Mayeux, R., 2008. Peripheral Abeta Subspecies as Risk Biomarkers of Alzheimer's Disease. *Proc. Natl. Acad. Sci. U. S. A.* **105** (37), 14052-14057.

Schwartz, J.L., Muscat, J.E., Baker, V., Larios, E., Stephenson, G.D., Guo, W., Xie, T., Gu, X., Chung, F.L., 2003. Oral Cytology Assessment by Flow Cytometry of DNA Adducts, Aneuploidy, Proliferation and Apoptosis shows Differences between Smokers and Non-Smokers. *Oral Oncol.* **39** (8), 842-854.

Schweizer, J., Winter, H., Hill, M.W., Mackenzie, I.C., 1984. The Keratin Polypeptide Patterns in Heterotypically Recombined Epithelia of Skin and Mucosa of Adult Mouse. *Differentiation* **26** (2), 144-153.

Selkoe, D.J., 2001. Alzheimer's Disease Results from the Cerebral Accumulation and Cytotoxicity of Amyloid Beta-Protein. *J. Alzheimers Dis.* **3** (1), 75-80.

Selkoe, D.J., 1991. Amyloid Protein and Alzheimer's Disease. *Sci. Am.* **265** (5), 68-71, 74-6, 78.

Shapiro, I.M., Moar, M.H., Ohno, S., Klein, G., 1978. Acetic Acid Treatment Denatures DNA while Preserving Chromosomal Morphology during the in Situ Hybridization Procedure. *Exp. Cell Res.* **115** (2), 411-414.

Sherr, C.J., 1994. G1 Phase Progression: Cycling on Cue. *Cell* **79** (4), 551-555.

Sjogren, M., Davidsson, P., Tullberg, M., Minthon, L., Wallin, A., Wikkelso, C., Granerus, A.K., Vanderstichele, H., Vanmechelen, E., Blennow, K., 2001. Both Total and Phosphorylated Tau are Increased in Alzheimer's Disease. *J. Neurol. Neurosurg. Psychiatry.* **70** (5), 624-630.

Sloane, P.D., Zimmerman, S., Suchindran, C., Reed, P., Wang, L., Boustani, M., Sudha, S., 2002. The Public Health Impact of Alzheimer's Disease, 2000-2050: Potential Implication of Treatment Advances. *Annu. Rev. Public Health* **23** 213-231.

Smith, A.D., 2008. The Worldwide Challenge of the Dementias: A Role for B Vitamins and Homocysteine? *Food Nutr. Bull.* **29** (2 Suppl), S143-72.

Soderberg, M., Edlund, C., Kristensson, K., Dallner, G., 1990. Lipid Compositions of Different Regions of the Human Brain during Aging. *J. Neurochem.* **54** (2), 415-423.

Soderberg, M., Edlund, C., Alafuzoff, I., Kristensson, K., Dallner, G., 1992. Lipid Composition in Different Regions of the Brain in Alzheimer's disease/senile Dementia of Alzheimer's Type. *J. Neurochem.* **59** (5), 1646-1653.

Song, F., Poljak, A., Valenzuela, M., Mayeux, R., Smythe, G.A., Sachdev, P.S., 2011. Meta-Analysis of Plasma Amyloid-Beta Levels in Alzheimer's Disease. *J. Alzheimers Dis.* **26** (2), 365-375.

Song, J., Wang, S., Tan, M., Jia, J., 2012. G1/S Checkpoint Proteins in Peripheral Blood Lymphocytes are Potentially Diagnostic Biomarkers for Alzheimer's Disease. *Neurosci. Lett.* **526** (2), 144-149.

Sotgiu, S., Piras, M.R., Barone, R., Arru, G., Fois, M.L., Rosati, G., Musumeci, S., 2007. Chitotriosidase and Alzheimer's Disease. *Curr. Alzheimer Res.* **4** (3), 295-296.

Spires-Jones, T.L., Stoothoff, W.H., de Calignon, A., Jones, P.B., Hyman, B.T., 2009. Tau Pathophysiology in Neurodegeneration: A Tangled Issue. *Trends Neurosci.* **32** (3), 150-159.

Spivack, S.D., Hurteau, G.J., Jain, R., Kumar, S.V., Aldous, K.M., Gierthy, J.F., Kaminsky, L.S., 2004. Gene-Environment Interaction Signatures by Quantitative mRNA Profiling in Exfoliated Buccal Mucosal Cells. *Cancer Res.* **64** (18), 6805-6813.

Squier, C.A., Kremer, M.J., 2001. Biology of Oral Mucosa and Esophagus. *J. Natl. Cancer. Inst. Monogr.* **(29)** (29), 7-15.

Squier, C.A., Johnson, N.W., Hopps, R.M., 1976. Human Oral Mucosa: Development, Structure and Function *Blackwell Scientific* 7-44.

Staquet, M.J., Viac, J., Thivolet, J., 1981. Keratin Polypeptide Modifications Induced by Human Papilloma Viruses (HPV). *Arch. Dermatol. Res.* **271** (1), 83-90.

Steinert, P.M., Peck, G.L., Idler, W.W., 1980. Structural Changes of Human Epidermal Alpha-Keratin in Disorders of Keratinization. *Curr. Probl. Dermatol.* **10** 391-406.

Stoopler, E.T., Sollecito, T.P., Chen, S.Y., 2003. Amyloid Deposition in the Oral Cavity: A Retrospective Study and Review of the Literature. *Oral Surg. Oral Med. Oral Pathol. Oral Radiol. Endod.* **95** (6), 674-680.

Strittmatter, W.J., Saunders, A.M., Goedert, M., Weisgraber, K.H., Dong, L.M., Jakes, R., Huang, D.Y., Pericak-Vance, M., Schmechel, D., Roses, A.D., 1994. Isoform-Specific Interactions of Apolipoprotein E with Microtubule-Associated Protein Tau: Implications for Alzheimer Disease. *Proc. Natl. Acad. Sci. U. S. A.* **91** (23), 11183-11186.

Strittmatter, W.J., Saunders, A.M., Schmechel, D., Pericakvance, M., Enghild, J., Salvesen, G.S., Roses, A.D., 1993. Apolipoprotein-E - High-Avidity Binding to

Beta-Amyloid and Increased Frequency of Type-4 Allele in Late-Onset Familial Alzheimer-Disease. *Proc. Natl. Acad. Sci. U. S. A.* **90** (5), 1977-1981.

Sun, T.T., Eichner, R., Nelson, W.G., Tseng, S.C., Weiss, R.A., Jarvinen, M., Woodcock-Mitchell, J., 1983. Keratin Classes: Molecular Markers for Different Types of Epithelial Differentiation. *J. Invest. Dermatol.* **81** (1 Suppl), 109s-15s.

Taddei, K., Clarnette, R., Gandy, S.E., Martins, R.N., 1997. Increased Plasma Apolipoprotein E (apoE) Levels in Alzheimer's Disease. *Neurosci. Lett.* **223** (1), 29-32.

Takubo, K., Aida, J., Izumiyama-Shimomura, N., Ishikawa, N., Sawabe, M., Kurabayashi, R., Shiraishi, H., Arai, T., Nakamura, K., 2010. Changes of Telomere Length with Aging. *Geriatr. Gerontol. Int.* **10 Suppl 1** S197-206.

Tanaka, T., Halicka, D., Traganos, F., Darzynkiewicz, Z., 2009. Cytometric Analysis of DNA Damage: Phosphorylation of Histone H2AX as a Marker of DNA Double-Strand Breaks (DSBs). *Methods Mol. Biol.* **523** 161-168.

Tanaka, T., Huang, X., Halicka, H.D., Zhao, H., Traganos, F., Albino, A.P., Dai, W., Darzynkiewicz, Z., 2007. Cytometry of ATM Activation and Histone H2AX Phosphorylation to Estimate Extent of DNA Damage Induced by Exogenous Agents. *Cytometry A.* **71** (9), 648-661.

Tarnok, A., Gerstner, A.O., 2003. Immunophenotyping using a Laser Scanning Cytometer. *Curr. Protoc. Cytom* **Chapter 6** Unit 6.13.

Tesseur, I., Van Dorpe, J., Spittaels, K., Van den Haute, C., Moechars, D., Van Leuven, F., 2000. Expression of Human Apolipoprotein E4 in Neurons Causes Hyperphosphorylation of Protein Tau in the Brains of Transgenic Mice. *Am. J. Pathol.* **156** (3), 951-964.

Thambisetty, M., Lovestone, S., 2010. Blood-Based Biomarkers of Alzheimer's Disease: Challenging but Feasible. *Biomark Med.* **4** (1), 65-79.

Thomas, D.R., 2001. Age-Related Changes in Wound Healing. *Drugs Aging* **18** (8), 607-620.

Thomas, P., Holland, N., Bolognesi, C., Kirsch-Volders, M., Bonassi, S., Zeiger, E., Knasmueller, S., Fenech, M., 2009. Buccal Micronucleus Cytome Assay. *Nat. Protoc.* **4** (6), 825-837.

Thomas, P., Fenech, M., 2008. Chromosome 17 and 21 Aneuploidy in Buccal Cells is Increased with Ageing and in Alzheimer's Disease. *Mutagenesis* **23** (1), 57-65.

Thomas, P., Harvey, S., Gruner, T., Fenech, M., 2008a. The Buccal Cytome and Micronucleus Frequency is Substantially Altered in Down's Syndrome and Normal Ageing Compared to Young Healthy Controls. *Mutat. Res.* **638** (1-2), 37-47.

Thomas, P., O'Callaghan, N.J., Fenech, M., 2008b. Telomere Length in White Blood Cells, Buccal Cells and Brain Tissue and its Variation with Ageing and Alzheimer's Disease. *Mech. Ageing Dev.* **129** (4), 183-190.

Thomas, P., Fenech, M., 2007. A Review of Genome Mutation and Alzheimer's Disease. *Mutagenesis* **22** (1), 15-33.

Thomas, P., Hecker, J., Faunt, J., Fenech, M., 2007. Buccal Micronucleus Cytome Biomarkers may be Associated with Alzheimer's Disease. *Mutagenesis* **22** (6), 371-379.

Trippi, F., Botto, N., Scarpato, R., Petrozzi, L., Bonuccelli, U., Latorraca, S., Sorbi, S., Migliore, L., 2001. Spontaneous and Induced Chromosome Damage in Somatic Cells of Sporadic and Familial Alzheimer's Disease Patients. *Mutagenesis* **16** (4), 323-327.

Tseng, S.C., Jarvinen, M.J., Nelson, W.G., Huang, J.W., Woodcock-Mitchell, J., Sun, T.T., 1982. Correlation of Specific Keratins with Different Types of Epithelial Differentiation: Monoclonal Antibody Studies. *Cell* **30** (2), 361-372.

Tsujioka, T., Tochigi, A., Kishimoto, M., Kondo, T., Tasaka, T., Wada, H., Sugihara, T., Yoshida, Y., Tohyama, K., 2008. DNA Ploidy and Cell Cycle Analyses in the Bone Marrow Cells of Patients with Megaloblastic Anemia using Laser Scanning Cytometry. *Cytometry B. Clin. Cytom* **74** (2), 104-109.

Tulchin, N., Chambon, M., Juan, G., Dikman, S., Strauchen, J., Ornstein, L., Billack, B., Woods, N.T., Monteiro, A.N., 2010. BRCA1 Protein and Nucleolin Colocalize in Breast Carcinoma Tissue and Cancer Cell Lines. *Am. J. Pathol.* **176** (3), 1203-1214.

Vaidya, M.M., Borges, A.M., Pradhan, S.A., Rajpal, R.M., Bhisey, A.N., 1989. Altered Keratin Expression in Buccal Mucosal Squamous Cell Carcinoma. *J. Oral Pathol. Med.* **18** (5), 282-286.

Van Schooten, F.J., Besaratinia, A., De Flora, S., D'Agostini, F., Izzotti, A., Camoirano, A., Balm, A.J., Dallinga, J.W., Bast, A., Haenen, G.R., Van't Veer, L., Baas, P., Sakai, H., Van Zandwijk, N., 2002. Effects of Oral Administration of N-Acetyl-L-Cysteine: A Multi-Biomarker Study in Smokers. *Cancer Epidemiol. Biomarkers Prev.* **11** (2), 167-175.

Veiro, J.A., Cummins, P.G., 1994. Imaging of Skin Epidermis from various Origins using Confocal Laser Scanning Microscopy. *Dermatology* **189** (1), 16-22.

Villemagne, V.L., Rowe, C.C., Macfarlane, S., Novakovic, K.E., Masters, C.L., 2005. Imaginem Oblivionis: The Prospects of Neuroimaging for Early Detection of Alzheimer's Disease. *J. Clin. Neurosci.* **12** (3), 221-230.

Waldemar, G., Dubois, B., Emre, M., Georges, J., McKeith, I.G., Rossor, M., Scheltens, P., Tariska, P., Winblad, B., EFNS, 2007. Recommendations for the Diagnosis and

Management of Alzheimer's Disease and Other Disorders Associated with Dementia: EFNS Guideline. *Eur. J. Neurol.* **14** (1), e1-26.

Wang, J.Z., Grundke-Iqbal, I., Iqbal, K., 2007. Kinases and Phosphatases and Tau Sites Involved in Alzheimer Neurofibrillary Degeneration. *Eur. J. Neurosci.* **25** (1), 59-68.

Wang, W., Bu, B., Xie, M., Zhang, M., Yu, Z., Tao, D., 2009. Neural Cell Cycle Dysregulation and Central Nervous System Diseases. *Prog. Neurobiol.* **89** (1), 1-17.

Watabe-Rudolph, M., Song, Z., Lausser, L., Schnack, C., Begus-Nahrmann, Y., Scheithauer, M.O., Rettinger, G., Otto, M., Tumani, H., Thal, D.R., Attems, J., Jellinger, K.A., Kestler, H.A., von Arnim, C.A., Rudolph, K.L., 2012. Chitinase Enzyme Activity in CSF is a Powerful Biomarker of Alzheimer Disease. *Neurology* **78** (8), 569-577.

Weiss, R.A., Eichner, R., Sun, T.T., 1984. Monoclonal Antibody Analysis of Keratin Expression in Epidermal Diseases: A 48- and 56-Kdalton Keratin as Molecular Markers for Hyperproliferative Keratinocytes. *J. Cell Biol.* **98** (4), 1397-1406.

WHO Press., 2006. Mental Health: Evidence and Research Department of Mental Health and Substance Abuse World Health Organization, Disease Control Priorities Related to Mental, Neurological, Developmental and Substance Abuse Disorders. Geneva.

Wilson, D.M.,3rd, Bohr, V.A., McKinnon, P.J., 2008. DNA Damage, DNA Repair, Ageing and Age-Related Disease. *Mech. Ageing Dev.* **129** (7-8), 349-352.

Winter, H., Schweizer, J., Goerttler, K., 1983. Keratin Polypeptide Composition as a Biochemical Tool for the Discrimination of Benign and Malignant Epithelial Lesions in Man. *Arch. Dermatol. Res.* **275** (1), 27-34.

Woodcock-Mitchell, J., Eichner, R., Nelson, W.G., Sun, T.T., 1982. Immunolocalization of Keratin Polypeptides in Human Epidermis using Monoclonal Antibodies. *J. Cell Biol.* **95** (2 Pt 1), 580-588.

Wu, X., Amos, C.I., Zhu, Y., Zhao, H., Grossman, B.H., Shay, J.W., Luo, S., Hong, W.K., Spitz, M.R., 2003. Telomere Dysfunction: A Potential Cancer Predisposition Factor. *J. Natl. Cancer Inst.* **95** (16), 1211-1218.

Xiong, H., Callaghan, D., Jones, A., Walker, D.G., Lue, L.F., Beach, T.G., Sue, L.I., Woulfe, J., Xu, H., Stanimirovic, D.B., Zhang, W., 2008. Cholesterol Retention in Alzheimer's Brain is Responsible for High Beta- and Gamma-Secretase Activities and Abeta Production. *Neurobiol. Dis.* **29** (3), 422-437.

Yang, M., Crawley, J.N., 2009. Simple Behavioral Assessment of Mouse Olfaction. *Curr. Protoc. Neurosci.* **Chapter 8** Unit 8.24.

Yao, J.K., Wengenack, T.M., Curran, G.L., Poduslo, J.F., 2009. Reduced Membrane Lipids in the Cortex of Alzheimer's Disease Transgenic Mice. *Neurochem. Res.* **34** (1), 102-108.

Ye, S., Huang, Y., Mullendorff, K., Dong, L., Giedt, G., Meng, E.C., Cohen, F.E., Kuntz, I.D., Weisgraber, K.H., Mahley, R.W., 2005. Apolipoprotein (Apo) E4 Enhances Amyloid Beta Peptide Production in Cultured Neuronal Cells: ApoE Structure as a Potential Therapeutic Target. *Proc. Natl. Acad. Sci. U. S. A.* **102** (51), 18700-18705.

Zhao, H., Traganos, F., Darzynkiewicz, Z., 2009a. Kinetics of the UV-Induced DNA Damage Response in Relation to Cell Cycle Phase. Correlation with DNA Replication. *Cytometry A.* **77** (3), 285-293.

Zhao, H.L., Sui, Y., Guan, J., He, L., Gu, X.M., Wong, H.K., Baum, L., Lai, F.M., Tong, P.C., Chan, J.C., 2009b. Amyloid Oligomers in Diabetic and Nondiabetic Human Pancreas. *Transl. Res.* **153** (1), 24-32.

Zhao, H., Albino, A.P., Jorgensen, E., Traganos, F., Darzynkiewicz, Z., 2009. DNA Damage Response Induced by Tobacco Smoke in Normal Human Bronchial Epithelial and A549 Pulmonary Adenocarcinoma Cells Assessed by Laser Scanning Cytometry. *Cytometry A.* **75** (10), 840-847.

Zhong, N., Ramaswamy, G., Weisgraber, K.H., 2009. Apolipoprotein E4 Domain Interaction Induces Endoplasmic Reticulum Stress and Impairs Astrocyte Function. *J. Biol. Chem.* **284** (40), 27273-27280.

Zhong, N., Weisgraber, K.H., 2009. Understanding the Association of Apolipoprotein E4 with Alzheimer Disease: Clues from its Structure. *J. Biol. Chem.* **284** (10), 6027-6031.

Zhu, X., Lee, H.G., Perry, G., Smith, M.A., 2007. Alzheimer Disease, the Two-Hit Hypothesis: An Update. *Biochim. Biophys. Acta* **1772** (4), 494-502.

Zhu, X., Raina, A.K., Smith, M.A., 1999. Cell Cycle Events in Neurons. Proliferation Or Death? *Am. J. Pathol.* **155** (2), 327-329.

APPENDIX 1

Leifert, W.R., **François, M.**, Thomas, P., Luther, E., Holden, E., Fenech, M., 2011. **Automation of the Buccal Micronucleus Cytome Assay using Laser Scanning Cytometry.** *Methods Cell Biol.* **102** 321-339.

CHAPTER 13

Automation of the Buccal Micronucleus Cytome Assay Using Laser Scanning Cytometry

Wayne R. Leifert,[*] Maxime François,[*,†] Philip Thomas,[*] Ed Luther,[‡] Elena Holden[§] and Michael Fenech[*]

[*]CSIRO Food and Nutritional Sciences, Genome Health Nutrigenomics, Adelaide, SA, Australia

[†]Edith Cowan University, Centre of Excellence for Alzheimer's Disease Research and Care, Joondalup, WA, Australia

[‡]Independent LSC Consultant, Wilmington, Massachusetts, USA

[§]CompuCyte Corporation, Westwood, Massachusetts, USA

METHODS IN CELL BIOLOGY, VOL 102

0091-679X/10 $35.00
DOI 10.1016/B978-0-12-374912-3.00013-4

Abstract

Laser scanning cytometry (LSC) can be used to quantify the fluorescence intensity or laser light loss (absorbance) of localized molecular targets within nuclear and cytoplasmic structures of cells while maintaining the morphological features of the examined tissue. It was aimed to develop an automated LSC protocol to study cellular and nuclear anomalies and DNA damage events in human buccal mucosal cells. Since the buccal micronucleus cytome assay has been used to measure biomarkers of DNA damage (micronuclei and/or nuclear buds), cytokinesis defects (binucleated cells), proliferative potential (basal cell frequency), and/or cell death (condensed chromatin, karyorrhexis, and pyknotic and karyolytic cells), the following automated LSC protocol describes scoring criteria for these same parameters using an automated imaging LSC. In this automated LSC assay, cells derived from the buccal mucosa were harvested from the inside of patient's mouths using a small-headed toothbrush. The cells were washed to remove any debris and/or bacteria, and a single-cell suspension prepared and applied to a microscope slide using a cytocentrifuge. Cells were fixed and stained with Feulgen and Light Green stain allowing both chromatic and fluorescent analysis to be undertaken simultaneously with the use of an LSC.

I. Introduction

The buccal mucosa is an easily accessible tissue for sampling cells in a minimally invasive manner and does not cause undue stress to study subjects. Buccal cells can be used to study the regenerative capacity of the buccal mucosa that is dependent on the number and division rate of the proliferating basal cells, their genomic stability, and their propensity for cell death. This approach is increasingly being used in molecular epidemiological studies to investigate the impact of nutrition, lifestyle factors, genotoxin exposure, and genotype on DNA damage and cell death (Thomas *et al.*, 2009). Since the buccal mucosa is of ectodermal origin, defects in buccal mucosa cells may allow it to act as a surrogate tissue to reflect potential physiological changes that occur in other ectoderm-derived tissues such as fibroblasts and nervous tissue. A method utilizing light and fluorescence microscopy has previously been developed to study DNA damage events such as micronucleus frequency in buccal cells adopting a buccal micronucleus cytome approach (Darzynkiewicz *et al.*, 2011; Thomas *et al.*, 2007, 2008). Furthermore, the presence of micronuclei in epithelial cells is of particular interest because micronuclei are one of the best established biomarkers of DNA damage, representing chromosome breakage and mal-segregation events (Fenech and Crott, 2002).

The buccal micronucleus cytome assay has also been used to measure distinct differences between the cytome profiles associated with normal ageing relative to that for premature ageing clinical outcomes such as Down syndrome and

Alzheimer's disease. These studies highlight the potential diagnostic value of the cytome approach for determining genome instability events (Thomas *et al*., 2007, 2008). Biomarkers that may identify individuals who are at increased risk or are at an early stage of age-related diseases such as Alzheimer's disease would be valuable to the community since it would be possible not only to monitor the progress of the disease but also to determine the effectiveness of potential therapeutic strategies.

II. Rationale

Laser scanning cytometry (LSC) is a new technology that combines the principles of flow cytometry, quantitative imaging, and immunohistochemistry with high-content, multicolor fluorescence analysis, and can be used to identify specific cells in a heterogeneous population as well as scoring unique molecular events within them (Luther *et al*., 2004; Pozarowski *et al*., 2006). Additionally, LSC provides intracellular and within-tissue localization of specific protein targets, generating data that offers the advantage of high-throughput analysis without sample loss. The buccal micronucleus cytome assay is well validated by our group using visual scoring by light microscopy; however, applicability on a large scale for appropriate biomonitoring is hampered by lack of automated high-throughput technology. Visual scoring of the buccal cytome and micronuclei can be time consuming and large numbers of cells and/or donors need to be analyzed to obtain statistically relevant data. This is particularly important when scoring micronuclei due to the low baseline frequencies observed (Ceppi *et al*., 2010).

The LSC protocol developed here could also be adapted to make use of molecular probes for DNA adducts, aneuploidy, chromosome break measures (Ramirez *et al*., 1999; Schwartz *et al*., 2003; Van Schooten *et al*., 2002), DNA double-strand break (e.g., γH2AX (Tanaka *et al*., 2007, 2009; Zhao *et al*., 2009), and measures of oxidative damage to DNA (e.g., 8-oxo-dG) within the nuclei of buccal cells (unpublished observations).

III. Methods

The buccal mucosa is a stratified squamous epithelium. The bottom layer of this epithelium contains actively dividing basal cells and basal stem cells, which produce progeny that differentiate and maintain the structural profile and integrity of the buccal mucosa. The time frame for cellular migration from the basal layer to the keratinized surface layer is thought to range from 7 to 21 days; however, there are only limited data investigating migration rates in buccal mucosa (Bjarnason *et al*., 1999; Squier and Kremer, 2001). The various cell types and nuclear anomalies among the various cell types in the buccal mucosa, which are observed and scored in a buccal micronucleus cytome assay, are shown schematically in Fig. 1.

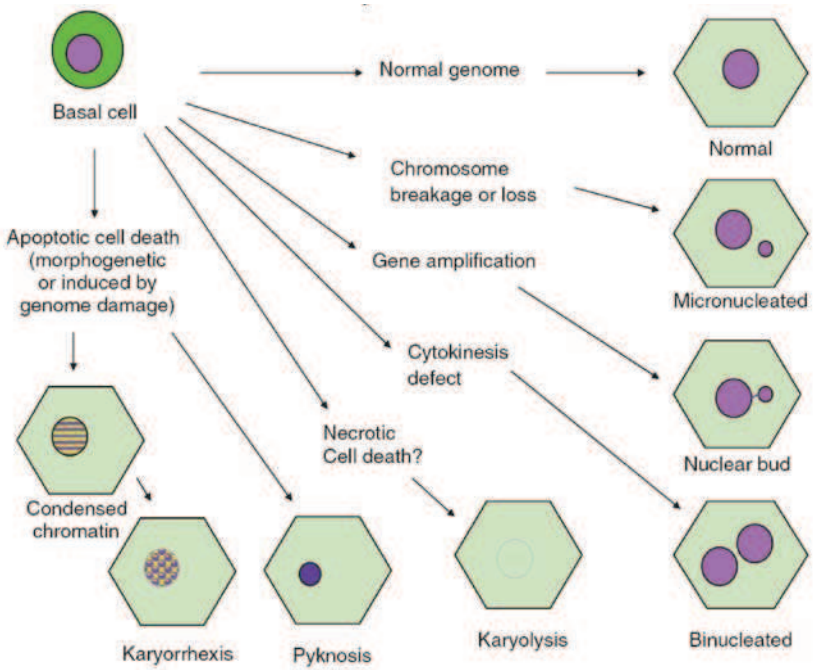

Fig. 1 The various cell types scored in the buccal micronucleus cytome assay (adapted from Thomas *et al*. (2009)).

A. Buccal Cell Sampling and Preparation

Buccal cell isolation and preparation are as previously described by Thomas *et al*. (2009). Human research ethics approval was obtained from CSIRO Food and Nutritional Sciences, Adelaide, South Australia, Adelaide University and Southern Cross University human experimentation ethics Committees. Before sampling, the inside of the mouth was rinsed gently with 30 mL distilled water to remove debris. Buccal cells were sampled using a soft bristle, flat headed toothbrush rotated 20 times against one cheek in a circular motion, and then the toothbrush containing cells was transferred to 30 mL tubes containing "buccal cell buffer" (0.01 M tris (hydroxymethyl)aminomethane, 0.1 M ethylenediaminetetraacetic acid, 0.02 M NaCl, pH 7.0) and cells were dislodged from the toothbrush by agitation of the toothbrush in the buffer. A new toothbrush was used to take the sample from the contralateral cheek, as above and placed in the same buccal cell buffer. The suspension was then centrifuged 10 min at 581*g* at room temperature. Supernatant was discarded and 10 mL of fresh buccal cell buffer was added. Cells were centrifuged twice more and finally resuspended into 5 mL of fresh buccal cell buffer, separated using a syringe with an 18-gauge needle, and then filtered with a 100 μm nylon filter. The cell concentration was determined using a Coulter counter and adjusted to

80,000 cells/mL. Buccal cells were cytocentrifuged (using a Shandon cytocentrifuge) for 5 min at 600 rpm onto microscope slides and air-dried for 10 min.

B. Buccal Cell Fixation and Staining

Cells were fixed in a slide-staining rack containing 50 mL of ethanol:acetic acid mix (3:1) for 10 min at room temperature followed by further air-drying for 10 min at room temperature. Microscope slides containing the fixed cells were immersed for 1 min each in Coplin jars containing 50% (v/v) and then 20% (v/v) ethanol. Cells were washed for 2 min in a Coplin jar containing purified (Milli-Q) water. Slides were placed in a Coplin jar containing 5 M HCl for 30 min and then rinsed in running tap water for 3 min. Slides were drained and placed in a Coplin Jar containing Schiff's reagent for 60 min in the dark at room temperature, and then rinsed for 5 min in tap water and then in Milli-Q water. The cells were counterstained by immersing in Coplin jars containing 0.2% (w/v) Light Green for 30 s and rinsed in Milli-Q water. Slides were then air-dried for at least 45 min before coverslips were applied with DePex mounting medium.

C. Laser Scanning Cytometry

Microscope slides containing fixed/stained buccal cells were inserted into a standard four-slide carrier and analyzed by iCyte® Automated Imaging Cytometer (CompuCyte Corporation, Westwood, MA) with full autofocus function, inverted microsope, three laser excitation (Argon 488 nm, Helium-Neon 633 nm, and Violet 405 nm), four photomultiplier tubes (PMTs) for the quantitation of blue, green, orange, and red fluorescence and dual channel absorption/scatter detector. It is important to select the appropriate excitation lasers and PMT detectors for the analysis of different chromatic or fluorescent probes. In this study, excitation was at 488 and 633 nm, a Long Red emission filter was used for fluorescence, and 488 light loss and 633 light loss photodetectors for absorption were used (Table I). Typically 1000–3000 cells were analyzed using iCyte cytometric analysis software version 3.4.10. The "CompuColor" feature in iCyte was used to provide a green pseudocolor in the cytoplasm (as it is observed when visualized under light microscopy); additionally, nuclei were colored orange.

Table I
Laser and detector selection for buccal cells

Target	Dyes	Excitation lasers	Detectors
Nuclei	Feulgen	488	488 LL (Absorbance) + Long Red (Fluorescence)
Micronuclei	Feulgen	488	488 LL (Absorbance) + Long Red (Fluorescence)
Cytoplasm	Light Green	633	633 LL (Absorbance) + Long Red (Fluorescence)

Abbreviations; LL, light loss (absorption)

D. Low-Resolution Scan

Routinely, a rapid overview scan is initially performed at low resolution using a 20× objective to locate and capture the entire area of the sample (cytospot) that was subsequently analyzed in greater detail. The resolution of an overview scan is low due to large (10 μm) step increments used to acquire the image of the entire sample.

E. High-Resolution Scan

To obtain high-resolution images for analysis, smaller individual (rectangular) scan areas are defined for the high-resolution scan using a 20× objective, outlined in Fig. 2B. In high-resolution scans, small (0.5 μm) laser increment steps are used thus yielding higher resolution detailed "images." It was found that a 20× objective was sufficiently adequate for both the low- and high-resolution scans to analyze the buccal cell cytome.

The user typically defines the size and shape of these regions (shown as user-defined rectangular regions in Fig. 2A,B) and where they will be placed. We routinely place these rectangular regions randomly over the cytospot within the defined low-resolution region being careful not to overlap these scan regions. If there was an obvious artifact present, for example, an air bubble, then this area was excluded from analysis. The size of the high-resolution scan regions was always set to 1500 × 1110 pixels (or multiples thereof). We have found empirically that this size accommodates the most optimal scanned image size for buccal cells contained within the "field images." Furthermore, by doing this, the LSC will automatically refocus at the start of each scanned 1500 × 1110 pixel region. This conveniently allows for any refocusing corrections that might be required if a larger single scan region was used. Additionally, if there is a particular reason that a scan region should be excluded from analysis in the main data set, it can easily be excluded later when analyzing data or defining the scattergrams. The other advantage of having multiple analysis scan regions is that each 1500 × 1110 pixel region represents replicates within the sample being scanned.

In the protocol currently described here, a multipass scan was performed to increase the range of signals that can be detected and optimize image quality. The blue (488 nm) and red (633 nm) excitation lasers are used separately to allow separation of fluorescence from dyes that have similar emission spectra, but different excitation spectra. The two component dyes in this analysis that fall into that category are as follows: Feulgen targets the DNA of cells and fluoresces in the long red region when excited with a 488 nm laser light source, whereas Light Green targets the cytoplasm of cells that also fluoresces in the long red region when excited with the red laser (633 nm). Additionally, the absorbance (light loss) can also be detected using the 488 and 633 light loss photodetectors.

When quantification of the fluorescence signal was required, the photomultiplier voltages should be set so that the brightest pixel value (equivalent to 16,000 units) is

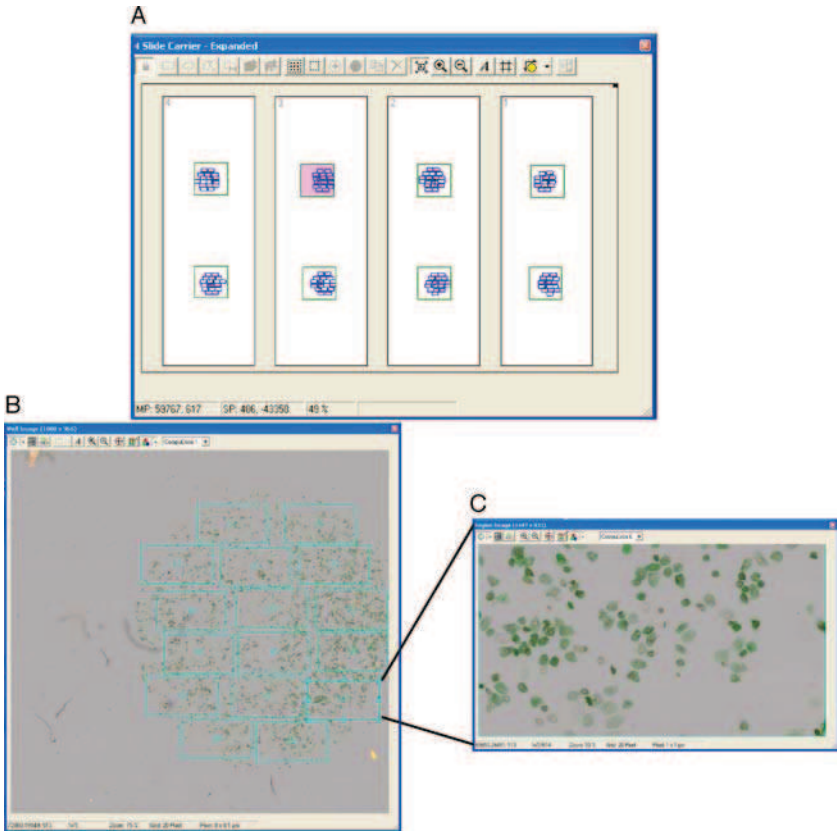

Fig. 2 (A) Shows a diagram of four slides to be analyzed by LSC from right to left. Typically, two cytospots containing buccal cells are prepared on a microscope slide. The large square boxes are the regions in which a "low-resolution" scan of the cytospots are initially performed. This allows the user to define the cytospot region containing the cells. The smaller rectangles within the larger boxes are regions that are scanned at higher resolution for data analysis (see text for full explanation). (B) A typical low-resolution scan "well image" of buccal cells on an entire cytospot also showing the 1500 × 1110 pixel size rectangular regions to be analyzed at high resolution. (C) An example of a "region image" that consists of a mosaic image showing individual buccal cells stained with Light Green (cytoplasm) and Feulgen (nuclei). (See plate no. 20 in the color plate section.)

just below saturation (e.g., 15,000 units). In the example shown (Fig. 3), this was set to 38 for the blue laser with excitation in the long red channel. The signal intensity can be viewed using the profile feature in the profile window. The "Offset" values (which are used to set the background fluorescence) were set to decrease the background to a pixel value between 200 and 400 units; in this case, for long red (with blue laser excitation), the offset setting was –0.03. By carrying out the above procedure, this will ensure the maximum dynamic range of fluorescence data that can be obtained, hence this will be ideal for the quantification and comparison of data between samples.

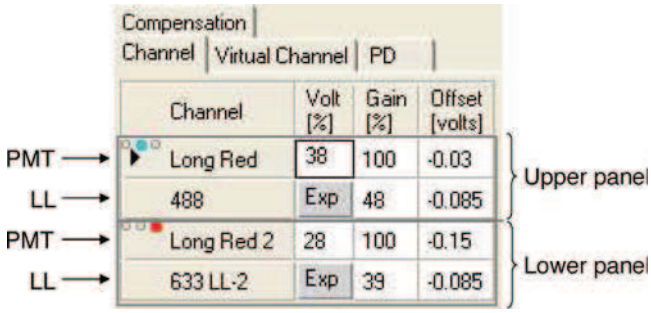

Fig. 3 Setting the channels for excitation and emission: the settings show that in this example the 488 nm excitation laser was used in the first pass of the scan (as indicated in the upper panel), while the text in the upper panel shows the PMT settings and light loss detector settings used for detecting emission, that is, "Long Red" and "488" (which are filters for fluorescence at 647 nm and absorbance at 488 nm, respectively). These settings were used to quantify Feulgen fluorescence and absorbance (light loss) for nuclei and micronuclei. The lower panel shows that the red laser was used to excite the sample on the second pass of the scan. In this instance, the fluorescence emission was at long red ("Long Red 2"), and light loss (absorbance) at 633 (red) was also being recorded ("633 light loss-2"). These settings were used to quantify red fluorescence and absorbance (light loss) of Light Green stain (for cytoplasm). The "volt" and "offset" features are described in the text. (For interpretation of the references to color in this figure legend, the reader is referred to the Web version of this chapter.)

F. Virtual Channels and Compensation

Virtual Channels are used to perform mathematical operations on originally acquired channels to create new "virtual" channels. They are used to increase a weak signal, to add signals together or to isolate the individual fluorescence signals when two or more may overlap in one or more channels (typically termed "compensation"). In our experiment, several virtual channels were created to allow compensation of both absorbance and fluorescence as shown in Table II.

Table II
Creation of virtual channels to compensate for fluorescence and absorbance

Virtual channel	Input channel	Operator	Purpose
		Fluorescence compensation	
LR Fluor M	Long Red	Multiply 0.25	Adjustment factor for Light Green compensation
LR2 Fluor M	Long Red 2	Multiply 0.3	Adjustment factor for Feulgen compensation
Feulgen	Long Red	Subtract LR2 Fluor M	Compensated for Feulgen stain
Light Green	Long Red 2	Subtract LR Fluor M	Compensated for Light Green stain
		Absorbance compensation	
Blue I	488 LL	Invert	Convert from bright field to dark field
Red I	633 LL2	Invert	Convert from bright field to dark field
Blue M	Blue I	Multiply 0.05	Adjustment factor for Light Green compensation
Red M	Red I	Multiply 0.05	Adjustment factor for Feulgen compensation
Blue C	Blue I	Subtract Red M	Compensated for Feulgen stain
Red C	Red I	Subtract Blue M	Compensated for Light Green stain

To properly define and evaluate the compensation settings, it was necessary to monitor the distribution of events in scattergrams using the random segmentation "phantom" feature (Fig. 4). In the scattergram shown in Fig. 4, a region (R35) was drawn around events that fall on areas of the slide where there are no cells and a complementary region (R25) was defined around the events that fall on cells. Events from R35 are excluded and region 25 was used as a gate for further compensation. Both the fluorescence (Fig. 4C) and the absorbance (Fig. 4E) scattergrams of the uncompensated events show a slant in the *Y*-direction toward the *X*-direction. In the compensated scattergrams (Fig. 4D,F), that line moves toward a more vertical positioning, indicating that proper compensation has been achieved.

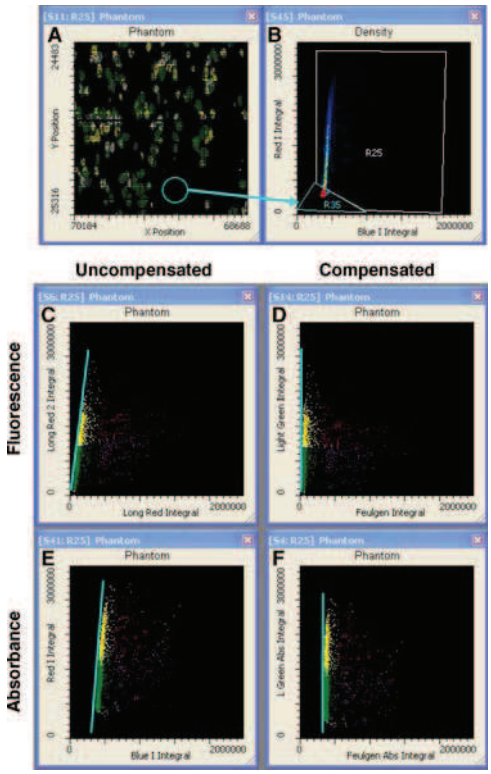

Fig. 4 (A) Phantom contours were generated using the "phantom" feature in iCyte which shows the location of cells (highlighted spots) and where there are no cells (black). This allows the user to define the compensation parameters as described in detail in the text and shown in (B). Uncompensated (C) and compensated (D) fluorescence while uncompensated (E) and compensated (F) absorbance data are shown. The "integral" data was defined as fluorescence per event for the selected channel.

G. Segmentation of Events

In this study, one of the aims was to capture three main buccal cell events that could be analyzed further for scoring and quantification, namely, the cell boundary for identifying and scoring whole cells as well as the nucleus boundary and micronuclei boundary (Fig. 5). Following a high-resolution scan using a 20× objective and using the "protocol" settings as shown in Fig. 6, the clear segmentation lines for cell periphery, nuclei, and micronuclei were generated in iCyte as shown in Fig. 5. The contour lines are automatically drawn around an event such as the cytoplasmic boundary, nucleus, or micronucleus using a user-defined threshold for the pixel values for a particular fluorescent, absorption or virtual channel. Buccal cells are large in diameter and occasionally the cells overlap over two scan fields. In our version of the iCyte software, cells falling on the scan boundaries were excluded from the analysis.

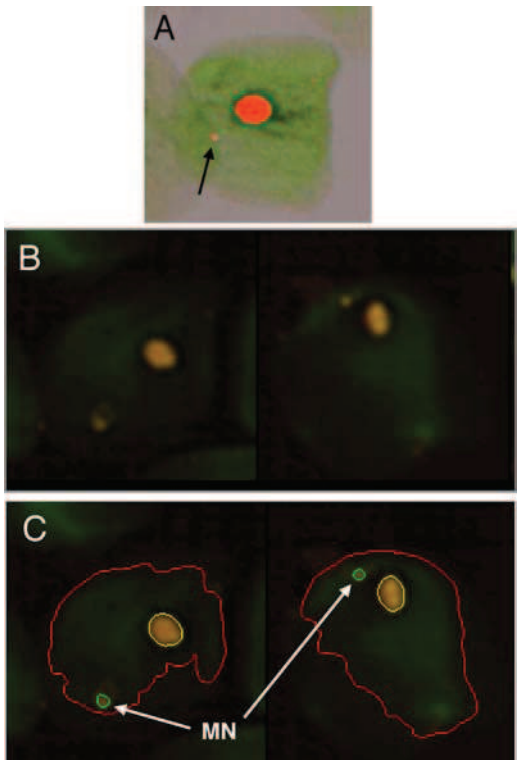

Fig. 5 LSC generated images of buccal cells showing micronuclei. (A) High-resolution image of buccal cells showing a single micronucleus within the cytoplasm. (B) "CompuColor"-generated gallery images of two buccal cells showing distinct micronuclei, and (C) the same cells shown in (B) demonstrating the "segmentation" feature of the iCyte-generated contour lines around the cytoplasmic periphery, nucleus, and micronucleus. (See plate no. 21 in the color plate section.)

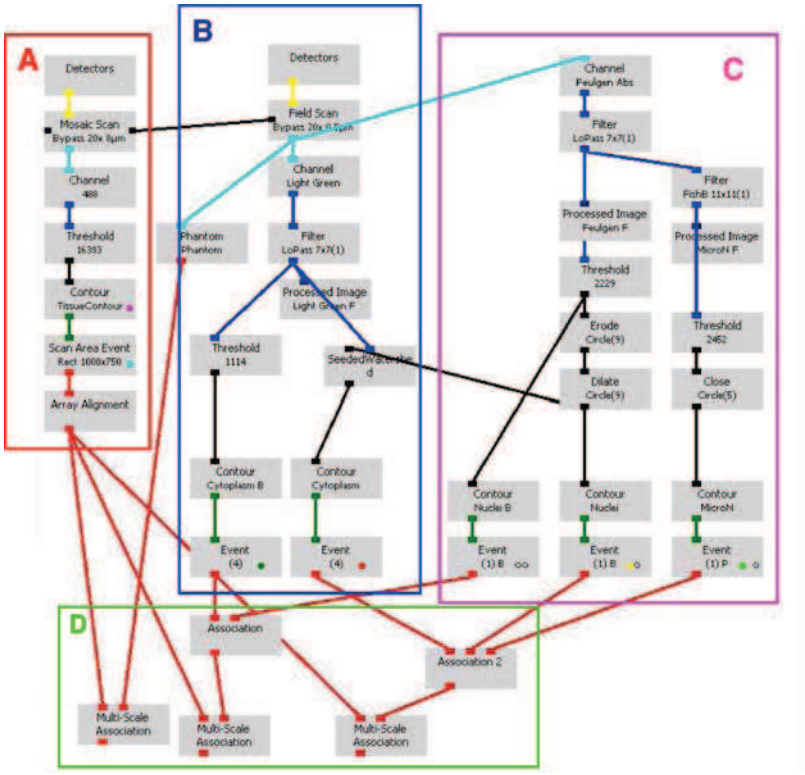

Fig. 6 The iCyte "protocol" was separated into four parts (A, B, C, and D) with all parts being associated together using the "association" module (part D). The first scale (A) provides the settings used for the high-speed overview scan using a 20× objective. The resulting mosaic scan (shown in Fig. 2B) was associated with the second scale settings including parts B and C that contain all the settings for the "high-resolution" scan (as described in text). Part D was the individual component association. All events are associated with each other, which provides a very powerful analysis tool that link parent events to subevents.

H. Identification of Buccal Cell Types

To classify all buccal cells, we generated a scoring system similar to that used previously (Thomas *et al*., 2009), which consisted of the following cell types: basal, transitional, and differentiated normal viable cells, karyolytic cells (i.e., lacking a nucleus), dead/dying cells (<2N), and hyperdiploid cells (>4N) using the protocol pathways, as shown in Fig. 6.

Ideally, the iCyte-identified events are defined by a single segmentation of the cytoplasmic periphery. Since buccal cells are occasionally grouped together, it was necessary to use the iCyte algorithm "seeded watershed." This feature divides the groups of cells into individual cells using nuclei as the basis for segmentation. The assumption was that each cell segmented from a group of cells will contain a single nucleus. As a result, however, karyolytic cells, which do not contain nuclei,

are eliminated from the segmentation. However, it is rare to see karyolytic cells in groups. To fully score all cells on the slides, the scores obtained from the two segmentation scales, that is, "Contour Cytoplasm B" (which is used only to identify the number of cells without nuclei, i.e., karyolytic) and "Contour Cytoplasm" (which identifies cell types with nuclei) are combined, one without and one with the seeded watershed feature, respectively (also see Fig. 6B). The score of the karyolytic cells obtained from "Contour Cytoplasm B" are then added to the scores of all other cell types obtained from "Contour Cytoplasm."

Cell type segregation was defined by using a scattergram to separate cell aggregates (Fig. 7A) (that could not be separated adequately by the seeded watershed algorithm) followed by another scattergram plotting the Light Green integral value against the circularity of the cytoplasm (a measure of the roundness of the object), where a lower circularity value indicates a higher roundness for the event measured allowing identification of debris (Fig. 7B). From the gate R1, a scattergram was designed to separate cells based on differences in nuclear staining by plotting their DNA content versus the area of the cytoplasm. Figure 7C shows "<2N" (R45) and ">4N" (R13) cells, while regions 46 and 47 were defined as euploid cells. Region 47 was defined as "differentiated cells" due to their large cytoplasmic area. Region 46 was a source for a new scattergram of the area of cytoplasm versus Light Green intensity (Fig. 7D). The following regions are then defined; intensely stained green "basal" cells (R6) and lighter stained "transitional" cells (R4), and are also shown in Fig. 8.

Identification of karyolytic cells (cells without a nucleus) is determined based on the original segmentation (cytoplasm B) pathway (i.e., "no seeded watershed" algorithm applied) shown in Figs. 6B and 9A and B. The percentage of karyolytic cells was obtained with gating region "R23" in Fig. 9B. An example gallery of the cell types scored is shown in Fig. 8. The results of buccal cells obtained from normal healthy "young" (mean age = 22.5 years, $n = 10$) or "old" (mean age = 68.7 years, $n = 10$) volunteers that were scored using the LSC protocol are shown in Fig. 10.

I. Nucleus and Micronucleus

In order to identify and score nuclei and micronuclei (Fig. 6C), various input parameters are used in iCyte such as Feulgen absorption and area of the Feulgen-stained event. The identification of nuclei can be used in conjunction with the cellular segmentation. Both features become associated with the "Cell event," and data obtained from identified nuclei can be correlated to the data obtained from identified cells. The total amount of signal detected (usually the "Integral") in nuclei will define the "DNA content" and hence the ploidy status of that cell. The two modules in Fig. 6C labeled "Contour Nuclei B" and "Contour Nuclei" have identical settings. However, "Contour Nuclei B" was associated with "Contour Cytoplasm B" (in part B); and "Contour Nuclei" events were associated with the

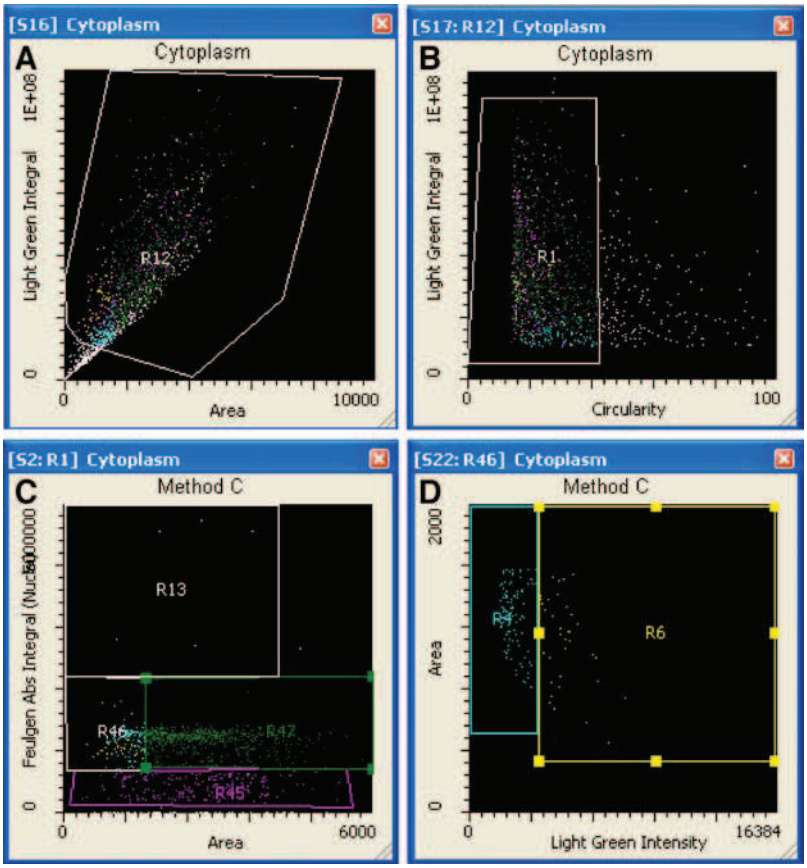

Fig. 7 The identification and scoring of basal, transitional, and differentiated buccal cell types. The scoring of the buccal cell types was achieved by the following criteria: (A) excluding "events" that are either too small or too large to be a buccal cell, (B) have a high "cicrcularity" feature (i.e., are not round in shape), (C) cells that have abnormally high or low nuclear content (i.e., >4N or <2N as shown in R13 and R45, respectively), and euploid cells shown in R46 and R47, with R47 containing the differentiated cells, and (D) was the final stage of cellular classification of basal (R6) and transitional (R4) cells (obtained from scattergram region R46 in (C)). Karyolytic cells are not scored in this set of gating procedures; however, Fig. 9A,B demonstrates the scoring procedure for karyolytic cells.

"Contour Cytoplasm" segmentation in part B. It was necessary to create these two linked events to allow association of nuclei detection with each cell segmentation pathway. The "micronuclei segmentation" was based on the nuclei segmentation; however, a smaller size (area) restriction was defined, since buccal cell micronuclei are typically 1/16 to 1/3 of the main nucleus size (Thomas *et al*., 2009). A "FISH B" filter was added to the micronucleus segmentation to enhance the spatial resolution of the images, highlight small spots, and therefore increases detection of micronuclei. A peripheral contour around the micronuclei was

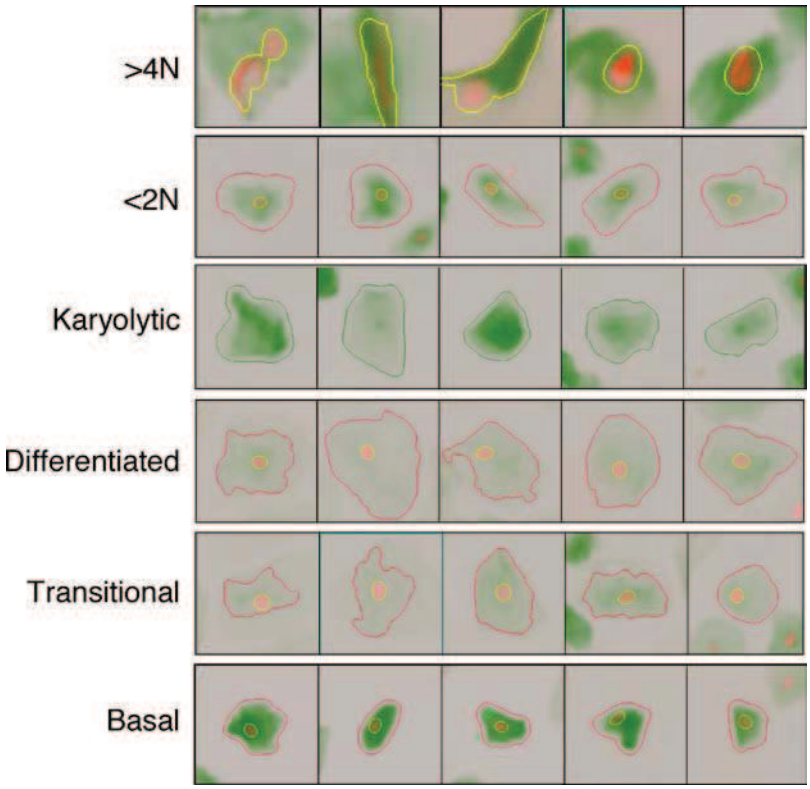

Fig. 8 Gallery images of buccal cells showing the various cell types scored using the automated human buccal cell micronucleus cytome assay by LSC.

routinely applied to segregate the micronuclei that are located within a cell from those that are not (by quantifying the Light Green intensity of the peripheral contour), as shown in Fig. 9. Using these approaches, it was possible to accurately score micronuclei in human buccal cells using LSC, and indeed there was a significantly ($P < 0.001$) higher score of micronuclei in a Down syndrome cohort compared with age-matched controls (Fig. 11). This result compares favorably with our visual scoring observations on an elevated micronucleus frequency in Down syndrome (Thomas *et al.*, 2008).

J. DNA Content

The total DNA content of the cells was based on the Feulgen Absorbance Integral (Fig. 12). The Feulgen Absorbance Max Pixel, a feature that is closely related to the condensation state of the chromatin, is plotted as a scattergram in Fig. 12A. The total

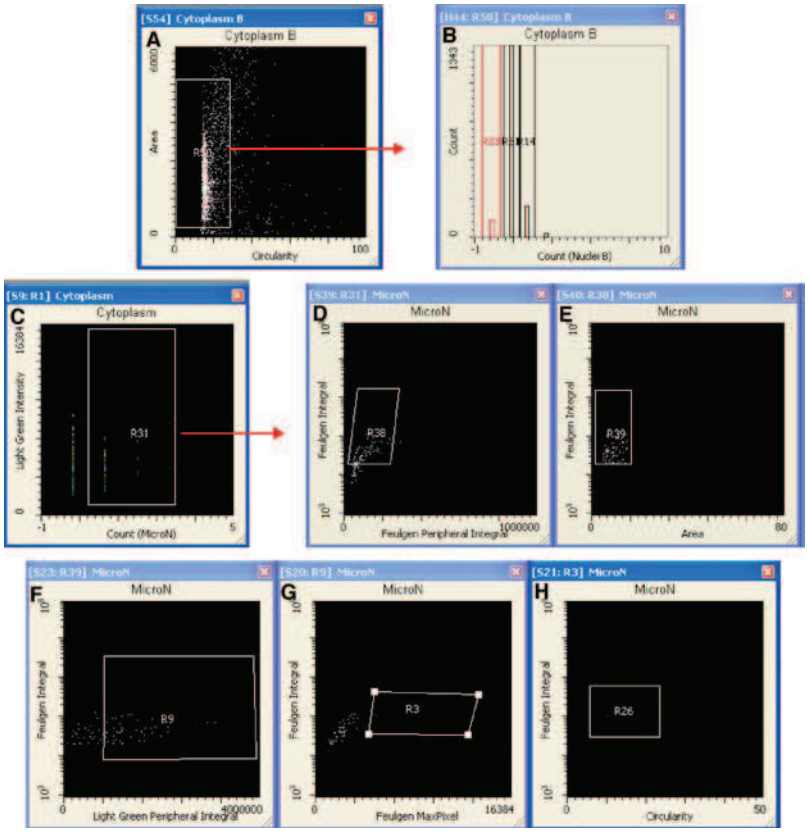

Fig. 9 (A,B) Identification of karyolytic cells (cells without a nucleus) is determined based on the segmentation (cytoplasm B) pathway (i.e., "no seeded watershed" algorithm applied). The percentage of karyolytic cells was obtained with gating region "R23" in panel B. The micronuclei segmentation pathway yields many events that are not micronuclei, and the process of filtering through the events to define true micronuclei entails several steps. The micronuclei identification starts with the same two scattergrams as for cell differentiation status (Fig. 7A,B) and a further scattergram is gated on region R1 (of Fig. 7B). Following this step, all cells that contain a nucleus and with potential micronuclei are identified from the region 31 (C) and several criteria are applied to the micronuclei; an initial gate (R38 in D) was defined to eliminate candidate events that have Feulgen staining surrounding them; this precludes counting bright spots in nuclei. From region 38, another gate (R39 in E) restricts candidates to those with a predetermined area. Then a scattergram showing the Light Green stain (fluorescence) peripheral integral value of the micronuclei versus the Feulgen integral (DNA ploidy) of the micronuclei (F) was used to differentiate candidate micronuclei with no Light Green staining around them and those with (green) cytoplasm surrounding them (R9). Candidates not having the proper intensity of the Feulgen staining are excluded by plotting the Feulgen MaxPixel value of micronuclei and defining a gate (R3 in G). The final step in the micronuclei process was to use a morphology based "circularity feature" to eliminate very irregular candidates from the scoring (H). The circularity feature was plotted against the Feulgen integral (DNA content) of the cells. Lower circularity values translate to round objects. The region was defined around low-circularity objects (R26). Micronuclei detected in region 26 can further be associated to their cell type. (For interpretation of the references to color in this figure legend, the reader is referred to the Web version of this chapter.)

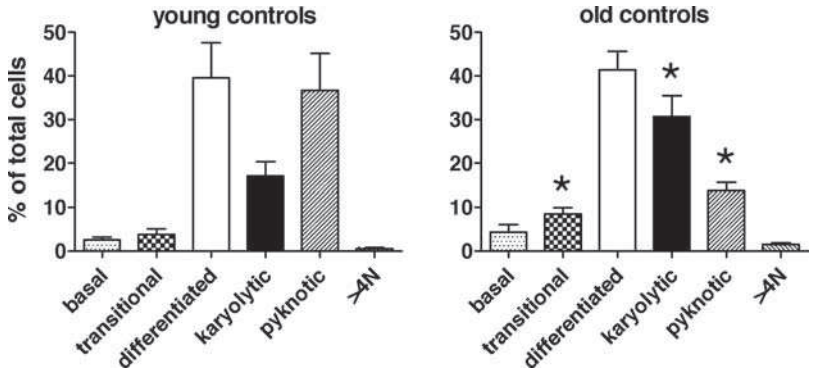

Fig. 10 Classification of the buccal cell types as measured by LSC from "young" (mean age = 22.5 years, $n = 10$) or "old" (mean age = 68.7 years, $n = 10$) healthy volunteers. Data shown are mean ± SEM. $^{*}P < 0.05$ compared with young controls.

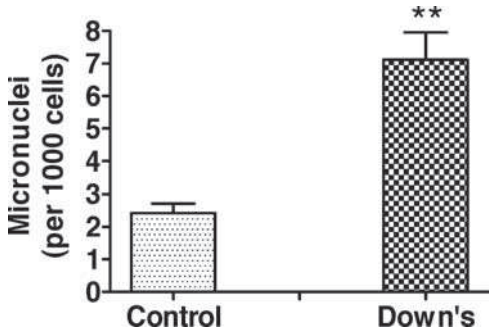

Fig. 11 Frequency of micronuclei in human buccal cells. Human buccal cells on microscope slides were scanned by LSC using the features described in the text. Micronuclei were identified and scored in a Down syndrome cohort ($n = 10$) and an age-matched control group ($n = 10$). Data shown are mean ± SEM, $^{**}P < 0.001$.

DNA content (Feulgen Absorbance Integral) is plotted as a histogram in Fig. 12B. Several regions were gated defining different nuclei states; <2N, 2N, 2N–4N, 4N, and >4N. Additionally, we split the Feulgen Absorbance MaxPixel into two groups, that is, Low MaxPixel and High MaxPixel, where "MaxPixel" is the brightest pixel value per event; in this case, it is the brightest pixel value scored within the nuclei. This allowed us to differentiate subtle changes in DNA content of buccal cells (particularly for other studies where we compared buccal cell DNA content of individuals with Down syndrome, which is characterized by trisomy 21, as well as other age-related diseases such as Alzheimer's disease).

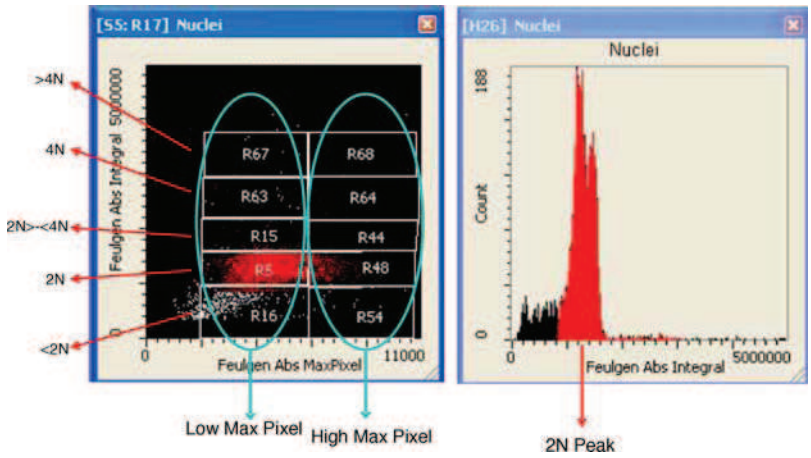

Fig. 12 DNA content of human buccal cells. Scoring criteria were based on Feulgen Absorbance Integral (integrated fluorescence per event) and Feulgen Absorbance MaxPixel (brightest pixel value per event). (Left panel) Nuclear content can be subdivided into two categories "low" and "high" Feulgen Absorbance MaxPixel to allow the detection of subtle changes in DNA staining intensity. (Right panel) A histogram plot of the same data from the left panel showing the delineation of <2N and 2N and the frequency of DNA content "events" scored, with most cells being scored as 2N.

IV. Summary

Our previous studies (Thomas *et al*., 2009) have shown that the buccal cell micronucleus cytome assay could be used for identifying changes in buccal cell morphology and nuclear parameters in age-related diseases such as Alzheimer's disease and Down syndrome (Thomas *et al*., 2007, 2008). In this study, a proof-of-principle for an automated LSC approach was used for determining differences in the buccal micronucleus cytome assay. Furthermore, simultaneous scoring of the frequency of buccal cell micronuclei (which are biomarkers for whole chromosome loss and chromosome breakage) was included in the protocol. Indeed, we have also presented preliminary data ($n = 10$ per group) showing an increase in the frequency of micronuclei in a Down syndrome cohort compared with age-matched controls, confirming our previous data using visual scoring techniques.

The automated LSC buccal cell micronucleus cytome assay developed here will be useful for future studies investigating the buccal cell maturation status, cell death, and micronuclei frequency in population-based studies. The nonbiased and automated nature of the protocol will be useful for screening populations of individuals at risk of age-related diseases. Furthermore, this protocol may be extended with standard immunohistochemistry techniques to investigate more specific markers of DNA damage (e.g., histone H2AX/ATM phosphorylation), cell proliferation (Ki67 or cytokeratin(s) expression), and to compare the

nutriome, transcriptome, proteome, and cytome status in human buccal epithelial cells that may reveal predictive markers of mild cognitive impairment and Alzheimer's disease risk in asymptomatic individuals. Our aim is to use LSC for "high-content" analysis in single cells as a tool for diagnostic biomarker discovery using a nutrigenomic approach. These biomarkers in combination with the nutriome profile and life-style data may yield valuable information for designing diet and life-style interventions aimed at preventing DNA damage, accelerated ageing, the initiation of mild cognitive impairment, and its progression to Alzheimer's disease.

References

Bjarnason, G. A., Jordan, R. C., and Sothern, R. B. (1999). Circadian variation in the expression of cell-cycle proteins in human oral epithelium. *Am. J. Pathol.* **154**(2), 613–622.

Ceppi, M., Biasotti, B., Fenech, M., and Bonassi, S. (2010). Human population studies with the exfoliated buccal micronucleus assay: statistical and epidemiological issues. *Mutat. Res.* **705**(1), 11–19.

Darzynkiewicz, Z., Smolewski, P., Holden, E., Luther, E., Henriksen, M., François, M., Leifert, W., Fenech, M. (2011). Laser scanning cytometry for automation of the micronucleus assay. *Mutagenesis* **26**(1), 153–161.

Fenech, M., and Crott, J. W. (2002). Micronuclei, nucleoplasmic bridges and nuclear buds induced in folic acid deficient human lymphocytes-evidence for breakage-fusion-bridge cycles in the cytokinesis-block micronucleus assay. *Mutat. Res.* **504**(1–2), 131–136.

Luther, E., Kamentsky, L., Henriksen, M., and Holden, E. (2004). Next-generation laser scanning cytometry. *Methods Cell Biol.* **75**, 185–218.

Pozarowski, P., Holden, E., and Darzynkiewicz, Z. (2006). Laser scanning cytometry: principles and applications. *Methods Mol. Biol.* **319**, 165–192.

Ramirez, M. J., Surralles, J., Galofre, P., Creus, A., and Marcos, R. (1999). FISH Analysis of 1cen-1q12 breakage, chromosome 1 numerical abnormalities and centromeric content of micronuclei in buccal cells from thyroid cancer and hyperthyroidism patients treated with radioactive iodine. *Mutagenesis* **14** (1), 121–127.

Schwartz, J. L., Muscat, J. E., Baker, V., Larios, E., Stephenson, G. D., Guo, W., Xie, T., Gu, X., Chung, F. L. (2003). Oral cytology assessment by flow cytometry of DNA adducts, aneuploidy, proliferation and apoptosis shows differences between smokers and non-smokers. *Oral Oncol.* **39**(8), 842–854.

Squier, C. A., and Kremer, M. J. (2001). Biology of oral mucosa and esophagus. *J. Natl. Cancer. Inst. Monogr.* **29**(29), 7–15.

Tanaka, T., Halicka, D., Traganos, F., and Darzynkiewicz, Z. (2009). Cytometric analysis of DNA damage: phosphorylation of histone H2AX as a marker of DNA double-strand breaks (DSBs). *Methods Mol. Biol.* **523**, 161–168.

Tanaka, T., Huang, X., Halicka, H. D., Zhao, H., Traganos, F., Albino, A. P., Dai, W., Darzynkiewicz, Z. (2007). Cytometry of ATM activation and histone H2AX phosphorylation to estimate extent of DNA damage induced by exogenous agents. *Cytometry A.* **71**(9), 648–661.

Thomas, P., Holland, N., Bolognesi, C., Kirsch-Volders, M., Bonassi, S., Zeiger, E., Knasmueller, S., Fenech, M. (2009). Buccal micronucleus cytome assay. *Nat. Protoc.* **4**(6), 825–837.

Thomas, P., Harvey, S., Gruner, T., and Fenech, M. (2008). The buccal cytome and micronucleus frequency is substantially altered in Down's syndrome and normal ageing compared to young healthy controls. *Mutat. Res.* **638**(1–2), 37–47.

Thomas, P., Hecker, J., Faunt, J., and Fenech, M. (2007). Buccal micronucleus cytome biomarkers may be associated with Alzheimer's disease. *Mutagenesis* **22**(6), 371–379.

Van Schooten, F. J., Besaratinia, A., De Flora, S., D'Agostini, F., Izzotti, A., Camoirano, A., Balm, A. J., Dallinga, J. W., Bast, A., Haenen, G. R., Van't Veer, L., Baas, P., Sakai, H., Van Zandwijk, N. (2002). Effects of oral administration of *N*-Acetyl-L-cysteine: a multi-biomarker study in smokers. *Cancer Epidemiol. Biomarkers Prev.* **11**(2), 167–175.

Zhao, H., Albino, A. P., Jorgensen, E., Traganos, F., and Darzynkiewicz, Z. (2009). DNA damage response induced by tobacco smoke in normal human bronchial epithelial and A549 pulmonary adenocarcinoma cells assessed by laser scanning cytometry. *Cytometry A.* **75**(10), 840–847.

APPENDIX 2

Darzynkiewicz, Z., Smolewski, P., Holden, E., Luther, E., Henriksen, M., **François, M.**, Leifert, W., Fenech, M., 2011. **Laser Scanning Cytometry for Automation of the Micronucleus Assay.** *Mutagenesis* **26** (1), 153-161.

Mutagenesis vol. 26 no. 1 pp. 153–161, 2011 doi:10.1093/mutage/geq069

REVIEW

Laser scanning cytometry for automation of the micronucleus assay

Zbigniew Darzynkiewicz[1,*], Piotr Smolewski[1,2], Elena Holden[3], Ed Luther[3], Mel Henriksen[3], Maxime François[4,5], Wayne Leifert[4] and Michael Fenech[4]

[1]Department of Pathology, New York Medical College, Valhalla, NY 10595, USA, [2]Department of Experimental Hematology, Medical University of Lodz, Copernicus Memorial Hospital, Ciolkowskiego 2 Street, 95-510 Lodz, Poland, [3]CompuCyte Corporation, 385 University Avenue, Westwood, MA 02090, USA, [4]Commonwealth Scientific and Industrial Organization (CSIRO), Nutritional Genomics and DNA Damage Diagnostics Research Group, Gate 13 Kintore Avenue, Adelaide, SA, 5000, Australia and [5]Centre of Excellence for Alzheimer's Disease, Edith Cowan University, 270 Joondalup Drive, Joondalup, WA 6027, Australia

*To whom correspondence should be addressed. Department of Pathology, New York Medical College, BSB 438, Valhalla, NY 10595, USA. Tel: +1 914 594 3780; Fax: +1 914 594 3790; Email: darzynk@nymc.edu

Received on June 9, 2010; revised on July 4, 2010; accepted on August 27, 2010

Laser scanning cytometry (LSC) provides a novel approach for automated scoring of micronuclei (MN) in different types of mammalian cells, serving as a biomarker of genotoxicity and mutagenicity. In this review, we discuss the advances to date in measuring MN in cell lines, buccal cells and erythrocytes, describe the advantages and outline potential challenges of this distinctive approach of analysis of nuclear anomalies. The use of multiple laser wavelengths in LSC and the high dynamic range of fluorescence and absorption detection allow simultaneous measurement of multiple cellular and nuclear features such as cytoplasmic area, nuclear area, DNA content and density of nuclei and MN, protein content and density of cytoplasm as well as other features using molecular probes. This high-content analysis approach allows the cells of interest to be identified (e.g. binucleated cells in cytokinesis-blocked cultures) and MN scored specifically in them. MN assays in cell lines (e.g. the CHO cell MN assay) using LSC are increasingly used in routine toxicology screening. More high-content MN assays and the expansion of MN analysis by LSC to other models (i.e. exfoliated cells, dermal cell models, etc.) hold great promise for robust and exciting developments in MN assay automation as a high-content high-throughput analysis procedure.

Attempts to automatise MN assay: flow cytometry—virtues and vices

Exposure of cells to ionising radiation or chemical agents that damage chromosomes or components of mitotic spindle leads to formation of micronuclei (MN; for reviews, see refs. 1–3). Either whole chromosomes or chromosome fragments that become separated from the rest of chromosomes during mitosis and at completion of telophase are not included into the daughter nuclei may form MN. Similar to whole nuclei, MN are coated with a nuclear envelope, their DNA is often transcriptionally active and undergoes replication (4,5). The frequency of MN is considered to be a biological dosimeter of the *in vitro* or *in vivo* exposure to mutagens and carcinogens reporting the extent of chromosome damage. The MN assay, therefore, has become a preferred method to estimate mutagenic or carcinogenic properties of environmental factors and other agents.

The conventional approach for quantitative analysis of micronucleation by visual microscopy is tiresome and subjective leading to variability in results between scorers (6). Therefore, attempts have been made to use semi-automatic image analysis as the means for quantification of MN (7–15). Another approach to quantify MN semi-automatically involves the use of flow cytometry [FC; (16–26)]. By providing the means for rapid and unbiased quantitative analysis of MN based on DNA content measurement, FC offers certain advantages over the visual MN scoring or their enumeration by image analysis.

However, there are shortcomings of FC that limit its applications in the MN assay. The major limitation stems from the requirement to destroy integrity of the plasma membrane by lysing cells in order to release MN and measure them in suspension. Their identification is then based on characteristic distribution on DNA frequency histograms within a particular range of DNA content. Unfortunately, other particles that can be erroneously classified as MN may be present in such a suspension. Among them are (i) individual chromosomes or chromosome aggregates isolated from the lysed mitotic cells, (ii) fragments of nuclear chromatin from mechanically damaged cells, (iii) chromatin granules from the fragmented nuclei of apoptotic cells, (iv) individual apoptotic bodies and (v) contaminating microorganisms that can be present either in culture, in rinse buffers or in staining solutions. Since these objects may have similar DNA content as MN, they can be misidentified as MN ('false-positive MN').

Although strategies have been designed to discriminate between cell debris and MN (21,26,27), they may not always be effective. It is particularly difficult to differentiate between isolated chromosomes, fragments of chromatin or apoptotic bodies versus MN. This problem is amplified when among the cells subjected to the MN assay are numerous cells undergoing apoptosis. Then, the proportion of cellular fragments or apoptotic bodies versus MN is high. It should be noted that some apoptotic bodies are abundant in DNA, with DNA content close to that of MN (28). Likewise, lysis of cell suspensions containing a high percentage of mitotic cells (e.g. in cultures treated with mitotic poisons) releases a large number of individual chromosomes that masquerade as MN and can be misidentified by FC. Thus, unless the measured particles are sorted and examined by microscopy, their identity is uncertain and therefore the frequency of false-positive or 'false-negative' MN is unknown.

Still another limitation of FC is the inability to relate MN to individual cells and cell types. To give an extreme example, it is impossible to distinguish between the instances when (i) among 10 cells a single one contained 10 MN while 9 other had no MN versus and (ii) all 10 cells contained a single MN each. In both instances, 10 MN per 10 nuclei are detected by FC. Yet, the distinction is of relevance since in the first case only one cell in 10 (10%) while in the second all 10 cells (100%) demonstrated chromosomal damage. FC cannot be adapted to the cytokinesis-block micronucleus cytome (CBMNcyt) assay, which in addition to MN allows the measurement of other important biomarkers of chromosome damage such as nucleoplasmic bridges and nuclear buds (1,2,29). Still another shortcoming of FC is that the measured sample cannot be stored, e.g. for confirmation of the analysis, archival preservation or retrospective studies with other probes.

Laser scanning cytometry

Laser scanning cytometers (LSC; CompuCyte Corporation, Westwood, MA, USA) are the instruments offering unique analytical capabilities that combine those of flow and image cytometry (30–35) (Figure 1). Unlike the fluorescence imaging analysis (FIA) instrumentation in which the fluorescence intensity of individual cells is recorded by charge-coupled device (CCD) cameras, in LSC it is measured by photomultiplier tubes (PMTs). The dynamic range of fluorescence intensity measurement by LSC, therefore, is greater, offering higher sensitivity and accuracy in fluorescence measurement than FIA instruments. The dynamic range of PMTs is adjusted by altering the voltage applied to the device, whereas output signal levels from CCDs are a function of time: low-light samples require extended CCD exposure times. The latest version of the LSC software (iGeneration) offers powerful analytical tools for very accurate and multivariate data analysis.

New generation (iGeneration: iCyte®, iCys® and iColor®) LSCs provide fluorescence excitation with up to four laser wavelengths (selected from 405, 488, 532, 561, 594 and 633 nm) and four PMTs allowing fluorescence measurements in wavelength bands appropriate for the respective excitation lasers. Forward laser light scatter and/or laser light loss can be measured simultaneously with the fluorescence measurements, using photodiode detectors. Forward scatter measurement yields images similar to differential interference contrast (DIC; Nomarski illumination) while laser light loss measurements allow imaging and quantification of chromatic dyes. Combining three concurrent measurement modes namely fluorescence, scatter and absorption enables simultaneous utilisation of both fluorescent and chromatic dyes in the analysis.

Scanning is done either with multiple lasers in a single pass or by one or more lasers in multiple passes. While spectral compensation may be employed to isolate signals from dyes whose fluorescence emission spectra overlap, multiple laser passes may eliminate or minimise the need for this spectral correction. LSC provides compensated images so that the isolated dye signals may be visualised and event segmentation may be based on these compensated images. LSC produces a full set of 14-bit image data from the fluorescence and light loss signals as well as the feature data derived from the processing and segmentation of these images.

LSC imaging and analysis are non-confocal by design. The resulting very high depth of focus allows collection of the total signal through the width of most samples. This in turn provides precise quantification of the measured signals (DNA content, for example), which is superior to many alternative technologies. Camera-based microscopy imaging systems (FIA) and (to a much greater extent) confocal imaging systems collect data from a very narrow plane through the sample and therefore do not provide the level of quantification available using LSC.

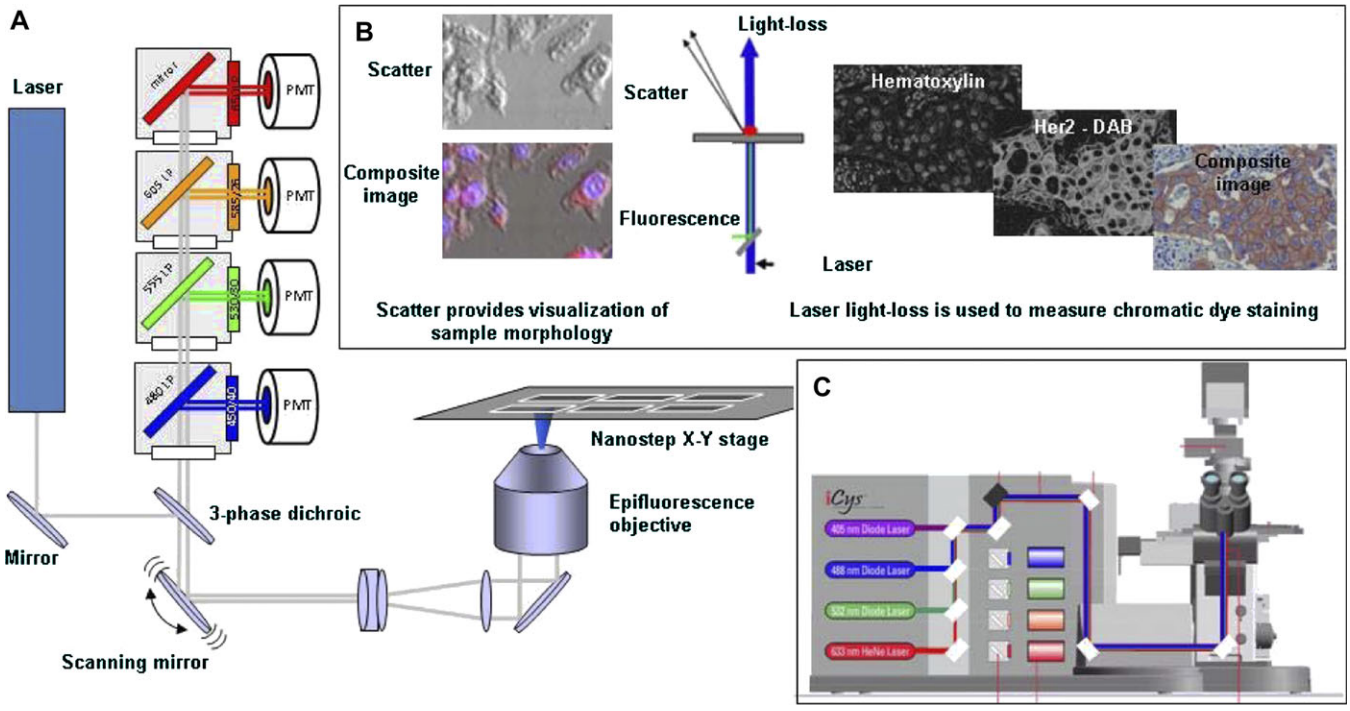

Fig. 1. iGeneration LSC technology schematic diagrams (CompuCyte Corporation). (**A**) Fluorescent measurement optical path; (**B**) Absorbance/scatter optical path and examples of corresponding images; (**C**) iCys Research Imaging Cytometer diagram.

Application of LSC for detection of MN was first reported in mice erythrocytes by Styles *et al*. (36) but the greater challenge was to develop methods for use with nucleated cells as described below.

LSC analysis of MN in nucleated cells growing *in vitro*

The cells analysed by LSC have to be deposited either on microscope slides or on multiwell culture plates. In the case of cells adapted to grow attached to culture flasks, the most convenient approach is to maintain them on mono- or multi-chamber microscope slide tissue culture vessels such as provided by the Lab-Tek, Nalge Nunc, Naperville, IL, USA (37–40). The subsequent steps of fixation, fluorochrome staining and fluorescence intensity measurement are then carried out with no need for cell detachment (trypsinization), on the same platform on which they were exposed to the agents expected to induce MN in cultures. In the case of cells that grow in suspension, the initial step, prior to fixation, is to deposit them on microscope slides by cytocentrifugation (38).

It has been observed that concurrent differential staining of DNA and protein of the cells subjected to MN analysis by LSC with fluorochromes of different emission colour is more advantageous than staining DNA alone. This is due to the fact that the ratiometric analysis of protein/DNA versus DNA content offers better means of MN identification than DNA content alone (38). A variety of fluorochromes can be used to differentially stain cellular DNA and protein within a given sample. A simple approach, in which fluorescence is excited with a single 488 nm laser, utilises propidium iodide (PI) and fluorescein isothiocyanate (FITC) as DNA and protein fluorochromes, respectively (41). The use of PI to selectively stain DNA requires removal of RNA which is accomplished by incubation of the fixed and permeabilized cells with RNase A. Alternatively, DNA can be stained with 4′-6-diamidino-2-phenylindole (DAPI), 7-aminoactinomycin D (7-AAD) or other DNA-specific fluorochromes with no need for RNase treatment (42).

Two strategies (methods) can be used to measure fluorescence intensity of the protein (e.g. FITC) and DNA-bound (e.g. PI) fluorochromes in assessing frequency of MN by LSC. In the first method (Figure 2A), the 'threshold' contour is set based on the data computed from the photomultiplier measuring red fluorescence of PI. The 'integration' contour is then set within a range between zero and two pixels outside the threshold contour. In this way, the integral values of DNA (PI)- and protein (FITC)-associated fluorescence intensity of nuclei as well as MN are recorded in the same file. The distinction between nuclei and MN is then made based on difference in their DNA content. The data thus resemble those obtained by FC as the latter also rely on analysis of DNA content alone (20). As mentioned, however, the concurrent analysis of DNA and protein content of MN, in particular, the ratio of protein/DNA, which is similar in nuclei and MN, provides an additional parameter useful to distinguish MN from artifacts (Figure 3).

The second strategy makes use of the feature of LSC software that was designed for fluorescence *in situ* hybridisation (FISH) analysis (43). In this method, the threshold contour is set on the protein-associated (green-FITC) fluorescence (Figure 2B). Each cell is therefore identified, which allows one to obtain information about the number of nuclei and MN per individual cell (number of 'FISH spots'), as well as to measure intensity (integrated value) of red (DNA) and green (FITC) fluorescence per each spot as well as per whole cell (nucleus + MN). The value of DNA-associated fluorescence integrated over nucleus + MN provides information on the cell cycle position, discriminating between G_1, S and G_2M cells. A similar strategy of threshold contouring based on cellular protein-associated fluorescence has been used to analyse individual cells within cell colonies (44).

The capability of LSC to obtain and save images of the measured events allows their visual identification and thus makes it possible to accurately distinguish and separate MN from other objects, primarily cell fragments and debris. The image analysis revealed that >93% of the objects localised within the bivariate distribution window spanning the range between 0.1 and 5% of DNA content (PI fluorescence) of that of nuclei of G_1 (diploid) cells and having similar protein/DNA (FITC/PI) ratio as the nuclei (Figure 3) were MN (38). Thus, on

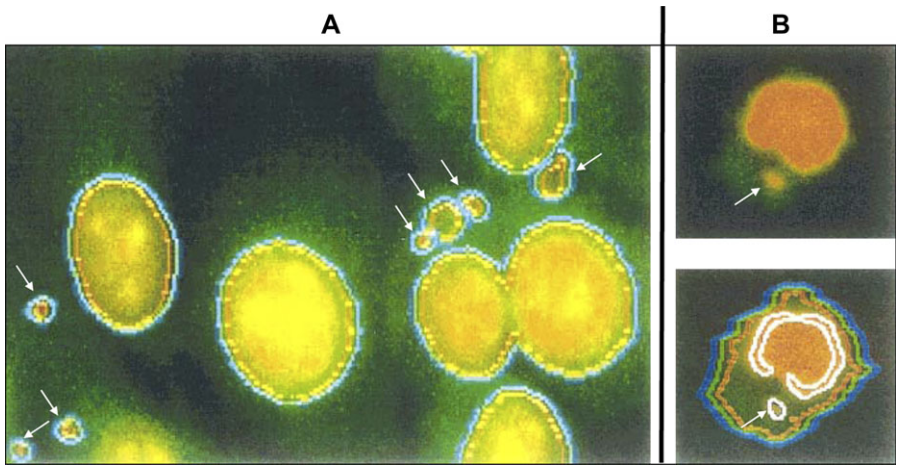

Fig. 2. Two different strategies for setting the threshold contour. (**A**) The mitomycin C-treated MCF-7 cells were fixed and then stained with FITC and PI. The threshold contour was set on red fluorescence of PI and the integrated values of green (FITC) and red fluorescence intensity were recorded for each nucleus and MN. (**B**) The mitomycin C-treated U-937 cells were cytocentrifuged on slides, fixed and then stained with FITC and PI. The threshold contour was set on green fluorescence and the LSC software dedicated for FISH analysis was used to contour the nucleus and MN within the cell. Thus, the number of nuclei plus MN and intensity of fluorescence emitted by each of them can be recorded for each measured cell. In panels A and B, MN are marked with arrows (38).

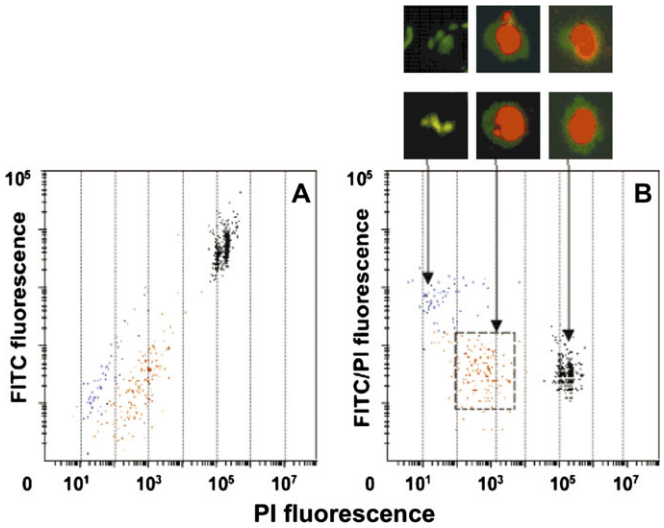

Fig. 3. Identification of MN based on analysis of DNA content (**A**) and protein/DNA ratio (**B**). To induce MN, HL-60 cells were treated with mitomycin C, then fixed and stained with FITC and PI. The threshold contour was set on the data from the photomultiplier measuring red fluorescence of PI. The events from different regions of these bivariate distributions were relocated and imaged to identify MN. The whole nuclei have the highest PI fluorescence and a pattern resembling G_1-S-G_2/M cell cycle distribution of DNA and because of treatment with mitomycin C, with a greater accumulation of cells on G_2/M. The highest proportion of MN can be found within the rectangular window marked on the PI versus FITC/PI bivariate distributions with dashed lines (B). This window had the top and bottom borders at the maximum and minimum range of FITC/PI fluorescence ratio of the whole nuclei, respectively. The lower and higher PI fluorescence borders of the window were within a range between 0.1 and 5% of the PI fluorescence of the G_1-phase nuclei. The events with the FITC/PI ratio higher than the upper limit of the whole nuclei (within the oval dashed line outline) were mostly cytoplasm fragments and other cell debris. The representative cell images from each region are shown as a 'cell gallery' above B. By the 'paint-a-gate' analysis, the events within the discussed regions in panel B reveal their distribution with respect to intensity of PI versus FITC fluorescence (A).

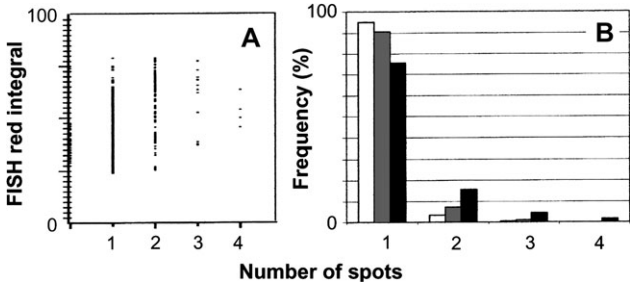

Fig. 4. Quantification of MN per cell using the FISH-dedicated software of LSC. The mitomycin C-treated HL-60 cells were fixed and stained with FITC and PI. The threshold contour was set on green fluorescence of FITC, as shown in Figure 2B and the data were collected using the FISH spot analysis software of LSC to count the number of nuclei plus MN per cell (30,43). The raw data plot is shown in panel (**A**). The bar plot (**B**) shows the frequency of cells with a single nucleus (1 'spot') and with the nucleus plus single MN (2 spots), plus two MN (3 spots) and plus three MN (4 spots) in cultures of HL-60 cells untreated (white bars) treated with 0.1 (grey bars) and 0.01 μg/ml of mitomycin C (black bars). This approach allows one also to present the integrated PI fluorescence (DNA content) of each detected nucleus and MN (data not shown).

the bivariate PI versus FITC/PI fluorescence plots, three distinct clusters can be seen: (i) the cluster of the recorded events with the highest FITC/PI ratio and the lowest PI fluorescence which are the non-specific particles, mainly fragments of cells' cytoplasm; (ii) the cluster representing whole nuclei that had the highest PI fluorescence with the typical pattern reflecting the G_1-S-G_2M cell cycle and (iii) the cluster representing predominantly MN.

Analysis of MN using the FISH approach is illustrated in Figure 4. Setting the threshold contour on FITC fluorescence makes it possible to record each individual cell and count the frequency of the objects emitting PI fluorescence such as MN ('FISH spots') and also to measure the integrated PI fluorescence over the whole cell (nucleus + MN). Thus, the cells with a single nucleus could be distinguished from the cells having a nucleus and one MN, from the cells having one nucleus and two MN, etc. It is evident from this data that in the cultures treated with increasing doses of mitomycin C (a cytotoxic and genotoxic drug), the percentage of cells without MN decreased concurrently with the increase in frequency of the cells with one, two and more MN.

To make the conditions of analysis of chromosome damage independent of the cell cycle kinetics, the MN assay has to be restricted to cells that made only a single division after exposure to the damaging agent. Towards this end, cytochalasin B is added into cultures to prevent cytokinesis in cells completing nuclear division after genotoxin exposure (1,2,29). In this CBMNcyt assay, only cells that have completed one nuclear division, identified as binucleated cells, are scored. Further nuclear division in the presence of cytochalasin leads to formation of multi-nucleated cells, which are not scored. The strategy of setting the threshold contour on green (FITC) fluorescence combined with selection of cells within a specific range of cellular DNA content can be used to adapt the CBMNcyt assay to LSC (Figure 5). Specifically, the cytochalasin-arrested binucleated cells are expected to contain DNA content between 2.0 (both nuclei in G_1) and 4.0 DNA index (DI) (both nuclei in G_2). However, the binucleated cells with 2.0 DI overlap on DNA content frequency histograms with single-nucleated G_2-phase cells. Furthermore, the tetra-nucleated cells containing G_1-phase nuclei may have 4.0–8.0 DI DNA content and overlap in DNA content with binucleated cells containing G_2-phase nuclei. Therefore, the range of cellular DNA content between 2.2 and 3.8 DI is the most reliable to represent the binucleated cells. Indeed, imaging of cells whose PI fluorescence (DNA content) was within this range confirmed that >80% of these cells were binucleated (38). The remaining objects were aggregates consisting of two or three cells in close proximity to each other; the contouring can mistakenly recognise such aggregates as single cells. Strategies that can be used to overcome the problem of close cell proximity or overlap in analysis of MN by LSC are discussed at the end of this chapter: 'Potential challenges'.

When cultured cells were treated with mitomycin C, the frequency of MN detected visually by microscopy at different mitomycin C concentrations correlated well with that assessed by LSC in both cases evaluated in binucleated cells (Figure 6). The highest MN frequency (12–14%) was seen at 0.1 μg/ml concentration. However, the MN frequency was diminished at both <0.1 μg/ml and >0.1 μg/ml concentrations of mitomycin C. At 10.0 μg/ml mitomycin C concentration, the cells were arrested in the G_2 phase (as was evident from the DNA content frequency histograms) which prevented cells from completing nuclear division and expressing the damage as MN. When the frequency of MN in the same specimens was analysed visually

by microscopy and compared with that assayed by LSC, in double-blind tests, rather good correlation (r = 0.87) was observed between both assays (See legends to Figures 5 and 6).

Buccal cell MN analysis by LSC

The buccal mucosa (BM) is a stratified squamous epithelium consisting of four distinct layers. The 'stratum corneum' or keratinised layer lines the oral cavity comprising cells that are constantly being lost as a result of everyday abrasive activities such as mastication. Below this layer lie the 'stratum granulosum' or granular cell layer and the 'stratum spinosum' or prickle cell layer containing populations of both differentiated and apoptotic cells. Integrated within these layers are convoluted structures known as rete pegs, containing the actively dividing basal cells known as the 'stratum germinativum' which produce cells that differentiate and maintain the profile and integrity of the buccal mucosa. The regenerative capacity of tissues and organs within the body is fundamental to growth, development as well as healthy ageing and is dependent on genomic stability and gene expression profile of the basal stem cells. The BM is an easily accessible epithelial tissue that can be sampled in a minimally invasive manner without causing pain to study participants and for this reason is

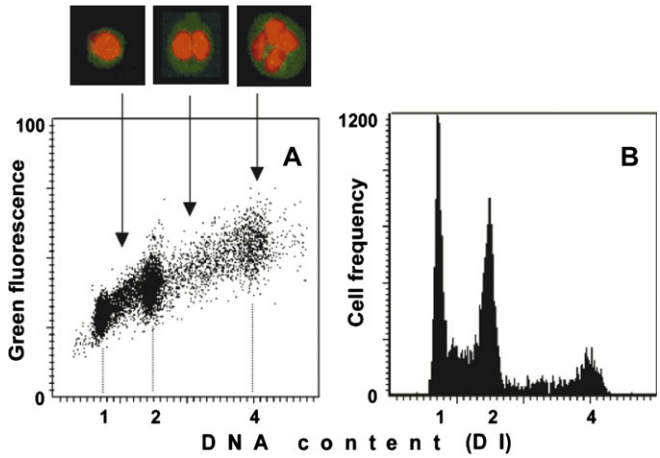

Fig. 5. Identification of cytochalasin B induced binucleated cells by gating analysis of the DNA content frequency histograms. U-937 cells were in the culture with cytochalasin B for 24 h, then fixed and stained with FITC and PI. The threshold contour was set on green fluorescence of FITC as shown in Figure 2, panel B, and PI fluorescence from all nuclei within the cell measured. The intensity of PI fluorescence integrated over the cell, thus, reflects total DNA content (DI) of either the mono-, bi- or multi-nucleated cell. The gating window can be set either on the bivariate DNA content versus green fluorescence scattergram (**A**) or on the DNA content frequency histogram (**B**). Within the gating window of DNA content between 2.2 and 3.8 DI, nearly all cells are binucleated and therefore they can be subjected to the CBMN analysis (38).

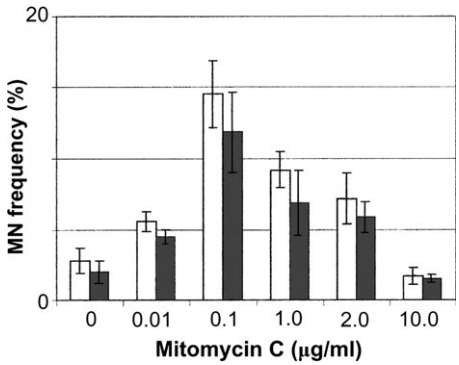

Fig. 6. Comparison of frequency of MN binucleated cells in relation to concentration of mitomycin C assessed visually by microscopy (white bars) and by LSC (black bars). MCF-7 cells were treated with different concentrations of mitomycin C for 6 h then transferred to fresh medium without mitomycin C and cultured for 24 h in the presence of cytochalasin B. The cells were stained with FITC and PI and the threshold contour on LSC was set on red fluorescence of PI. In double-blind test, the same slides were also subjected to scoring MN visually by fluorescence microscopy. The frequency is expressed as mean percentage of MN in relation to total events, nuclei plus MN, counted by LSC or by microscopy. Minimum 1200 binucleated cells were scored by LSC and 500 visually per sample. Standard deviation (five experiments) is shown atop the bars. The regression analysis has shown the correlation coefficient r = 0.87 between the visual versus LSC counts (38).

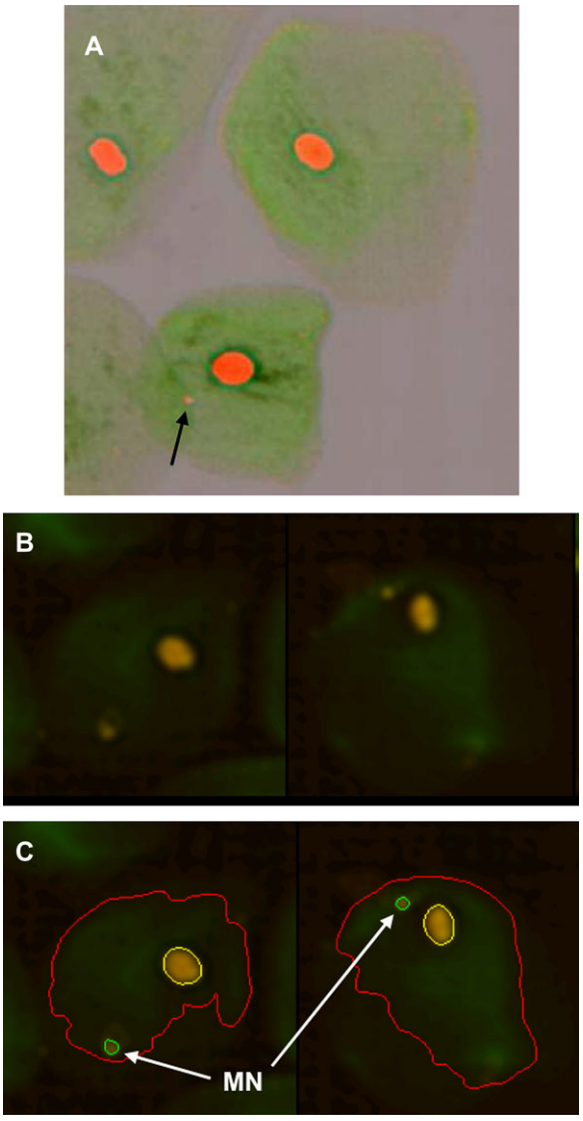

Fig. 7. LSC image of human buccal cells. Human buccal cells were stained with light green (cytoplasm) and Feulgen (nuclei). The Feulgen-stained nuclei are prominent and MN were indicated by an arrow. (**A**) High-resolution image of buccal cells showing a single MN (orange) within the (green) cytoplasm. (**B**) 'CompuColor' generated gallery images of two buccal cells showing distinct MN and (**C**) the same cells shown in (B) demonstrating the accuracy of the iCys-generated contour lines around the cytoplasmic periphery (red), nucleus (yellow) and MN (green).

an ideal tissue for *in vivo* MN diagnostics. This tissue provides a unique opportunity to study the regenerative capacity of epithelial tissue of ectodermal origin in humans and has been used successfully to study DNA damage by scoring MN using visual/microscopy techniques (45).

Micronucleated buccal cells are visually characterised by the presence of both a main nucleus and one or more smaller MN (Figure 7). The MN in buccal cells are usually round or oval in shape and their diameter may range between 1/3 and 1/16, the diameter of the main nucleus. Cells with MN usually contain a single MN, however, it is possible but rare to find cells with more than two MN. The nuclei in micronucleated cells may have the morphology of normal cells or that of dying cells (i.e. condensed chromatin). The MN must be located within the cytoplasm of the cells to be scored. The presence of MN is indicative of chromosome loss or fragmentation occurring during previous nuclear division. Indeed in our previous study, the frequency of MN was significantly elevated in the Down's syndrome cohort and were found to be roughly 10-fold higher than in the age-matched control group, confirming the observation of elevated genome damage in this syndrome (45).

LSC has been used at Commonwealth Scientific and Industrial Organization to score MN in fixed human buccal cells on microscope slides. Buccal cells that were stained initially for visual scoring of the buccal cytome MN assay using light green (cytoplasm) and Feulgen (nuclei) (45) were subsequently scanned with the LSC. We noted strong red fluorescence from the 'light green' stain (cytoplasmic contents) when the 633 nm excitation laser was used. The LSC iCys software enabled us to use a feature termed 'CompuColor' to force the colour of the cytoplasm to appear as the pseudo colour green (the closest possible as it is observed when visualised under light microscopy). Additionally, in the same scan, we set-up the protocol to also quantify the nuclear (Feulgen) staining of buccal cells; however, some 'compensation' was required, and it should be noted that the LSC software is well equipped to manage overlapping or background signals. Feulgen fluorescence was also detected with a red filter following 488-nm excitation (Table I). Interestingly, when the Feulgen 'absorbance' was used to determine the chromatic light loss at 488 nm, we found that the DNA histograms yield more reproducible data upon analysis compared with Feulgen fluorescence, and for this reason, we chose to use the Feulgen chromatic light loss (absorbance) at 488 nm to quantify nuclei and MN in human buccal cells.

The Feulgen absorbance of the nuclei can be used in conjunction with the cellular segmentation of the cytoplasm by incorporating an 'association' function in iCys. In this instance, the nuclei that are scored become associated with the 'cell event' and data obtained from nuclei can be correlated to the all set of data obtained from the different stages of cell differentiation in the buccal cell samples. The total amount of signal detected in nuclei defines the 'DNA content' as mentioned earlier for cultured cells. MN segmentation was based on the same iCys-defined features of 'nuclei' segmentation but a smaller size restriction was used since MN are always much smaller than a typical '2N' nucleus. A filter 'FISH B' was added to the segmentation features to enhance the spatial resolution of the images, highlight small spots and therefore increase MN detection. In fact, by doing this, we noted that we could detect MN with the LSC that were far less apparent by visual scoring using a light microscope. To ensure that scored MN are only within the buccal cells, a 'peripheral contour' around the identified MN is applied to segregate the MN that are located within a cell from those that are not, by quantifying the light green fluorescence intensity of this contour. Using these approaches, it was possible to accurately score MN in human buccal cells using LSC, and indeed, there was a significantly higher score of MN in a Down's syndrome cohort (a model of premature ageing) compared with age-matched controls (Figure 8). These promising initial data suggest that it is possible to score MN frequency in buccal cells using LSC. Ongoing research is also exploring the possibility of scoring automatically by LSC other biomarkers and other buccal cell types including assessment of frequency of karyolitic cells, binucleated cells and basal cells. Such analysis could provide additional information on the regenerative potential of the buccal epithelium.

Table I. Laser and detector selection for MN assay of buccal cells

Target	Dyes	Excitation lasers (nm)	Detectors
Nuclei	Feulgen	488	488LL PD (absorbance) + long red PMT (fluorescence)
MN	Feulgen	488	488LL PD (absorbance) + long red PMT (fluorescence)
Cytoplasm	Light green	633	Long red PMT (fluorescence)

In vivo erythrocyte MN analysis by LSC

The mouse erythrocyte MN assays are standard *in vivo* genotoxicity tests. After administration of the investigated agent at specified times, bone marrow or peripheral blood samples are collected and cellular smears are prepared on microscope slides. Genotoxic effects manifest in the formation of MN, which generally are scored in polychromatic erythrocytes (46). The conventional visual scoring assay of MN is laborious, susceptible to observer fatigue and bias. Attempts therefore have been made to assess MN in erythrocytes by FC (17,18,24,47–50). Styles *et al.* (36) have shown, however, that LSC can be effectively used to perform the erythrocyte MN assay automatically (36). The authors analysed 5000 cells per sample using the instrument with a ×40 objective, 488-nm argon laser at 5 mW output. No distinction was made between normocytes and polychromatic erythrocytes. The results of the comparison between slides analysed by visual microscopy and LSC showed a good

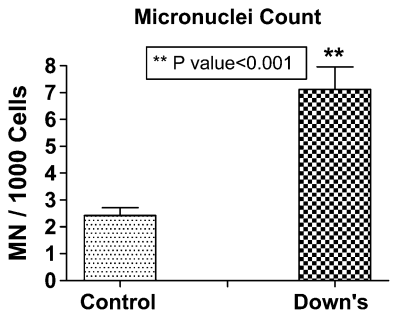

Fig. 8. Frequency of MN in human buccal cells. Human buccal cells on microscope slides were scanned by LSC. Using the features described in the text, MN were identified and scored in a Down's syndrome cohort (n = 10) and an age-matched control group (n = 10). Date are mean values ± SEM, $P < 0.001$.

correlation ($R = 0.96$) between the data from the two assays; the percent of MN in their samples varied between 0 and 6%. The authors conclude that 'LSC is likely to become the preferred method for the performance of standard genotoxicity assays' (36). New models of LSC having multiple laser excitation capability allow one to differentially stain DNA and RNA (e.g. DAPI versus thiazole orange) and thereby to restrict the MN analysis to polychromatic erythrocytes.

Advantages of MN assay by LSC

The presented data demonstrate that LSC can be easily adapted for the MN assay. The cell preparation is simple and the actual measurement is rapid and straightforward. In most specimens, the approximate time of analysis of MN in 1000 cells by LSC was 3–5 min. The LSC assay yielded a similar MN index as visual count under a light microscope. The assay can be carried on both types of cultured cells, i.e. the cells that grow attached to the slides such as MCF-7, as well as on cells that grow in suspension and then are deposited on slides by cytocentrifugation. Furthermore, we also demonstrated that the MN assay was particularly useful in scoring MN in buccal cells showing the expected higher level in Down's syndrome (45).

Instead of using only DNA fluorochromes, as it is conventionally done for detecting MN by image analysis or FC, we chose the double-colour differential staining of DNA with PI (or Feulgen for buccal cells) and protein with FITC (or 'light green' for buccal cells). This led to several advantages. The first advantage was that the non-specific objects could be distinguished from MN based on their higher protein/DNA ratio. The protein/DNA ratio measured by LSC, thus, was a useful parameter making identification of MN more reliable compared to staining DNA alone. The second advantage resulting from staining protein in addition to DNA was the possibility to use the protein-associated FITC fluorescence to set the threshold contour. Using the software of LSC developed for the determination of the FISH fluorochrome spots (30,43), the specimen was subjected to the analysis that revealed the frequency of MN and their DNA content in each individual cell. This approach offers a possibility to assess whether particular clastogenic agents generate cells with single or multiple MN. Thus, mechanistic studies can be carried out, for example to study the difference between the aneugen- and clastogen-induced MN or to study whether different clastogen types preferentially induce a particular chromosome or set of chromosomes to separate and from a single or multiple MN per cell. In analogy to the present application, the FISH capabilities of LSC were extended before to analyse individual cell nuclei within cell colonies, in the clonogenicity assays (44).

The approach based on setting the threshold contour on FITC (or light green cytoplasmic stain) fluorescence offers still another advantage, namely the possibility of CBMNcyt assay. Indeed, using the specific range of cellular DNA content as a marker of binucleated cells, we were able to relocate them and visually confirm their identity. The MN count, thus, can be restricted to the cells that completed only one round of nuclear division, making it independent of differences in cell cycle kinetics.

Confirming the measurements by FC (19), we observed high variability in intensity of PI fluorescence, reflecting differences in DNA content, between individual MN (38). We were able, however, to detect MN with lower DNA content than that of MN detected by FC. Specifically, while our bottom limit of DNA content of MN was ~0.1% of DNA content of the G_1-phase nuclei, the lower limit measured by FC was reported to be between 0.5 and 0.75% (19). It is possible, thus, that the smallest MN measured by LSC may not be detectable by FC.

It is apparent that the more attributes of MN are measured the greater fidelity of their positive identification. With the capability of LSC for multi-laser excitation and multiparameter analysis, one may include additional features characterising MN, such as the presence of centromeres, telomeres, nuclear proteins (e.g. histones), chromosome identification markers, etc. Such multiparametric analysis of MN may not only be helpful for their identification but may provide new insight in mechanistic studies, e.g. aimed to correlate frequency, size and composition of MN with properties of the inducer, cell cycle position or other variables. Likewise, it is possible to detect DNA replication in MN by labelling cells with 5-bromo-2′-deoxyuridine (BrdU) or 5-ethynyl-2′-deoxyuridine (EdU) followed by bivariate analysis of the incorporated precursor and DNA content (39).

Potential challenges in MN analysis by LSC

The analysis based on setting the threshold contour on protein-associated (e.g. FITC) fluorescence requires that the measured cells have to be separated from each other. Otherwise, with close cell proximity or partial overlap of their cytoplasm, the contouring encompasses cell doublets or larger aggregates. Thus, in order to analyse CBMNcyt by LSC, as well as by other automated imaging techniques, a caution should be exercised to have optimal cell density and relatively uniform spacing between the cells growing on slides. Similarly, in buccal cell, scoring the cells that are not completely separated may present a scoring challenge. We overcame this problem by using the 'seeded watershed' feature available in the LSC software, which very accurately defines the cytoplasmic boundaries of single cells in a clump of cells into well-defined single cells for scoring. The separation of the cellular boundaries can be assessed in either 'real-time' or post-acquisition to determine if this algorithm has adequately identified single cells in a clump. For any cell clumps remaining, a procedure can be used to 'gate out' events (cell clumps) that have a larger 'cytoplasmic area' and higher total cytoplasmic staining intensity ('integral') than the single cells. This is accomplished by plotting these twoparameters versus each other. 'Events' (cell clumps) that are obviously larger than a single cell can be identified using the 'create gallery' feature in iCyte/iCys and then removed from subsequent analyses.

Potential difficulty arises in analysis of cultured cells having low cytoplasm/nucleus ratio and are spherical in shape. MN in such cells may not be adequately spatially separated from the nucleus and thus they cannot be individually segmented. Cytocentrifugation at higher centrifugal force or treatment with mild hypotonic solution (e.g. 0.075 M KCl) also leads to more extensive cell spreading on slides. It would be expected, however, that because of the unfavourable geometry of spherical cells having low cytoplasm content, the MN index, assessed by any automated imaging including LSC, will be consistently lower compared to visual scoring. The extent of this bias, likely to be restricted to particular cell types, can be estimated by comparison of the same specimen scored visually versus by automated imaging.

As discussed, the strategy to use cellular DNA content (histograms) for gating binucleated cells in the CBMNcyt

assay does not allow one to distinguish between, e.g. G_2 versus binucleated cells having G_1 nuclei. However, by contouring on cytoplasm (e.g. protein—FITC fluorescence and using the FISH algorithm), it is possible to identify cells having two nuclei each with DI = 1.0 and one nucleus with DI = 2.0; the latter to be gated out. Alternatively, the contoured bi-nuclei can be distinguished from G_2 nuclei by use of the circularity parameter. This parameter is typically elevated in bi-nuclei as the 'pinch-point' at the interface of the nuclei pair creates an elongated perimeter in relation to the nuclear area. In doubtful cases, the imaging can be used to identify the binucleated cells.

Funding

National Institutes of Health, National Cancer Institute (CA R01 28 704).

Acknowledgements

Conflict of interest statement: As stated, three authors (E.H., E.L. and M.H.) are affiliated with CompuCyte, the company that designed and manufactured the Laser Scanning Cytometer used in this study.

References

1. Fenech, M. (2000) The *in vitro* micronucleus technique. *Mutat. Res.*, **455**, 81–95.
2. Fenech, M. (2006) Cytokinesis-block micronucleus assay evolves into a ''cytome'' assay of chromosomal instability, mitotic dysfunction and cell death. *Mutat. Res.*, **600**, 58–66.
3. Thomas, P., Holland, N., Bolognesi, C., Kirch-Volders, M., Bonassi, S., Zeiger, E., Knassmueller, S. and Fenech, M. (2009) Buccal micronucleus cytome assay. *Nat. Protoc.*, **4**, 825–837.
4. Nüsse, M. (1981) Cell cycle kinetics of irradiated synchronous and asynchronous tumor cells with DNA distribution analysis and BrdUrd-Hoechst 33258 technique. *Cytometry*, **2**, 70–79.
5. Kramer, J., Schaich-Walch, G. and Nüsse, M. (1990) DNA synthesis in radiation induced micronuclei studied by bromodeoxyuridine (BrdUrd) labeling and anti-BrdUrd antibodies. *Mutagenesis*, **5**, 491–495.
6. Fenech, M., Bonassi, S., Turner, J. *et al.* (2003) HUman MicroNucleus project. Intra- and inter-laboratory variation in the scoring of micronuclei and nucleoplasmic bridges in binucleated human lymphocytes. Results of an international slide-scoring exercise by the HUMN project. *Mutat. Res.*, **534**, 45–64.
7. Fenech, M., Jarvis, L. R. and Morley, A. A. (1988) Preliminary studies on scoring micronuclei by computerized image analysis. *Mutat. Res.*, **203**, 33–38.
8. Hayashi, M., Norppa, H., Sofuni, T. and Ishidate, M. (1990) Automation of mouse micronucleus test by flow cytometry and image analysis. *Cytometry Suppl.*, **4**, 35.
9. Tates, A. D., van Wellie, M. T. and Ploem, J. S. (1990) The present state of the automated micronucleus test for lymphocytes. *Int. J. Radiat. Biol.*, **58**, 813–825.
10. Verhaegen, F., Vral, A., Seuntjens, J., Schipper, N. M., de Ridder, N. W. and Thierens, H. (1994) Scoring of radiation-induced micronuclei in cytokinesis-blocked human lymphocytes by automated image analysis. *Cytometry*, **17**, 119–127.
11. Bocker, W., Streffer, C., Muller, W. U. and Yu, C. (1996) Automated scoring of micronuclei in binucleated human lymphocytes. *Int. J. Radiat. Biol.*, **70**, 529–537.
12. Thierens, H., Vral, A., De Scheerder, F., De Ridder, L. and Tates, A. (1997) Semi-automated micronucleus scoring in cytokinesis-blocked lymphocytes after irradiation. *Int. J. Radiat. Biol.*, **72**, 319–324.
13. Frieauff, W., Potter-Locher, F., Cordier, A. and Suter, W. (1998) Automatic analysis of the in vitro micronucleus test on V79 cells. *Mutat. Res.*, **413**, 57–68.
14. Castelain, P., VanHummelen, P., Deleener, A. and Kirsch-Volders, M. (1993) Automated detection of cytocholasin-B blocked binucleated lymphocytes for scoring micronuclei. *Mutagenesis*, **8**, 285–293.
15. Decordier, I., Papine, A., Plas, G. *et al.* (2009) Automated image analysis of cytokinesis-blocked micronuclei: an adapted protocol and a validated scoring procedure for biomonitoring. *Mutagenesis*, **24**, 85–93.
16. Ludwikow, G., Stalnacke, C. G., Johanson, K. J., Sundell-Bergman, S. and Richter, S. (1990) Microscopic and flow cytometric study of micronuclei in iododeoxyuridine labelled cells irradiated with soft X-rays. *Acta Oncol.*, **29**, 761–767.
17. Tometsko, A. M. and Leary, J. F. (1990) A peripheral blood micronucleus assay based on flow cytometry. *Cytometry Suppl.*, **4**, 35.
18. Hayashi, M., Norrpa, H., Sofuni, T. and Ishidate, M., Jr. (1992) Mouse bone marrow micronucleus test using flow cytometry. *Mutagenesis*, **7**, 251–256.
19. Schreiber, G. A., Beisker, W., Bauchinger, M. and Nüsse, M. (1992) Multiparametric flow cytometric analysis of radiation-induced micronuclei in mammalian cell cultures. *Cytometry*, **13**, 90–102.
20. Nüsse, M., Beisker, W., Kramer, J., Miller, B. M., Schreiber, G. A., Viaggi, S., Weller, E. M. and Wessels, J. M. (1994) Measurement of micronuclei by flow cytometry. *Methods Cell Biol.*, **42**, 149–160.
21. Nüsse, M. and Marx, K. (1997) Flow cytometric analysis of micronuclei in cell cultures and human lymphocytes: advantages and disadvantages. *Mutat. Res.*, **392**, 109–115.
22 Fiedler, R. D., Weiner, S. K. and Schuler, M. (2010) Evaluation of a modified CD71 MicroFlow® method for the flow cytometric analysis of micronuclei in rat bone marrow erythrocytes. *Mutat. Res.*, 2010 Aug. 17 [Epub ahead of print].
23. Cammerer, Z., Schumacher, M. M., Kirsch-Volders, M., Suter, W. and Elhajouji, A. (2010) Flow cytometry peripheral blood micronucleus test *in vivo*: determination of potential thresholds for aneuploidy induced by spindle poisons. *Environ. Mol. Mutagen.* **51**, 278–284.
24. Liu, L., Liu, Y., Ni, G. and Liu, S. (2010) Flow cytometric scoring of micronucleated reticulocytes as a possible high-throughput radiation biodosimeter. *Environ. Mol. Mutagen.*, **51**, 215–221.
25. Elhajoui, A., Van Hummelen, P. and Kirsch-Volders, M. (1995) Indications for a threshold of chemically-induced aneuploidy in vitro in human lymphocytes. *Environ. Mol. Mutagen.*, **26**, 292–304.
26. Avlasevich, S. L., Bryce, S. M., De Boeck, M., Elhajouji, A., Van Goethem, F., Lynch, A., Nicolette, J., Shi, J. and Dertinger, S. (2010) Flow cytometric analysis of in vitro mammalian cell micronuclei: past, present, and future. *Mutagenesis*, **26**, 147–152.
27. Avlasevich, S. L., Bryce, S. M., Cairns, S. E. and Dertinger, S. D. (2006) In vitro micronucleus scoring by flow cytometry: differential staining of micronuclei versus apoptotic and necrotic chromatin enhances assay reliability. *Environ. Mol. Mutagen.*, **47**, 56–66.
28. Halicka, H. D., Bedner, E. and Darzynkiewicz, Z. (2000) Segregation of RNA and separate packaging of DNA and RNA in apoptotic bodies during apoptosis. *Exp. Cell Res.*, **260**, 248–255.
29. Fenech, M. (2007) Cytokinesis-block micronucleus cytome assay. *Nat. Protoc.*, **2**, 1084–1094.
30. Kamentsky, L. A. (2001) Laser scanning cytometry. *Methods Cell Biol.*, **63**, 51–87.
31. Darzynkiewicz, Z., Bedner, E., Li, X., Gorczyca, W. and Melamed, M. R. (1999) Laser scanning cytometry. A new instrumentation with many applications. *Exp. Cell. Res.*, **249**, 1–12.
32. Henriksen, M. (2010) Quantitative imaging cytometry: instrumentation of choice for automated cellular and tissue analysis. *Nat. Methods*, **7**, 331–332.
33. Luther, E., Kamentsky, L., Henriksen, M. and Holden, E. (2004) Next-generation laser scanning cytometry. *Methods Cell Biol.*, **75**, 185–218.
34. Peterson, R. A., Krull, D. L. and Butler, L. (2008) Applications of laser scanning cytometry in immunohistochemistry and routine histopathology. *Toxicol. Pathol.*, **36**, 117–132.
35. Pozarowski, P., Holden, E. and Darzynkiewicz, Z. (2005) Laser scanning cytometry. Principles and applications. *Methods Mol. Biol.*, **319**, 165–192.
36. Styles, J. A., Clark, H., Festing, M. F. and Rew, D. A. (2001) Automation of mouse micronucleus genotoxicity assay by laser scanning cytometry. *Cytometry*, **44**, 153–155.
37. Huang, X., Okafuji, M., Traganos, F., Luther, E., Holden, E. and Darzynkiewicz, Z. (2004) Assessment of histone H2AX phosphorylation induced by DNA topoisomerase I and II inhibitors topotecan and mitoxantrone and by DNA crosslinking agent cisplatin. *Cytometry A*, **58A**, 99–110.
38. Smolewski, P., Ruan, Q., Vellon, L. and Darzynkiewicz, Z. (2001) The micronuclei assay by laser scanning cytometry. *Cytometry*, **45**, 19–26.
39. Zhao, H., Traganos, F. and Darzynkiewicz, Z. (2010) Kinetics of the UV-induced DNA damage response in relation to cell cycle phase. Correlation with DNA replication. *Cytometry A*, **77A**, 285–293.

40. Tanaka, T., Huang, X., Halicka, H. D., Zhao, H., Traganos, F., Albino, A. P., Dai, W. and Darzynkiewicz, Z. (2007) Cytometry of ATM activation and histone H2AX phosphorylation to estimate extent of DNA damage induced by exogenous agents. *Cytometry A*, **71A**, 648–661.
41. Crissman, H. A., Darzynkiewicz, Z., Tobey, R. A. and Steinkamp, J. A. (1985) Correlated measurements of DNA, RNA and protein content in individual cells by flow cytometry. *Science*, **228**, 1321–1324.
42. Darzynkiewicz, Z. (2010) Critical aspects in analysis of cellular DNA content. *Curr. Protoc. Cytom.*, Chapter 7 Unit 7.2, pp. 7.2.1–7.2.8.
43. Kamentsky, L. A., Kamentsky, L. D., Fletcher, J. A., Kurose, A. and Sasaki, K. (1997) Methods for automatic multiparameter analysis of fluorescence *in situ* hybridized specimens with a laser scanning cytometer. *Cytometry*, **27**, 117–125.
44. Bedner, E., Ruan, Q., Chen, S., Kamentsky, L. A. and Darzynkiewicz, Z. (2000) Multiparameter analysis of progeny of individual cells in clonogenicity assays by laser scanning cytometry (LSC). *Cytometry*, **40**, 271–279.
45. Thomas, P., Harvey, S., Gruner, T. and Fenech, M. (2008) The buccal cytome and micronucleus frequency is substantially altered in Down's syndrome and normal ageing compared to young healthy controls. *Mutat. Res.*, **638**, 37–47.
46. Heddle, J., Fenech, M., Hayashi, M. and MacGregor, J. T. (2010) Reflections of the development of micronucleus assays. *Mutagenesis*, **26**, 3–10.
47. Hutter, K. J. and Stöhr, M. (1982) Rapid detection of mutagen induced micronucleated erythrocytes by flow cytometry. *Histochemistry*, **75**, 353–362.
48. Grawe, J. (2005) Flow cytometric analysis of micronuclei in erythrocytes. *Methods Mol. Biol.*, **291**, 69–83.
49. Criswell, K. A., Krishna, G., Zielinski, D., Urda, G. A., Theiss, J. C., Juneau, P. and Bleavins, M. R. (1998) Use of acridine orange in flow cytometric assessment of micronuclei induction. *Mutat. Res.*, **414**, 63–75.
50. Grawe, J., Zetterberg, G. and Amneus, H. (1993) DNA content determination of micronucleated polychromatic erythrocytes induced by clastogens and spindle poisons in mouse bone marrow and peripheral blood. *Mutagenesis*, **8**, 249–255.